UNIVERSITY OF SOUTHAMPTON

FACULTY OF NATURAL AND ENVORONMENTAL SCIENCES

School of Chemistry

Batteries Beyond Li-ion: An Investigation of Li-Air and Li-S Batteries

by

Luyi Yang

Thesis for the degree of Doctor of Philosophy

13/10/2015

UNIVERSITY OF SOUTHAMPTON

ABSTRACT

FACULTY OF NATURAL AND ENVORONMENTAL SCIENCES

Electrochemistry

Thesis for the degree of Doctor of Philosophy

BATTERIES BEYOND LI-ION: AN INVESTIGATION OF LI-AIR AND LI-S BATTERIES

Luyi Yang

This thesis describes studies on both Li-air and Li-sulfur batteries. First, the application of redox mediators/shuttles in the Li-air battery system is discussed. On one hand, by using ethyl viologen as the redox mediator/shuttle for oxygen reduction reactions (ORR), the discharge capacity of Li-air batteries could be improved. In addition, the UV/Vis spectroscopy results show that ethyl viologen can greatly reduce the lifetime of reactive superoxide radicals.

On the other hand, a cobalt complex was tested as the redox mediator/shuttle for oxygen evolution reactions (OER). The oxidised form of the complex directly reacts with lithium peroxide – the insoluble product of ORR which passivates the electrode. As a result, the passivation on the positive electrode is mitigated.

In the study on Li-sulfur batteries, two types of carbon were used as the conductive materials – carbon blacks and activated carbons. The sulfur/carbon composites for positive electrodes were prepared via different methods and with different sulfur content. To determine the properties of these composites, they were characterised with physical methods and electrochemical methods.

In addition, some measures were taken in order to suppress the shuttle mechanism in Li-S batteries which leads to capacity fading and overcharge. By using electrolyte additives or extra separators in Li-S cells, the Coulombic efficiencies were significantly improved.

Table of Contents

List of Tables

List of Figures

DECLARATION OF AUTHORSHIP

I, Luyi Yang declare that this thesis and the work presented in it are my own and has been generated by me as the result of my own original research.

Batteries Beyond Li-ion: An Investigation of Li-Air and Li-S batteries

I confirm that:

1. This work was done wholly or mainly while in candidature for a research degree at this University;
2. Where any part of this thesis has previously been submitted for a degree or any other qualification at this University or any other institution, this has been clearly stated;
3. Where I have consulted the published work of others, this is always clearly attributed;
4. Where I have quoted from the work of others, the source is always given. With the exception of such quotations, this thesis is entirely my own work;
5. I have acknowledged all main sources of help;
6. Where the thesis is based on work done by myself jointly with others, I have made clear exactly what was done by others and what I have contributed myself;
7. Parts of this work have been published as:

   L. Yang, J. T. Frith, N. Garcia-Araez and J. R. Owen, A new method to prevent degradation of lithium–oxygen batteries: reduction of superoxide by viologen, *Chem. Comm.*, 2015, **51**, 1705-1708, DOI: 10.1039/C4CC09208B

Signed:

Date: 13/10/2015

Acknowledgements

Firstly, I would like to thank my supervisors – Professor John Owen and Dr Nuria Garcia-Araez for the continual help, ideas and guidance throughout my study. Their knowledge and enthusiasm have been invaluable inspiration for me. I also want to thank Professor Andrew Hector and Dr Peter Birkin for the useful comments and advice.

I owe a debt of gratitude to several people who helped me in lab with their expertise: Alistair Clark, for his help with BET instrument; Dr Alex Madsen and Saddam Allehebe, for their help with the Li-S battery experiments; Dr Matt Lacey, James Frith, Dr Andy Lodge and Tom Homewood, for their help with the Li-air battery experiments. Thanks also go to all other members in my group: Jake Locke, Nora Intaranont, Mike Palmer, Will Richardson and James Dibden. It has been a pleasure to work with them.

I would like thank European Commission for funding LABOHR project, which made this thesis possible.

Finally, special thanks go to my parents and friends, whose support was priceless to me.

List of Symbols

Symbol	Explanation	Units
A	Surface area	cm^2
A	Absorbance	–
c	BET constant	–
c	Concentration	$mol\ L^{-1}$
C	Velocity of light	$m\ s^{-1}$
C_{dl}	Double layer capacitance	F
D	Diffusion coefficient	$cm^2\ s^{-1}$
d	Lattice space	Å
E	Potential	V
E^0	Standard potential of redox couple	V
F	Faraday constant	$C\ mol^{-1}$
G	Gradient	–
h	Plank's constant	$m2\ kg\ s^{-1}$
i	Current	A
I	Intensity of light	cd
k_2	Second-order reaction rate constant	$mol^{-1}\ L\ s^{-1}$
k_3	Third-order reaction rate constant	$mol^{-2}\ L^2\ s^{-1}$
L	Thickness	cm
l	Thickness of absorption cell	cm
N	Avogadro's number	–
n	Number of electron transfer	–
p	Equilibrium pressure	Pa
p_0	Saturation pressure	Pa
R	Resistance	Ohm
R	Gas constant	$J\ K^{-1}\ mol^{-1}$
R_{Ct}	Charge transfer resistance	Ohm
R_k	Radius of curvature	cm
R_s	Uncompensated resistance	Ohm
T	Temperature	K
t	Thickness of multilayer	cm
V	Adsorbed gas volume	cm^3
V_m	Monolayer adsorbed gas volume	cm^3
Z_W	Warburg diffusion impedance	–
γ	Liquid surface tension	$N\ m^{-1}$
ϵ	Extinction coefficient	$cm^{-1}\ mol^{-1}\ L^3$
θ	Contact angle	Degree
λ	wavelength	nm
ν	Scan rate	$V\ s^{-1}$
ν	Frequency	s^{-1}
σ	Conductivity	S
τ	Time constant	s
ω	Raman shit	cm^{-1}

List of Abbreviations

AB	Acetylene black
BET	Brunauer-Emmett-Teller
BJH	Barrett-Joyner-Halenda
BM	Ball mill
CMC	Carboxyl methyl cellulose
CNF	Carbon nanofibre
CNT	Carbon nanotube
DMCT	2,5-Dimercapto-1,3,4-thiadiazole
DME	Dimethoxyethane
DMSO	Dimethyl sulfoxide
DOL	1.3-Dioxolane
EtV	Ethyl viologen
GCPL	Galvanostatic cycling with potential limitation
HOMO	Highest occupied molecular orbital
LiPF6	Lithium hexafluorophosphate
LiTFSI	Bis(trifluoromethane)sulfonimide lithium
LTO	Lithium titanium oxide
LUMO	Lowest unoccupied molecular orbital
MPG	Multichannel potentialstats/galvanostats
OER	Oxygen evolution reaction
ORR	Oxygen reduction reaction
OTf	Trifluoromethanesulfonate
PAN	Polyacrylonitrile
PANI	Polyaniline
PEO	Polyethylene oxide
PFA	Perfluoroalkoxy alkane
PTFE	Polytetrafluoroethylene
PVDF	Polyvinylidene fluoride
$Pyr_{14}TFSI$	1-Butyl-1-Methylpyrrolidinium bis(trifluoromethane)sulfonimide
S/C	Sulfur/carbon
SEM	Scanning electron microscope
SOMO	Singly occupied molecular orbital
TEGDME	Tetra ethylene glycol dimethyl ether
XRD	X-Ray Diffraction

Chapter 1: Introduction

1.1 Significance of Research

With rapid growth of portable electric devices and hybrid vehicles, the needs for energy-storing devices with high capacity, reasonable size and weight are increasing. In the past decades, rechargeable batteries have been commercially utilised as important energy-storing devices in many areas due to their portability, long working life, high capacity and stable working voltage.

Since Planté first developed the rechargeable lead-acid battery in 1859, secondary batteries have been in existence for over 150 years.[1] During this period, people have managed to increase the capacity of rechargeable batteries as different types of chemical energy storing system have emerged. The specific energy of commercialised rechargeable batteries have been developed from lead-acid of 10~35 W h/ kg, nickel-cadmium of 10~40 W h/ kg to lithium-ion systems of approximately 150 W h/ kg. In addition, scientists have also managed to boost the cycle life from less than 25 cycles up to over 1000 cycles.

Among all the new chemical energy storing systems, lithium metal has the highest capacity (3861 mA h g^{-1}) and the lowest potential (-3.045 V vs. standard hydrogen electrode) among all the candidates as negative electrode materials. With high specific energy and capacity, lithium ion batteries are desirable for portable electronic devices such as cell phones, mp3s and laptops. In recent years, the demand for providing energy to hybrid energy vehicles has posed new problems for scientists: how to improve the specific energy and capacity of the batteries even further. In that case, the overall capacity of lithium batteries will be greatly limited by the positive electrode materials. For instance, the battery using $LiCoO_2$ as positive electrode material is one of the dominating products in the market due to its high theoretical specific energy and high operating voltage (3~4.2 V vs Li/Li^+)[2]. However, the practical gravimetric capacity of $LiCoO_2$ is limited to 140 mA h g^{-1},[2] which is not sufficient to become a power source for electric vehicles. In practice, people will only extract about half of the lithium from Li_2CoO_2 to prevent overcharge and for the safety issues. In addition, cobalt is toxic and expensive, layered oxides may trigger safety issues.[3]

Limited by the weight of the transition-metal-based structure in lithium-ion intercalation electrodes, it is not possible to significantly increase the specific

energy and capacity of lithium ion batteries. Therefore, scientists has turned to other systems for inspiration – lithium air (Li-air) and lithium sulfur (Li-S) batteries are two promising alternatives[4].

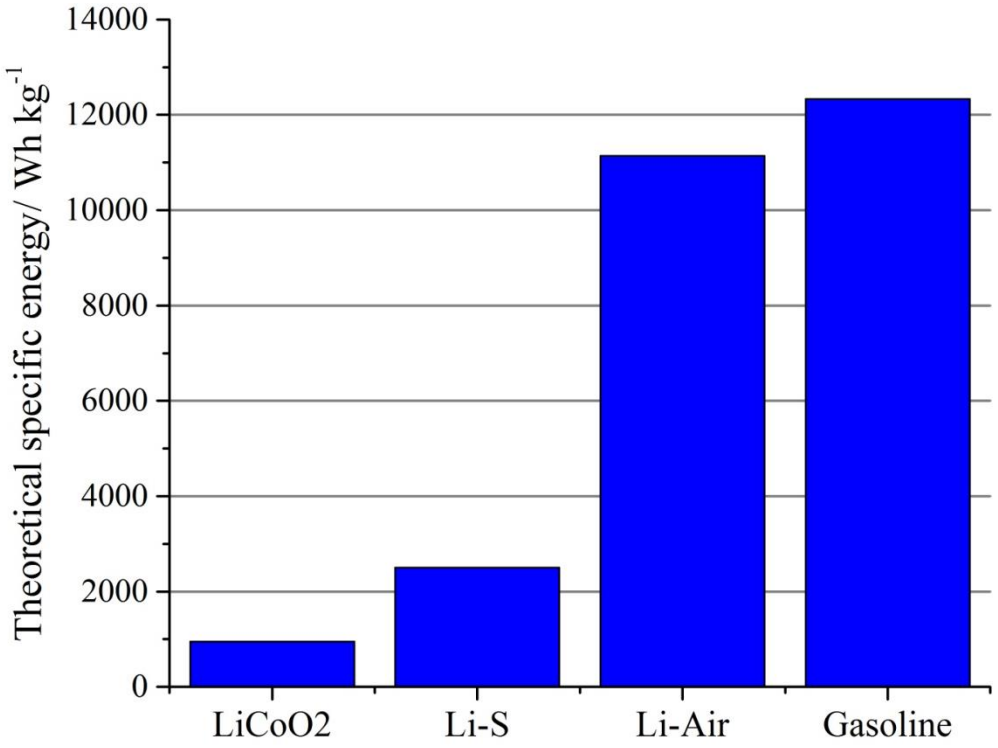

Figure 1.1 Theoretical specific energy for various types of rechargeable batteries compared to gasoline.

As shown in Figure 1.1, the specific energies of lithium air and lithium sulfur batteries are much higher than lithium ion batteries, which have made them promising candidates for the next generation batteries. Since Abraham reported the first experimental result on lithium air battery[5], it has been studied extensively because of its high theoretical specific energy (11140 W h/ kg).[4] In 1996, lithium air batteries in organic system were first reported by Abraham[6], the working voltage was between 2.0 and 2.8 V with specific energy of 250~350 W h/ kg. IBM also launched a lithium-air battery project called "Battery 500 Project" to develop battery that could keep electric vehicles running for 500 miles per charge.[4] In 2006, Bruce[7] reported a lithium air battery with capacity of 600 mA h g^{-1} for 50 cycles.

The use of sulfur as a positive electrode active material has also attracted a lot attention in recent years due to its high specific capacity (1675 mA h/ g). By coupling sulfur with Li metal, an average cell voltage of 2.15 V (vs Li/Li^+) can be obtained[8], as well as high specific capacity (1165 mA h g^{-1}) and high theoretical specific energy (2504 W h/ kg) when the masses of both electrodes are taken into

account. These values are much higher than any commercial lithium ion cell. Furthermore, other advantages such as low cost, abundance in nature, and environment friendliness have made sulfur one of the most promising positive electrode candidates for rechargeable lithium batteries.

1.2 Lithium Air Batteries

1.2.1 Principles of Li-Air Batteries

Metal-air batteries generate electricity from the redox reaction between oxygen and metal. Oxygen, which is the positive electrode material, can be continuously supplied from the atmosphere. This feature makes metal-air batteries similar to fuel cells, except that the negative electrode material is metal instead of hydrogen. Various types of metal-air battery are being studied: Li-air[4], Na-air[9], Zn-air[10,11], Al-air[12] and Mg-air[13]. Among them, the Li-air battery has the highest theoretical specific energy.

In general, there are four types of lithium air battery systems: non-aqueous[14], aqueous[15], solid state[16] and mixed aqueous/non-aqueous[17]. In this report, only the non-aqueous system will be discussed. The reason is that the non-aqueous system does not require lithium protection, which is necessary in the aqueous system and it is not affected by the low conductivity and slow reaction kinetics of the solid state system.

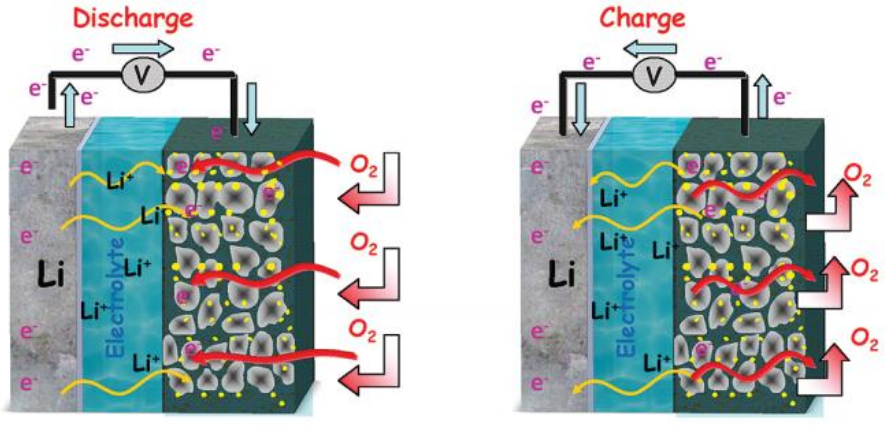

Figure 1.2 Schematic operation proposed for non-aqueous Li-air batteries.
(Reprinted from Ref[4]. Copyright 2010 American Chemical Society)

As shown in Figure 1.2, in a non-aqueous Li-air battery, during the discharge process, oxygen is reduced on the positive electrode (normally carbon) while the lithium metal negative electrode is oxidised which ideally generates a voltage of

2.96 V at equilibrium[4], forming lithium peroxide. During the charge reaction, Li_2O_2 is oxidised back to oxygen.

The overall discharge reaction is expressed as:

$$2Li + O_2 \rightarrow Li_2O_2 \quad \text{(Equation 1.1)}$$

It has been reported[18] that the first reaction product of oxygen reduction reaction (ORR) was superoxide, O_2^-, involving a one-electron process. Then the lithium superoxide will either disproportionate into lithium peroxide and oxygen,

$$2LiO_2 \rightarrow Li_2O_2 + O_2 \quad \text{(Equation 1.2)}$$

Or be reduced to lithium peroxide.

$$LiO_2 + Li^+ + e^- \rightarrow Li_2O_2 \quad \text{(Equation 1.3)}$$

To achieve rechargeability, Li_2O_2 should be oxidised back to oxygen during the re-charge.

$$Li_2O_2 \rightarrow O_2 + 2Li \quad \text{(Equation 1.4)}$$

1.2.2 Features and Challenges of Li-Air Batteries

As stated above, the specific energy of the lithium air battery is much higher than lithium-ion batteries, which is its most attractive feature. In addition, the Li-air battery also has the following advantages:

a. The theoretical specific energy is much higher compared to other lithium batteries.

b. Environmental friendly. Compared to lithium-ion batteries which contained metal oxide, the active material of the battery is oxygen and there is no toxic gas produced during its operation.

c. The active material is free in the atmosphere as long as dry oxygen can be extracted from the air.

Despite the great potentials in lithium air batteries, there are still many problems yet to be solved in aprotic lithium air batteries.

a. Because lithium peroxide is insulating and insoluble in most aprotic solvents used, it will form a passivating layer on the positive electrode. As

the battery is cycled, the passivation layer will gradually block the porous structure of the carbon positive electrode and cause capacity decay.

b. Superoxide free radical, the one-electron reduction product of oxygen, was reckoned aggressive to most of the organic solvent. Investigated with different methods, it has been shown that superoxide radicals can react irreversibly with carbonates[19,20] and the impurities in glymes[21]. Therefore, it is vital to find an electrolyte stable to the attack of superoxide radicals or to reduce the lifetime of superoxide.
c. The high overpotential during charging due to the insolubility of lithium peroxide not only decreases the energy efficiency of lithium air batteries but also requires larger potential stability window for the electrolyte because organic electrolytes might degrade under high potential.

1.2.3 Previous Studies of Li-Air Batteries

Representative studies of the progress in the Li-air battery research are selected in this chapter.

1.2.3.1 Positive Electrode Materials of Li-Air Batteries

The most common positive electrode material in lithium air batteries is porous carbon. The porous structure of carbon acts as the transfer channel for the electrolyte and oxygen, which also determines the diffusion process of oxygen in the positive electrode. Generally the oxygen is dissolved in the electrolyte and the concentration of oxygen depends on the solubility in different solvents. The free surface area of carbon that available for oxygen in electrolyte determines the performance of lithium air batteries - the ORR terminates as Li_2O_2 fully covers the pores. Therefore, the previous study of the positive electrode was mainly focus on the porous carbon that creates spaces where oxygen, electrolyte and electrode can meet – either a three phase junction (oxygen undissolved in electrolyte) or a two phase junction (oxygen dissolved in electrolyte), as shown in circled area a and b respectively in Fig. 1.3.

Previously, Mirzaeian et al.[22] studied the discharge capacity and potential of lithium air cells using carbon aerogels with controlled pore structure, pore size and surface area. As a result, the carbon with highest specific pore volume and surface area demonstrated highest capacity (1290 mA h g^{-1}, current density = 20 mA /g). Later on, they found that as they increased the volume of mesopores, higher capacity was obtained, indicating that mesoporous structure played an

important role in a Li-air battery.[23] It can be learned that by choosing or designing carbon with proper surface area and pore structure, the blocking process on the positive electrode can be slowed and the capacity can be improved.

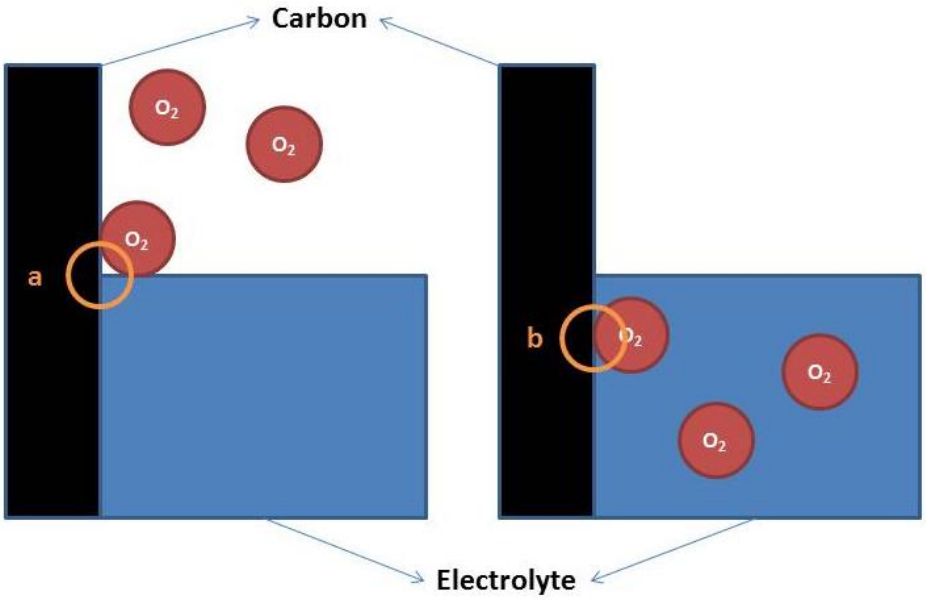

Figure 1.3 Schematic diagrams of three phase junction (a) and two phase junction (b) of carbon, oxygen and electrolyte.

It was also reported that the relationship between pore size distribution of positive electrode and capacity can be established. Tran et al.[24] reported that micropores and small mesopores were more likely to be blocked by the passivation layer which accounted for significant capacity fading. They also found a positive correlation between the average pore size and the capacity, which agreed with Mirzaeian's results. However, by building different models, Xue et al.[25] argued that large surface area and large pore size can both slow down the blockage of the positive electrode; therefore a compromise between the surface area and pore size should be made.

To further study the performance porous carbon as the positive electrode, Zhang et al.[26] applied single walled carbon nanotubes and carbon fibre mixture as the working positive electrode. The effect of electrode thickness and discharge rate on the capacity was studied. They found that for the same current density, the capacity decreased as the positive electrode thickness increased. For positive electrodes with same thickness, higher discharge rate led to lower capacity. By characterise the discharged electrode using scanning electron microscope (SEM), it was suggested that the side electrode close to oxygen source was fully blocked

while the carbon close to the separator was not fully covered with lithium peroxide.

However, all the experimental works above were performed in organic carbonate electrolytes. Since the stability of carbonates were proven to be poor against reduction products of oxygen (will be described in the next section), their suitability as positive electrode will need to be re-examined.

1.2.3.2 Electrolyte of Li-Air Batteries

Choosing a stable electrolyte with good cycling performance is also crucial. The study of electrolytes for lithium air batteries has drawn increasing attention since it was realized that the oxygen reduction reaction can produce various reactive intermediates towards aprotic electrolyte.

Apart from good ion conductivity and electrochemical window like in other batteries, a suitable electrolyte for lithium air should also have a high solubility of oxygen. Carbonates, ethers, alkanes and ionic liquids have been investigated as potential electrolytes for lithium air batteries.

The investigation started with carbonate-based electrolyte. But then it was reported that organic carbonate can degrade during the battery cycling based on the fact that the main discharge product of the cells was Li_2CO_3 or $LiRCO_3$ instead of Li_2O_2[27]. It was attributed to the high reactivity of O_2^- and O_2^{2-} towards other materials via various pathways[19,28,29], the decomposition of electrode was indicated by the evolution of CO_2[30].

McCloskey et al.[31] then reported that when using dimethoxyethane (DME), the main discharge product was Li_2O_2. However, the result also showed DME was unstable during the discharge process. In addition, the high vapour pressure (48 mmHg at 20°C) of DME also made it unsuitable as an electrolyte for lithium air batteries. Later on, other ether based systems were tested by Freunberger et al.[32] The result showed no evidence of Li_2O_2 formation after the 5th cycle.

The physical properties of electrolytes can also play an important role in their electrochemical performance. Read[33] reported that the solubility of oxygen in the electrolyte can determine the rate performance and the capacity of the battery. In addition, the viscosity had a large impact on the capacity under high current density (0.5 mA cm^{-2}). Xu et al.[34–36] suggested that the diffusion of oxygen in open channel (which was determined by the contact angle between the electrolyte and the electrode) was several magnitudes higher than the diffusion through the

liquid. Therefore, the wettability of the organic solvent can play a more important role in the cell performance compared to other physical properties such as oxygen solubility, viscosity and ion conductivity. They also proposed that by adding small amounts of crown ether (10-15 wt%) into the electrolyte, better cycling performance can be obtained.

Laoire et al.[37] studied organic solvents representing wide range of donor number: acetonitrile, DME, dimethyl sulfoxide (DMSO) and tetra ethylene glycol dimethyl ether (TEGDME). They found that the solvent and the cations in the electrolyte had a combined action on the final products and the rechargeability. In the presence of tetrabutylammonium ion (TBA^+), the rechargeability was greatly enhanced, which can be explained by the hard soft acid base theory involving the TBA^+-O_2^- complex. In this case, the superoxide species will neither disproportionate nor be further reduced into lithium peroxide.

The Lithium-Air Batteries with split Oxygen Harvesting and Redox process (LABOHR) project proposed using ionic liquids as the electrolyte, which have been vastly investigated in areas such as batteries, super-capacitors, actuators, dye sensitised solar cells and thermo-electrochemical cells due to their non-volatile, non-flammable and high ion conductivity properties[38]. Pyrrolidinium-based ionic liquids were tested[39] with and without lithium bis(trifluoromethanesulfonyl) imide (LiTFSI). The result have suggested that 1-butyl-1-methylpyrrolidinium bis(trifluoromethylsulfonyl)imide ($Pyr_{14}TFSI$) was resistant towards degradation in lithium-oxygen batteries.

To sum up, the ideal electrolyte of Li-air batteries should have following properties: 1. stability and electrochemical window; 2. low viscosity; 3. low volatility; 4. high oxygen solubility.

1.2.3.3 Catalysts/Mediators for Li-Air Batteries

It has been stated above that the accumulation of lithium peroxide on the positive electrode was the main cause for the capacity fading in lithium air batteries. There are two main approaches to solve the problem: one is to increase the solubility of lithium peroxide in the electrolyte, the other is to use catalysts or mediators to prevent the formation of the passivation layer. The catalysts and mediators can be classified into heterogeneous and homogeneous ones based on their phases. As for heterogeneous catalysts there are three types of material being investigated: porous carbon, transition metal oxide and noble metal.

Normally, carbon only served as the positive electrode (porous current collector) in lithium air batteries. However carbons can sometimes act as catalysts. Xiao et al.[40] have reported that the use of hierarchically porous graphene as positive electrode material demonstrated excellent capacity (15000 mA h g^{-1}). It was suggested that the good performance was attributed to the defects and functional groups on the graphene, which favoured the formation of isolated nano-sized Li_2O_2 hence the blocking was prevented. Similarly, it was reported by Kichambare et al.[41] that by using nitrogen doped porous carbon, the performance in ORR was enhanced with higher surface area and larger pore size.

Débart et al.[42] proposed using manganese oxide with different structures as the catalyst for lithium air batteries. As a result, α- MnO_2 nanowire demonstrated higher cycling capacity than other structures (initial capacity = 3000 mA h g^{-1}, capacity after 10 cycles = 1500 mA h g^{-1}). Then they looked into other metal oxides such as Fe_2O_3, Fe_3O_4, CuO, $CoFe_2O_4$, and Co_3O_4. Though Fe_2O_3 exhibited better initial capacity, its cycling performance was poor; whereas Co_3O_4 showed both good initial capacity and cyclability. Oh et al.[43] used pyrochlore (Na, $Ca)_2Nb_2O_6$(OH, F) as the solid catalyst, which also showed good electrochemical performance. Precious metal oxides have also been used as catalysts. RuO_2 was coated on the surface of CNT to protect it from contacting with Li_2O_2[44].

Lu et al.[45] used commercialised XC-72 carbon loaded with 40 % Au and Pt nanoparticles respectively as the positive electrode. The results indicated that Au/C positive electrode was effective on ORR while Pt/C was effective on OER. They also used positive electrode loaded with Pt-Au alloy nanoparticles as the catalyst[46], which proved to be active on both ORR and OER. The discharge potential was 150-360 mV higher in the presence of catalyst and the average charging potential was 3.6 V, which was much lower than 4.5 V. By using differential electrochemical mass spectroscopy, Bondue et al.[47] measured that with Au loaded positive electrode, the final product of oxygen reduction product was Li_2O_2. More recently, Lu et al.[48] used Al_2O_3 coating on carbon to prevent the decomposition of electrolyte on carbon. In addition, palladium nanoparticles were also deposited on the positive electrode as the catalyst. The new positive electrode not only lowered the charging potential but also extended the cycle life of the cell. Thapa et al.[49] have demonstrated that using Pd/MnO_2 mixture as the catalyst can also significantly decrease the charging potential to 3.7 V due to the fact that by adding Pd, the oxidation of carbon was avoided. Li et al.[50] deposited Ru nanoparticles onto a carbon nanotube paper, with current density of 500 mA g^{-1}, stable capacity of 5000 mA h g^{-1} was obtained over 20 cycles. Similarly, Sun

et al.[51] deposited Ru particles on graphene sheets, low charge/discharge overpotential of 0.355 V and stable capacity of 1000 mA h g^{-1} was obtained over 200 cycles.

Another type of catalyst is transition metal nitride. Displaying similar catalytic properties as precious metals, transition metal nitrides have attracted a lot of attention. Previous studies have focused on their catalytic capability in aqueous systems[52–54]. In later researches on non-aqueous systems, MoN[55], Fe/N[56] and TiN[57] particles were deposited on the carbon. They all exhibited superior cycle life.

It was also reported that even though some materials, such as MnO_2 and Pt, might result in higher capacity and lower overpotential, they would lead to electrolyte degradation.[58]

In recent years, homogeneous redox shuttles and mediators in Li-air batteries have drawn increasing attention due to their excellent electrochemical behaviour. The concept of redox shuttle was firstly introduced to the lithium-ion battery system to prevent overcharge. A wide range of chemicals have been chosen as the redox shuttles such as 2,5-ditertbutyl-1,4-dimethoxybenzene[59], n-butylferrocene[5] and dimethoxydiphenylsilane[60]. Compared to heterogeneous catalysts, the homogeneous mediators have the following advantages:

a. More accessible to reaction sites: because the mediators are normally dissolved in the electrolyte, therefore they can almost access every corner in the positive electrode, especially the small porous structure which is hard to access for solid catalysts.

b. Faster reaction rate: because the mediator exists in the electrolyte, the reaction between mediator and dissolved oxygen does not require an interface. The reaction rate is expected to be significantly faster.

c. Easier to prepare: the mediator can be dissolved in the electrolyte in any concentration desired and the preparation is much easier compared to doping catalyst in the carbon.

In 2013 Lacey et al.[61] proposed ethyl viologen (EtV) as a discharge shuttle facilitating remote chemical oxygen reduction so that the formation of lithium peroxide can be kept away from the positive electrode. The results from cyclic votammograms showed that EtV can greatly increased the peak current for the oxygen reduction in the ionic liquid. This was because the reduced viologen can quickly react with oxygen, forming its oxidised form (shown in Fig. 1.4).

Afterwards, Sun et al.[62] then used iron phthalocyanine as a redox shuttle which delivered superoxide and electrons between the electrode and the insulating lithium peroxide product. As a result, no Li_2O_2 was observed contacting with the carbon, which greatly enhanced the performance of the cell.

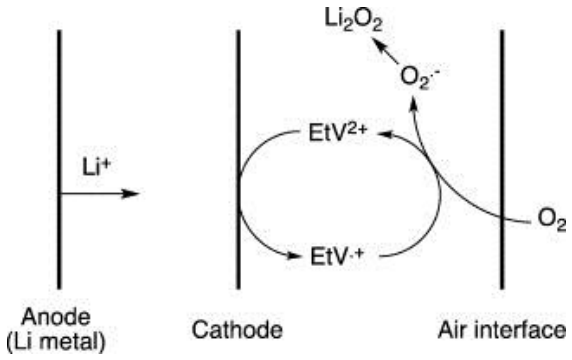

Figure 1.4 Schematic diagram of ORR in the Li-Air battery with EtV. (Reprinted from Ref[61]. Copyright 2013 Elsevier)

Later on, articles about redox mediators for the recharge process were published in succession. Chen et al.[63] published an article in Nature Chemistry, in which they used tetrathiafulvalene (TTF) as a redox mediator for the charging process. They demonstrated that TTF can efficiently oxidise Li_2O_2 and promote the recharge process by cycling a cell containing TTF for 100 times with excellent reversibility. Triiodide/iodide, which is normally used as shuttle in dye sensitised solar cells, was applied as the photo-assisted redox mediator in the lithium air battery by Yu[64]. In addition, Matsuda et al.[65] also reported using tetra-tert-butylphthalocyanine cobalt and tetrabutoxyphthalocyanine cobalt as redox mediators. As a result, a lower charging potential was achieved.

Lim et al.[66] used soluble mediator (LiI) combined with hierarchical nanoporous positive electrode in the Li-Air battery system. The 3D network electrode facilitated fast transport of Li^+, O_2 and the mediator. In the presence of the mediator, the charging potential significantly decreased and high capacity (1000 mA h g^{-1}) after 900 cycles was obtained. Bergner et al.[67] reported that by adding 2,2',6,6-tetramethylpiperidinyloxyl (TEMPO) into the electrolyte, the charge potential was also reduced by 500 mV (Fig. 1.5). Moreover, the addition of TEMPO managed to double the cycle life of the cell.

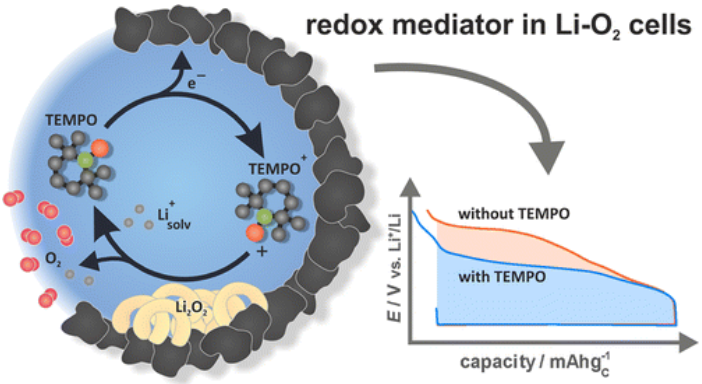

Figure 1.5 Schematic catalytic cycle for the electrochemical charging of Li-O_2 cell with TEMPO. (Reprinted from Ref[67]. Copyright 2014 American Chemical Society)

In Li-air batteries, the difference between a shuttle and a mediator is that a shuttle has relatively high diffusion coefficient or high concentration so the oxygen will be consumed before it can diffuse to the positive electrode.

1.2.3.4 Negative Electrode for Li-Air Batteries

Conventionally, lithium metal was used as the negative electrode for lithium air batteries. However, some problems still need to be solved with lithium negative electrode: the formation of dendrites and dead lithium might bring safety issues and loss of negative electrode material; complex reactions on the interface might lead to low efficiency of cycling[68].

The formation of lithium dendrites is due to the uneven deposition and dissolution of lithium on the negative electrode surface. The continuous growth of lithium dendrites might eventually cause short circuit of the battery. Different approaches have been tested in order to avoid dendrite formation. One way of protecting lithium was to deposit a protecting ion conducting layer on the lithium surface, such as lithium aluminium titanium phosphate layer [$Li_{1+x}Al_xTi_{2-x}(PO_4)_3$, $Li_{1+x+y}Al_xTi_{2-x}Si_yP_{3-y}O_{12}$][4]. Lee et al.[69] proposed a composite protective layer made of Al_2O_3 and polyvinylidene fluoride-hexafluoro propylene on the lithium negative electrode. The results showed that the protective layer improved the cycling stability of the cell.

Ding et al.[70] proposed a new dendrite-free lithium deposition using a mechanism called self-healing electrostatic shield. In this system, low concentration of selected cation (such as Cs^+) formed a positive charged electrostatic shield around the initial dendrite tip without reduction or deposition

of additive. This shield can repel the adjacent and keep the dendrite from growing.

1.2.3.5 Oxygen Selective Membrane

So far, most lithium air cell systems have been operated under dry oxygen atmosphere. However, before the cell can be tested under air, which contains water, certain problems need to be solved.

The water in the air might enter the cell and corrode the lithium metal negative electrode, causing safety issues. Moreover, in the system with poor sealing, the organic solvent in the electrolyte might evaporate or absorb water, which will affect the capacity and the lifetime of the cell. By introducing an oxygen selective film that can both filter out the water and keep the electrolyte in the cell, the lithium air system can be greatly improved.

By using Teflon coated fiberglass cloth as an oxygen selective membrane, Crowther et al.[71] have managed to protect the cell from water contamination. Their results showed that after 40 days of cycling only 2% of the electrolyte evaporated, also the lithium metal still looked shiny with only 13–24 mV over potential.

Highly conductive polyaniline membranes synthesised by a proton doping method were tested as an oxygen membrane by Fu et al.[72] It was reported that under the humidity of 20 %, the cell with membrane exhibited higher capacity compared to one without membrane. In addition, impedance spectroscopy showed that with the membrane, the impedance increase with cycle number had slowed down.

1.3 Lithium Sulfur Batteries

1.3.1 Principles of Li-S Batteries

Since Herbet and Ulam[73] introduced sulfur as a positive electrode material in 1962, sulfur batteries were considered promising energy storage devices. At room temperature, sulfur exists as an octatomic ring molecule S_8.

Unlike the insertion mechanism in lithium-ion batteries, the energy was released and stored by breaking or forming S-S bonds. As reported in previous research, sulfur reduction is a multistep electrochemical process in which different intermediate species are produced[74-76]. The reaction between lithium metal and elemental sulfur (S_8) will result in lithium polysulfide with general formula Li_2S_n. As shown in Fig 1.6, similar to Li-air cells, the reduction of S_8 also takes place at the three phase junction between sulfur, conductive material and electrolyte.

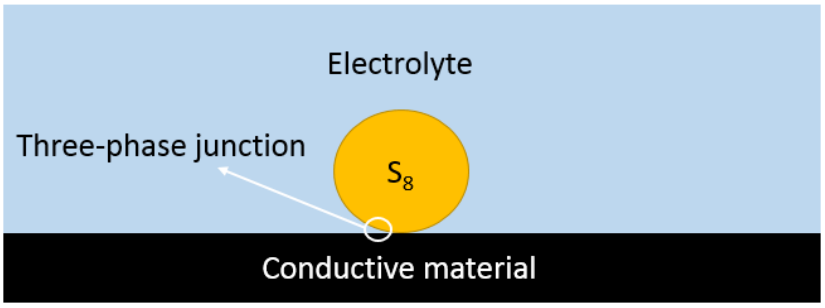

Figure 1.6 Schematic figure of a three-phase junction between sulfur, electrolyte and conductive material in the Li-S cell.

Long chain polysulfides such as Li_2S_8 and Li_2S_6 are first produced and gradually shortened as the reduction process continues. Ideally, when the sulfur is completely reduced, the overall reaction is:

$$16Li + S_8 \rightarrow 8Li_2S \quad \text{(Equation 1.5)}$$

After decades of research, the discharge mechanism of Li-S batteries is still in debate. On the one hand, some authors, e.g. Mikhaylik and Shim[74,76], have proposed relatively simple discharge process, in which only some major polysulfides, such as Li_2S_4 and Li_2S_2 were considered as intermediate species.

$$4Li + S_8 \rightarrow 2Li_2S_4 \quad \text{(Equation 1.6)}$$

$$Li_2S_4 + 2Li \rightarrow 2Li_2S_2 \quad \text{(Equation 1.7)}$$

$$2Li_2S_2 + 2Li \rightarrow 2Li_2S \text{ (Equation 1.8)}$$

It is generally assumed that due to the insolubility and insulating property of Li_2S_2, it is difficult to reduce it to Li_2S completely.

On the other hand, more complex processes were proposed. Barchasz et al.[75] investigated this process by using high-performance liquid chromatography, UV-visible absorption, and electron spin resonance spectroscopies. The results confirmed the existence of other forms of polysulfide, such as Li_2S_8, Li_2S_6, and Li_2S_3

The discharge profile of Li-S batteries in most literature as well as in this report was recorded as a two-plateau reduction process (Figure 1.6). Since the discharge mechanism will not be discussed in depth in this report, the assumption of simple mechanism will be taken. Therefore, the first plateau (E = 2.4-2.1 V vs Li/Li^+) represents the process of reduction from S_8 to high order polysulfides and the second plateau (E = 2.1-1.8 V vs Li/Li^+) represents the further reduction from polysulfides to Li_2S_2 or Li_2S.

As for the charge of lithium sulphur batteries, there are also two plateaus which are much less distinctive.

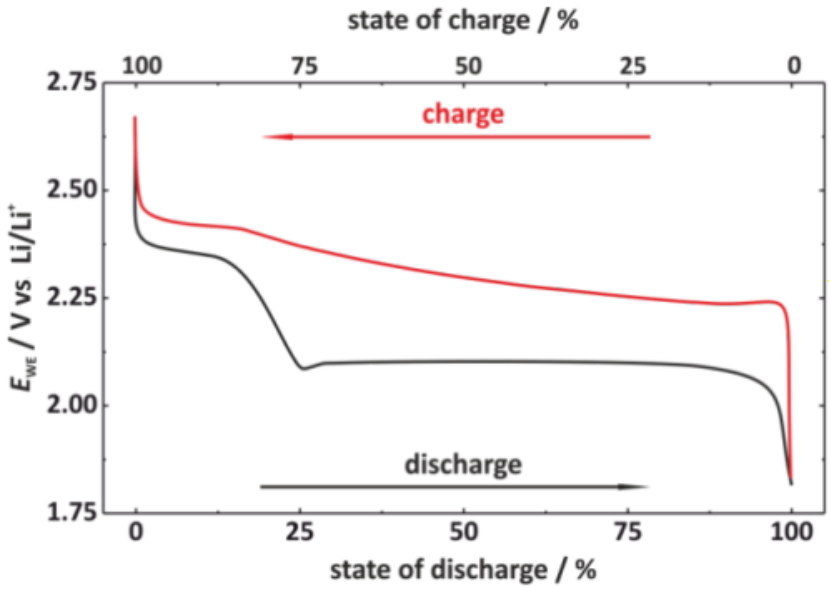

Figure 1.7 Typical discharge/charge profile of lithium sulfur batteries (Reprinted from Ref[77], open access material)

1.3.2 Features and Challenges of Li-S Batteries

Compared to other secondary batteries, the Li-S battery has the following advantages:

a. High theoretical specific capacity (1675 mA h g^{-1}) and specific energy (2600 Wh Kg^{-1}).

b. Sulfur is abundant on earth (17th most abundant element) and inexpensive.

c. Sulfur is non-toxic; no toxic gas will be produced during the charge-discharge processes.

However, there are also some issues remained to be solved for the Li-S battery:

a. Sulfur is an insulating material (5×10^{-30} S cm^{-1} at 25°C), and so are the final products Li_2S_2 and Li_2S.

b. Long chain polysulfides (Li_2S_n, $3\leq n\leq 8$) are soluble in the electrolyte. The polysulfide will increase the viscosity of the electrolyte, leading to lower conductivity. More importantly, they can also diffuse to the negative electrode through the separator. The “escaped” polysulfides will be chemically reduced by lithium, forming lower-order polysulfide - the insoluble ones like Li_2S and Li_2S_2 will deposit on the negative electrode while the longer ones will diffuse back to positive electrode. This process, which is called “shuttle effect”, results in loss of active material and columbic efficiency.

c. The proposed final product Li_2S has a lower density than S_8. Therefore, a volume expansion of sulfur is expected, which will destroy the positive electrode structure and cause capacity fading.

d. If Li metal is chosen as negative electrode, the growth of lithium dendrite needs to be inhibited since it will lead to short-circuit and safety issues.

1.3.3 Previous Research of Li-S Batteries

Representative studies of the progress in the Li-S battery research are selected in this chapter.

1.3.3.1 Positive Electrode Studies of Li-S Batteries

The study on positive electrode materials has been the main focus of the lithium sulfur battery researches. The main effort to improve the positive electrode was to either increase the sulfur loading in the positive electrode or suppress the shuttle effect. Many research results have showed that porous

electrode with nano-structure can improve the performance of the Li-S battery since a higher surface area can enhance the contact between electrode and electrolyte, hence increase the number of reaction sites. Therefore, it is important to find a positive electrode material with proper morphology and structure in order to optimise the overall performance of the cell.

1.3.3.1.1 Metal Sulfide Positive Electrode

The conventional negative electrode for the Li-S battery was lithium metal, which might lead to dendrite growth and safety issues. Therefore, pre-lithiated sulfur – Li_2S has been tested as a positive electrode material. The theoretical capacity of Li_2S is 1165 mA h g^{-1}, which is still much higher than Li-ion batteries. Same as element sulfur, Li_2S is also an insulator[78], so conductive material is needed.

Takeuchi et al.[79] prepared Li_2S/carbon (acetylene black) composite via spark plasma sintering method. The first charge and discharge capacity for the composite material prepared under 600 °C achieved 1200 mA h g^{-1} and 200 mA h g^{-1} respectively. Yi Cui group[78] also studied the properties of Li_2S as a positive electrode material. By reducing the sulfur in sulfur/CMK-3 composite with butyl-lithium, Li_2S/CMK-3 was prepared. Under the rate of C/8, the first discharge capacity was obtained as 482 mA h g^{-1}. However the capacity retention was poor. Lin et al.[80] coated graphene oxide on Li_2S nanoparticles in order to immobilise the Li_2S. As a result, the cycling performance was enhanced due to the higher utilization of active material.

Instead of mixing with carbon based material, Li_2S was also mixed with metals such as Fe[81], Co[82] and Cu[83,84]. In these systems, the reaction was:

$$M + xLi_2S \rightarrow MS_x + 2xLi^+ + 2xe^- \quad \text{(Equation 1.9)}$$

As a result, the discharge potential decreased to 1~2 V and the capacity was also affected due to the fact that the metals are heavier than carbon.

1.3.3.1.2 Organic Sulfide Positive Electrode

Organic sulfide positive electrode is defined as organics or polymer that release or restore energy by breaking or forming S-S bond. Various organic sulfide compounds have been proposed as potential positive electrode materials.[85]

In the 1990s, dimercaptan (DMCT) was studied as a possible material for positive electrode. Because its redox rate under room temperature was slow, it was proposed that using polyaniline (PANI) as a catalyst can enhance the electrochemical performance of DMCT.[86,87] Since PANI is a conducting polymer as well as an electrochemical active material, it can work as a conductive material but also provide some amount of capacity. Park et al.[88] also suggested that the addition of Ag particles can improve the performance of DMCT.

Thereafter organic sulfide with multiple S–S bond, was studied.[89] Dimers of disulfide, trisulfide, tetrasulfide of 5-methyl-1,3,4-thiadiazole-2-thiol and polymers of DMCT were tested in terms of electrochemical performances. Cyclic voltammetry results showed that the reduction peak of trisulfide and tetrasulfide was higher than the peak of disulfide. The specific energy for Li–DMCT-disulfide, Li–DMT-trisulfide, and Li–DMCT-tetrasulfide batteries was tested as 385, 590, and 700 Wh kg^{-1}, respectively.

It was also reported that by heating polymer–sulfur mixture, conductive sulfurized polymer can be prepared. Wang et al.[90,91] prepared sulfurized polyacrylonitrile (PAN) which is conductive in room temperature. The electrochemical tests showed that the capacity was 850 mA h g^{-1} for the first cycle and 600 mA h g^{-1} after 50 cycles. Further studies showed that, with this material, the modification using carbon nanotubes[92] or graphene[93] could increase the usage of the active material and cycling performance.

1.3.3.1.3 Carbon–Sulfur positive electrode

Compared to using metal sulfide and organic sulfide, the use of elementary sulfur as active material in positive electrode has advantages such as higher capacity, higher specific energy and lower cost. However, elementary sulfur is an insulator in room temperature and suffers from active material loss[94] and shuttle effect[74] due to the solubility of polysulfide in the electrolyte. In addition, the insoluble discharge product Li_2S and Li_2S_2 will precipitate on both positive electrode[95,96] and negative electrode[97], causing the capacity decay. There are three types of carbon under investigation: porous carbon, graphene and carbon nanotubes.

When mixed with porous carbon, elementary sulfur was usually loaded into the pore structure of carbon. One the one hand, the high electric conductivity of carbon can greatly enhance the electrochemical activity of sulfur; on the other hand, the large surface area and pore structure was expected to confine more

polysulfide so the diffusion of polysulfide can be suppressed. In 2002, Wang et al.[98,99] proposed impregnating melted 30 wt% sulfur into pores of activated carbon by using step-heating method. The capacity was 800 mA h g^{-1} for first cycle and 440 mA h g^{-1} after 25 cycles. However, when the weight percent of sulfur reached 60 %, the first cycle capacity was only 180 mA h g^{-1}.

In recent years, with the development of nano-material synthesis, meso-porous carbon, which is defined as carbon with pore size between 2 to 50 nm, has been widely reported in the use of Li-S batteries[100]. Other than having large surface area, they also have large pore volume, which is beneficial to sulfur loading and ion transfer.

By heating sulfur and a porous carbon with high surface area (1472.9 m^2 g^{-1}), Lai et al.[101] prepared an S/C composite. Due to the high surface area of carbon, the sulfur was expected to fully contact with carbon. The surface area was reduced to 24.4 m^2 g^{-1} after the mixing with sulfur, which indicated the filling of the pores. The S/C composite with 57 wt% sulfur delivered an initial high specific capacity up to 1155 mA h g^{-1} and a capacity of 745 mA h g^{-1} after 84 cycles at the current density of 40 mA g^{-1}. Wang et al.[102] synthesised mesoporous carbon through the co-polymerization of sodium silicate and sucrose and heated it with sulfur in mass ratio of 6:1. The initial capacity was 1100 mA h g^{-1}.

By choosing more ordered mesoporous carbon, the performance might be further improved. It was reported by Nazar group[103] that ordered mesoporous carbon CMK-3 (pore diameter 3-4 nm, pore separation 6.5 nm) was used as conducting material in the lithium sulfur battery and 70 wt% sulfur was loaded in the carbon (Fig. 1.7). The electrochemical results showed that the initial capacity was 1005 mA h g^{-1} and the capacity after 20 cycles was still 800 mA h g^{-1}. In addition, polymer modification with polyethyleneglycol successfully improved the initial capacity and capacity after 20 cycles to 1320 and 1100 mA h g^{-1} respectively. Similarly, Liang et al.[104] used template to synthesis mesoporous carbon with pore size of 7.3 nm. Then KOH was used to activate the carbon, secondary pores with 2 nm diameter was made. However, using this carbon the capacity fading was severe with relatively high sulfur loading (51.7 wt%). Balach et al.[105] demonstrated improved electrochemical performance by inserting a mesoporous carbon interlayer between the positive electrode and separator. The mesoporous carbon interlayer acted as polysulfide reservoir which stopped the polysulfide diffusion.

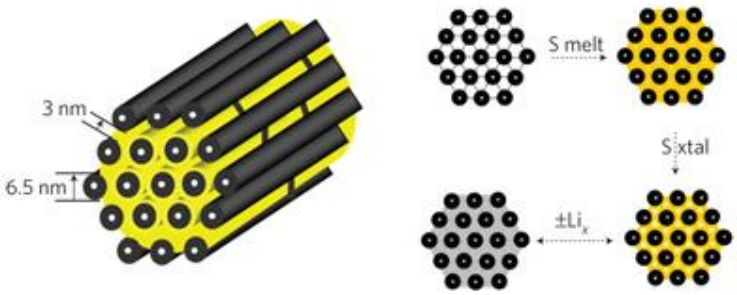

Figure 1.8 Schematic diagram of the sulphur (yellow) confined in the interconnected pore structure of mesoporous carbon, CMK-3 (Reprinted from Ref[103]. Copyright 2009 Nature Publishing Group.)

Instead of using commercialized carbon or templates, researchers have turned to natural sources for the synthesis of carbon - fish scale[106], crab shell[107] and apricot shell[108] have been used. These carbons not only have highly ordered structure, but also showed good electrochemical performance.

Jayaprakash et al.[109] used scalable approach to prepare hollow carbon capsules to encapsulate elementary sulfur in its interior pores. S/C composite with 70 wt% sulfur content was tested and under rate of 0.5 C the initial capacity was 1071 mA h g^{-1}, the capacity remained 91 % after 100 cycles, which is better than other results have been published.

As a commonly used conducting material in battery systems, acetylene black has its advantages such as high conductivity, good wettability and good flexibility. Zhang et al.[110] heated acetylene black (specific surface area = 65 m^2 g^{-1}) with sulfur under Ar atmosphere and S/C composite with 36 wt% sulfur was prepared. After 50 cycles, the capacity was 500 mA h g^{-1}. However, according to the study, the conductivity was affected as the sulfur content increased, leading to lower capacity.

Wang et al.[111] reported using expanded graphite as conductive material in the lithium sulfur battery. They studied the electrochemical performance of S/C composite with 20-80 wt% sulfur. The result showed that with 60 wt% of sulfur, the initial capacity was 1210.4 mA h g^{-1} and the capacity after 70 cycles was still 879.5 mA h g^{-1}. Li et al.[112] also studied sulfur/graphite composite. It was proposed that the good electrochemical performance was due to that graphite acted as micro container and current collector which not only confined sulfur in the positive electrode but also provided sufficient electrons.

Different from 3D network of graphite, graphene is a 2D sheet consists of carbon atoms. Due to its excellent conductivity, mechanical strength and large surface area, it has been intensively investigated in energy storage area[113,114]. However, due to its lack of closed structure, graphene cannot capture sulfur through the simple heating treatment.[115]

More studies proposed that reducing sodium thiosulfate in solution was a more efficient method to prepare S-graphene composite.[116-119] Wang and Yang et al.[116] used acetylene black decorated graphene sheets to wrap around sulfur particles coated with poly (ethylene glycol) (shown in Fig. 1.8). After 100 cycles, the capacity remained approximately 600 mA h g^{-1}, however the rate performance was not satisfactory.

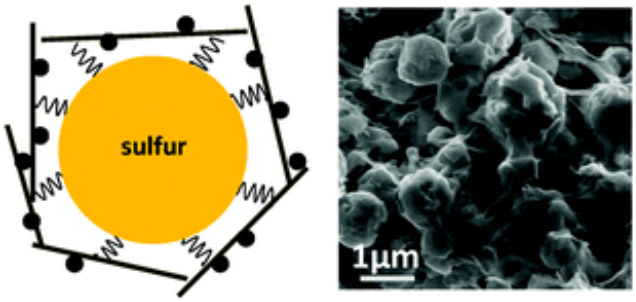

Figure 1.9 Schematic (left) and SEM characterization (right) of S-graphene composite. (Reprinted from Ref[116]. Copyright 2011 American Chemical Society)

Cao et al.[118] prepared sandwich-like S-graphene composite by inserting sulfur into the spaces between graphene layers. The results showed that the composite which containing 70 wt% sulfur provided 505 mA h g^{-1} at the C-rate of 1C. By further wrapping the composite with Nafion, the capacity was kept up to 75 % after 100 cycles. Functionalization of graphene is another approach to immobilise sulfur. Zu et al.[120] prepared hydroxylated graphene-sulfur composite by modifying graphene under room temperature. The composite exhibited good rate performance due to the hydroxyl group can bind with sulfur, rendering the sulfur in amorphous state during deposition and preventing the shuttle effect. Alternatively, sulfur loaded graphene foam, which had better flexibility, was also investigated[121]. The loading on the foam was tuneable between 3.3 to 10.1 mg cm^{-2} and with sulfur loading of 10.1 mg cm^{-2} an extremely high areal capacity was achieved (13.4 mA h cm^{-2}).

Another important carbon-based material used in lithium batteries is carbon nanofibre (CNF)/ carbon nanotube (CNT). They can form a stable and conductive network, providing good contact between active material and the current collector.

Elazari et al.[122] took advantage of the large surface area and absorbing ability of CNF, using it to absorb sulfur vapour. The synthesis of S/C composite (33 wt% of S) did not require any binder. The capacity after 80 cycles was still 800 mA h g^{-1}. Zheng et al.[123] used anodic aluminium oxide template to prepare CNF and impregnate sulfur into the nanofibre. By doing so, they expect to prevent the insoluble product depositing on the exterior wall of the fibre. In addition, the high aspect ratio helped to capture the sulfur and the thin wall of the fibre allowed rapid ion transport. Sulfur/CNT composite was also reported by different groups[124–126]. Guo et al.[127] synthesised sulfur/CNT composite via heating treatment, the composite showed good cycling performance (700 mA h g^{-1} after 80 cycles).

Recently, titanium based conductive materials have drawn considerable amount of attention. A sulfur/TiO_2 yolk-shell nanostructure composite was reported by Yi Cui group[128]. The structure had a void space which can accommodate the volume expansion of sulfur so that the TiO_2 shell remained intact. At the C-rate of 0.5 C, the capacity was 1030 mA h g^{-1} and the Coulombic efficiency was 98.4% over 1000 cycles. Most importantly, only 33 % capacity decay was observed over 1000 cycles, demonstrating a good long-term cycling ability. More recently, a sulfur/Ti_2C composite[129] also exhibited good cycling performance (80 % capacity retention over 400 cycles) due to the strong interaction between polysulfide and titanium atoms on the electrode surface.

1.3.3.1.4 Conductive Polymer-Sulfur Positive Electrode

Unlike carbon, conducting polymer can be dispersed in the solvent and the polymerization can occur at relatively low temperature. Therefore, certain composites with structures that are difficult to design with carbon can be synthesised with polymer. In addition, some functional group on the polymer can form chemical bond with sulfur, which also helps the immobilization of sulfur.[130,131] Polymers also have good mechanical flexibility and self-repairing ability, which may be advantage in the case of positive electrode volume expansion.[132]

It has been reported that a sulfur/PANI nanotube composite demonstrated good cycling ability. They first prepared PANI nanotube, and then heated it with

sulfur. As a result, sulfur not only was absorbed into the nanotube but also formed S-S bonds with the polymer. The capacity was still 568 mA h g^{-1} after 100 cycles and 432 mA h g^{-1} after 400 cycles at rate of 1C. The capacity fading was explained as the result of shuttle effect and some irreversible break of S-S bond.

Other polymers have also been used in Li-S batteries such as polypyrrole[133], polythiphene[130] and PAN[134]. It was reported good cycling lifetime can be obtained by using PAN-sulfur composite[92,135,136]. In this composite, part of sulfur will bond with PAN, and the unbonded sulfur will be impregnated into the polymer structure. Although the capacity retention was 90 % over 380 cycles, the sulfur content was low and the discharge potential was below 2.0 V.

Polymer can be also used to improve the performance of C-S composites. By coating poly(3,4-ethylenedioxythiophene) and poly(styrenesulfonate) on the S/CMK3 composite, the Coulombic efficiency was improved from 93 % to 97 % and the capacity fading dropped from 40 % to 10 % over 100 cycles. Other polymers such as Nafion[137] and polydopamine[138] were used as coating layer of C-S composite, good electrochemical performance was obtained.

Therefore, by introducing conducting polymers into the lithium sulfur battery, the chemical fixation or physical confinement of sulfur can be more efficiency. However, their long-term stability in the organic solvent and adaptability to volume expansion needs more investigation.

1.3.3.1.5 Binder for Positive Electrode

Because there's no specific bonding between the conductive materials and sulfur, binder is needed for the positive electrode preparation. Polymers such as poly (tetrafluoroethylene) (PTFE) and p*oly* (vinylidene fluoride) (PVDF) have been widely used as binder in batteries. The purpose of adding binders is to bind the active materials and conductive materials together so they will not come off during the charging-discharging process. Meanwhile, the binder should be chemically inert to the battery system. Kim et al.[139] investigated the performance of various types of binder for Li-S batteries. The result showed that the choice of binder only has small effects on the capacity. In contrast, Schneider et al.[140] reported that the choice of binder used in the positive electrode material does influence the cycling behaviour and stability of electrodes. It was stated that the PTFE is a better binder for Li-S cells compared to Nafion and sodium carboxymethyl cellulose (CMC) because the latter ones were brittle and tended to crack during cycling. However, this report excluded PVDF, which is widely used as

binder in Li-ion batteries. This is due to the drying process needs a high temperature (generally 90 ℃) at which the sulfur will sublime.

1.3.3.2 Electrolyte Study of Li-S Batteries

For most lithium batteries, the main function of electrolyte is to transfer lithium ions. For the lithium sulfur battery, since the polysulfide can dissolve in most liquid electrolyte, causing shuttle effect, other factors needs to be considered. Generally the electrolyte can be categorised based on their phases: organic liquid electrolyte and solid electrolyte. Unlike liquid electrolyte systems, separators are unnecessary for solid electrolyte systems since the electrolyte itself can work as separator.

Lithium perchlorate ($LiClO_4$), lithium hexafluorophosphate ($LiPF_6$) and LiTFSI are three commonly used lithium salts in lithium batteries. Kim et al.[141] compared LiTFSI and $LiClO_4$, it was stated that the choice of lithium salt will barely affect the performance of Li-S cells.

Possible choices of electrolyte solvent such as tetrahydrofuran (THF) [10], 1,3-dioxolane (DOL) [11,12], dimethoxyethane (DME) [13] and tetra(ethylene glycol)-dimethyl ether (TEGDME) [14] have been tested in recent years due the high solubility of polysulfide and absence of reaction with S_n^{2-}.Even though the results are still not very satisfactory, certain trends have emerged: (1) solvent with high permittivity, (2) high donor number which can dissolve lithium polysulfides with different length and (3) a viscosity high enough to prevent the dissociation of polysulfides.[8] Since a single solvent can hardly meet the demand for Li-S batteries, before a new direction (for example, reversible organic solvent or inorganic solvent which can bind with polysulfide) can be successfully achieved, one of the main focuses of improving the electrolytes is to test binary-electrolyte (or more) systems in different ratio. The most frequently used combinations are DME+DOL and TEGDME+DOL, in which DOL decreases the viscosity of the electrolyte, forms an passivation layer on the surface of Li metal and enhance the ion mobility in the electrolyte while DME/TEGDME demonstrates good solubility of lithium salts and polysulfide. Ideally, the electrolyte should be able to dissolve as much polysulfide as possible without compromising the ion conductivity of the cell. To further improve the ion conductivity of the electrolyte, a solvent-in-salt electrolyte was proposed with ultrahigh salt concentration and high lithium ion transfer number. The results showed that not only the cycle life and safety

performance was remarkably enhanced, but also that the dissolution of lithium polysulfide in the electrolyte was inhibited by such method.[142]

To promote the reaction kinetics of the cell, similar measures can be taken as in redox flow cell -- dissolved polysulfide can be added into positive electrode electrolyte. In recent years, some progresses in the development of the Li-polysulfide battery have been made by using carbon nanotube/nanofibre as current collector.[143,144] It was believed that the kinetics for polysulfide in liquid phase was faster than the solid sulfur and the 3D structure from carbon nanotube/nanofibre provided more space for the reaction product.

Another potential solvent choice for the Li-S battery electrolyte system is ionic liquid[145], which has been widely applied in other energy storage systems.[38] Although ionic liquids have not been commonly used in the Li-S battery due to their high viscosity, low wettability and high cost, the mixture of ionic liquid and ether solvent was proven to be able to improve the thermo-stability and the ion conductivity of the electrolyte.[146]

Instead of using liquid electrolyte, solid electrolytes in Li-S cells have also been reported. The most important benefit of using an all-solid-state Li-S cell is to stop the diffusing of the polysulfides to the lithium metal. Poly ethylene oxide (PEO) based polymer electrolytes[147–149] have been tested in Li-S batteries. By mixing polymer, lithium salts and ceramic nanoparticles, polymer electrolytes with good cycling performances were prepared. However, they only showed good ion conductivity above 70 °C, which limited their applications. Beside polymers, glass-ceramic electrolyte systems were also investigated.[150–152]

1.3.3.3 Negative Electrode Study of Li-S Batteries

In a Li-S battery system, Li metal is used as negative electrode. During the charging-discharging processes, the lithium metal near the negative electrode surface will be constantly dissolved and re-formed. However, the re-formation of lithium on the negative electrode while charging also comes with dendrite formation, which may cause short-circuiting and the loss of active materials.[153,154] In addition, as the insoluble Li_2S and Li_2S_2 deposit on the negative electrode, a passivation layer will be formed, which will results in the loss of active material and higher impedance. Therefore, many researches have been done to protect the negative electrode.

The most common approach is to add some electrolyte salts or additives to protect the negative electrode. Mikhaylik[155] used $LiNO_3$ as additive in the electrolyte and managed to improve the cycle life. The mechanism was studied by Aurbach et al.[156], it was suggested that in polar aprotic solutions, very thin films will grow on the lithium metal surface, which will passivate the metal with a certain thickness. Then the $LiNO_3$ is directly reduced near the surface to Li_xNO_y and oxidise the sulfur species into Li_xSO_y. As a result, the shuttle effect will be greatly diminished. Lithium bis(oxalate)borate was also added into the electrolyte as an additive, the result showed that small amount of lithium bis(oxalate)borate can improve the cycling performance. In some other reports, pre-made protective layers were introduced on lithium metal.[157,158]

By using Li_2S as positive electrode, non lithiated negative electrodes can be used in the Li-S battery. Hassoun et al.[159] used Li_2S/C as positive electrode and Sn as negative electrode, good cycling stability was achieved. Similarly, Yang et al.[160] and Xiong et al.[161] successfully applied pre-lithiated silicon as negative electrode for sulfur batteries.

1.3.3.4 Separator for Li-S Batteries

Separator is also an important part in liquid electrolyte batteries because its properties have considerable effects on specific energy, energy density, cycle life and safety.[162] For lithium ion batteries, on the one hand, the separator should be an insulator for electron, so it will prevent short-circuiting caused by the direct contact between the electrodes; on the other hand, the separator should also have a low resistance to lithium ion, so that it can carry lithium ions through it without much energy consumption. Moreover, a good separator should also have high ion conductivity. Therefore, by choosing a suitable separator, the capacity, cycle life and Coulumbic efficiency of batteries will be remarkably improved.

Some improvements can still be made to the separator for Li-S batteries. One of them is to modify a separator or to develop a new one so it can prevent the shuttle effect. In this case, this separator should be able to block the polysulfide from diffusing to the negative electrode while still being able to transfer lithium ions, without causing large internal impedance.

Jin et al.[163] proposed using lithiated Nafion ionomer film as a functional separator for Li-S cells. As a result, improved cycling performances were obtained. Its unique structure with sulfonate groups on Teflon backbone has made it a potential material for cation-exchange membrane. The experiment of

elemental sulfur permeability through the separator also showed mitigated shuttle effect: it was found that the sulfide anions barely transport through the electrolyte by element analysis. Yao et al. also reported that by coating a thin conductive polymer layer on the Celgard separator, the accumulation of sulfur-related species on the positive electrode can be prevented as the cycling performance was greatly improved.[164]

Alternatively, a hybrid separator was reported by stacking commercially used Celgard and glassy fibre separators[165], a good cell performance was obtained over 500 cycles.

1.4 Aims and Objectives

Aim

a. To use redox mediators in lithium air batteries in order to improve their performance.

b. To understand the effect of choice of carbon on the performance of Li-S batteries.

Objective

a. To Test the stability, reaction mechanism and the electrochemical performance of ethyl viologen as an ORR mediator in lithium air batteries.
b. To test cobalt complex as an OER mediator in lithium air batteries.
c. To characterise surface area properties of different carbon-sulfur mixture.
d. To test the cycling performance of Li-S cells using different carbon, different sulfur content and different preparation methods.
e. To improve the performance of Li-S cells by optimizing experimental conditions.

1.5 References

1 D. Linden and T. Reddy, *Handbook of Batteries*, McGraw-Hill, Newyork, 3rd edn., 2001.

2 H. Xia, L. Lu, Y. S. Meng and G. Ceder, *J. Electrochem. Soc.*, 2007, **154**, A337-A342.

3 M. Armand and J.-M. Tarascon, *Nature*, 2008, **451**, 652-657.

4 G. Girishkumar, B. McCloskey, A. C. Luntz, S. Swanson and W. Wilcke, *J. Phys. Chem. Lett.*, 2010, **1**, 2193-2203.

5 K. M. Abraham, D. M. Pasquariello and E. B. Willstaedt, *J. Electrochem. Soc.* , 1990, **137** , 1856-1857.

6 K. M. Abraham and Z. Jiang, *J. Electrochem. Soc.* , 1996, **143** , 1-5.

7 T. Ogasawara, A. Débart, M. Holzapfel, P. Novák and P. G. Bruce, *J. Am. Chem. Soc.*, 2006, **128**, 1390-1393.

8 U. S. Patent, 5814420, 1998.

9 Q. Sun, Y. Yang and Z. W. Fu, *Electrochem. Commun.*, 2012, **16**, 22-25.

10 Y. Li, M. Gong, Y. Liang, J. Feng, J.-E. Kim, H. Wang, G. Hong, B. Zhang and H. Dai, *Nat. Commun.*, 2013, **4:**1805.

11 S. Müller, F. Holzer and O. Haas, *J. Appl. Electrochem.*, 1998, **28**, 895-898.

12 Q. Li and N. J. Bjerrum, *J. Power Sources*, 2002, **110**, 1-10.

13 T. Zhang, Z. Tao and J. Chen, *Mater. Horizons*, 2014, **1**, 196-206.

14 K. M. Abraham and Z. Jiang, *J. Electrochem. Soc.* , 1996, **143** , 1-5.

15 P. He, Y. Wang and H. Zhou, *Electrochem. Commun.*, 2010, **12**, 1686-1689.

16 B. Kumar, J. Kumar, R. Leese, J. P. Fellner, S. J. Rodrigues and K. M. Abraham, *J. Electrochem. Soc.* , 2010, **157** , A50-A54.

17 Y. Wang and H. Zhou, *J. Power Sources*, 2010, **195**, 358-361.

18 C. O. Laoire, S. Mukerjee, K. M. Abraham, E. J. Plichta and M. A. Hendrickson, *J. Phys. Chem. C*, 2009, **113**, 20127-20134.

19 J. Herranz, A. Garsuch and H. A. Gasteiger, *J. Phys. Chem. C*, 2012, **116**, 19084–19094.

20 V. S. Bryantsev and M. Blanco, *J. Phys. Chem. Lett.*, 2011, **2**, 379–383.

21 K. U. Schwenke, S. Meini, X. Wu, H. A. Gasteiger and M. Piana, *Phys. Chem. Chem. Phys.*, 2013, **15**, 11830–11839.

22 M. Mirzaeian and P. J. Hall, *Electrochim. Acta*, 2009, **54**, 7444–7451.

23 M. Mirzaeian and P. J. Hall, *J. Power Sources*, 2010, **195**, 6817–6824.

24 C. Tran, X.-Q. Yang and D. Qu, *J. Power Sources*, 2010, **195**, 2057–2063.

25 K.-H. Xue, T.-K. Nguyen and A. A. Franco, *J. Electrochem. Soc.* , 2014, **161** , E3028–E3035.

26 G. Q. Zhang, J. P. Zheng, R. Liang, C. Zhang, B. Wang, M. Hendrickson and E. J. Plichta, *J. Electrochem. Soc.* , 2010, **157** , A953–A956.

27 F. Mizuno, S. Nakanishi, Y. Kotani, S. Yokoishi and H. IBA, *Electrochemistry*, 2010, **78**, 403–405.

28 V. S. Bryantsev, V. Giordani, W. Walker, M. Blanco, S. Zecevic, K. Sasaki, J. Uddin, D. Addison and G. V Chase, *J. Phys. Chem. A*, 2011, **115**, 12399–12409.

29 S. Hyoung Oh, T. Yim, P. Ekaterina and L. F. Nazar, *Electrochem. Solid-State Lett.* , 2011, **14** , A185–A188.

30 B. D. McCloskey, A. Speidel, R. Scheffler, D. C. Miller, V. Viswanathan, J. S. Hummelshøj, J. K. Nørskov and A. C. Luntz, *J. Phys. Chem. Lett.*, 2012, **3**, 997–1001.

31 B. D. McCloskey, D. S. Bethune, R. M. Shelby, G. Girishkumar and A. C. Luntz, *J. Phys. Chem. Lett.*, 2011, **2**, 1161–1166.

32 S. A. Freunberger, Y. Chen, N. E. Drewett, L. J. Hardwick, F. Bardé and P. G. Bruce, *Angew. Chemie Int. Ed.*, 2011, **50**, 8609–8613.

33 J. Read, *J. Electrochem. Soc.* , 2006, **153** , A96–A100.

34 W. Xu, J. Xiao, D. Wang, J. Zhang and J.-G. Zhang, *Electrochem. Solid-State Lett.* , 2010, **13** , A48–A51.

35 W. Xu, J. Xiao, J. Zhang, D. Wang and J.-G. Zhang, *J. Electrochem. Soc.* , 2009, **156** , A773-A779.

36 W. Xu, J. Xiao, D. Wang, J. Zhang and J.-G. Zhang, *J. Electrochem. Soc.* , 2010, **157** , A219-A224.

37 C. O. Laoire, S. Mukerjee, K. M. Abraham, E. J. Plichta and M. A. Hendrickson, *J. Phys. Chem. C*, 2010, **114**, 9178-9186.

38 D. R. MacFarlane, N. Tachikawa, M. Forsyth, J. M. Pringle, P. C. Howlett, G. D. Elliott, J. H. Davis, M. Watanabe, P. Simon and C. A. Angell, *Energy Environ. Sci.*, 2014, **7**, 232-250.

39 S. Monaco, A. M. Arangio, F. Soavi, M. Mastragostino, E. Paillard and S. Passerini, *Electrochim. Acta*, 2012, **83**, 94-104.

40 J. Xiao, D. Mei, X. Li, W. Xu, D. Wang, G. L. Graff, W. D. Bennett, Z. Nie, L. V Saraf, I. A. Aksay, J. Liu and J.-G. Zhang, *Nano Lett.*, 2011, **11**, 5071-5078.

41 P. Kichambare, J. Kumar, S. Rodrigues and B. Kumar, *J. Power Sources*, 2011, **196**, 3310-3316.

42 A. Débart, A. J. Paterson, J. Bao and P. G. Bruce, *Angew. Chemie Int. Ed.*, 2008, **47**, 4521-4524.

43 S. H. Oh and L. F. Nazar, *Adv. Energy Mater.*, 2012, **2**, 903-910.

44 Z. Jian, P. Liu, F. Li, P. He, X. Guo, M. Chen and H. Zhou, *Angew. Chemie Int. Ed.*, 2014, **53**, 442-446.

45 Y.-C. Lu, H. A. Gasteiger, M. C. Parent, V. Chiloyan and Y. Shao-Horn, *Electrochem. Solid-State Lett.* , 2010, **13**, A69-A72.

46 Y.-C. Lu, Z. Xu, H. A. Gasteiger, S. Chen, K. Hamad-Schifferli and Y. Shao-Horn, *J. Am. Chem. Soc.*, 2010, **132**, 12170-12171.

47 C. J. Bondue, A. A. Abd-El-Latif, P. Hegemann and H. Baltruschat, *J. Electrochem. Soc.*, 2015, **162,** A479-A487.

48 J. Lu, Y. Lei, K. C. Lau, X. Luo, P. Du, J. Wen, R. S. Assary, U. Das, D. J. Miller, J. W. Elam, H. M. Albishri, D. A. El-Hady, Y.-K. Sun, L. A. Curtiss and K. Amine, *Nat. Commun.*, 2013, **4**:2383.

49 A. K. Thapa, K. Saimen and T. Ishihara, *Electrochem. Solid-State Lett.* , 2010, **13** , A165–A167.

50 F. Li, Y. Chen, D.–M. Tang, Z. Jian, C. Liu, D. Golberg, A. Yamada and H. Zhou, *Energy Environ. Sci.*, 2014, **7**, 1648–1652.

51 B. Sun, X. Huang, S. Chen, P. Munroe and G. Wang, *Nano Lett.*, 2014, **14**, 3145–3152.

52 D. Xia, S. Liu, Z. Wang, G. Chen, L. Zhang, L. Zhang, S. Hui and J. Zhang, *J. Power Sources*, 2008, **177**, 296–302.

53 H. R. Byon, J. Suntivich and Y. Shao–Horn, *Chem. Mater.*, 2011, **23**, 3421–3428.

54 P. He, Y. Wang and H. Zhou, *Chem. Commun.*, 2011, **47**, 10701–10703.

55 S. Dong, X. Chen, K. Zhang, L. Gu, L. Zhang, X. Zhou, L. Li, Z. Liu, P. Han, H. Xu, J. Yao, C. Zhang, X. Zhang, C. Shang, G. Cui and L. Chen, *Chem. Commun.*, 2011, **47**, 11291–11293.

56 J.–L. Shui, N. K. Karan, M. Balasubramanian, S.–Y. Li and D.–J. Liu, *J. Am. Chem. Soc.*, 2012, **134**, 16654–16661.

57 F. Li, R. Ohnishi, Y. Yamada, J. Kubota, K. Domen, A. Yamada and H. Zhou, *Chem. Commun.*, 2013, **49**, 1175–1177.

58 B. D. McCloskey, R. Scheffler, A. Speidel, D. S. Bethune, R. M. Shelby and a C. Luntz, *J. Am. Chem. Soc.*, 2011, **133**, 18038–18041.

59 J. R. Dahn, J. Jiang, L. M. Moshurchak, M. D. Fleischauer, C. Buhrmester and L. J. Krause, *J. Electrochem. Soc.* , 2005, **152** , A1283–A1289.

60 L. Chen, M. Xu, B. Li, L. Xing, Y. Wang and W. Li, *J. Power Sources*, 2013, **244**, 499–504.

61 M. J. Lacey, J. T. Frith and J. R. Owen, *Electrochem. Commun.*, 2013, **26**, 74–76.

62 D. Sun, Y. Shen, W. Zhang, L. Yu, Z. Yi, W. Yin, D. Wang, Y. Huang, J. Wang, D. Wang and J. B. Goodenough, *J. Am. Chem. Soc.*, 2014, **136**, 8941–8946.

63 Y. Chen, S. A. Freunberger, Z. Peng, O. Fontaine and P. G. Bruce, *Nat. Chem*, 2013, **5**, 489–494.

64 M. Yu, X. Ren, L. Ma and Y. Wu, *Nat. Commun.*, 2014, **5**:5111.

65 S. Matsuda, S. Mori, Y. Kubo, K. Uosaki, K. Hashimoto and S. Nakanishi, *Chem. Phys. Lett.*, 2015, **620**, 78–81.

66 H.-D. Lim, H. Song, J. Kim, H. Gwon, Y. Bae, K.-Y. Park, J. Hong, H. Kim, T. Kim, Y. H. Kim, X. Lepró, R. Ovalle-Robles, R. H. Baughman and K. Kang, *Angew. Chem. Int. Ed.*, 2014, **53**, 3926–3931.

67 B. J. Bergner, A. Schürmann, K. Peppler, A. Garsuch and J. Janek, *J. Am. Chem. Soc.*, 2014, **136**, 15054–15064.

68 W. Xu, J. Wang, F. Ding, X. Chen, E. Nasybulin, Y. Zhang and J.-G. Zhang, *Energy Environ. Sci.*, 2014, **7**, 513–537.

69 D. J. Lee, H. Lee, J. Song, M.-H. Ryou, Y. M. Lee, H.-T. Kim and J.-K. Park, *Electrochem. Commun.*, 2014, **40**, 45–48.

70 F. Ding, W. Xu, G. L. Graff, J. Zhang, M. L. Sushko, X. Chen, Y. Shao, M. H. Engelhard, Z. Nie, J. Xiao, X. Liu, P. V Sushko, J. Liu and J.-G. Zhang, *J. Am. Chem. Soc.*, 2013, **135**, 4450–4456.

71 O. Crowther, D. Keeny, D. M. Moureau, B. Meyer, M. Salomon and M. Hendrickson, *J. Power Sources*, 2012, **202**, 347–351.

72 Z. Fu, Z. Wei, X. Lin, T. Huang and A. Yu, *Electrochim. Acta*, 2012, **78**, 195–199.

73 U. S. Patent, 3043896, 1962.

74 Y. V Mikhaylik and J. R. Akridge, *J. Electrochem. Soc.* , 2004, **151** , A1969–A1976.

75 C. Barchasz, F. Molton, C. Duboc, J. C. Leprêtre, S. Patoux and F. Alloin, *Anal. Chem.*, 2012, **84**, 3973–3980.

76 J. Shim, K. A. Striebel and E. J. Cairns, *J. Electrochem. Soc.* , 2002, **149** , A1321–A1325.

77 P. Adelhelm, P. Hartmann, C. L. Bender, M. Busche, C. Eufinger and J. Janek, *Beilstein J. Nanotechnol.*, 2015, **6**, 1016–1055.

78 Y. Yang, G. Zheng, S. Misra, J. Nelson, M. F. Toney and Y. Cui, *J. Am. Chem. Soc.*, 2012, **134**, 15387–15394.

79 T. Takeuchi, H. Sakaebe, H. Kageyama, H. Senoh, T. Sakai and K. Tatsumi, *J. Power Sources*, 2010, **195**, 2928–2934.

80 Z. Lin, C. Nan, Y. Ye, J. Guo, J. Zhu and E. J. Cairns, *Nano Energy*, 2014, **9**, 408–416.

81 M. N. Obrovac and J. R. Dahn, *Electrochem. Solid-State Lett.* , 2002, **5** , A70–A73.

82 Y. Zhou, C. Wu, H. Zhang, X. Wu and Z. Fu, *Electrochim. Acta*, 2007, **52**, 3130–3136.

83 A. Hayashi, R. Ohtsubo, T. Ohtomo, F. Mizuno and M. Tatsumisago, *J. Power Sources*, 2008, **183**, 422–426.

84 X. Wang, Y. Wang, X. Li, B. Liu and J. Zhao, *J. Power Sources*, 2015, **281**, 185–191.

85 Q. Dong, C. Wang and M. Zheng, *Huaxue Jinzhan*, 2011, **23**, 533–539.

86 N. Oyama, T. Tatsuma, T. Sato and T. Sotomura, *Nature*, 1995, **373**, 598–600.

87 L. Yu, X. Wang, J. Li, X. Jing and F. Wang, *J. Electrochem. Soc.* , 1999, **146** , 3230–3233.

88 J.-E. Park, S.-G. Park, A. Koukitu, O. Hatozaki and N. Oyama, *J. Electrochem. Soc.* , 2003, **150** , A959–A965.

89 K. Naoi, K. Kawase and Y. Inoue, *J. Electrochem. Soc.* , 1997, **144** , L170–L172.

90 J. L. Wang, J. Yang, J. Y. Xie and N. X. Xu, *Adv. Mater.*, 2002, **14**, 963–965.

91 J. Wang, J. Yang, C. Wan, K. Du, J. Xie and N. Xu, *Adv. Funct. Mater.*, 2003, **13**, 487–492.

92 L. Yin, J. Wang, J. Yang and Y. Nuli, *J. Mater. Chem.*, 2011, **21**, 6807–6810.

93 L. Yin, J. Wang, F. Lin, J. Yang and Y. Nuli, *Energy Environ. Sci.*, 2012, **5**, 6966–6972.

94 Y. J. Li, H. Zhan, S. Q. Liu, K. L. Huang and Y. H. Zhou, *J. Power Sources*, 2010, **195**, 2945–2949.

95 S.-E. Cheon, K.-S. Ko, J.-H. Cho, S.-W. Kim, E.-Y. Chin and H.-T. Kim, *J. Electrochem. Soc.* , 2003, **150** , A800–A805.

96 S. E. Cheon, *J. Electrochem. Soc.*, 2003, **150**, A796–A799.

97 M. Lécuyer, J. Gaubicher, M. Deschamps, B. Lestriez, T. Brousse and D. Guyomard, *J. Power Sources*, 2013, **241**, 249–254.

98 J. L. Wang, J. Yang, J. Y. Xie, N. X. Xu and Y. Li, *Electrochem. Commun.*, 2002, **4**, 499–502.

99 J. Wang, L. Liu, Z. Ling, J. Yang, C. Wan and C. Jiang, *Electrochim. Acta*, 2003, **48**, 1861–1867.

100 C. Lai, G. Li, S. Ye and X. Gao, *Prog. Chem.*, **23**, 2011, 527–532.

101 C. Lai, X. P. Gao, B. Zhang, T. Y. Yan and Z. Zhou, *J. Phys. Chem. C*, 2009, **113**, 4712–4716.

102 J. Wang, S. Y. Chew, Z. W. Zhao, S. Ashraf, D. Wexler, J. Chen, S. H. Ng, S. L. Chou and H. K. Liu, *Carbon N. Y.*, 2008, **46**, 229–235.

103 X. L. Ji, K. T. Lee and L. F. Nazar, *Nat. Mater.*, 2009, **8**, 500–506.

104 C. Liang, N. J. Dudney and J. Y. Howe, *Chem. Mater.*, 2009, **21**, 4724–4730.

105 J. Balach, T. Jaumann, M. Klose, S. Oswald, J. Eckert and L. Giebeler, *J. Phys. Chem. C*, 2015, **119**, 4580–4587.

106 S. Zhao, C. Li, W. Wang, H. Zhang, M. Gao, X. Xiong, A. Wang, K. Yuan, Y. Huang and F. Wang, *J. Mater. Chem. A*, 2013, **1**, 3334–3339.

107 H. Yao, G. Zheng, W. Li, M. T. McDowell, Z. Seh, N. Liu, Z. Lu and Y. Cui, *Nano Lett.*, 2013, **13**, 3385–3390.

108 K. Yang, Q. Gao, Y. Tan, W. Tian, L. Zhu and C. Yang, *Microporous Mesoporous Mater.*, 2015, **204**, 235–241.

109 N. Jayaprakash, J. Shen, S. S. Moganty, A. Corona and L. A. Archer, *Angew. Chemie-International Ed.*, 2011, **50**, 5904–5908.

110 B. Zhang, C. Lai, Z. Zhou and X. P. Gao, *Electrochim. Acta*, 2009, **54**, 3708–3713.

111 Y.-X. Wang, L. Huang, L.-C. Sun, S.-Y. Xie, G.-L. Xu, S.-R. Chen, Y.-F. Xu, J.-T. Li, S.-L. Chou, S.-X. Dou and S.-G. Sun, *J. Mater. Chem.*, 2012, **22**, 4744–4750.

112 S. Li, M. Xie, J. Liu, H. Wang and H. Yan, *Electrochem. Solid-State Lett.* , 2011, **14** , A105–A107.

113 S. Han, D. Wu, S. Li, F. Zhang and X. Feng, *Small*, 2013, **9**, 1173–1187.

114 A. Ambrosi, C. K. Chua, A. Bonanni and M. Pumera, *Chem. Rev.*, 2014, **114**, 7150–7188.

115 J.-Z. Wang, L. Lu, M. Choucair, J. A. Stride, X. Xu and H.-K. Liu, *J. Power Sources*, 2011, **196**, 7030–7034.

116 H. Wang, Y. Yang, Y. Liang, J. T. Robinson, Y. Li, A. Jackson, Y. Cui and H. Dai, *Nano Lett.*, 2011, **11**, 2644–2647.

117 N. Li, M. Zheng, H. Lu, Z. Hu, C. Shen, X. Chang, G. Ji, J. Cao and Y. Shi, *Chem. Commun.*, 2012, **48**, 4106–4108.

118 Y. Cao, X. Li, I. A. Aksay, J. Lemmon, Z. Nie, Z. Yang and J. Liu, *Phys. Chem. Chem. Phys.*, 2011, **13**, 7660–7665.

119 S. Evers and L. F. Nazar, *Chem. Commun.*, 2012, **48**, 1233–1235.

120 C. Zu and A. Manthiram, *Adv. Energy Mater.*, 2013, **3**, 1008–1012.

121 G. Zhou, L. Li, C. Ma, S. Wang, Y. Shi, N. Koratkar, W. Ren, F. Li and H.-M. Cheng, *Nano Energy*, 2015, **11**, 356–365.

122 R. Elazari, G. Salitra, A. Garsuch, A. Panchenko and D. Aurbach, *Adv. Mater.*, 2011, **23**, 5641–5644.

123 G. Zheng, Y. Yang, J. J. Cha, S. S. Hong and Y. Cui, *Nano Lett.*, 2011, **11**, 4462–4467.

124 S. Dorfler, M. Hagen, H. Althues, J. Tubke, S. Kaskel and M. J. Hoffmann, *Chem. Commun.*, 2012, **48**, 4097–4099.

125 W. Ahn, K.-B. Kim, K.-N. Jung, K.-H. Shin and C.-S. Jin, *J. Power Sources*, 2012, **202**, 394–399.

126 J. Chen, Q. Zhang, Y. Shi, L. Qin, Y. Cao, M. Zheng and Q. Dong, *Phys. Chem. Chem. Phys.*, 2012, **14**, 5376–5382.

127 J. C. Guo, Y. H. Xu and C. S. Wang, *Nano Lett.*, 2011, **11**, 4288–4294.

128 Z. Wei Seh, W. Li, J. J. Cha, G. Zheng, Y. Yang, M. T. McDowell, P.-C. Hsu and Y. Cui, *Nat Commun*, 2013, **4**, 1331.

129 X. Liang, A. Garsuch and L. F. Nazar, *Angew. Chemie Int. Ed.*, 2015, **127**, 3979–3983.

130 F. Wu, J. Z. Chen, R. J. Chen, S. X. Wu, L. Li, S. Chen and T. Zhao, *J. Phys. Chem. C*, 2011, **115**, 6057–6063.

131 L. Xiao, Y. Cao, J. Xiao, B. Schwenzer, M. H. Engelhard, L. V Saraf, Z. Nie, G. J. Exarhos and J. Liu, *Adv. Mater.*, 2012, **24**, 1176–1181.

132 M. D. Hager, P. Greil, C. Leyens, S. van der Zwaag and U. S. Schubert, *Adv. Mater.*, 2010, **22**, 5424–5430.

133 Y. Zhang, Z. Bakenov, Y. Zhao, A. Konarov, T. N. L. Doan, M. Malik, T. Paron and P. Chen, *J. Power Sources*, 2012, **208**, 1–8.

134 J. Fanous, M. Wegner, J. Grimminger, M. Rolff, M. B. M. Spera, M. Tenzer and M. R. Buchmeiser, *J. Mater. Chem.*, 2012, **22**, 23240–23245.

135 X. Yu, J. Xie, J. Yang, H. Huang, K. Wang and Z. Wen, *J. Electroanal. Chem.*, 2004, **573**, 121–128.

136 X. Yu, J. Xie, Y. Li, H. Huang, C. Lai and K. Wang, *J. Power Sources*, 2005, **146**, 335–339.

137 Q. W. Tang, Z. Q. Shan, L. Wang, X. Qin, K. L. Zhu, J. H. Tian and X. S. Liu, *J. Power Sources*, 2014, **246**, 253–259.

138 L. Wang, D. Wang, F. Zhang and J. Jin, *Nano Lett.*, 2013, **13**, 4206–4211.

139 N. I. Kim, C. B. Lee, J. M. Seo, W. J. Lee and Y. B. Roh, *J. Power Sources*, 2004, **132**, 209–212.

140 H. Schneider, A. Garsuch, A. Panchenko, O. Gronwald, N. Janssen and P. Novak, *J. Power Sources*, 2012, **205**, 420–425.

141 H. S. Kim and C. S. Jeong, *Bull. Korean Chem. Soc.*, 2011, **32**, 3682–3686.

142 L. Suo, Y.-S. Hu, H. Li, M. Armand and L. Chen, *Nat. Commun.*, 2013, **4**:1481.

143 C. Zu, Y. Fu and A. Manthiram, *J. Mater. Chem. A*, 2013, **1**, 10362–10367.

144 Y. Z. Fu, Y.-S. Su and A. Manthiram, *Angew. Chem. Int. Ed.*, 2013, **52**, 6930–6935.

145 L. X. Yuan, J. K. Feng, X. P. Ai, Y. L. Cao, S. L. Chen and H. X. Yang, *Electrochem. commun.*, 2006, **8**, 610–614.

146 J. H. Shin and E. J. Cairns, *J. Power Sources*, 2008, **177**, 537–545.

147 S. S. Jeong, Y. T. Lim, Y. J. Choi, G. B. Cho, K. W. Kim, H. J. Ahn and K. K. Cho, *J. Power Sources*, 2007, **174**, 745–750.

148 X. A. Liang, Z. Y. Wen, Y. Liu, H. Zhang, L. Z. Huang and J. Jin, *J. Power Sources*, 2011, **196**, 3655–3658.

149 J. Hassoun and B. Scrosati, *Adv. Mater.*, 2010, **22**, 5198–5201.

150 Z. Lin, Z. Liu, W. Fu, N. J. Dudney and C. Liang, *Angew. Chemie Int. Ed.*, 2013, **52**, 7460–7463.

151 A. Hayashi, T. Ohtomo, F. Mizuno, K. Tadanaga and M. Tatsumisago, *Electrochem. Commun.*, 2003, **5**, 701–705.

152 C. Zhang, Y. Lin and J. Liu, *J. Mater. Chem. A*, 2015, **3**, 10760–10766.

153 M. Winter and R. J. Brodd, *Chem. Rev.*, 2004, **104**, 4245–4270.

154 J. R. Owen, *Chem. Soc. Rev.*, 1997, **26**, 259–267.

155 U.S.Patent, 7,352,680, 2008.

156 D. Aurbach, E. Pollak, R. Elazari, G. Salitra, C. S. Kelley and J. Affinito, *J. Electrochem. Soc.*, 2009, **156**, A694–A702.

157 Y. M. Lee, N.-S. Choi, J. H. Park and J.-K. Park, *J. Power Sources*, 2003, **119–121**, 964–972.

158 S. Neuhold, D. J. Schroeder and J. T. Vaughey, *J. Power Sources*, 2012, **206**, 295–300.

159 J. Hassoun and B. Scrosati, *Angew. Chemie Int. Ed.*, 2010, **49**, 2371–2374.

160 Y. Yang, M. T. McDowell, A. Jackson, J. J. Cha, S. S. Hong and Y. Cui, *Nano Lett.*, 2010, **10**, 1486–1491.

161 X. Pu, G. Yang and C. Yu, *Nano Energy*, 2014, **9**, 318–324.

162 P. Arora and Z. Zhang, *Chem. Rev.*, 2004, **104**, 4419–4462.

163 Z. Jin, K. Xie and X. Hong, *J. Mater. Chem. A*, 2013, 8889–8898.

164 H. Bin Yao, K. Yan, W. Li, G. Zheng, D. Kong, Z. W. Seh, V. K. Narasimhan, Z. Liang and Y. Cui, *Energy Environ. Sci.*, 2014, **7**, 1–10.

165 L. Wang, J. Liu, S. Haller, Y. Wang and Y. Xia, *Chem. Commun.*, 2015, **51**, 6996–6999.

Chapter 2: Experimental Techniques and Theoretical Background

2.1 Surface Area Analysis

There are several ways to measure surface area and pore size. Gas adsorption is one of the most commonly used methods in determination of surface area and pore size distribution of solid materials. Despite its wide application, there are still different theories about how the absorption data should be interpreted. Generally, during the measurement, the adsorptive, i.e. the adsorbable gas, will be physically adsorbed on the adsorbent, i.e. the surface, forming the adsorbate. During desorption process, the amount of adsorbate will decrease. Under constant temperature (normally in liquid nitrogen, 77K), the relationship between the amount of gas being adsorbed/desorbed and the relative pressure (p/p_0) is known as adsorption/desorption isotherm.

Most materials examined by gas adsorption method have pores which are conventionally categorized into three types based on their pore diameters: micropores (less than 2 nm), mesopores (between 2 nm and 50 nm) and macropores (over 50 nm).[1]

In this report, the BET and BJH models are applied to calculate the specific surface area and the pore size distribution, respectively.

2.1.1 BET Model

BET theory is an extension of the Langmuir theory, which is a theory for monolayer adsorption, to multilayer adsorption. Three assumptions are made in this theory:

a. Gas molecules physically adsorb in layers infinitely;
b. No interactions between layers;
c. The Langmuir theory applies to each layer.

The resulting BET equation is expressed by:[1]

$$\frac{1}{V\left[\left(\frac{V_0}{p}\right)-1\right]} = \frac{c-1}{V_m c}\left(\frac{p}{p_0}\right) + \frac{1}{V_m c} \quad \text{(Equation 2.1)}$$

In which p and p_0 are the equilibrium and saturation pressures of adsorbates at the given temperature, V is the adsorbed gas volume and V_m is the monolayer adsorbed gas volume; c is the BET constant, which is an empirical parameter that indicates the magnitude of adsorbent-adsorbate interaction energy.

In the range of $0.05 < p/p_0 < 0.35$, the BET equation gives a linear relationship between p/p_0 and $1/v[(p_0/p)-1]$. By drawing a plot of $1/v[(p_0/p)-1]$ against p/p_0, the slope G and the y-intercept I_y can be obtained. According to the following equations, v_m and c can be calculated.

$$V_m = 1/ (G+I_y) \text{ (Equation 2.2)}$$

$$c = 1+G/I_y \text{ (Equation 2.3)}$$

From the value of v_m, the total surface area S_{total} of the sample can be calculated by:

$$S_{total} = v_m N_s/V \text{ (Equation 2.4)}$$

Where N is Avogadro's number; s is the adsorption cross section of the adsorbate (N_2). Then divided by the mass of adsorbent, the specific surface area can be calculated.

First the sample is cooled to approximately 77 K under vacuum. Then the adsorptive (typically nitrogen) is dosed to the sample in controlled increments. After each dose, the pressure will reach equilibrium and the quantity of adsorptive can be calculated. The quantity adsorbed at different pressure defines an adsorption isotherm, from which the quantity of gas forming a monolayer on the external surface is determined. Nitrogen is considered a suitable adsorption gas for BET measurement as the BET constant of nitrogen is large on many solid surfaces.[1]

Although commonly used to measure surface area, BET calculation was claimed to underestimate the surface area of ultra-microporous structures in which the assumption of multilayer formation is invalidated due to overlap of monolayer and multilayer adsorption.[2,3]

2.1.2 BJH Model

Usually in an isotherm, a hysteresis loop can be observed (shown in Fig. 2.1). The formation of this loop is due to the condensation of adsorbate in the mesopores. From the shape of the hysteresis loops, the shapes of the pores can

also be estimated.[1] In this case, instead of further forming multilayer, the adsorbate will start filling into the spaces of the pores. Figure 2.2 shows the processes of adsorption and desorption. For adsorption, the first stage is forming multilayer followed by the pore filling process. The desorption process started with the formation of a meniscus, followed by further evaporation of adsorbates.

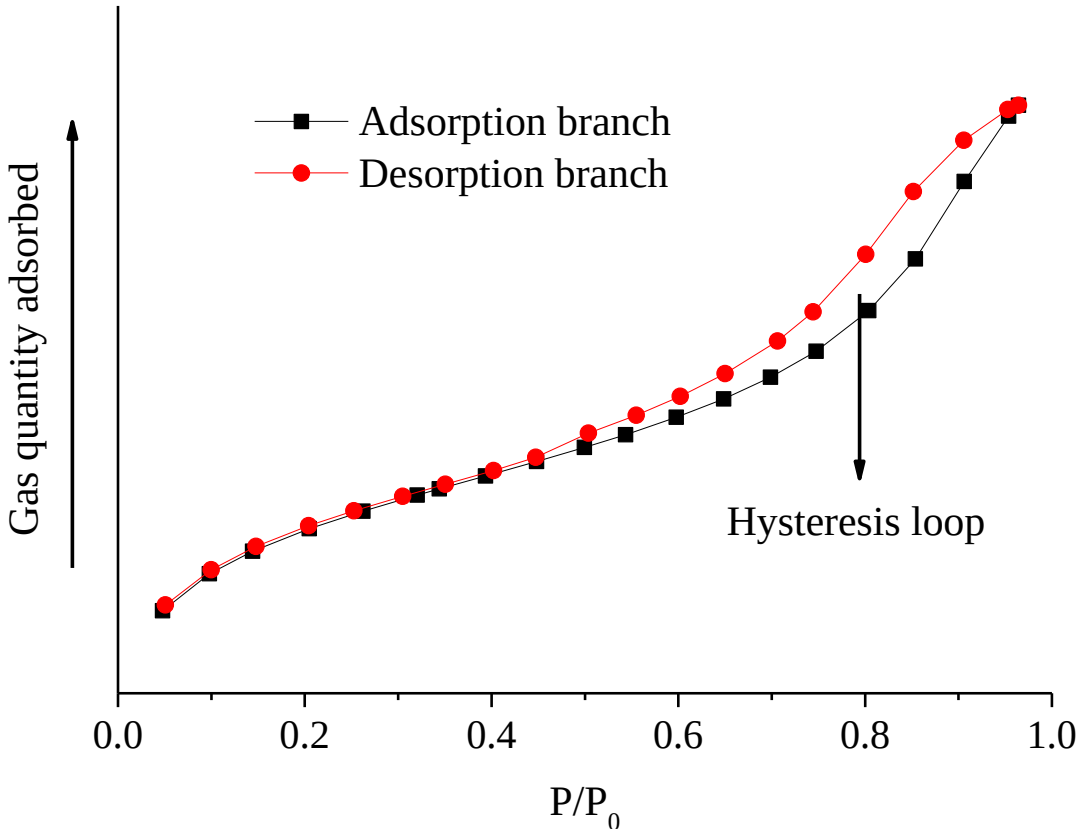

Figure 2.1 Example of gas adsorption/desorption isotherms.

The principle of BJH model is based on the Kelvin equation, which predicts the pressure at which adsorbed materials will spontaneously condense or evaporate in a cylindrical pore of a given size. This pressure is called the critical pressure.

The Kelvin equation is expressed by[1]:

$$\ln\left(\frac{p}{p_0}\right) = -\frac{2\gamma v cos\theta}{RTR_k} \quad \text{(Equation 2.5)}$$

Where R_k is the radius of curvature of the cylinder, γ is the liquid surface tension and θ is the contact angle between solid and condensed phase. At p when radius of pore equals to R_k, the pore will be filled in with condensed gas.

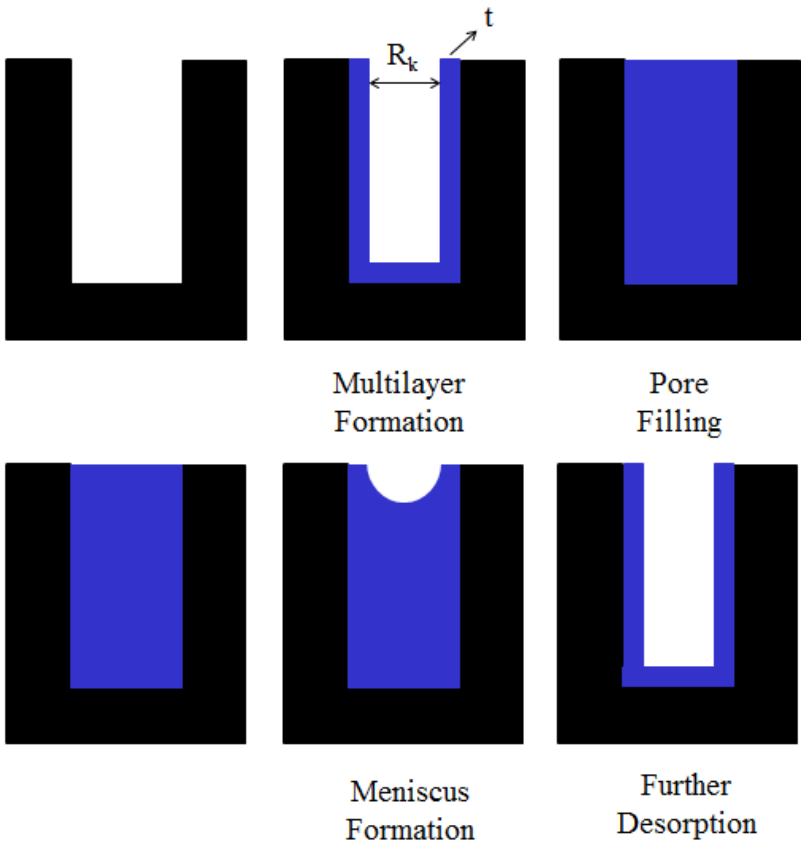

Figure 2.2 Suggested schematic diagrams of adsorption (upper) and desorption (lower) process in pores.

In the equation, R_k is positively related to p, which means condensation will first occur in smaller pores as pressure increases. When all pores are filled with liquid, the pressure then started to decrease gradually. The condensed gas started to evaporate from pores with larger sizes. The model is based on the assumption that pore radius is equal to the sum of Kelvin radius and the thickness of the film adsorbed on the pore wall.[4] The thickness of multilayer (in Fig. 2.2), t, can be estimated by different calculation method. For pore size evaluation, the Halsey-Faas correction is applied[1]:

$$t = 3.54\left[\frac{5}{\log\left(\frac{P_0}{P}\right)}\right]^{\frac{1}{3}} \quad \text{(Equation 2.6)}$$

Then the pore diameter can be calculated via Equation 2.7:

$$\text{Pore diameter} = R_k + 2t \quad \text{(Equation 2.7)}$$

Because different mechanisms are proposed in adsorption (pore filling) and desorption (meniscus forming) processes, differences may occur in the isotherms.

By studying the desorption branch of isotherms, the pore size and surface area information can be obtained.

The drawback of the BJH model is that it is inaccurate for micropores measurement. Alternatively, calculation method based on the density function theory (DFT) has been used to measure the pore size distrutibutions of porous materials.[5-8] However, those techniques required more sophisticated modelling and calculation. In this report, BJH model was chosen over DFT due to its simplicity and its previous application in the characterization of battery materials.[9-11] In this study, the standard errors of the measurement are approximately from 5 to 10 %, which depends on the total surface area. In general, higher surface area gives less error.

2.2 UV/Visible Spectroscopy

When a molecule absorbs energy from radiation, it will pass from a lower energy state (initial or ground state) to a higher energy state (excited state). This energy increase is represented by:

$$E = h\nu = hc/\lambda \quad \text{(equation 2.8)}$$

Where h is the Planck's constant, c is the velocity of light; ν and λ are frequency and wavelength of the radiation respectively. There are three types of energy change in a molecule depending on the intensity: rotational energy, vibrational energy and electronic energy (shown in Fig. 2.3)

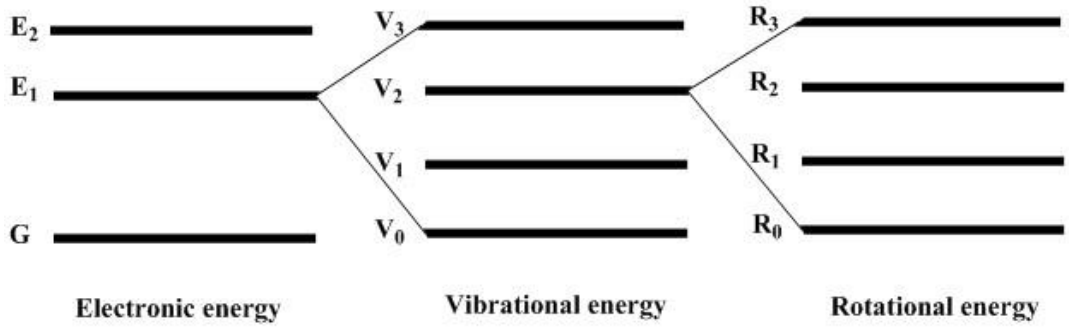

Figure 2.3 Energy levels for a polyatomic molecule. (G is the ground state; E_1– E_2 are different electronic states; V_0 – V_3 are different vibrational states; R_0 – R_3 are different rotational states.)

In the case of UV/Visible spectroscopy, the transitions are between electronic energy levels. As a molecule absorbs electromagnetic radiation, the electron in an occupied orbital will be promoted to an unoccupied orbital with higher energy

level. Generally speaking, the lowest occupied orbitals are σ orbitals. The π and non-bonding (n) orbitals have higher energy levels. The unoccupied anti-bonding orbitals have even higher energy levels (shown in Fig. 2.4).

In addition, molecules usually have many excited modes of vibration and rotation which are closely spaced. Those energy levels will superimpose on electronic levels and the spectrophotometer cannot resolve them. As a result, the UV/Visible spectrum of a molecule usually consists of a broad absorption band.

The light absorption of a given wavelength can be expressed by the equation below known as the Beer-Lambert Law:[12]

$$A = \log (I_0/I) = \epsilon c l \quad \text{(Equation 2.9)}$$

where A is the absorbance, I_0 is the intensity of incident light, I is the intensity of light leaving cell, ϵ is the extinction coefficient, c is the concentration and l is the length of sample cell. In this study, the error measured in the absorbance is normally less than 3%.

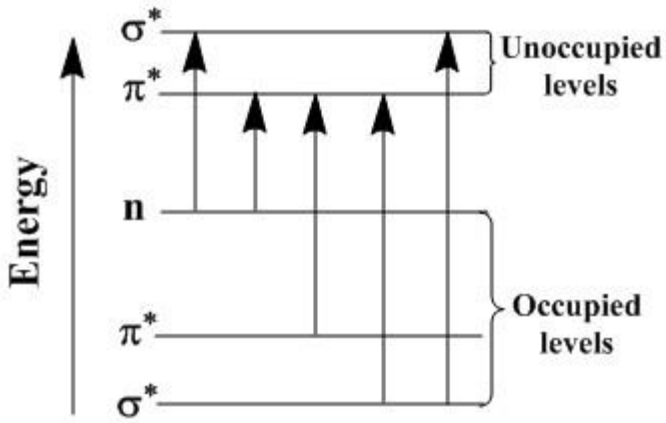

Figure 2.4 Electronic energy levels and transitions.

The extinction coefficient is a property of a molecule; therefore the Beer-Lambert law can be used to quantitatively determine species that can absorb UV/Vis light. It has been reported that this technique can be applied in batteries such as in-situ UV/Vis in lithium battery systems. For instance, people have used in-situ UV/Vis spectroscopy to identify the composite changes of polysulfide spicies in Li-S cells during the charge/discharge processes.[13-15]

2.3 X-ray Diffraction

X-ray diffraction (XRD) is a non-destructive analysis technique which reveals the crystal structure, chemical composition and physical properties of materials. When a beam of X-rays hits atoms or ions within the materials, it interacts with electrons and scatters, which is due to the similarity between the distance between atoms or ions (normally a few Å) and the wave length of X-rays. The interaction of the incident rays with the sample produces constructive patterns when the conditions satisfying Bragg's Law are met (see Fig. 2.6).[16] Its quick measurement rate and good accuracy have made XRD a very useful technique for the identification of solid species with crystalline structure.

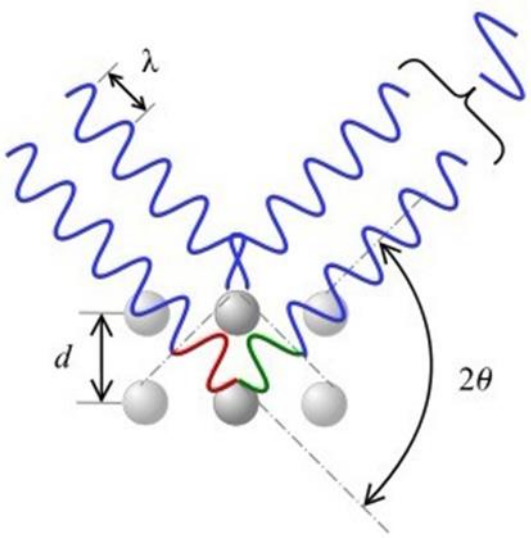

Figure 2.5 Schematic diagram of Bragg diffraction, adapted from Wikipedia, by Author Christophe Dang Ngoc Chan, 2011, Retrieved from http://commons.wikimedia.org/wiki/File:Braggs_Law.svg. Adapted with permission.

In Fig. 2.5,

path difference = red curve + green curve

Therefore, the Bragg's law is deduced as Equation 2.10:

$$2d \sin \theta = n \lambda \quad \text{(Equation 2.10)}$$

In which, λ is the wavelength, n is a positive integer, d is the lattice spacing and θ is the incidence angle. If a beam of X-rays with wavelength of λ hits the sample with lattice spacing of d at an incidence angle of θ, constructive interference will

occur. By comparing the experimentally recorded diffraction patterns with the database, the crystal structure of the sample may be determined.

2.4 Raman Spectroscopy

In Raman spectroscopy, a laser beam is shined upon the sample. By interaction with the molecular bonds or the electron cloud in the molecule, the molecules will be excited to higher energy states then release another photon (see Fig. 2.6). By comparing the energy of incident light and the scattered light, there are three types of scattering: when they have the same energy, it is called Rayleigh (elastic) scattering; in the case of the photon energy being shifted (inelastic scattering), the scattered light can be either lower (Stokes scattering) or higher (Anti-Stokes scattering) in energy than the incoming beam. This energy shift is called the Raman shift and the theory of Raman spectroscopy was based on it. The Raman shift $\Delta\omega$ is expressed by:

$$\Delta\omega = \frac{1}{\lambda_0} - \frac{1}{\lambda_1} \quad \text{(Equation 2.11)}$$

where $\Delta\omega$ is the Raman shift expressed in wavenumber, λ_0 is the excitation wavelength and λ_1 is the Raman spectra wavelength.

Raman spectroscopy can be applied either in-situ or ex-situ. In-situ Raman spectroscopy has been previously used in the studies of the Li-air battery.[17] It was used to monitor the reaction in the electrochemical cell. The ex-situ Raman spectroscopy has been applied to determine the discharge product of Li-air cells.[18] In this report, only ex-situ technique will be used.

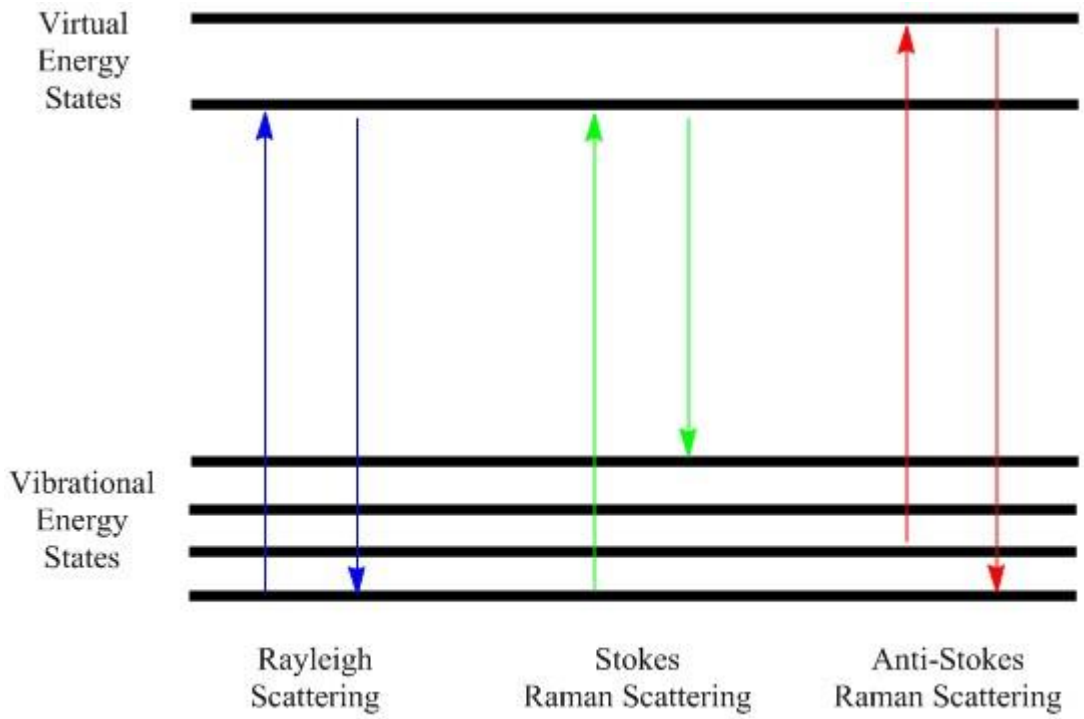

Figure 2.6 Schematic diagram of different scattering types.

2.5 Galvanostatic Cycling with Potential Limitation (GCPL)

This technique is widely used to test the behaviour of batteries upon cycling. The performance of a battery is determined under a given potential range and a given charge/discharge rate (current). By repetitively recording the potential as a function of time, the specific capacity can be calculated. The cycling performance and rate performance of a battery can also be obtained by repeating the cycling and applying different galvanostatic rate.

The galvanostatic rate is commonly expressed as C/h, h being the number of hours at which the total theoretical charge of the battery will be passed through. For a given electrode material, C is usually the charge corresponding to the total oxidation or reduction of the material.

2.6 Cyclic Voltammetry

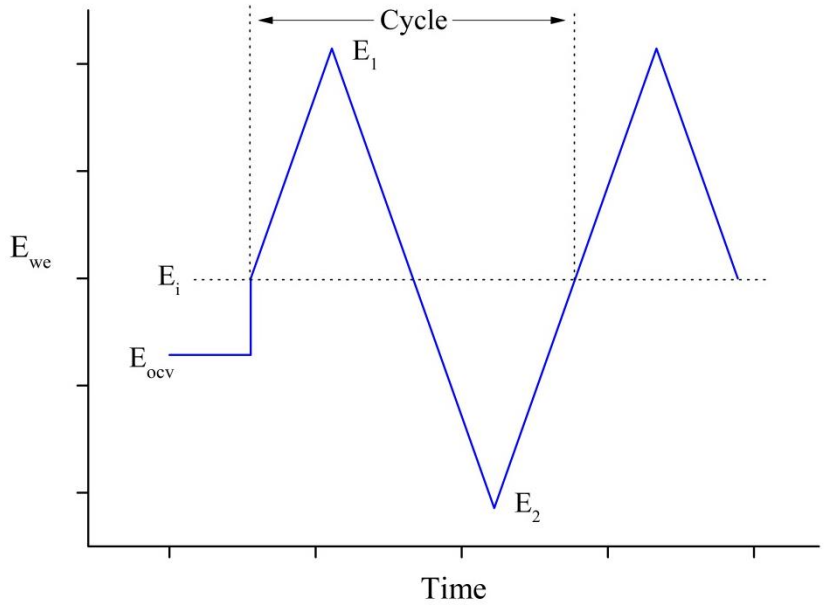

Figure 2.7 Potential sweeps with time in cyclic voltammetry

Cyclic voltammetry (CV) is the most widely used electrochemical technique in the analysis of reversible/irreversible redox reactions, surface electrochemical reactions and reaction kinetics. Information about thermodynamics, kinetics and mass transfer can be obtained by CV. The potential of working electrode is scanned linearly using a triangular potential waveform (see Fig. 2.7), During the sweeping process, the potentiostat measures the current resulting from the reactions.[19]

The current response to the voltage normally shows a peak as voltage ispositively or negatively changed, and then decreases due to the mass transport of species, whenever the reaction rate is diffusion limited. In this case, the peak current i_p is given by Randles-Sevcik equation:[19]

$$i_p = 0.4463nFAc\ (nFvD/RT)^{1/2} \quad \text{(Equation 2.12)}$$

Where n is the number of electrons transferred, F is the Faraday constant, A is the area of the electrode, c is the concentration of species to be studied, v is scan rate, D is diffusion coefficient, R is the gas constant and T is the temperature.

The Randles-Sevcik equation assumes a reversible redox couple whose concentration response instantly with the potential change which obeys Nernst equation:

$$E = E^0 + 59\ mV/n \log ([ox]/[red]) \quad \text{(Equation 2.13)}$$

Where [ox] and [red] are respectively the concentration of oxidized form and reduced form of the redox couple. The reversibility of a redox couple can be determined by whether the peak current is proportional to the square root of scan rate or by whether the peak separation (E_{pa}–E_{pc}) is 59 mV/n. Therefore, in a cyclic voltammogram, a large peak separation might indicate the effect of IR drop or slow electron transfer.

Generally in a CV experiment, the concentrations of reactants are much lower than the supporting electrolyte so the current is limited to a small value corresponding to the diffusion rate of the reactants and consequently the IR drop becomes negligible. However in Li/S cells, the concentration of the reactant could be much higher than the supporting electrolyte so the diffusion limited current and the consequent IR drop become more significant. In order to avoid this, a low scan rate was applied in the CV experiments for Li/S cells. Under low scan rates, the diffusion limited current and the consequent IR drop are small. A separator is often incorporated to minimise convection, which could potentially disturb the concentration gradient in a diffusion limited situation.

2.7 Electrochemical Impedance Spectroscopy (EIS)

Electrical impedance, Z, is the extension of direct current (DC) resistance to the alternating current (AC), including both amplitude and phase information of voltage and current.

In an EIS experiment, the electrical impedance of the sample is measured over a given frequency range. Either potentiostatic or galvanostatic mode can be achieved by applying a sinusoidal perturbation of voltage or current respectively. By recording the response for different frequency, the impedance spectrum is drawn.

The Randles circuit, shown in Fig. 2.8(A) is a fundamental equivalent circuit in EIS. The interfacial impedance is a parallel combination of the double layer capacitance, C_{dl}, and the faradaic impedance, which is the charge transfer resistance, R_{ct}, in series with Warburg diffusion impedance or mass transfer resistance, Z_w. The uncompensated resistance R_s, which determined by electrolyte resistance, is in series with the interfacial impedance. In a Nyquist plot, the resistance typically shows a dot on Z' axis and a capacitor shows a straight line parallel to $-Z''$ axis.

In the Nyquist plot shown in Fig. 2.8(B), a typical shape of Nyquist plot consists of a semicircle region with a straight line with gradient of 1, which is due to the Warburg diffusion impedance. The linear region observed in lower frequency range reveals the mass transfer limitation while the semicircle part observed in high frequency range implies the electron transfer controlled process. From this plot, R_{ct} and R_s can be determined and C_{dl} can be calculated.

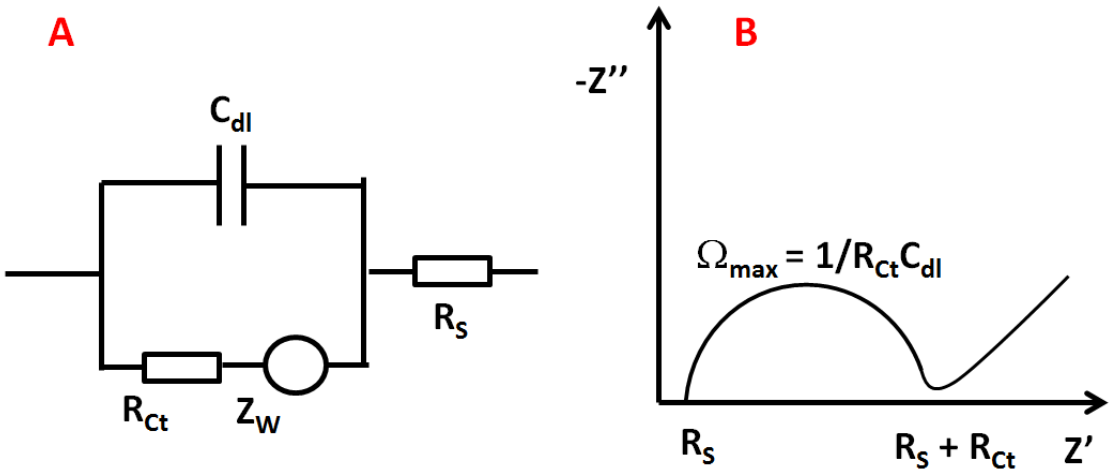

Figure 2.8 Equivalent circuit diagram for the Randles circuit (A) and typical Nyquist plot for the Randles circuit (B).

Potential electrochemical impedance spectroscopy (PEIS) method was used in the experiments described in this work. The alternating sinusoidal potential was applied around a DC potential E (generally the open circuit potential).

2.8 Reference

1 K. S. W. Sing, D. H. Everett, R. a. W. Haul, L. Moscou, R. A. Pierotti, J. Rouquérol and T. Siemieniewska, *Pure Appl. Chem.*, 1985, **57**, 603–619.

2 K. S. Walton and R. Q. Snurr, *J. Am. Chem. Soc.*, 2007, **129**, 8552–8556.

3 Y. S. Bae, A. Ö. Yazayd'n and R. Q. Snurr, *Langmuir*, 2010, **26**, 5475–5483.

4 E. P. Barrett, L. G. Joyner and P. P. Halenda, *J. Am. Chem. Soc.*, 1951, **73**, 373–380.

5 N. A. Seaton, J. P. R. B. Walton and N. Quirke, *Carbon N. Y.*, 1989, **27**, 853–861.

6 Z. Ryu, J. Zheng, M. Wang and B. Zhang, *Carbon N. Y.*, 1999, **37**, 1257–1264.

7 C. Lastoskie, K. E. Gubbins and N. Quirke, *J. Phys. Chem.*, 1993, **97**, 4786–4796.

8 J. P. Olivier, W. B. Conklin and M. v. Szombathely, in *Characterization of Porous Solids III*, ed. F. R.-R. J. Rouquerol K.S.W. Sing and K.K. Unger BT - Studies in Surface Science and Catalysis, Elsevier, 1994, vol. Volume 87, pp. 81–89.

9 X. Li, Y. Cao, W. Qi, L. V Saraf, J. Xiao, Z. Nie, J. Mietek, J.-G. Zhang, B. Schwenzer and J. Liu, *J. Mater. Chem.*, 2011, **21**, 16603–16610.

10 N. Tachikawa, K. Yamauchi, E. Takashima, J.-W. Park, K. Dokko and M. Watanabe, *Chem. Commun.*, 2011, **47**, 8157–8159.

11 J. Zheng, M. Gu, M. J. Wagner, K. A. Hays, X. Li, P. Zuo, C. Wang, J.-G. Zhang, J. Liu and J. Xiao, *J. Electrochem. Soc.* , 2013, **160** , A1624–A1628.

12 C. N. Banwell, *Fundamentals of Molecular Spectroscopy*, McGraw-Hill, London, 4th edn., 1994.

13 M. U. M. Patel, R. Demir-Cakan, M. Morcrette, J.-M. Tarascon, M. Gaberscek and R. Dominko, *ChemSusChem*, 2013, **6**, 1177–1181.

14 M. U. M. Patel and R. Dominko, *ChemSusChem*, 2014, **7**, 2167–2175.

15 N. A. Canas, D. N. Fronczek, N. Wagner, A. Latz and K. A. Friedrich, *J. Phys. Chem. C*, 2014, **118**, 12106–12114.

16 W. H. Bragg and W. L. Bragg, *Proc. R. Soc. London A Math. Phys. Eng. Sci.*, 1913, **88**, 428–438.

17 J. T. Frith, A. E. Russell, N. Garcia-Araez and J. R. Owen, *Electrochem. Commun.*, 2014, **46**, 33–35.

18 B. D. McCloskey, D. S. Bethune, R. M. Shelby, G. Girishkumar and A. C. Luntz, *J. Phys. Chem. Lett.*, 2011, **2**, 1161–1166.

19 A. J. Bard and L. R. Faulkner, *Electrochemical Methods: Fundamentals and Applications*, John Wiley & Sons, 2nd edn., 2001.

Chapter 3: ORR Mediator/Shuttle for Lithium Air Batteries – Studies of Ethyl Viologen

3.1 Introduction

3.1.1 Principle of ORR Mediator/Shuttle

As addressed in Chapter 1, there are still issues that remain to be solved in the study of lithium air batteries, including electrode passivation by the reduction product – lithium peroxide, which will cause capacity fading. One of many approaches to tackle this problem is to introduce a mediator/shuttle to the lithium-air battery system.

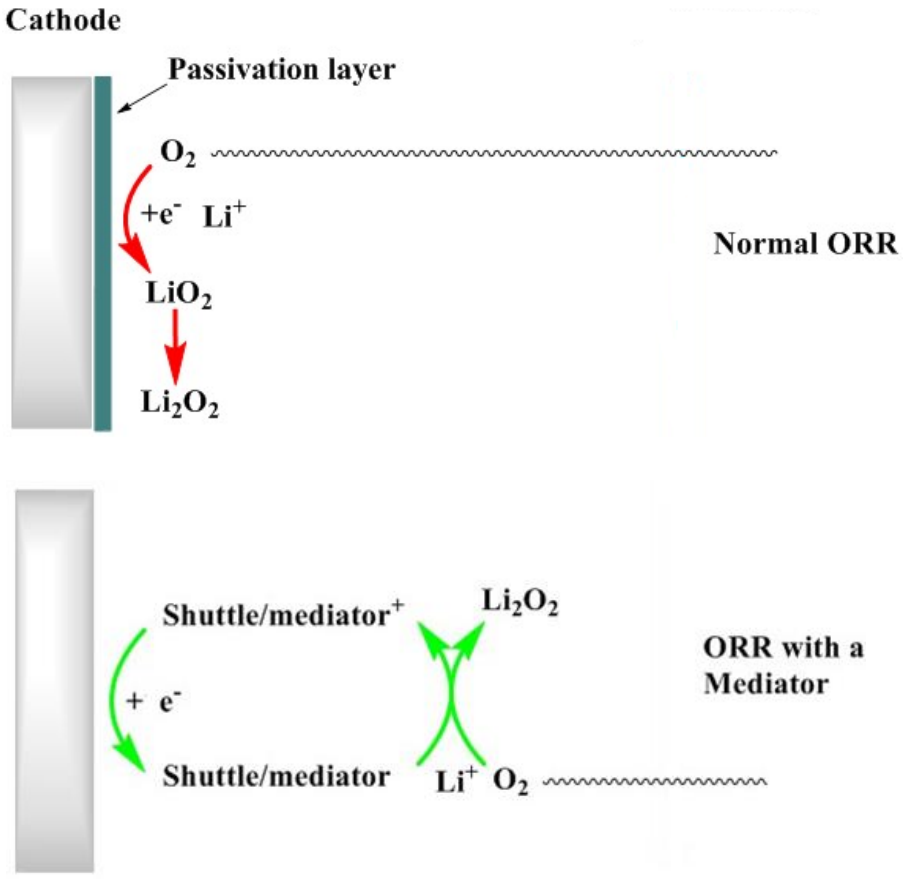

Figure 3.1 Schematic diagram of oxygen reduction reaction with and without shuttle and mediator in an organic lithium air battery system.

Figure 3.1 demonstrates how an ORR mediator/shuttle is expected to work in a lithium air battery system. In the system without mediator/shuttle, the oxygen reduction reaction takes place on the electrode surface, which will cause the

accumulation of lithium peroxide, hence leading to surface blocking. By adding a homogeneous mediator/shuttle, oxygen will be chemically reduced by the mediator/shuttle instead of being electrochemically reduced on the electrode. Therefore the formation of superoxide can be kept away from the electrode and the passivation can be mitigated.

To achieve this purpose, the ideal mediator/shuttle for ORR should have these properties: fast reaction rate with oxygen, redox reversibility, stability in the system and preferably a high diffusion coefficient. In this chapter, ethyl viologen will be used as a shuttle/mediator of oxygen reduction reaction in Li-air batteries.

3.1.2 Properties and Previous Applications of Viologen

It has been 80 years since Michaelis[1] reported the properties of derivatives of 4,4'-bipyridine named viologens. During the 1970s and 1980s the properties and applications of viologen has been intensively investigated.

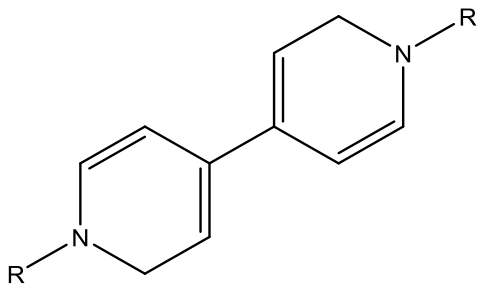

Figure 3.2 Structure of derivatives of 4,4'-bipyridine.

One of the important purposes of viologens is to be used as herbicides.[2,3] For instance, two of them are well-known as herbicides, paraquat (methyl viologen,1,1'-Dimethyl-4,4'-bipyridinium) and diquat (6,7-Dihydrodipyrido[1,2-a:2',1'-c] pyrazinediium). Their herbicidal properties were attributed to their redox potentials (e.g. for paraquat, E_0 = -0.446 V vs NHE). [4, 5] Different reaction schemes of viologen in the plant system have also been proposed.[6, 7]

In addition, viologens have also been applied in solar energy conversion. [8-12] The photoreduction of viologen can be achieved by the excited state of sensitizer such as tris (2,2'-bipyridine) ruthenium ($Ru(bipy)_3^{2+}$) [8-11] or zinc-tetraphenyl porphyrin (ZnTPP) [12]. This reaction can be coupled with photolysis of water generating H_2 and O_2.

Similarly, viologens have also been used as reaction mediators in other different systems due to their good electrochemical reversibility. In biological systems, both methyl viologen and phenyl viologen have been successfully tested as mediators in the reduction of cytochrome c, showing the efficiency almost 100 %.[13, 14] By using colourimetry, this system was also able to determine trace level of oxygen.[15]

Viologens were also widely investigated in many other industrial areas such as electrochromic displays [16–19], electroplating metal brighteners [20], glucose sensor [21] and film development accelerators [22].

Since the 1990s, the researchers have shown less interest in viologen until viologens were again applied in battery systems. It has been reported[23–25] that in the presence of viologen, carbohydrates can be readily oxidized by oxygen in alkaline solution, as shown in Fig. 3.3.

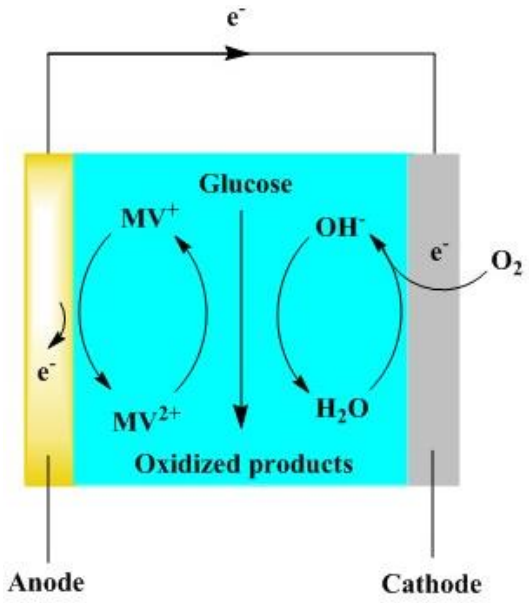

Figure 3.3 Schematic diagram of reaction in the fuel cell with methyl viologen.

The most important reason for choosing ethyl viologen in the system is that the reduced form of methyl viologen (MV^+) can react quickly with oxygen (k_2 = 7.7×10^{-8} M^{-1} S^{-1}), [7] forming superoxide radical. However, it was also reported that in aprotic system viologen might also irreversibly react with superoxide radicals, forming by-product. Therefore, it is a challenge to make sure the shuttle/mediator introduced is stable within the system. Previously, ethyl viologen was tested as a redox shuttle in lithium air cell. [26] The cyclic voltammogram showed that by introducing ethyl viologen, the oxygen reduction peak significantly increased, which indicated the fast reaction rate between

viologen and oxygen. Since it was been reported that methyl viologen with different oxidation state has distinguishable UV/Vis absorption peaks, [27–29] UV/Vis spectrometry will be applied to study its properties, including the chemical stability of viologen and the reaction kinetics. In addition the electrochemical behaviour of ethyl viologen will be further studied.

3.2 Experimental

3.2.1 Preparation of Chemicals

3.2.1.1 Preparation of ethyl viologen trifluoromethanesulfonate $EtV(OTf)_2$

0.468 g (1 mmol) of ethyl viologen diiodide (99 %, Sigma-Aldrich) and 0.514 g (2 mmol) of silver trifluoromethanesulfonate (≥99 %, Aldrich) was dissolved in 20 mL of deionized water respectively. Then the two solutions were mixed and stirred in room temperature for 1h. Yellow precipitation was formed upon mixing. Then the precipitation was filtered out by filter paper (Whatman), the clear solution was dried on petri dish in room temperature for 48h. The crystalized solid was collected from petri dish and dried under vacuum for 24 h in 120°C.

3.2.1.2 Lithiation of Lithium Titanium Oxide

In this report, lithiated lithium titanium oxide (LTO) was used as reducing agent for ethyl viologen. 2.18g dried $Li_4Ti_5O_{12}$ spinel (Sigma Aldrich, >99 %) and 90 mL anhydrous hexane (Sigma Aldrich, 95 %, dried with molecular sieves for 2 days before use) was transferred to a 3-neck round bottom flask under Ar atmosphere. 10 mL of butyl lithium solution (Sigma Aldrich, 1.6 M in hexane) was then injected into the flask through a syringe. The mixture was stirred under Ar atmosphere and the temperature was kept at 35 °C in an oil bath for 48 hours. In the end, the colour of LTO spinel changed from white to dark blue. The solution was allowed to settle for 30 min and upper layer of hexane was transferred out and destroyed by isopropanol. Then the rest of the mixture was diluted by anhydrous hexane twice in order to remove the residual butyl lithium. The solid was then dried under Ar atmosphere and vacuum, then transferred to glovebox (Mbraun, O_2<0.1 ppm, H_2O<0.1 ppm) for use the molecular formation of lithiated LTO was titrated by iodine as $Li_{6.8}Ti_5O_{12}$.

3.2.1.3 Chemical Reduction of Ethyl Viologen

After dissolving chosen amount of $EtV(OTf)_2$ in the chosen solvent, $Li_{6.8}Ti_5O_{12}$ spinel was added to the solution. The amount of LTO depends on the solvent, which will be discussed later. Then the solution was stirred overnight.

3.2.1.4 Pre-treating Chemicals

1-butyl-1-methylpyrrolidinium bis(trifluoromethylsulfonyl)imide (Pyr14TFSI, IoLiTec, 99 %, < 10 ppm water content) and lithium bis(trifluoromethylsulfonyl)imide (LiTFSI, 99.95 %, trace metal basis, Aldrich) were dried under vacuum at 120 °C for 48h. Acetonitrile (anhydrous, 99.8 %, Sigma-Aldrich) was purged with Ar gas for over 3 hours. Potassium superoxide (KO_2, Aldrich) was used as received.

3.2.2 UV/Vis Spectroscopy Measurement

The UV/Vis measurement was carried out using Lambda XLS UV/Vis spectrometer (PerkinElmer). Because reduced form of EtV is sensitive to air, therefore quartz cuvettes with screw caps (Starna, path length = 1 cm) were used. Solution containing solid spinel was filtered by syringe filter (Aldrich) before measurement.

Colourimetry was performed using WPA CO7500 Colourwave Colourimeter (Biochrom) under kinetic mode.

3.2.3 Electrochemical Tests

The electrochemical tests were conducted with variable-channel potentiostat (VMP, Biologic Science Instruments) and operated with EC-lab software package (Biologic Science Instruments). The parameters applied will be detailed with the results.

The type of electrochemical cell used was designed as U-shaped and shown in Fig 3.4. A glassy carbon electrode (d=3 mm) was used as the positive electrode and lithium foil (99.99 %, Chemetall GmbH) stabilized by stainless steel mesh was used as the counter/reference electrode. Two parts was separated by a frit (thickness c.a. 2 mm) to minimize the diffusion of mediator/shuttle to the lithium. Since the cell was prepared in an Ar filled glove box, the saturation of

the electrolyte with oxygen can be achieved by bubbling dry oxygen with needle through gas inlet 1 and outlet.

The ink for carbon coating is prepared by mixing pre-treated carbon nanotubes (fullerene, carbon nanotube, multi-walled, 3-20 nm OD, 1-3 nm ID, 0.1-10 micron long, 95 %, Alpha Aesar) and PVDF binder (Solvay Solexis Ltd) in mass ratio of 95:5 in N-methyl-2-pyrrolidone. The mixture was stirred with a digital homogenizer (T25, IKA) at the speed of 20000 RPM for 5 min. To pre-treat carbon nanotubes, the carbon nanotubes were stirred in 5 M HCl for 24 hours and washed with de-ionized water. For each coating, 2 μL of ink was carefully spread on the conductive part of the glassy carbon electrode, and then the electrode was dried at room temperature overnight. The mass of carbon on each electrode was calibrated each time before coating.

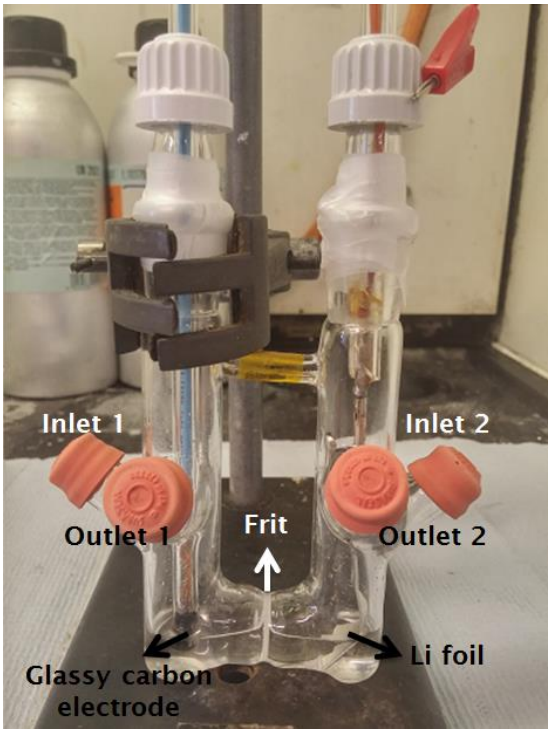

Figure 3.4 Photo of U-shaped cell used in electrochemical tests.

3.2.4 Raman Spectroscopy Measurement

Raman spectra were acquired using a 50X objective in combination with a Renishaw 2000 microscope equipped with a 632.8 nm He-Ne laser. The scanning range of the measurement was set from 100 cm^{-1} to 1200 cm^{-1}, the requisition time was 60 seconds and the scan number was 4. Raman spectra presented were baseline corrected using Origin 9.1.

3.3 Results and Discussion

3.3.1 Chemical Reduction of Ethyl Viologen

The UV/Vis spectra of 0.1 mM EtV^{2+} in $Pyr_{14}TFSI$ and acetonitrile are recorded and plotted in Figure 3.5. EtV^{2+} has an absorption peak at 260 nm with the extinction coefficient of 2×10^4 M^{-1}. DMSO was also tried in this experiment, however the colour became blue when viologen was dissolved, suggesting the reduction of viologen in DMSO (will be explained later).

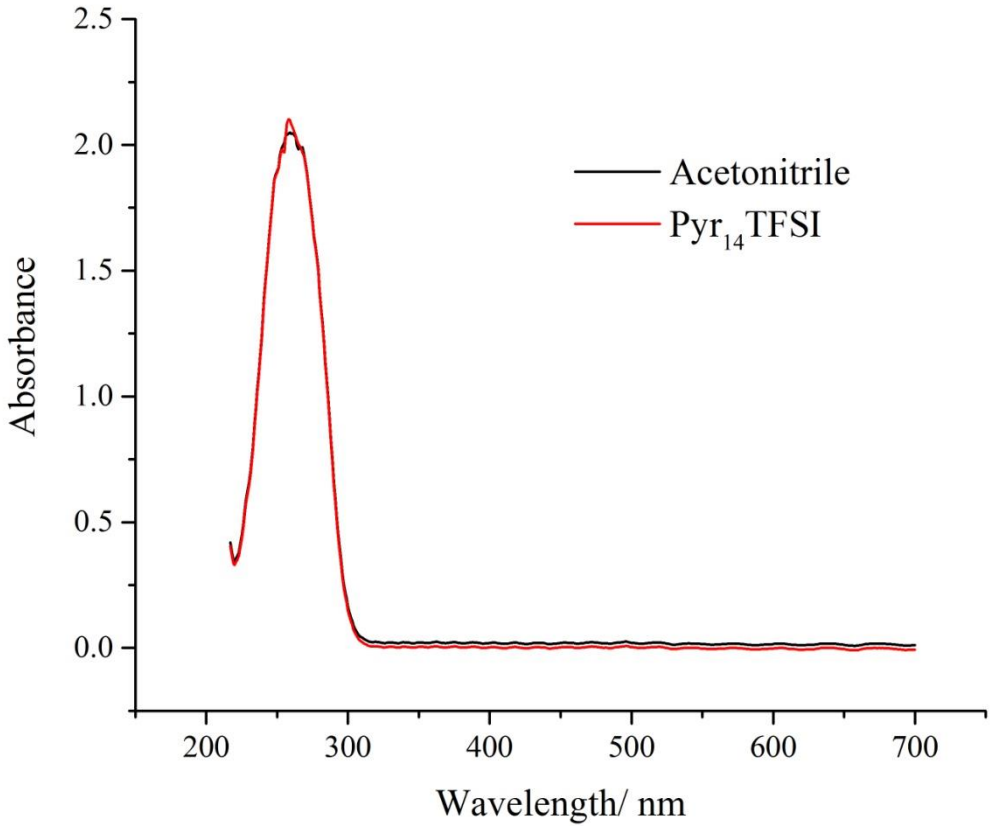

Figure 3.5 UV/Vis spectra of 0.1 M $EtV(OTf)_2$ in acetonitrile and $Pyr_{14}TFSI$.

The reduce EtV^{2+} to EtV^{+}, stoichiometric amount of $Li_{6.8}Ti_5O_{12}$ was added into the viologen solution and stirred with magnetic stirring bar. The UV/Vis spectra were taken at different time during the reaction. As shown in Fig 3.6, as the reaction went on, the absorption at 260 nm decreased as two new peaks emerged (396 nm and 605 nm), which agreed well with the previous results, [27-29] indicating that EtV^{2+} has been successfully reduced to EtV^{+}.

However the reaction rate, which indicated by how fast the EtV^{2+} peak decreased (or how fast the EtV^{+} peaks increased), slowed down with time. Even after 24 hours EtV^{2+} still cannot be completely reduced to EtV^{+}. Therefore, to

acquire EtV^{+} within a reasonable amount of time, larger amount of LTO should be added.

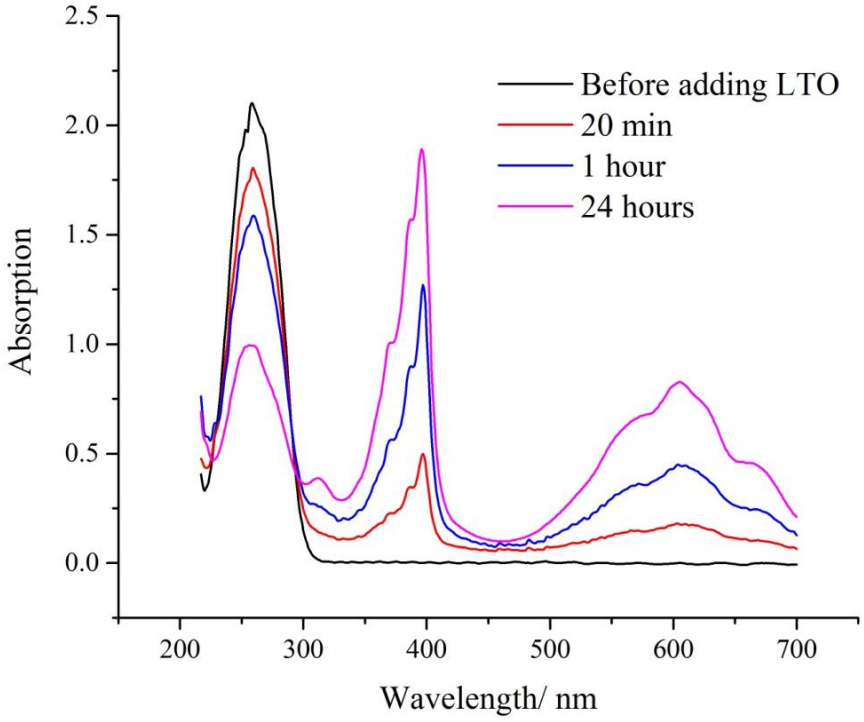

Figure 3.6 UV/Vis spectra of reduction of 0.1 M EtV^{2+} using stoichiometric amount LTO in $Pyr_{14}TFSI$, the wavelength range was selected from 200 nm to 700 nm.

To investigate the appropriate amount of LTO needed to completely reduce EtV^{2+} within hours, LTO was added into the solution with different amounts. As shown in Fig. 3.7, the amount of LTO required was 1.8 times of the stoichiometric amount. It can be observed that the EtV^{2+} peak red shifted as the reduction proceeded. The shifted peak with wavelength below 250 nm did not change linearly with the increase of EtV^{+} peak; therefore it could no longer directly reflect the concentration of EtV^{2+} by applying Beer-Lambert's law. The amount LTO needed in acetonitrile was also measured as 1.2 times of the stoichiometric amount by the same method. The extinction coefficient of two peaks were determined as $3.9\times10^{4}\,M^{-1}$ (λ = 396 nm) and $1.52\times10^{4}\,M^{-1}$ (λ = 605 nm), these numbers also agreed with previous studies. [27, 29]

As a result, in $Pyr_{14}TFSI$ by using 1.8 times of stoichiometric amount of LTO, almost all EtV^{2+} can be reduced EtV^{+} in 5 hours (Fig 3.7). The amount LTO needed in acetonitrile was also determined as 1.2 times of stoichiometric amount in same method.

In addition, by adding large excess amount of LTO, EtV^{2+} can be even further reduced to EtV^{0} (see Appendix 1), which can be oxidized to EtV^{+} by adding more EtV^{2+}.

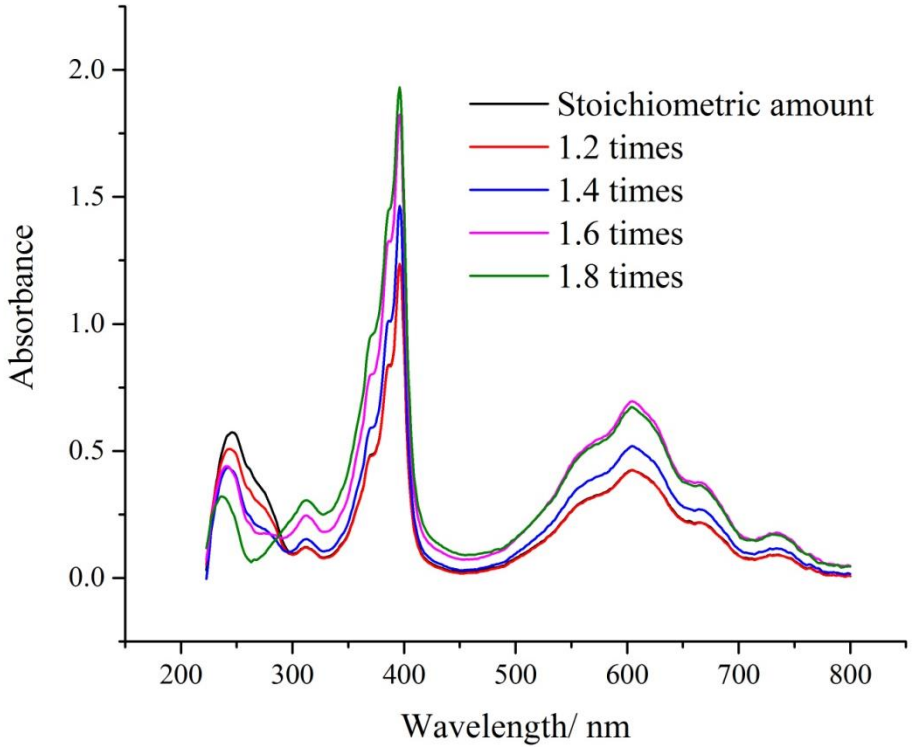

Figure 3.7 UV/Vis spectra of 0.05 M EtV^{2+} after reacting with different times of stoichiometric amount of LTO for 5 hours in $Pyr_{14}TFSI$.

3.3.2 Reaction between Ethyl Viologen and O_2

3.3.2.1 Study of Reaction Stoichiometry

The reaction between EtV^{+} and O_2 is very fast and can be observed with naked eye by seeing the colour change (see Appendix 2). In this experiment, the reaction between EtV^{+} and O_2 is quantitatively controlled by adding oxygen saturated solution into the viologen solution. In order to prepare oxygen saturated solution, dry oxygen was bubbled to anhydrous solution with seal for 1 hour and the solution was transferred into glove box for use. Then the oxygen saturated solution was added stepwise into the EtV^{+} solution. The mixed solution will be stirred for 20 min and measured by UV/Vis spectrometer before each addition. As the amount of aliquot added into the solution and the amount of liquid taken out for UV/vis measurement is insignificant compared to the bulk solution, the concentration change was neglected.

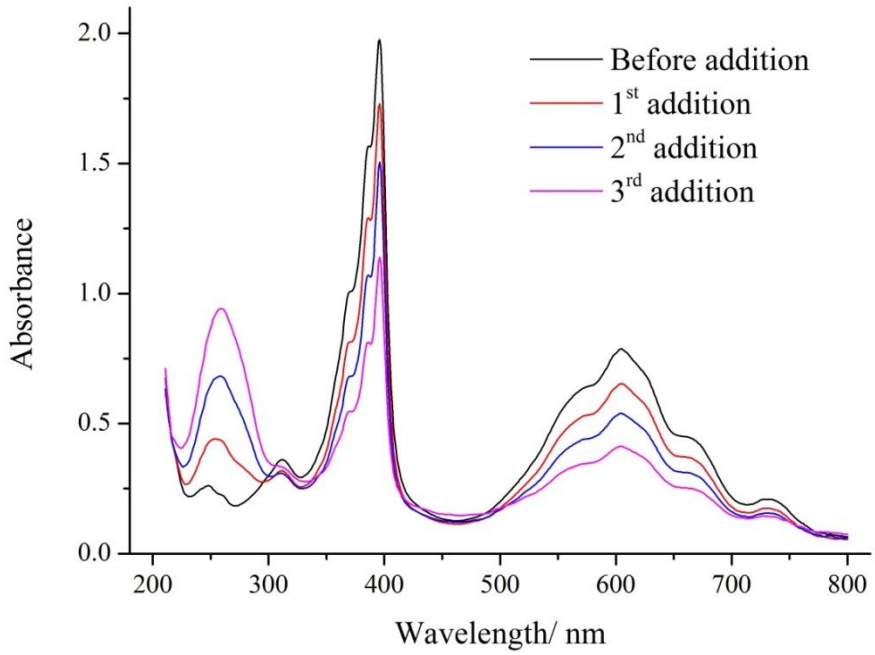

a

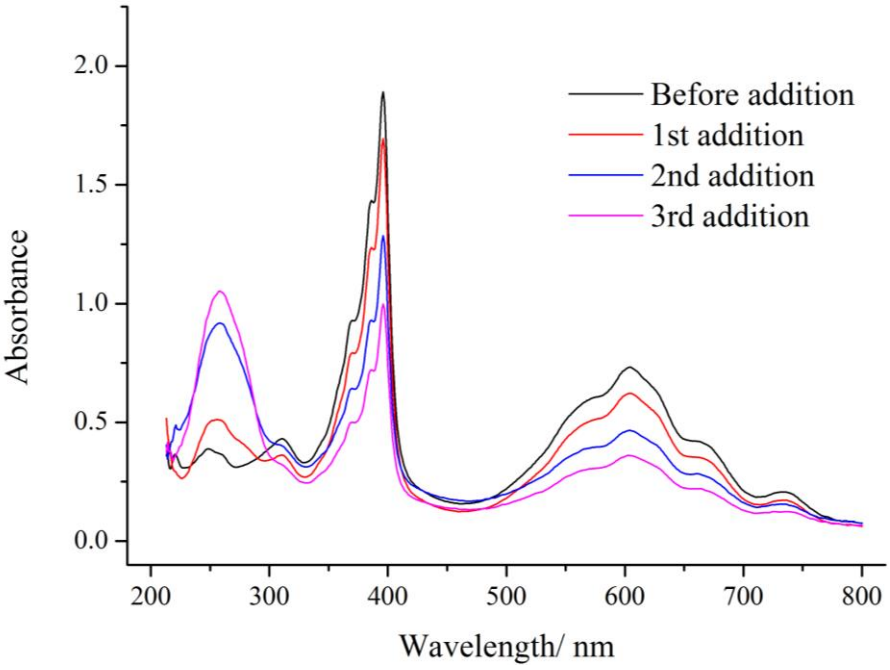

b

Figure 3.8 UV-vis spectra measured during the titration of 30 mL of 0.1 mM EtV^{+} + 0.3 M LiTFSI in acetonitrile (a) and $Pyr_{14}TFSI$ (b) with several aliquots of 0.03 mL (a) and 0.08 mL (b) of oxygen-saturated solvent. Before the UV-vis measurements, the solutions were half diluted with pure solvent.

As shown in Fig. 3.8, the peak (605 nm) corresponding to EtV^{+} gradually decreased while the peak for EtV^{2+} (260 nm) increased with additions of aliquots. From the magnitude of the peak, it can be observed that the decrease of the EtV^{+}

was very consistent after each addition. To calculate the reaction stoichiometry between oxygen and viologen, an extinction coefficient of 1.52×10^{4} $cm^{-1}M^{-1}$ for EtV^{+} at 605 nm and saturated concentration of oxygen in both solvent (8.1 mM in acetonitrile [30, 31] and 3 mM in $Pyr_{14}TFSI$ [32]) were applied. As a result, each oxygen molecule reacts with 2.05 and 2.12 EtV^{+} molecules respectively, which suggests that viologen can facilitate a two-electron reduction of oxygen.

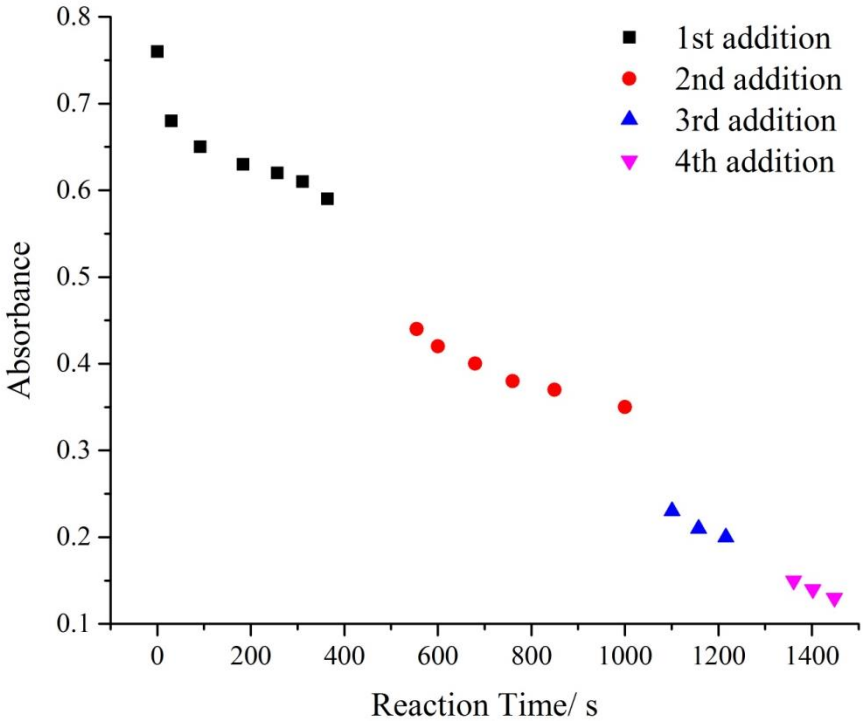

Figure 3.9 Absorbance at 590 nm of 20 mL $Pyr_{14}TFSI$ with approximately 0.1 mM EtV^{+} with additions of aliquots (25 μL) of oxygen saturated $Pyr_{14}TFSI$.

It was only reported that EtV^{+} reacted with oxygen in 1:1 ratio, therefore there should be a second step of this reaction which has not been reported. The preliminary results of oxygen titration experiment using colourimetry (see Fig 3.9), which only records the absorbance on 590 nm (within the peak that corresponding to the EtV^{+} species), also suggests a two-step reaction between oxygen and EtV^{+}. After each addition, the absorbance sharply decreased within seconds and the decrease slowed down afterwards, meaning that the reaction between viologen and oxygen was fast at first then the reaction rate slowed down with time. It was suggested that the reaction could be a two-step one. As stated before, the fast one-electron reduction between EtV^{+} and O_2 has been known as:

$$EtV^{+} + O_2 \rightarrow EtV^{2+} + O_2^{-} \quad \text{(Equation 3.1)}$$

which accords with the sharp decrease after each addition. Also, by roughly comparing the absorbance decrease during the first and second step of reduction

according to the assumption, they are in the ratio of approximately 1:1, which further inferred the existence two-step reaction. The second reaction should occur between viologen and O_2^-. Therefore, this two-electron reaction of oxygen can be proved by verifying that O_2^- can react with EtV^+ in 1:1 molar ratio.

To prove that O_2^- can react with EtV^+ in 1:1 ratio, similar titration experiments were performed in acetonitrile using O_2^- solution. KO_2 was used as the source of O_2^- in this experiment. Because KO_2 was insoluble in $Pyr_{14}TFSI$, only acetonitrile was tested. To make KO_2 solution with concentration of 1.5 mM, KO_2 powder was dissolved in acetonitrile and stirred overnight. The KO_2 solution was titrated into EtV^+ solution. The solution will be stirred for 20 min after each addition and measured by UV/Vis spectrometer before each addition.

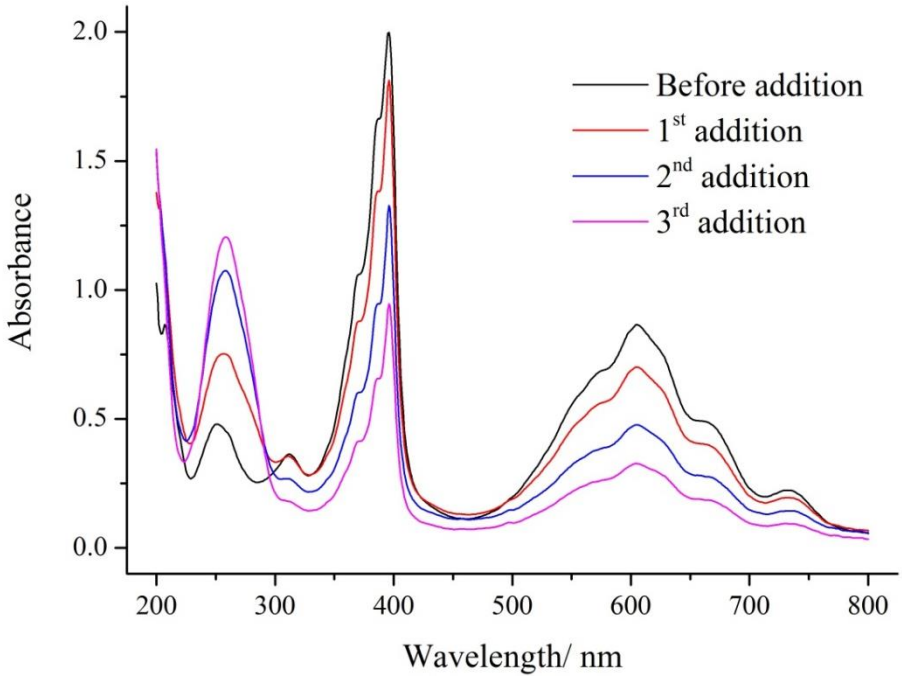

Figure 3.10 UV-vis spectra measured during the titration of 30 mL of 0.1 mM EtV^+ + 0.3 M LiTFSI in acetonitrile with several aliquots of 0.5 mL 1.5 mM KO_2 solution. Before the UV-vis measurements, the solutions were half diluted with pure solvent.

In Fig. 3.10, it can be seen that with each addition the EtV^+ absorption peak decreased as EtV^{2+} increased, indicating the oxidation of EtV^+ to EtV^{2+}. By measuring the absorbance, it can be calculated that the concentration of EtV^+ decreased by 0.071 mM, corresponding to 0.00213 mmol. Since the total amount of KO_2 was added to the solution was 0.00215 mmol, each mole of KO_2 can react with 0.95 mole of EtV^+. The fact that KO_2 can react with EtV^+ in the molar ratio of

1:1 not only confirmed the two-electron reduction of oxygen but also suggests the possibility of following reaction:

$$O_2^- + EtV^+ \rightarrow O_2^{2-} + EtV^{2+} \text{ (Equation 3.2)}$$

The mechanism of the reaction will be discussed in 3.3.3.

3.3.2.2 Study of Reaction Reversibility

In previous studies, superoxide radical was reported to be very reactive towards organic electrolytes [35, 36] and viologen [7], forming degradation products. Hence, it is important to identify whether the reaction between viologen and oxygen/superoxide was reversible. In this experiment, LTO was added again to the solution titrated with oxygen/superoxide. Therefore, if the reactions that have been observed were reversible, the ethyl viologen was expected to be fully reduced again. Since the direct contact between LTO and oxygen might introduce unnecessary complexity into the system, the titration was stopped before its end point intentionally to make sure the solution was oxygen/superoxide depleted.

After the titration, 1.7 mg of LTO was added to the solution and stirred for 1 hour. Then the UV/Vis spectra were taken again. As shown in Fig. 3.11 and Fig. 3.12, in all three cases, EtV^+ was almost fully recovered after the addition of LTO, suggesting little degradation product was formed. The reason for the inconsistency in the spectra under 300 nm still needed further investigation but it did not affect the quantitative analysis of EtV^+.

As a result, the good reaction reversibility between ethyl viologen and oxygen is demonstrated, which shows the potential of ethyl viologen as an effective shuttle/mediator in lithium-air batteries.

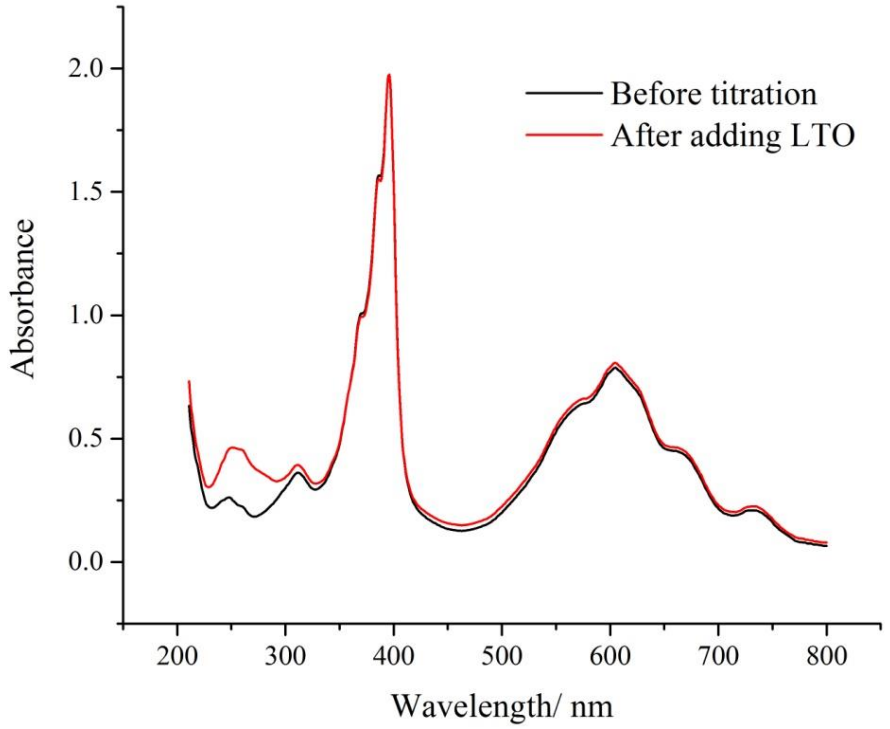

a

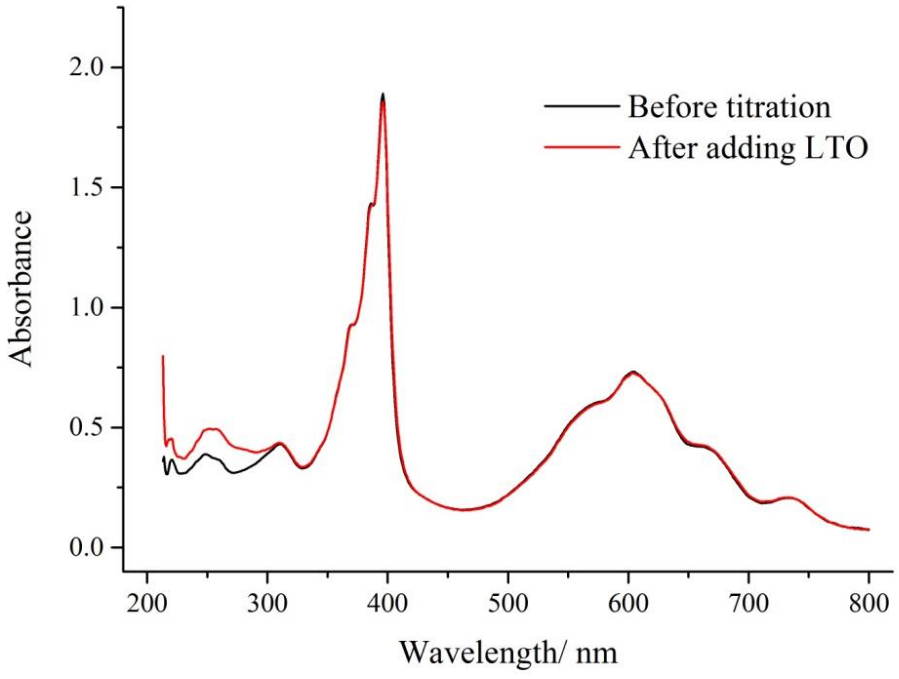

b

Figure 3.11 UV-vis spectra of 0.1 mM EtV^{+} in acetonitrile (a) and $Pyr_{14}TFSI$ (b) before the reaction with oxygen followed by re-reduction with LTO. Before the UV-vis measurements, the solutions were half diluted with pure solvent.

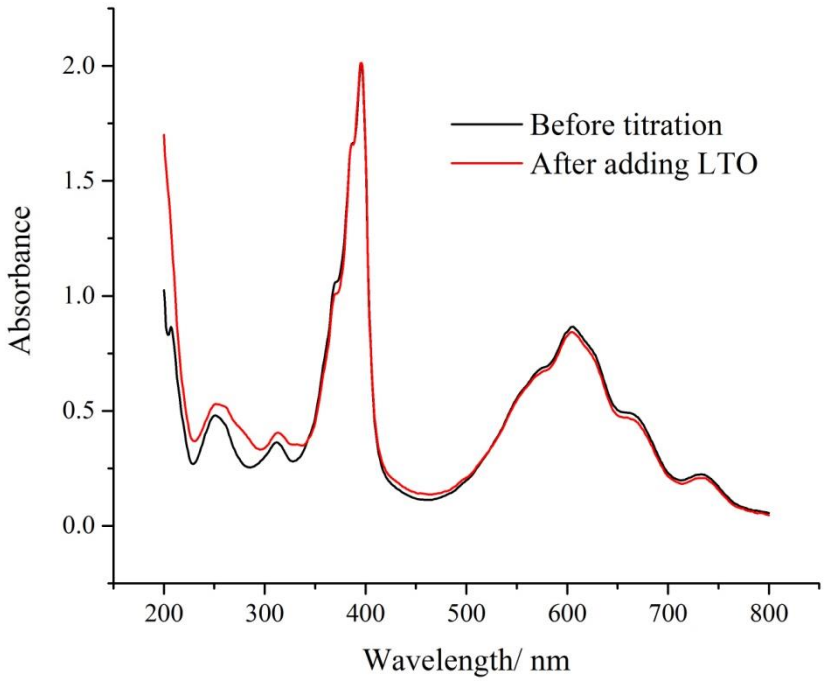

Figure 3.12 UV-vis spectra of 0.1 mM EtV^+ in acetonitrile before the reaction with KO_2 followed by re-reduction with LTO. Before the UV-vis measurements, the solutions were half diluted with pure solvent.

One thing to be noted is that the irreversible reaction described by Nanni[7] was not observed in this experiment. One of the differences between two experiments was that high concentration of Li^+ was used in this experiment. If there is evidence that lithium ions can play an important role in the reaction between viologen and O_2^-, the difference can be explained.

3.3.2.3 Effect of Lithium Ion

To find out the effect of Li^+ on the reaction between viologen and superoxide, viologen solution was again titrated with KO_2 solution in presence of different concentration of LiTFSI in acetonitrile. In this experiment, the reaction was monitored by colourimeter. Upon adding aliquots of KO_2, the mixed solution was stirred vigorously for 5 seconds and sampled out to the cuvette. Under kinetic mode, the colourimeter can measure and display the absorbance constantly with interval of about 2 seconds. The absorbance was observed and recorded with time manually. Due to the limitation of the absorbance, the wavelength displayed was chosen as 590 nm.

By plotting the absorbance change against the reaction time (Fig. 3.13), the reaction rate between viologen and superoxide is shown – a faster decrease in absorbance means a faster reaction rate. From Fig 3.13 it is clear that the reaction rate increased with Li^+ concentration. Also, from the shape of the curve it

can be seen that the absorbance did not change linearly with time, indicating the reaction was a first or higher order reaction. The sharp decrease of the absorbance at the beginning could be due to the high concentration of superoxide upon addition, which was not stirred homogenously during a short amount of time.

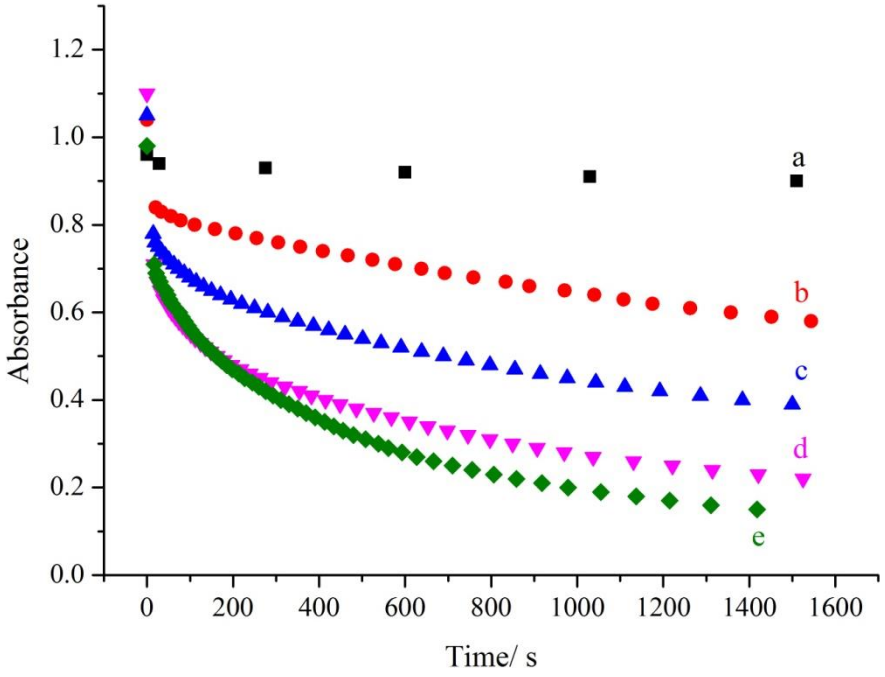

Figure 3.13 Absorbance at 590 nm of a solution of EtV^+ and KO_2 in acetonitrile, with initial concentrations of 0.1 mM EtV^+ and 0.1 mM KO_2. The concentration of LiTFSI in solution was: (a) 1 mM, (b) 75 mM, (c) 150 mM, (d) 300 mM, and (e) 600 mM.

It can be deduced that the reaction between EtV^+ and O_2^- is not reversible in the absence of Li^+. With increasing amount of Li^+, the reaction became not only reversible but also faster. One possible explanation might be that Li^+ participated in the reaction so with higher concentration, it speeded up the reversible reaction rate. In this case, viologen was protected from O_2^- by lithium ions. This graph also demonstrated a straightforward probe of the lifetime of O_2^-, showing that with high concentration of Li^+ and viologen, the lifetime of superoxide can be reduced greatly. This might be beneficial to the lithium air battery researches since the superoxide radical is aggressive to most organic electrolytes.

The other information can be learned was that with the irreversible reaction between EtV^+ and O_2^-, which happened under low Li^+ concentration, was slow according to the slow change of absorbance in curve a in Fig. 3.13. Therefore, even without the protection from Li^+, viologen was still stable against O_2^- within a

reasonable amount of time. However, discolouration of viologen can be observed by adding large excess of KO_2 (molar ratio = 1:100). Therefore, it would be useful to investigate the kinetics of the degradation reaction between EtV^+ and O_2^- in the future.

3.3.3 Investigation of Reaction Mechanisms

As described above Li^+ was involved in the reaction between O_2^- and EtV^+. The reaction mechanisms will be discussed in detail. Two possible mechanisms are proposed here: one was based on the disproportionation of lithium superoxide; the other one was that EtV^+ would react with lithium superoxide directly.

In the first assumption, one mole lithium ions combined with one mole superoxide, forming one mole of lithium superoxide which will disproportionate into half a mole of oxygen and half a mole of peroxide. The half mole of oxygen will react with half a mole of EtV^+, forming a ¼ mole of superoxide and the reaction goes on infinitely as shown in Fig 3.14.

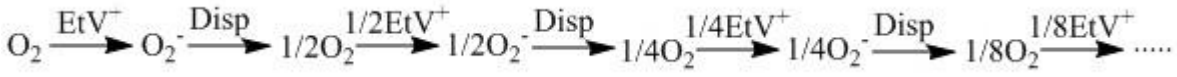

Figure 3.14 Scheme of "Infinite disproportionation" assumption.

To confirm this assumption, it needs to be determined whether lithium superoxide will disproportionate under the given reaction condition. First, a qualitative experiment was performed: 0.213 g of KO_2 (3 mmol) was added to 20 mL 300 mM LiTFSI solution in acetonitrile. A large amount of gas was generated instantly upon the addition of KO_2 powder and white precipitate was formed. The precipitate was filtered and washed by acetonitrile 3 times, then dried under vacuum overnight. The white powder was analysed by Raman spectrometer. In the Raman spectra (Fig. 3.15), by comparing with the standard Li_2O_2 sample, the two scattering peaks at 257 cm^{-1} and 789 cm^{-1} matched very well. This peak position also agreed with previous results, [37, 38] showing that the white precipitate was Li_2O_2.

Next, the reaction condition used in the titration was adopted to see if disproportionation reaction will occur under such condition. 1 mL of 1 mM KO_2 solution was added 9 mL acetonitrile solution with 333 mM LiTFSI to so the result concentration of KO_2 was 0.1 mM and the concentration of Li^+ was 0.3 M, which was the same concentration in the titration. By using UV/Vis spectrometry, 0.1

mM of KO_2 in acetonitrile had an absorption peak at 260 mM (Fig 3.16), which agrees with previous study [39]. After mixing with LiTFSI, the absorption peak remained unchanged after 3 hours, which indicated that the disproportionation did not occur when the concentration of superoxide was low. When the concentration increased to 1 mM, same result was obtained that there was no evidence of disproportionation (Appendix 3).

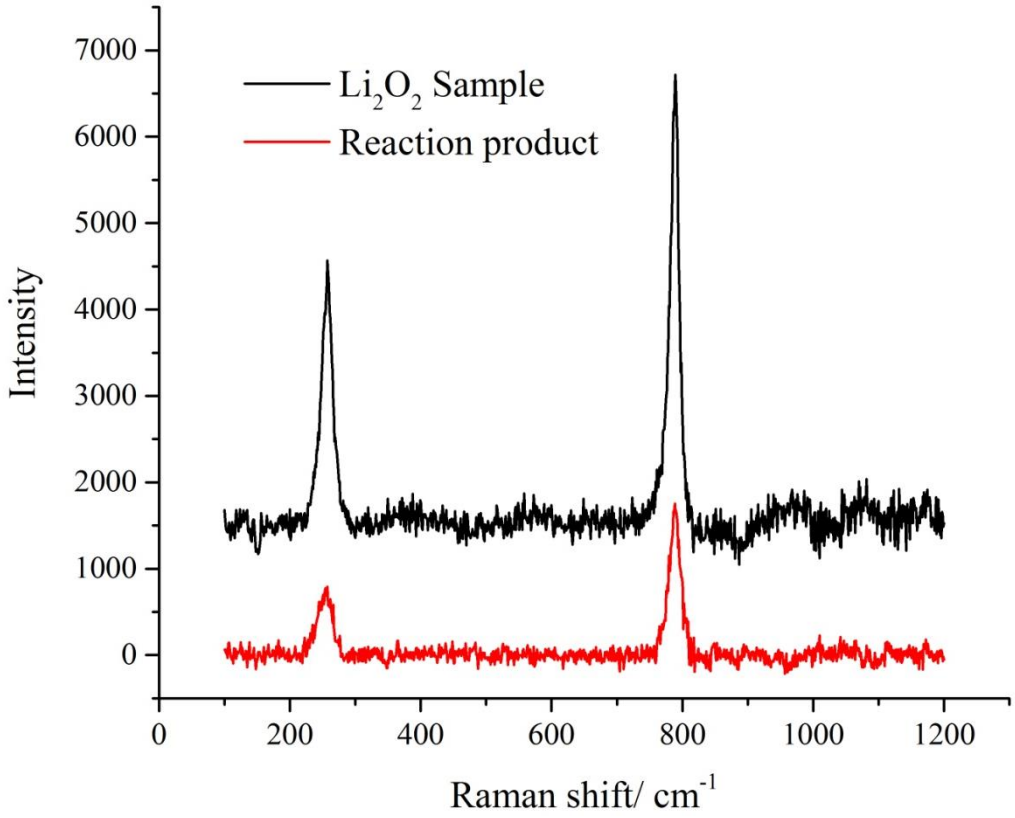

Figure 3.15 Raman spectra of standard Li_2O_2 sample and the precipitate obtained from adding 0.213g KO_2 in 20 mL 0.3 mM LiTFSI solution in acetonitrile. The base line was corrected using Origin 9.1.

In the absence of ethyl viologen, since the lifetime of O_2^- was so long that disproportionation reaction was undetectable under low O_2^- concentration, the first assumption about the reaction mechanism, which was based solely on the disproportionation of lithium superoxide, should be ruled out.

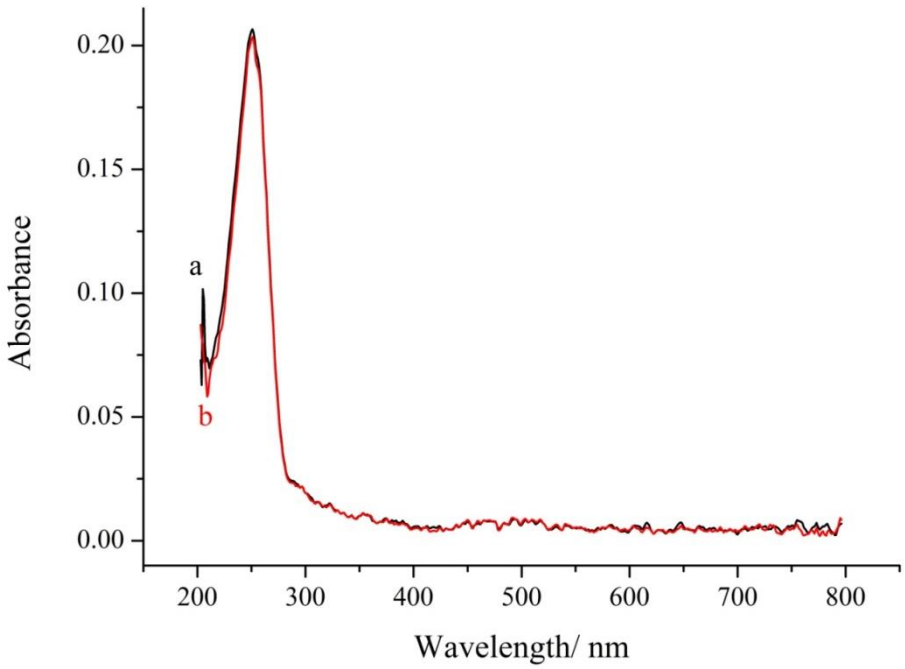

Figure 3.16 UV/Vis spectra of ca. 0.1 mM KO_2 solution in acetonitrile before (a) and 3 hours after the addition of 300 mM LiTFSI (b).

According to the second assumption, a third-order reaction was proposed:

$$EtV^+ + O_2^- + Li^+ \rightarrow EtV^{2+} + LiO_2^- \text{ (Equation 3.3)}$$

Since $[EtV^+] \approx [O_2^-] << [Li^+]$, the concentration of Li^+ can be regarded as a constant, hence, a second-order reaction can be estimated and the reaction rate of EtV^+ will be:

$$d[EtV^+]/dt = k_3[Li^+][EtV^+]^2 = k_2[EtV^+]^2 \text{ (Equation 3.4)}$$

In which, k is the reaction rate constant and $K_2 = k_3 [Li^+]$. The equation then can be deduced as:

$$[EtV^+]^{-1} = k_2t + c \text{ (Equation 3.5)}$$

In which, c is a constant.

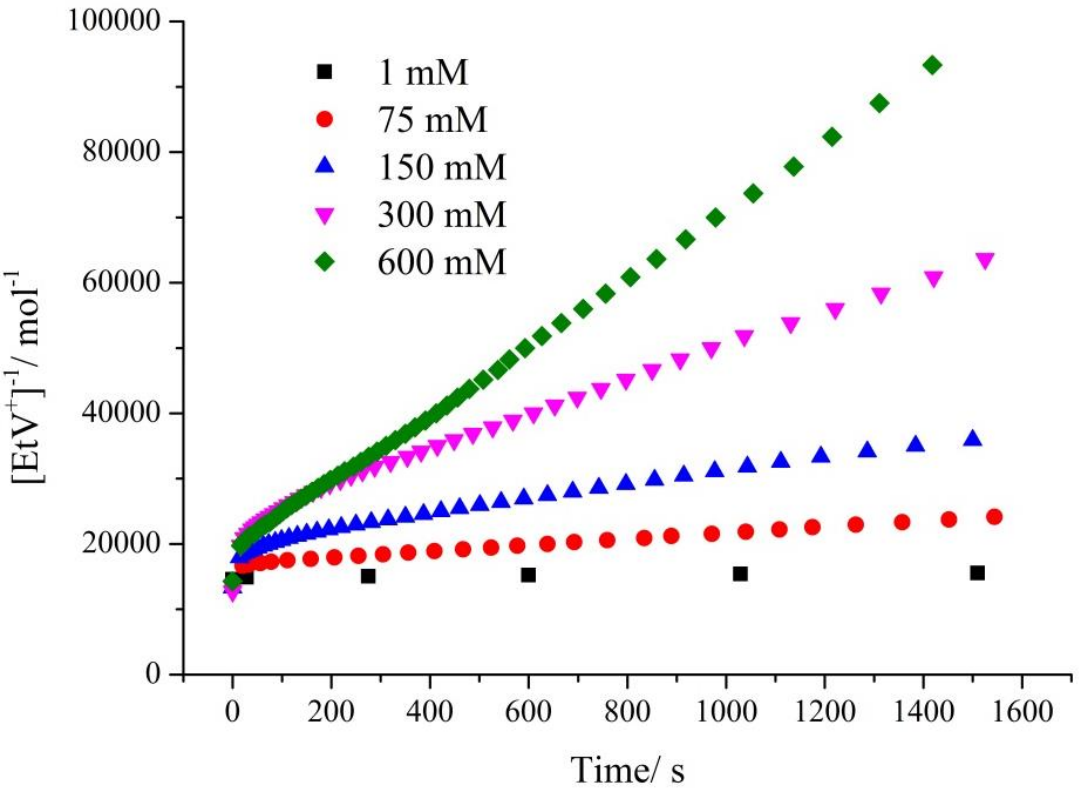

Figure 3.17 Plot of the reciprocal of the EtV^+ concentration against time.

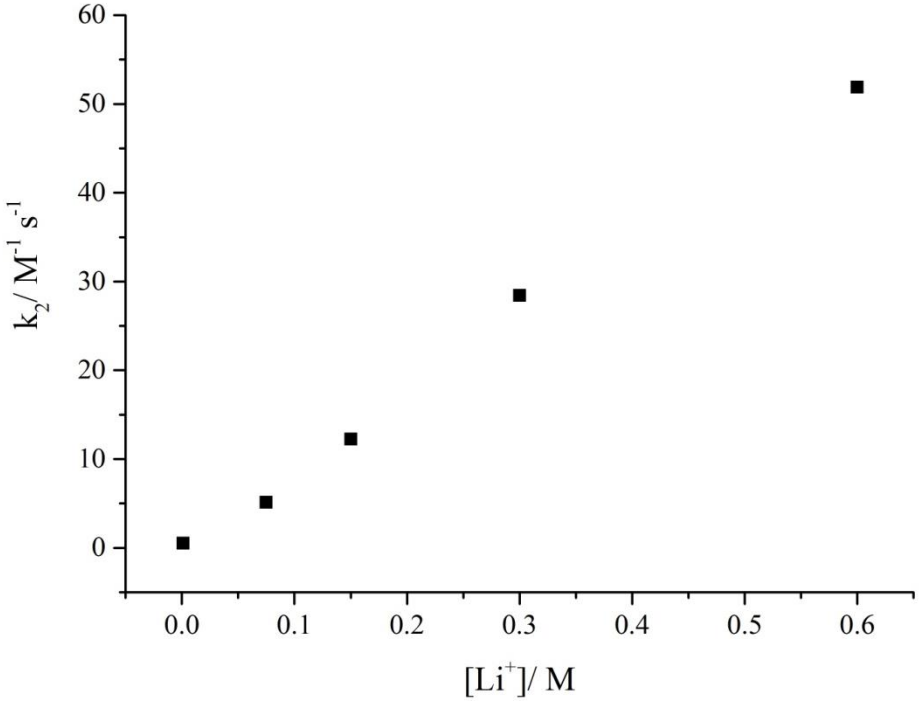

Figure 3.18 Plot of k_2 against $[Li^+]$.

The reciprocal of $[EtV^+]$ was plotted against time, as shown in Fig. 3.17. It can be seen that the data show good linearity, which means that the reaction follows a third-order reaction scheme as shown in Equation 3.3. Therefore, the second proposed mechanism fits the results. Then the data was processed in Origin with

linear fit, the slope of each curve (k_2) was obtained. According to Equation 3.4, k_2 should be proportional to [Li^+] since k should be a constant. By plotting k_2 against [Li^+] (see Fig. 3.18), a linear relationship was observed. By combining these data, it can be concluded that the reaction follows the scheme proposed above. In addition, based on the slope of the curve in Fig. 3, it can be also calculated that the value of k_3 is 87.6 M^{-2} s^{-1}.

In addition, the rate of reaction between oxygen and viologen was also measured. By dosing stoichiometric amount of oxygen (n_{O2}:n_{EtV} = 1:2) into the solution of 0.1 mM [EtV^+] in the presence of 300 mM of LiTFSI and comparing the result with the reaction between viologen and KO_2 (Fig. 3.13), it can be observed that the decrease of [EtV^+] was quicker with oxygen at the beginning. This is because the fast one electron reaction between oxygen and EtV^+ as shown in Equation 3.1:

$$O_2 + EtV^+ \rightarrow O_2^- + EtV^{2+}$$

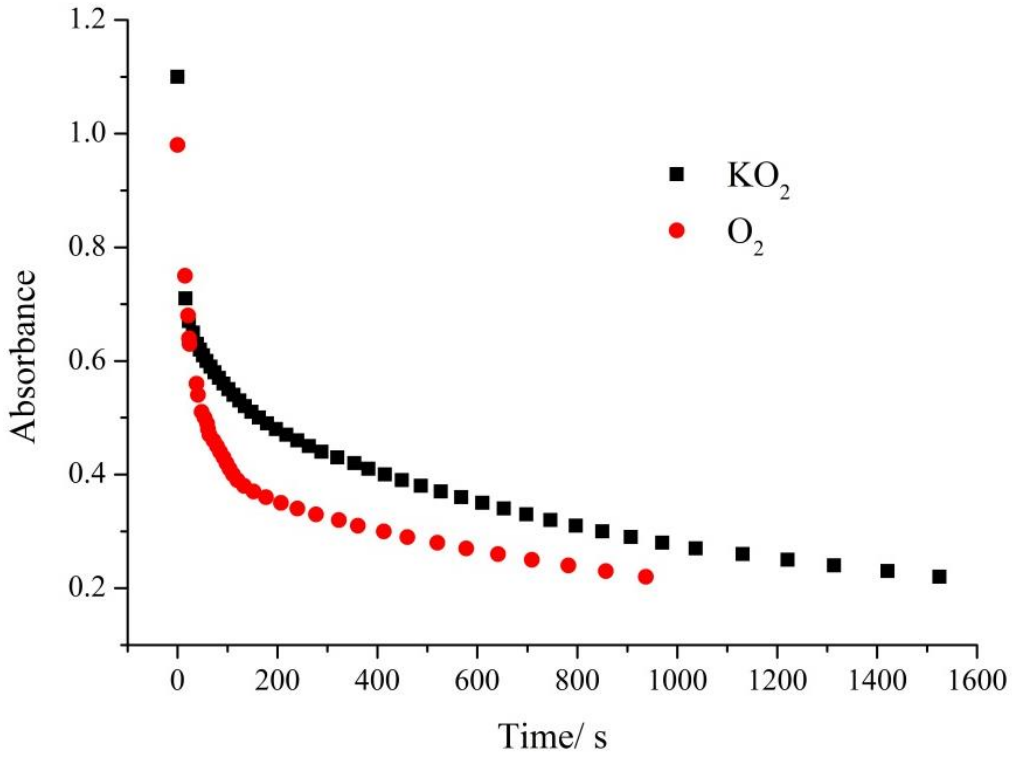

Figure 3.19 Absorbance of 0.1 mM EtV^+ in acetonitrile after addition of KO_2 and O_2 in the presence of 300 mM LiTFSI.

Therefore, after the absorbance decreased to half of the starting value, it can be estimated that the oxygen has been consumed. As a result, the rate of the reaction slowed down significantly. This might be due to the relatively slow

second electron reaction between EtV^+ and O_2^-. This is confirmed by comparing the kinetic data shown in Fig. 3.20.

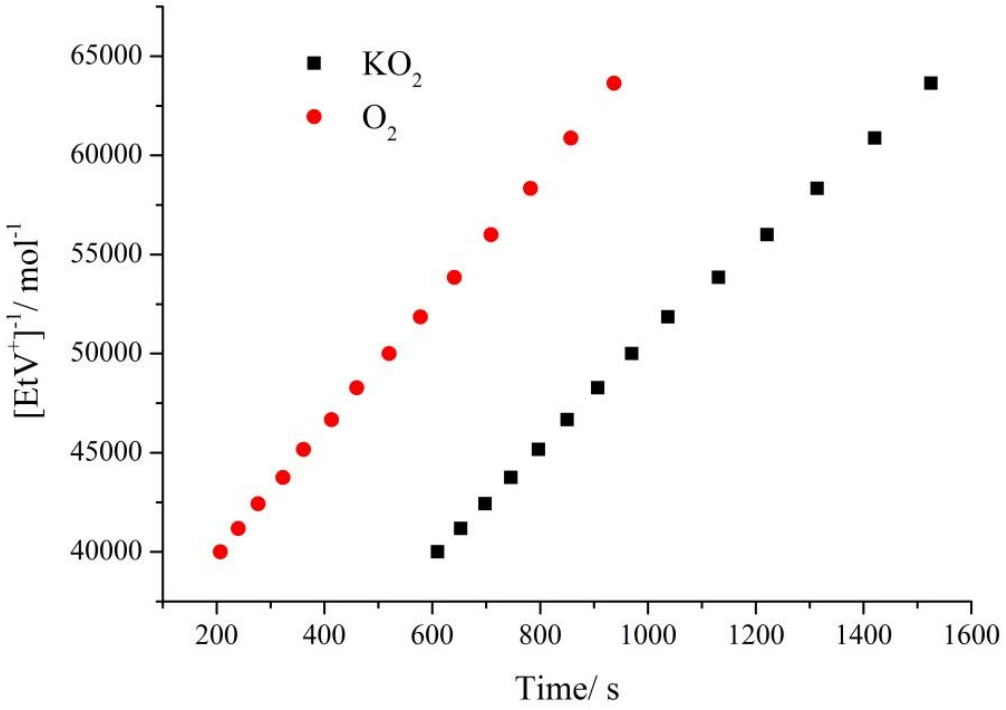

Figure 3.20 Plot of reciprocal of $[EtV^+]$ in Fig. 3.19 against time.

By comparing the slopes in both curves, it can be concluded that the reaction rate of oxygen titration slowed down to the similar rate of the KO_2 experiment. This result has confirmed the second electron reaction between O_2 and EtV^+ follows the same route of the O_2^-–EtV^+ reaction.

3.3.4 Electrochemical Performance of Ethyl Viologen

3.3.4.1 Surface Area Characterization of Carbon

The previous cyclic voltammogram results in $Pyr_{14}TFSI$ have showed that compared to the Ar saturated electrolyte, the reduction current peak of ethyl viologen was enhanced when the electrolyte was saturated by O_2 due to the mediation effect.[26] To evaluate the performance of EtV as a mediator in a battery, it is also necessary to test its electrochemical properties using galvanostatic cycling techniques.

As stated in Chapter 1, in terms of surface properties, the air breathing positive electrode should have high specific surface area and large pore volume – high specific surface area provides more reaction sites for electron transfer whereas the large pore capacity contains more Li_2O_2 and enhances ion transfer.

Therefore, the choice of positive electrode materials was based on the results of their surface area characterization. Three types of carbon were investigated using nitrogen adsorption method – activated carbon, carbon nanotube (CNT) and acetylene black (AB). The experimental detail was described in Chapter 5.

First, the surface area of different carbons is shown in Table 3.1. The result showed that activated carbon exhibited the highest specific surface area and acetylene black had the lowest, which indicated that activated carbon can facilitate most three-phase junction for the reaction.

Table 3.1 Specific surface area of different types of carbon

Type of Carbon	Specific Surface Area (m^2 g^{-1})
Activated carbon	732.1
CNT	273.4
AB	73.1

On the other hand, the pore size distribution of the carbon was also measured and plotted using BJH model in Fig. 3. 21. Although activated carbon has the highest surface area, its pore size was mainly distributed between 1- 4 nm, representing micropores and small mesopores, which was not ideal. As for the CNT, the pore size was evenly distributed from 10 nm to 50 nm, showing that a large portion of its pores are large mesopores, which is beneficial to the cycling performance. Lastly, the pore size of acetylene black was between the activated carbon and CNT.

As discussed in Chapter 1, pores with larger diameters are considered more suitable for Li-air cells because they are less likely to be blocked by lithium peroxide. Therefore, combining the above results, CNT was chosen as the positive electrode material for all the cycling tests in Li-air cells due to the fact that it exhibited the best pore size needed and a satisfactory surface area. However, since the choice of carbon was solely based on the surface area and the estimated pore size distribution, more electrochemical tests need to be done in order to have a fair comparison between the carbons.

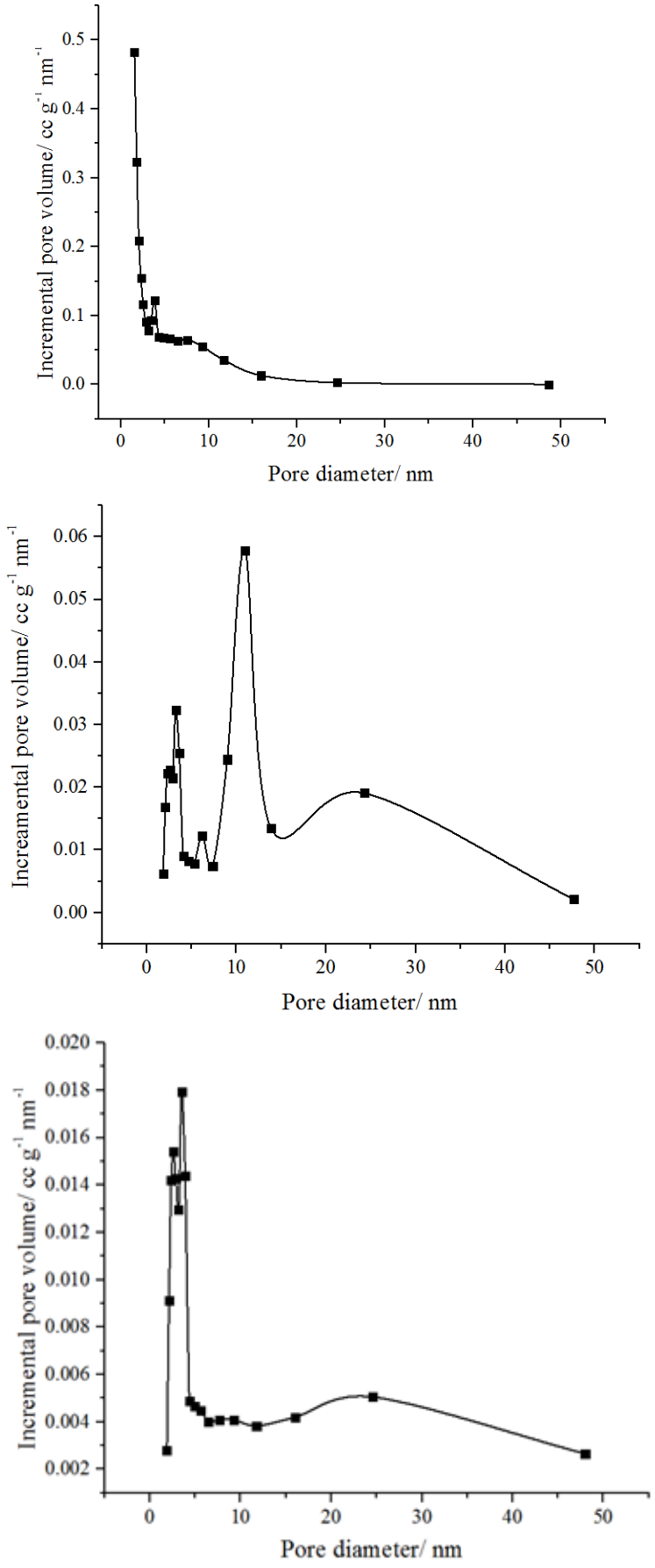

Figure 3.21 Pore size distribution of CA1 activated carbon (top), CNT (middle) and acetylene black (bottom).

3.3.4.2 Galvanostatic Cycling Results of Li-Air Cells with Ethyl Viologen

Fig. 3.22 showed the galvanostatic discharge curve in $Pyr_{14}TFSI$. By comparing the discharge of viologen, similarly to the cyclic voltammogram result, the capacity increased significantly when the electrolyte was saturated with oxygen, indicating a remarkable mediation effect in which the reduced form of EtV instantly reacted with oxygen. However, the short discharge plateau of EtV in Ar saturated electrolyte suggested the diffusion coefficient of EtV was low in the ionic liquid, which is a disadvantage as a shuttle and might be improved by increasing the concentration of EtV in the electrolyte.

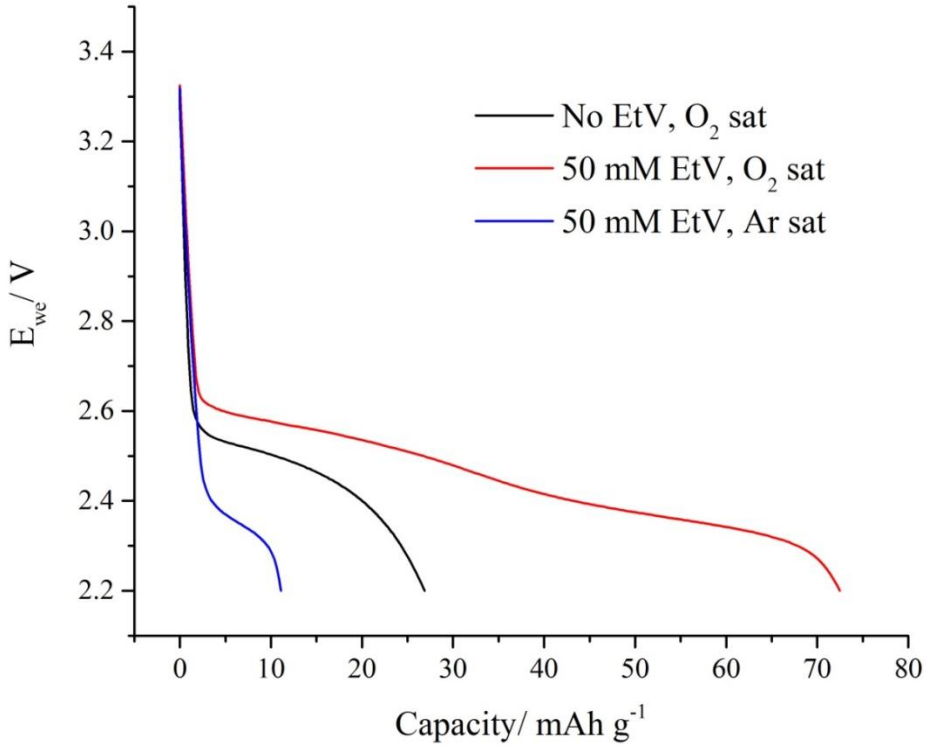

Figure 3.22 Galvanostatic discharge curve in the first cycle of cells using CNT coated glassy carbon electrode in $Pyr_{14}TFSI$ containing 0.1 M LiTFSI, with and without 50 mM EtV, I = 100 mA /g.

By comparing the discharge of oxygen saturated cell, the capacity improvement in the presence of EtV indicated that the surface area degradation might have been slowed. This might be due to the formation of Li_2O_2 was in the bulk electrolyte instead of on the electrode, therefore the passivation was less severe hence a higher capacity was obtained. The discharge curve also showed that the discharge voltage plateau was higher with EtV, suggesting the reaction was more thermodynamically favourable.

Figure 3.23 compared the capacity of the cells with and without ethyl viologen in 20 cycles. It can be learned that in the presence of viologen, even after 20 cycles, the capacity was still above 30 mA h/ g; while in the absence of viologen the capacity was only 13 mA h/ g, suggesting that ethyl viologen was still able to mitigate the electrode passivation after 20 cycles. This result also showed that ethyl viologen had the potential to be an effective mediator in long-term cycling of lithium air batteries. Similar experiment was also performed in diglyme, showing that ethyl viologen can slow down the electrode passivation (Appendix 4). Further cycling experiment (using better cell design, different EtV concentrations and different electrolytes) was required in order to have a better understanding about the electrochemical performance of ethyl viologen.

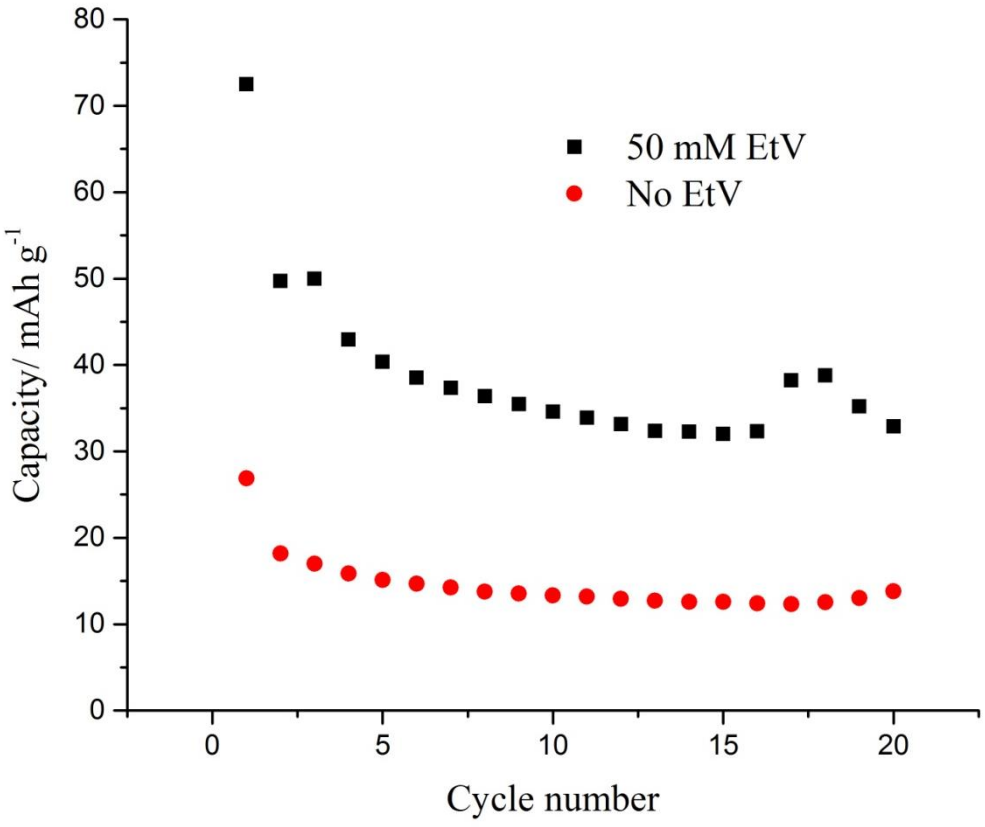

Figure 3.23 Galvanostatic discharge capacity of cells using carbon coated glassy carbon electrode in oxygen saturated $Pyr_{14}TFSI$ containing 0.1 M LiTFSI, with and without 50 mM EtV, I = 100 mA /g.

3.4 Summary

Using UV/Vis spectrometry, it was shown that ethyl viologen acts as a homogeneous mediator for the two-electron reduction of oxygen in aprotic lithium air batteries. Also the viologen demonstrated good stability against superoxide radicals in the presence of high lithium ion concentration. In addition, a sharp decrease in the lifetime of superoxide is observed upon addition of ethyl viologen at low concentration. These findings open up a new strategy to improve the performance and durability of lithium air batteries.

The aim of this work was not to propose ethyl viologen as the perfect solution to lithium air batteries, since we are aware of some shortcomings (toxicity, slightly low redox potential, slow diffusion, etc.). The aim was to demonstrate, the concept of employing a soluble redox couple in order to decrease the lifetime of superoxide in a lithium air battery by promoting the two-electron reduction of oxygen.

3.5 Reference

1 L. Michaelis and E. S. Hill, *J. Gen. Physiol.*, 1933, **6**, 859–873.

2 A. D. Dodge, *Endeavour*, 1971, **30**, 130–135.

3 J. H. Ross, L. O. Lim and R. I. Krieger, *Drug Chem. Toxicol.*, 1979, **2**, 193–205.

4 J. Pospisil, J. Kuta and J. Volke, *J. Electroanal. Chem. Interfacial Electrochem.*, 1975, **58**, 217–227.

5 J. E. Rockley and L. A. Summers, *Aust. J. Chem.* 1980, **33**, 1397–1400.

6 R. N. F. Thorneley, *Biochim. Biophys. Acta.,* 1974, **333**, 487–496.

7 E. J. Nani, C. T. Angelis, J. Dickson and D. T. Sawyer, *J. Am. Chem. Soc.*, 1981, **103**, 4268–4270.

8 E. Borgarello, J. Kiwi, E. Pelizzetti, M. Visca and M. Gratzel, *Nature*, 1981, **289**, 158–160.

9 T. W. Ebbesen, G. Levey and L. K. Patterson, *Nature*, 1982, **298**, 545–548.

10 K. Kalyanasundaram and M. Grazel, *Angew. Chem. Int. edn.*, 1979, **18**, 701–702.

11 D. N. Furlong, Y–M Tricot, J. D. Swift and W. H. F. Sasse, *Augs. J. Chem.*, 1984, **37**, 703–711.

12 M. P. Pileni, A. M. Braun and M. Gratzel, *Photochem. Photobiolog.*, 1930, **31**, 423–427.

13 E. Steckhan and T. Kwana, *Berichte der Bunsengesellschaft für Phys. Chemie*, 1974, **78**, 253–259.

14 L. N. Mackey and T. Kwana, *4th Bioelctrochem. Symp.*, 1975, Juelich.

15 P. B. Sweetser, *Anal. Chem.*, 1967, **39**, 979–982.

16 K. Belinko, *Appl. Phys. Lett.*, 1976, **29**. 363–365.

17 H. T. van Dam, *J. Elctrochem. Soc.*, 1976, **123**, 1181–1184.

18 J. Bruinink, C. Kregting and J. J. Ponjee, *J. Elctrochem. Soc.*, 1977, **124**, 1854–1858.

19 D. J. Barclay, B. F. Dowden, A. C. Lowe and J. C. Wood, *Appl. Phys. Lett.,* 1983, **42**, 911–913.

20 U. S. Patent, 3592943, 1971.

21 M. Ghica, C. Brett, *Anal. Chim. Acta*, 2005, **532**, 145–151.

22 U. S. Patent, 3932821, 1976.

23 M. Hao, X. Liu, M. Feng, P. Zhang and G. Wang, *J. Power Sources*, 2014, **251**, 222–228.

24 X. Liu, M. Hao, M. Feng, L. Zhang, Y. Zhao, X. Du and G. Wang, *Applied Ene*rgy, 2013, **106**, 176–183.

25 D. R. Wheeler, J. Nichols, D. Hansen, M. Andrus, S. Choi and G. D. Watt, *J. Elctrochem. Soc.*, 2009, **156**, B1201–B1207.

26 M. J. Lacey, J. T. Frith and J. R. Owen, *Electrochem. Comm.*, 2013, **26**, 74–76.

27 T. M. Bockman and J. K. Kochi*, J. Org. Chem.*, 1990, **55**, 4127–4135.

28 E. M. Kosower and J. L. Cotter, *J. Am. Chem. Soc.*, 1964, **86**, 5524–5527.

29 T. Watanabe and K. Honda, *J. Phys. Chem.*, 1982, **86**, 2617–2619.

30 J. M. Achord and C. L. Hussey, *Anal. Chem.* 1980, **52**, 601–602.

31 D. T. Sawyer, G. Chiericato, C. T. Angelis, E. J. Nanni and T. Tsuchiya, *Anal. Chem.* 1982, **54**, 1720–1724.

32 J. Herranz, A. Garsuch and H. A. Gasteiger, *J. Phys. Chem. C*, 2012, **116**, 19084–19094.

33 A. W. Lodge, M. J. Lacey, M. Fitt, N. Garcia-Araez and J. R. Owen, *Electrochimica Acta*, 2014, **140**, 168–173.

34 S. Monaco, A. M. Arangio, F. Soavi, M. Mastragostino, E. Paillard and S. Passerini, *Electrochimica Acta*, 2012, **83**, 94–104.

35 S. A. Freunberger, Y. H. Chen, Z. Q. Peng, J. M. Griffin, L. J. Hardwick, F. Barde, P. Novak and P. G. Bruce, *J. Am. Chem. Soc.*, 2011, **133**, 8040–8047.

36 D. M. Itkis, D. A. Semenenko, E. Y. Kataev, A. I. Belova, V. S. Neudachina, A. P. Sirotina, M. Havecker, D. Tschner, A. Knop-Gericke, P. Dudin, A. Barinov,

E. A. Goodlin, Y. Shao-Horn and L. V. Yashina, *Nano Lett.*, 2013, **13**, 4697–4701.

37 K. M. Abraham and Z. Jiang, *J. Electrochem. Soc.*, 1996, **143**, 1–5.

38 Z. Peng, S. A. Freunberger, L. J. Hardwick, Y. Chen, V. Giordani, F. Barde, P. Novak, D. Graham, J. Tarascon and P. G. Bruce, *Angew. Chem. Int. Ed. Engl.*, 2011, **50**, 6351–6355.

39 K. U. Schwenke, S. Meini, X. Wu, H. A. Gasteiger and M. Piana, *Phys. Chem. Chem. Phys.*, 2013, **15**, 11830–11839.

Chapter 4: OER Mediator/Shuttle for Lithium Air Batteries – Studies of Cobalt Complexes

4.1 Introduction

To enhance the oxygen evolution reactions on the positive electrode, two possible solutions can be used. One is to improve the solubility of Li_2O_2 in the electrolyte; the other is to add catalyst for the oxygen evolution reaction. In this report, a homogeneous OER mediator was investigated. OER mediators for lithium air batteries have been investigated in recent years[1,2]. As shown in Fig. 4.1, in a lithium air cell with an OER mediator during the charging process, the mediator will be oxidized and react with Li_2O_2, oxidizing it to oxygen. Compared to the heterogeneous catalyst, the homogeneous mediator/shuttle has better contact with the solid lithium peroxide, hence it is believed to be more efficient.

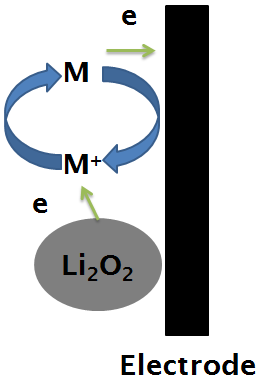

Figure 4.1 Schematic diagram of how an OER mediator works in Li-air batteries.

Cobalt bis-terpyridine complex ($Co^{II/III}(teryp)_2$, structure shown in Fig 4.2) and its derivatives are widely investigated in the research of metallo-coordination and supramolecular chemistry.[3,4] More recently, they were used as redox couples for dye sensitized solar cells[5,6].

It was previously reported that triiodide/iodide redox shuttle, which is normally used in dye-sensitized solar cells, was applied in the lithium-air battery systems.[7] Therefore it is likely that other redox couples used in dye sensitized solar cells can also be used in Li-air batteries. $Co^{II/III}(teryp)_2$ has standard potentials (3.1 to 3.4 V, depends on electrolyte) slightly higher than the oxygen evolution potentials. Therefore, it is possible that $Co^{II/III}(teryp)_2$ can also be used as

a redox mediator in Li-air batteries. In this work, the performance of $Co^{II/III}(teryp)_2$ was tested as a mediator in organic electrolyte for OER.

In this case, the proposed reaction equation would be:

$$2Co^{III}(terp)_2^{3+} + Li_2O_2 \rightarrow 2Co^{II}(terp)_2^{2+} + O_2 + 2Li^+ \text{ (Equation 4.1)}$$

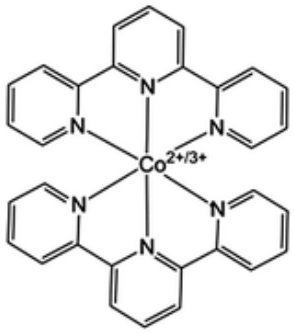

Figure 4.2 Molecular structure of $[Co^{II/III}(terpy)_2]$.

4.2 Experimental

4.2.1 Synthesis of $[Co^{II}(teryp)_2](TFSI)_2$

A solution of $CoCl_2$ (Fluka, ≥98.5 %) in water was added to a methanol solution of 2,2':6',2''-terpyridine (Sigma-Aldrich, 98 %) and the solution turned dark red immediately. Excess LiTFSI was added to this solution and a brown precipitate was obtained. The complex was filtered and washed with water, then dried under vacuum for 24 hours.

4.2.2 Synthesis of $[Co^{III}(terp)_2](TFSI)_3$

A solution of $CoCl_2$ (Fluka, ≥98.5 %) in water was added to a methanol solution of 2,2':6',2''-terpyridine (Sigma-Aldrich, 98 %) and the solution turned dark red immediately. Then Br_2 solution was added to the solution and precipitate was formed. Filtered out the precipitate and added excess of LiTFSI was added to the solution and orange precipitate was obtained. The complex was filtered and washed with water, then dried under vacuum for 24 hours.

4.2.3 Electrochemical Tests

The same electrochemical cell setup was used as described in Chapter 3. The cell was assembled and sealed in Ar atmosphere. To saturate the electrolyte with oxygen, dry oxygen was bubbled through using a needle for 1 hour.

The electrode preparation process was the same as described in Chapter 3. To coat carbon on the electrode, 2 µL of ink made from carbon nanotubes, PVDF binder and NMP was evenly dropped on the glassy carbon electrode. Then the electrode was dried overnight.

4.2.4 UV/Vis Spectroscopy

$Co^{II/III}(teryp)_2$ was dissolved in diglyme (Sigma-Aldrich, anhydrous, 99.5 %) with concentration of 0.1 mM. An excess of lithium peroxide powder (90 %, Aldrich) was added into the Co^{3+} complex solution, and then the solution was filtered with syringe filter for UV/Vis measurement. An Oceanview 2000+ spectrometer (Ocean Optics) was used to record the UV/Vis spectra. In addition, a deuterium-halogen light source (DH-2000-BAL, Ocean Optics) was used. The integration time was set as automatic, the average scan number was 10 and the carbox width was 1. The range of wavelength was set between 300 to 500 nm.

4.3 Results and Discussion

4.3.1 Cyclic Voltammogram of $Co^{II/III}(teryp)_2$

From the cyclic voltammogram of $Co^{II}(terpy)_2^{2+}$ in diglyme (Fig. 4.3), it can be learned that the redox potential of $Co^{III}(terpy)_2^{3+}/Co^{II}(terpy)_2^{2+}$ was around 3.32 V vs Li/Li^+, which is suitable for catalysing OER reaction. In addition, the redox potential of $Co^{II}(terpy)_2^{2+}/Co^{I}(terpy)_2^{+}$ was about 2.12 V, therefore the potential limit should be set above that to avoid the reduction of $Co^{II}(terpy)_2^{2+}$. The peak-to-peak separation of $Co^{III}(terpy)_2^{3+}/Co^{II}(terpy)_2^{2+}$ redox reaction in the voltammogram under the experimental condition was about 140 mV, indicating a good reversibility of this redox couple.

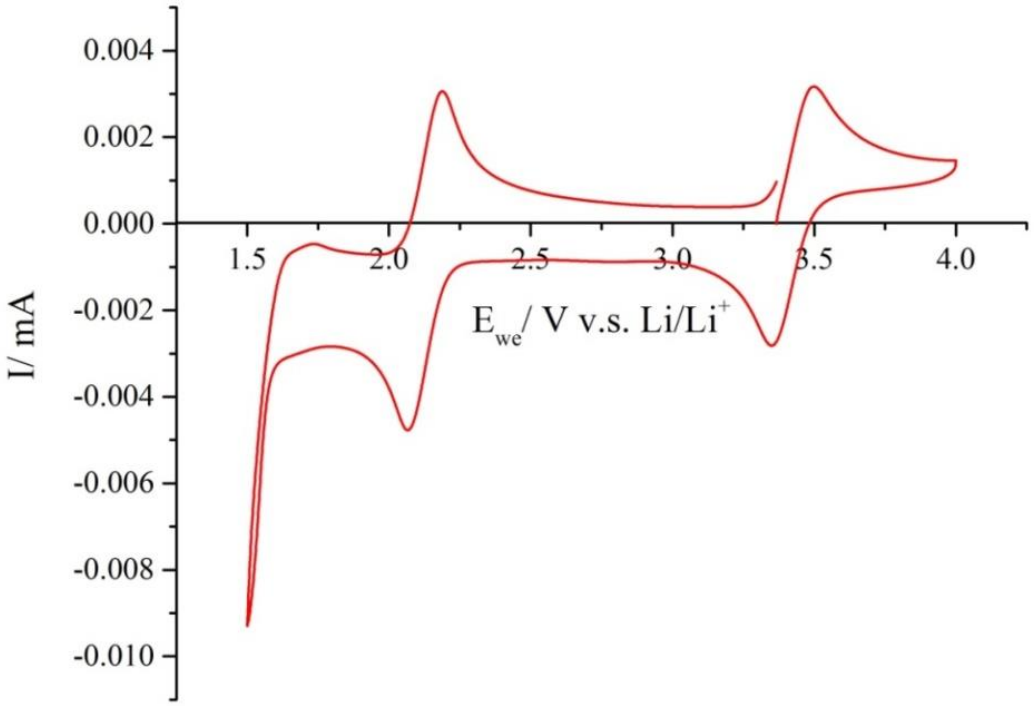

Figure 4.3 Cyclic voltammogram (first cycle) of 2 mM $Co^{II}(terpy)_2^{2+}$ + 1 M LiTFSI in diglyme under argon atmosphere (first cycle) using a glassy carbon electrode with 3 mm diameter. The scan rate is 20 mV/s

4.3.2 UV/Vis Spectroscopy Results

To investigate whether cobalt complex can oxidize lithium peroxide chemically resulting $Co^{II}(terpy)_2^{2+}$, one possible approach is to analyse the reaction products. It has been previously reported that $Co^{III}(terpy)_2^{3+}$ and $Co^{II}(terpy)_2^{2+}$ can be well distinguished in UV/Vis spectra[5]. Therefore, UV/Vis spectroscopy measurement was applied to study this reaction. As shown in Figure 4.4, the UV/Vis spectra of $Co^{II}(terpy)_2^{2+}$ and $Co^{III}(terpy)_2^{3+}$ solution with concentration of 0.1 mM in diglyme was recorded.

From the spectra it can be observed that $Co^{III}(terpy)_2^{3+}$ has two absorbance peaks at 340 nm and 360 while $Co^{II}(terpy)_2^{2+}$ has a broader absorbance peak from 300-350 nm. Therefore they can be distinguished qualitatively and quantitatively. This result also agrees with what has been reported before.[8]

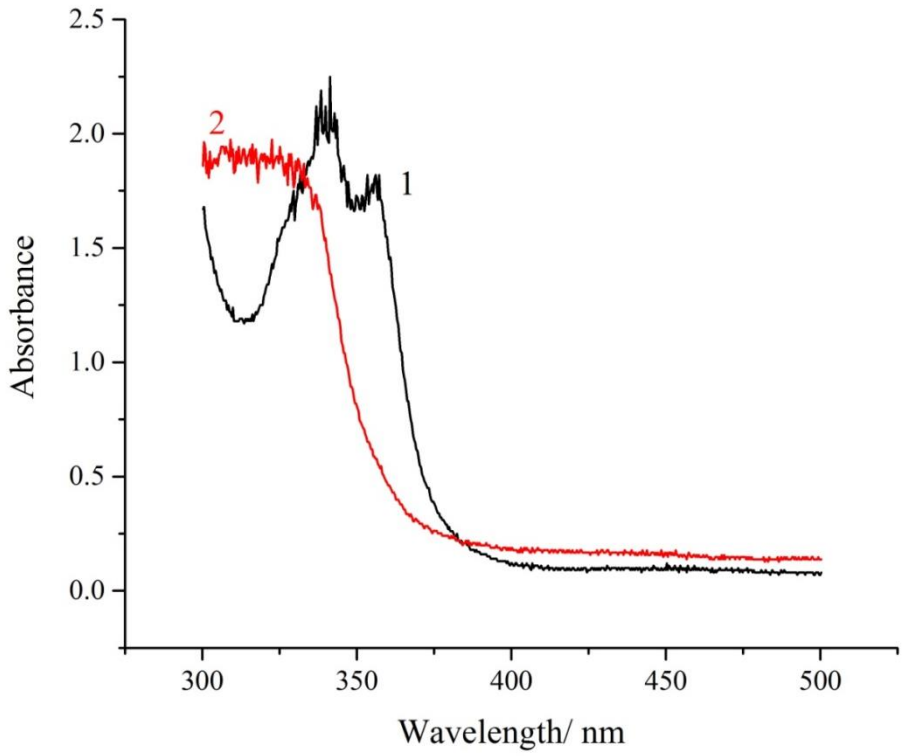

Figure 4.4 UV/Vis spectra of 0.1 mM of $Co^{III}(terpy)_2^{3+}$ (1) and $Co^{II}(terpy)_2^{2+}$ (2) in diglyme.

To investigate the reaction products between $Co^{II}(terpy)_2^{3+}$ and lithium peroxide, excess lithium peroxide powder was added into $Co^{III}(terpy)_2^{3+}$ solution. Gas bubbles can be observed upon the mixing, which might be due to the formation of oxygen as described in Equation 4.1. The mixture was stirred for 30 min in order to achieve a complete reaction between $Co^{III}(terpy)_2^{3+}$ and lithium peroxide. Then the extra lithium peroxide powder was filtered out, and the clear solution was examined by UV/Vis spectrometry.

By comparing the UV/Vis spectra of $Co^{II}(terpy)_2^{2+}$ and the reaction product between $Co^{III}(terpy)_2^{3+}$ and Li_2O_2 (Fig. 4.5), based on the peak shapes and peak positions it can be confirmed that the reaction product is $Co^{II}(terpy)_2^{2+}$. In addition, from the peak intensity it can be concluded that $Co^{III}(terpy)_2(TFSI)_3$ was fully reduced by Li_2O_2 to $Co^{II}(terpy)_2(TFSI)_2$. As a result, using cobalt complexes as mediators in Li-air batteries is thermodynamically feasible.

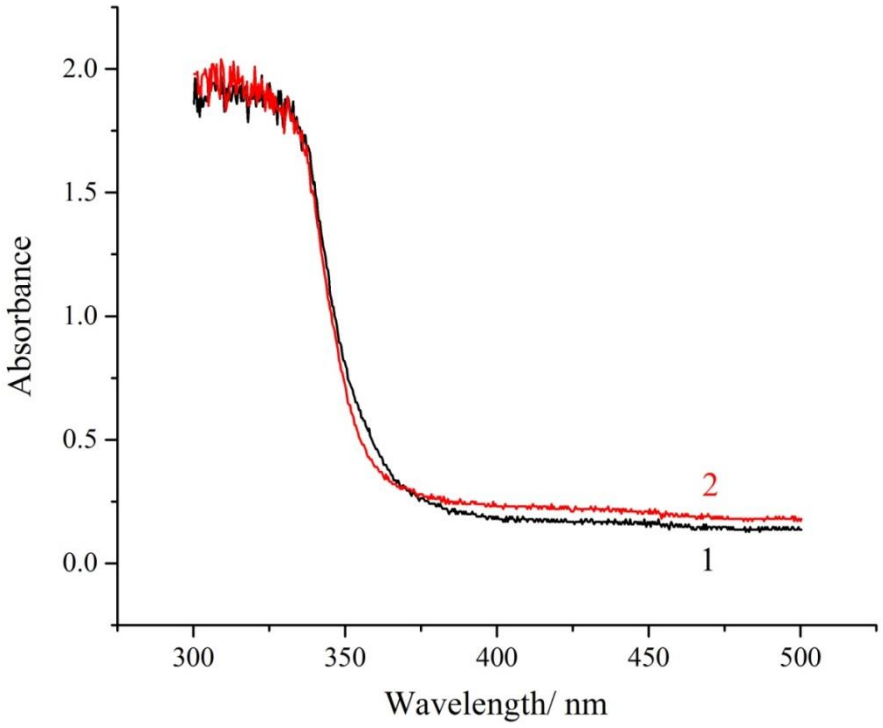

Figure 4.5 UV/Vis spectra of 0.1 mM of $Co^{II}(terpy)_2^{2+}$ in diglyme (1) and the product after adding excess of lithium peroxide to 0.1 mM of $Co^{III}(terpy)_2^{3+}$ (2).

In this experiment, in order to make sure the reaction was complete, large excess of lithium peroxide was added. Since it was a qualitative experiment instead of a quantitative one, the amount of lithium peroxide involved in the reaction was still not clear. Further experiments, including quantification and kinetic measurement, might be still needed in order to have a better understanding of the reaction.

4.3.2 Galvanostatic Cycling

4.3.2.1 Galvanostatic Cycling Results of $Co^{II}(terpy)_2^{2+}$

The results from UV/Vis spectra have shown that $Co^{III}(terpy)_2^{3+}$ can be reduced by Li_2O_2 forming $Co^{II}(terpy)_2^{2+}$. However, those results were obtained under the condition where excess amount of solid lithium peroxide existed. To evaluate the efficiency of the cobalt complex as a mediator/shuttle for the oxygen evolution reaction, it is necessary to test it in electrochemical cycling experiments.

As described before, carbon nanotube coated glassy carbon electrode was used as working electrode and lithium metal was used as reference and counter electrode. Both $Co^{II}(terpy)_2^{2+}$ and $Co^{III}(terpy)_2^{3+}$ were tested in the experiments.

According to the Sand equation:[9]

$$\frac{i\tau^{1/2}}{C_O^*} = \frac{nFAD_O^{\frac{1}{2}}\pi^{\frac{1}{2}}}{2} \quad \text{(Equation 4.2)}$$

in which i is the current, τ is the transition time of constant-current electrolysis, c_0^* is the concentration, n is the electron transfer number, F is the Faraday constant, A is the geometric surface area of the electrode and D_0 is the diffusion coefficient. In this equation, with given current density and concentration, τ is proportional to the diffusion coefficient. The diffusion coefficient indicates the efficiency of the mediation process since the mediator needs to diffuse to the electrode surface to react with Li_2O_2.

Hence the mediation effect can be estimated by studying the transition time in galvanostatic cycling. In order to test the performance of cobalt complex in different electrolytes, four electrolytes were used: diglyme, $Pyr_{14}TFSI$, TEGDME and diglyme: $Pyr_{14}TFSI$ (1: 1).

To begin with, $Co^{II}(terpy)_2^{2+}$ was investigated in Ar saturated electrolyte by performing galvanostatic cycling. 50 mM of $Co^{II}(terpy)_2^{2+}$ was dissolved in different electrolytes and discharged with current density of 500 mA h g^{-1} (per mass of coated carbon) from open circuit potential to 2.4 V then charged with same current density to 3.7 V. Since same current density was applied, the capacity can directly reflect the transition time.

As shown in Fig. 4.6, because the starting species is a reduced form of cobalt, the transition time is very small during the discharge sequences for all cases since no reduction reaction took place. However, during the charging process, the differences are significant. For n-ethylene glycol dimethyl ethers, both TEGDME and diglyme have similar chemical properties due to similar chain structure. However, TEGDME has much higher viscosity compared to diglyme,[10] which implies a lower diffusion coefficient. Therefore, the transition time of TEGDME is shorter than that of diglyme. For ionic liquid, it has even higher viscosity, so an even shorter charge plateau was obtained. To further prove this assumption, the mixture of diglyme and $Pyr_{14}TFSI$ in 1:1 ratio was used since mixing with diglyme will significantly reduce the viscosity of $Pyr_{14}TFSI$. As expected, a transition time that was much longer than $Pyr_{14}TFSI$ but shorter than diglyme was observed.

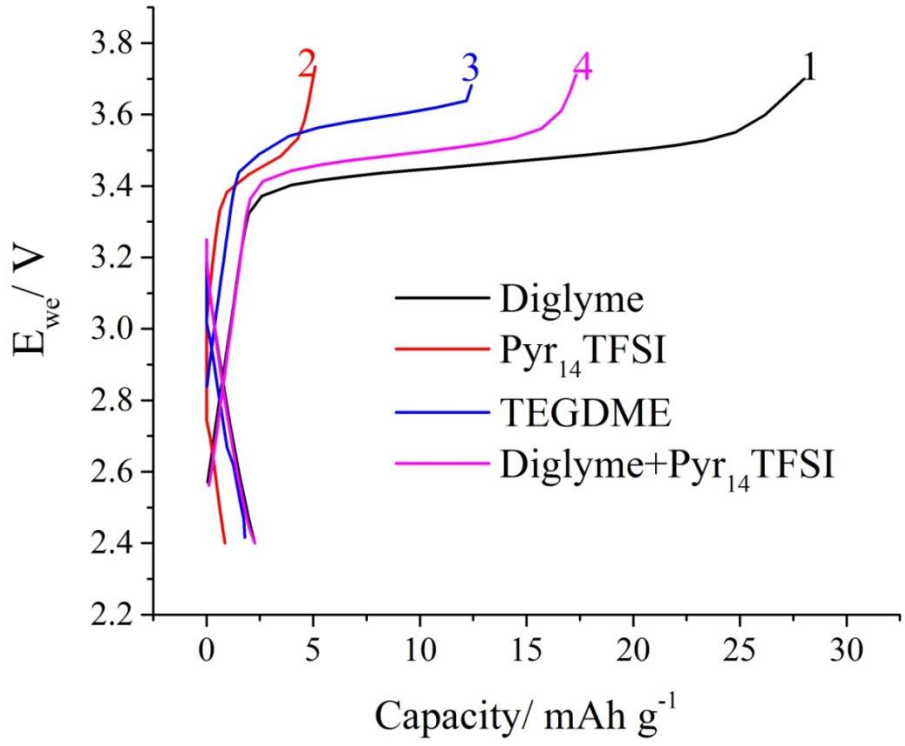

Figure 4.6 Galvanostatic cycling results in the first cycle of 50 mM $Co^{II}(terpy)_2^{2+}$ in diglyme + 1 M LiTFSI (1), $Pyr_{14}TFSI$ + 0.1 M LiTFSI (2), TEGDME + 1 M LiTFSI (3) and diglyme:$Pyr_{14}TFSI$ (1:1) + 0.1 M LiTFSI (4) with current density of 500 mA h g^{-1} and cut off potential of 2.4 –3.7 V.

By applying the Sand equation, the diffusion coefficient of $Co^{II}(terpy)_2^{2+}$ was calculated and listed in Table 4.1.

Table 4.1 Calculated diffusion coefficients of $Co^{II}(terpy)_2^{2+}$ in different electrolytes.

Solvent and electrolyte	Diffusion coefficient/ 10^{-6} cm^{-2} s^{-1}
Diglyme + 1 M LiTFSI	5.60
$Pyr_{14}TFSI$ + 0.1 M LiTFSI	1.02
TEGDME + 1 M LiTFSI	2.48
Diglyme: $Pyr_{14}TFSI$ (1:1) + 0.1 M LiTFSI	3.46

By introducing dry oxygen gas to the working electrode compartment for 1 hour, an oxygen saturated electrolyte can be prepared. Galvanostatic cycling experiments were performed with the oxygenated cells.

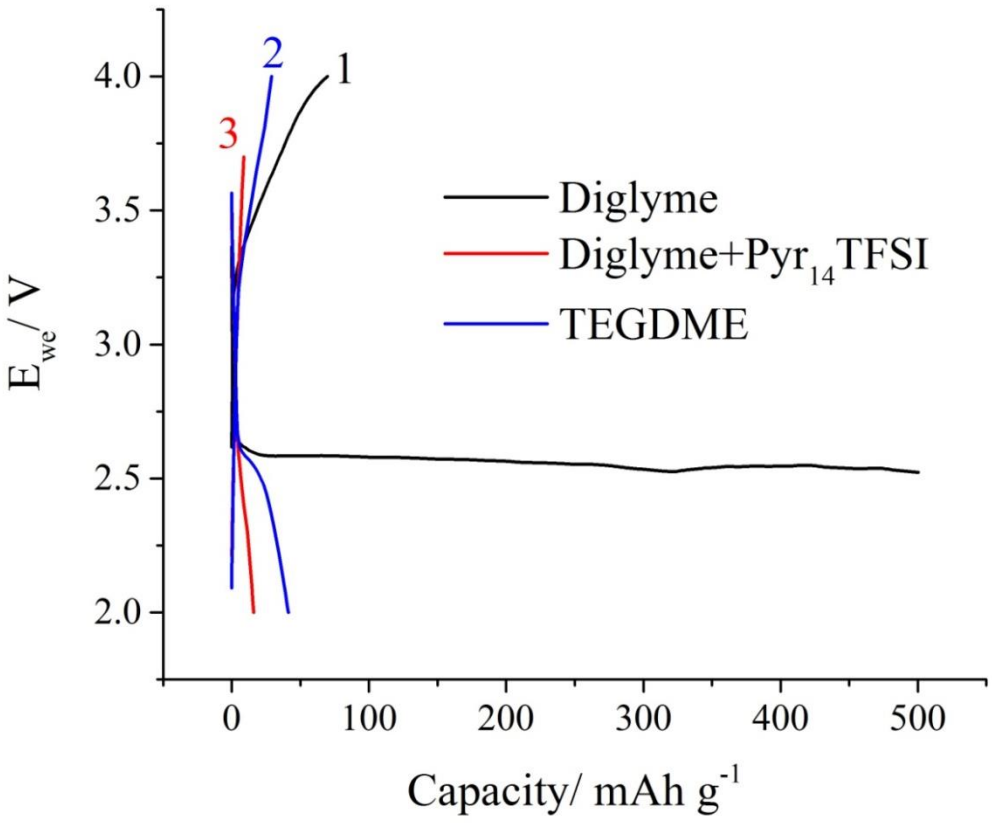

Figure 4.7 Galvanostatic cycling results in the first cycle of O_2 saturated diglyme with 1 M LiTFSI (1), diglyme: Pyr14TFSI (1:1) with 0.1 M LiTFSI (2) and TEGDME with 1 M LiTFSI (3)

The capacity of the oxygenated cells without mediator was tested and shown in Fig. 4.7. Similarly to Fig. 4.6, the capacity in diglyme was much higher than those in other electrolyte, which might be due to the higher diffusion coefficient of oxygen in diglyme. Therefore, it can be concluded that in terms of capacity, diglyme might be the best electrolyte for galvanostatic cycling experiments among all tested electrolytes.

Next, the galvanostatic cycling performance of $Co^{II}(terpy)_2^{2+}$ in diglyme was further tested. As shown in Fig. 4.8, by comparing curve 1 and 2, after introducing oxygen in the system, the charging plateau has become much longer, which means more species have been oxidized. This result might be attributed to two possibilities: oxygen evolution reaction from Li_2O_2 and mediation effect of $Co^{II}(terpy)_2^{2+}$.

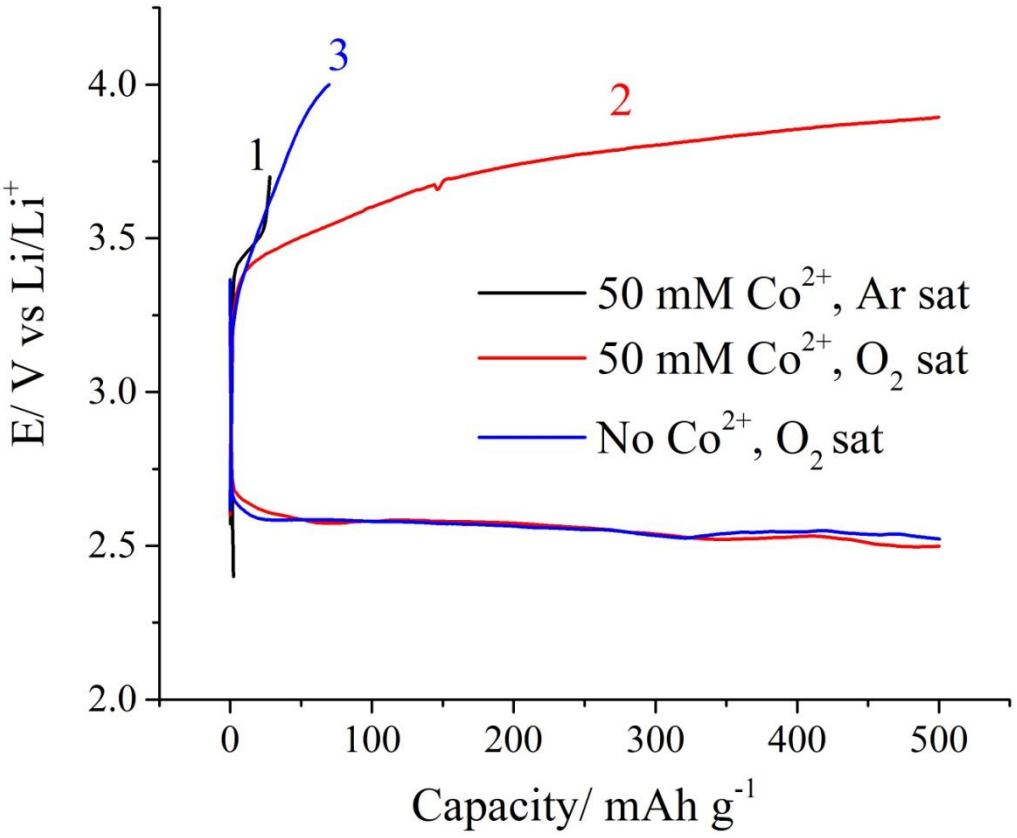

Figure 4.8 Galvanostatic cycling profiles in the first cycle of 50 mM $Co^{II}(terpy)_2^{2+}$ + 1 M LiTFSI in Ar (1), O_2 (2) saturated diglyme and 1 M LiTFSI in O_2 saturated diglyme (3). The current density was 500 mA /g.

The explanation for the first reason seems to be straightforward: since oxygen was reduced to Li_2O_2 during the discharge, it may be oxidized back during the charging sequence. Moreover, the potential of OER is very close to the oxidation potential of $Co^{II}(terpy)_2^{2+}$. Hence, by adding up two charging plateaus, a longer plateau might be formed. Curve 1 and 3 in Fig. 4.8 represented the galvanostatic cycling performance of cobalt complex and oxygen in the absence of each other. It was clear that even by adding up their charging capacity, it was still much shorter than the capacity when they were tested together (curve 2). Therefore, this reason cannot explain the enhanced charge capacity.

A more probable explanation would be the mediation effect, which was explained in Fig. 4.1, with the oxidation of $Co^{II}(terpy)_2^{2+}$, $Co^{III}(terpy)_2^{3+}$ was formed in the electrode, which will chemically react with Li_2O_2 forming $Co^{II}(terpy)_2^{2+}$. Therefore, more $Co^{II}(terpy)_2^{2+}$ can be oxidized chemically, hence the longer charging plateau. In the same time, the consumption of Li_2O_2 can also alleviate the electrode surface passivation, leading to lower impedance on the electrode, which can also explain the lower charging potential. Combining these two factors, a longer charging plateau was obtained.

The galvanostatic cycling experiment has showed the mediation effect of $Co^{II}(terpy)_2^{2+}$. However, like ethyl viologen, it would be necessary to scale up the amount of cobalt complex in the future in order to improve the mediation efficiency.

4.3.2.2 Galvanostatic Cycling Results of $Co^{III}(terpy)_2^{3+}$

By far, it had been learned that $Co^{II}(terpy)_2^{2+}$ could greatly improve the oxygen evolution reaction in lithium air cell through mediation effect. In that case, $Co^{II}(terpy)_2^{2+}$ only served as an electron carrier, it was $Co^{III}(terpy)_2^{3+}$ that directly react with Li_2O_2. If only $Co^{III}(terpy)_2^{3+}$ was added to the system, it would be introducing a homogeneous catalyst, instead of a mediator, into the cell. Therefore, it would be very helpful to understand how $Co^{III}(terpy)_2^{3+}$ works in the system. It can be seen from Fig. 4.9 that when the system only contained Co^{III} species, the discharge curves were very stable as cycle number increased. Not only the capacity was greatly improved, but also the potential drop was significantly reduced. This improvement might be due to most lithium peroxide precipitated on the electrode was constantly consumed by $Co^{III}(terpy)_2^{3+}$. The charge capacity also increased slightly with cycle number, indicating a gradual build-up of $Co^{II}(terpy)_2^{2+}$ in the system.

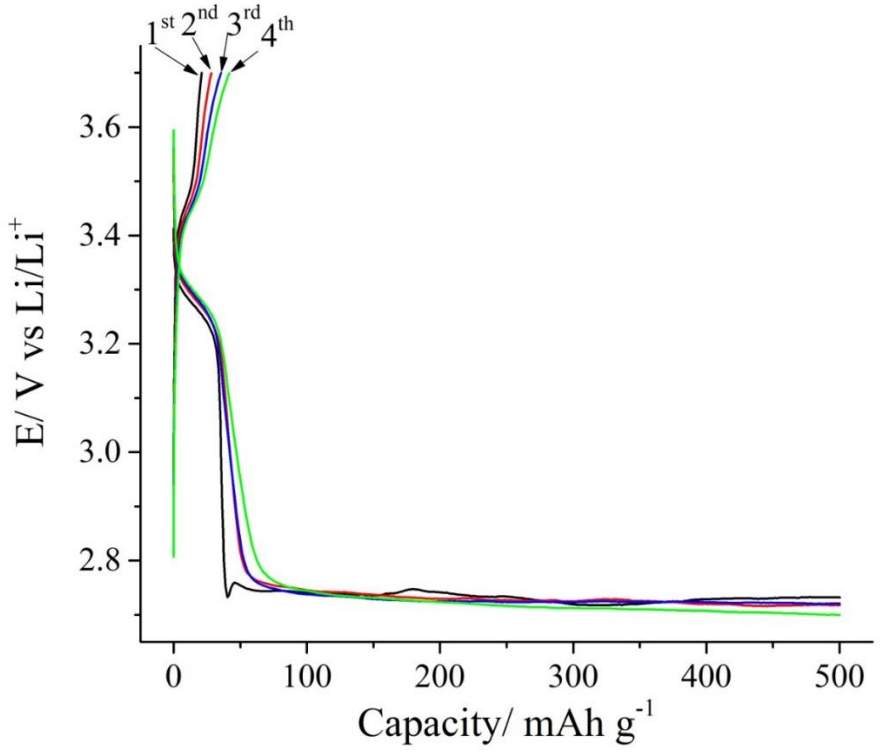

Figure 4.9 Galvanostatic cycling results (cycle 1-4) of 50 mM $Co^{III}(terpy)_2^{3+}$ + 1 M LiTFSI in oxygen saturated diglyme. The current density was 500 mA /g and the time limit for charge and discharge was 1 hour.

From this result, it can be concluded that using high concentration of $Co^{III}(terpy)_2^{3+}$ the lithium peroxide precipitation on electrode will be greatly inhibited.

If the discharge time was not limited (shown in Fig. 4.10), the first discharge capacity could reach over 1700 mA h g^{-1}. After the first cycle, the electrolyte was saturated with oxygen and the cell was cycled again. A discharge capacity of 1400 mA h g^{-1} was achieved during the second cycle without potential drop. The the process was then repeated again, and the discharge capacity retained over 700 mA h g^{-1} at the third cycle. This capacity fading might be due to the leakage of cobalt complex to the negative electrode through the frit. Therefore, it is necessary to improve the cell design for the future work. It can be assumed that the cobalt complex would potentially provide an even higher capacity and better cycling performance in a battery system given that the two electrolyte compartments are well separated and oxygen can be constantly replenished in the electrolyte.

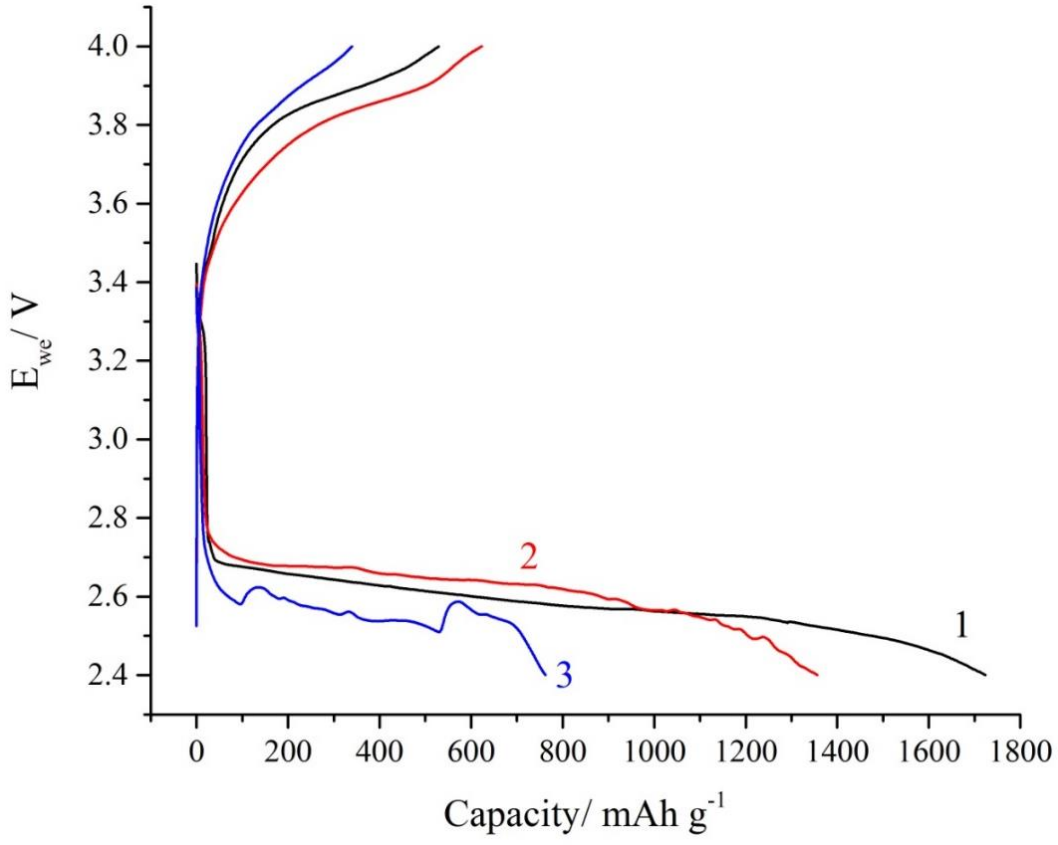

Figure 4.10 Galvanostatic cycling profiles of 50 mM $Co^{III}(terpy)_2^{3+}$ + 1 M LiTFSI in diglyme that saturated with oxygen for the first (1), second (2) and third time (3). The current density was 500 mA /g and there was no time limit for charge and discharge.

Furthermore, as shown in Fig. 4.11, by doubling the concentration of $Co^{III}(terpy)_2^{3+}$ as well as the current density used in the experiment corresponding to Fig. 4.9, the first discharge plateau obtained had higher potential (2.75 V). Even after 20 cycles, the potential was still above 2.5 V. This result showed that in high discharge/charge rate, the cobalt complex still showed its ability to oxidize lithium peroxide. The potential drop over cycles might be also due to the depletion of oxygen, or the blockage in the glass frit, further investigation is still required in the future work.

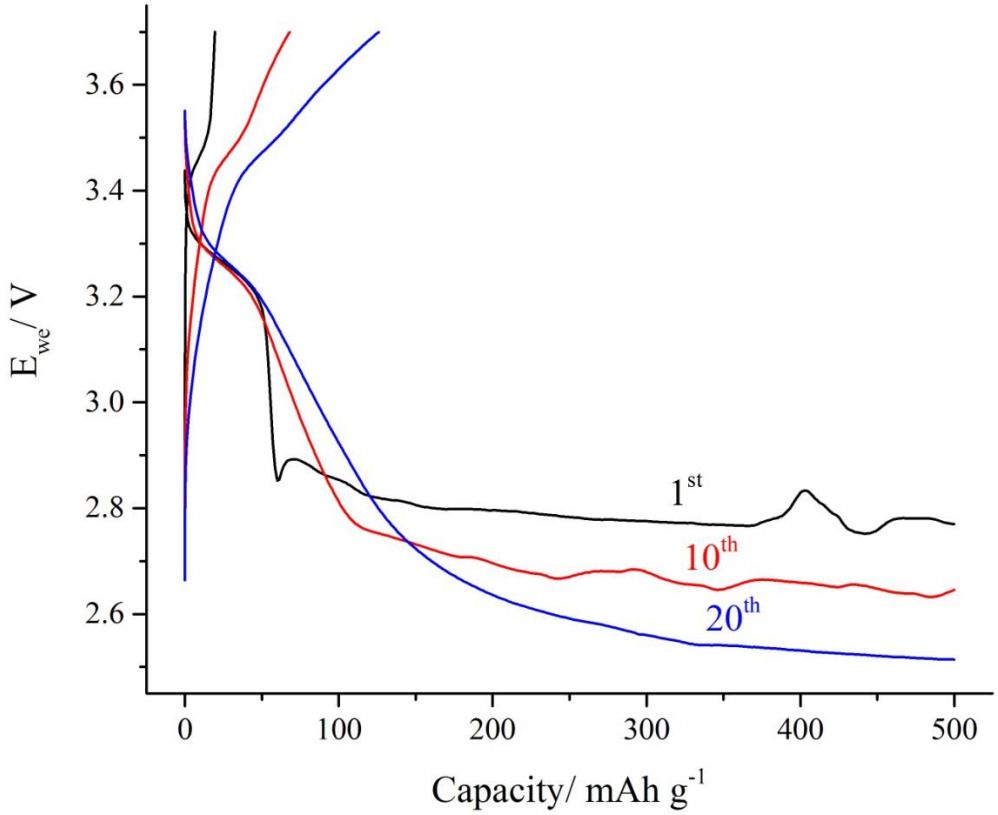

Figure 4.11 Galvanostatic cycling profiles of 100 mM $Co^{III}(terpy)_2^{3+}$ + 1 M LiTFSI in diglyme that saturated with oxygen in different cycle number. The current density was 1 A /g and the time limit for discharge and charge was 1 hour.

4.4 Summary

The performance of bis-terpyridine cobalt was tested as an OER mediator in lithium air batteries. The UV/Vis spectroscopy confirmed that $Co^{III}(terpy)_2$ can reversibly oxidize lithium peroxide to oxygen, forming $Co^{II}(terpy)_2^{2+}$, showing the thermodynamic feasibility of the cobalt complex as a mediator.

Galvanostatic cycling experiment of $Co^{II}(terpy)_2$ in diglyme, which was determined as the most suitable electrolyte for the experiment, has showed the ability to improve the charging of lithium air batteries due to its mediation effect. $Co^{III}(terpy)_2^{3+}$ was also tested as a catalyst for OER. The result showed that it can significantly alleviate the electrode passivation even after multiple cycles.

4.5 Reference

1 D. Sun, Y. Shen, W. Zhang, L. Yu, Z. Yi, W. Yin, D. Wang, Y. Huang, J. Wang, D. Wang and J. B. Goodenough, *J. Am. Chem. Soc.*, 2014, **136**, 8941–8946.

2 Y. Chen, S. A. Freunberger, Z. Peng, O. Fontaine and P. G. Bruce, *Nat Chem*, 2013, **5**, 489–494.

3 G. F. Swiegers and T. J. Malefetse, *Chem. Rev.*, 2000, **100**, 3483–3537.

4 G. R. Newkome, E. He and C. N. Moorefield, *Chem. Rev.*, 1999, **99**, 1689–1746.

5 P. Salvatori, G. Marotta, A. Cinti, E. Mosconi, M. Panigrahi, L. Giribabu, M. K. Nazeeruddin and F. De Angelis, *Inorg. Chim. Acta*, 2013, **406**, 106–112.

6 K. Ben Aribia, T. Moehl, S. M. Zakeeruddin and M. Grätzel, *Chem. Sci.*, 2013, **4**, 454–459.

7 M. Yu, X. Ren, L. Ma and Y. Wu, *Nat. Commun.*, 2014, **5:**5111.

8 J.-H. Yum, E. Baranoff, F. Kessler, T. Moehl, S. Ahmad, T. Bessho, A. Marchioro, E. Ghadiri, J.-E. Moser, C. Yi, M. K. Nazeeruddin and M. Grätzel, *Nat. Commun.*, 2012, **3**:631.

9 A. J. Bard and L. R. Faulkner, *Electrochemical Methods: Fundamentals and Applications*, John Wiley & Sons, 2nd edn., 2001.

10 A. Conesa, S. Shen and A. Coronas, *Int. J. Thermophys.*, 1998, **19**, 1343–1358.

Chapter 5: Sulfur/Carbon Black Composite Positive Electrode in Li-S Batteries

5.1 Introduction

Carbon based materials have been investigated as the conductive medium in the Li-S battery because of their high porosity, surface area, good conductivity and low prices. In this chapter, the application of carbon black – a carbon with relatively lower surface area, as the conductive material in the Li-S battery will be discussed. Carbon blacks consist of spherical particles with layered graphene. The layers are wrapped around the nucleus with the preferential orientation which is parallel to the particle surface.[1]

5.2 Experimental Details

5.2.1 Sulfur/carbon Composite Fabrication

Two methods have been applied to prepare the S/C composite – ball milling and thermal treating. For ball milling method the sulfur/carbon powder mixture was weighed and ground in ball miller (Retsch MM200) for 30 min at the frequency of 20 Hz. For further heating treatment, the ball milled powder was heated in a sealed vessel (hydrothermal reactor under 150 °C in the furnace for 24 h to make sure the sulfur was melted).

5.2.2 Surface Area Measurement

The surface area analysis was performed using BET method with Gemini 2375 Surface Area Analyser and Tristar 3000 (Micromeritics). Pure nitrogen was used as the adsorbate gas. For pre-treatment, sample tubes were evacuated over 12 hours. The evacuation rate during the measurement was 100 mmHg/min, the evacuation time was 5 min and the equilibration time was 5 second. The free space was measured. For BET measurement, pressure points (P/P_0) of 0.1, 0.15, 0.2, 0.25, 0.3 and 0.35 were used for calculation. The pore size distribution was measured with the same instrument and calculated using BJH model, pressure points (P/P_0) of 0.05, 0.1, 0.15, 0.2, 0.25, 0.3, 0.35, 0.4, 0.45, 0.5, 0.55, 0.6, 0.65, 0.7, 0.75, 0.8, 0.85, 0.9, 0.95, 0.97 (adsorption process); 0.95, 0.9, 0.85,

0.8, 0.75, 0.7, 0.65, 0.6, 0.55, 0.5, 0.45, 0.4, 0.35, 0.3, 0.25, 0.2, 0.15, 0.1 and 0.05 (desorption process). Halsey-Faas correction was used to process the data.

5.2.3 Powder X-Ray Diffraction

The XRD experiment was performed on D2 PHASER X-ray Diffractometer (Bruker) which uses a Cu Kα X-ray source. Poly (methyl methacrylate) specimen holder ring was used. The 2θ was between 20° and 70° with incremental of 0.01°. The acquisition time for each data point was 0.25 s.

5.2.4 Electrochemical Tests

PTFE was mixed with S/C composite in the weight ratio of 1:9. The mixture was then ground in a mortar until it formed a piece of rubber-like solid, which was rolled in a roller to sheets with thickness of 60-80 μm and cut to pellets with diameter of 1 cm. The prepared positive electrode pellets were dried in a vacuum tube (Buchi, TO-50) for 24 hours under 35°C to degas. The reason for choosing low temperature was because sulfur would sublime at high temperature. Then the pellets were transferred into the Ar-filled glove box for use. Before being put into electrochemical cells, the weights of the positive electrode pellets were measured and recorded.

Two-electrode Swagelok cells, which were made of PFA (perfluoroalkoxy alkane) (shown in Fig. 2.4) were used as test cells. In order to prevent the oxygen and water contamination to the cells, the assembly of cells was conducted in an Ar-filled glove box (Unilab from MBraun). Lithium metal foil disk (diameter = 10 mm) was served as negative electrode and micro glass fibre filter paper (Whatman, grade 25) was cut into disks with diameter of 12.5 mm and used as separator. To prepare the electrolyte, 1 mol/ L of LiTFSI was dissolved in DOL and TEGDME with volume ratio of 1:1. 120 μL of electrolyte was added into the each cell so that the separators can be wetted. After the cell was assembled, a few layers of “Parafilm M” laboratory films (Bemis) were wrapped around the cells in order to further protect the cell from water and oxygen in the atmosphere. After assembled, the cell was rested for 30 min before running.

The galvanostatic cycling was performed with multi-channel potentiostat/galvanostat (MPG) (Biologic Science Instruments) and operated with EC-lab software package (Biologic Science Instruments). The cells were kept in a

fridge under 25°C to eliminate the effect of temperature. The cut-off potential of discharge and charge were 1.5 V and 2.8 V, respectively.

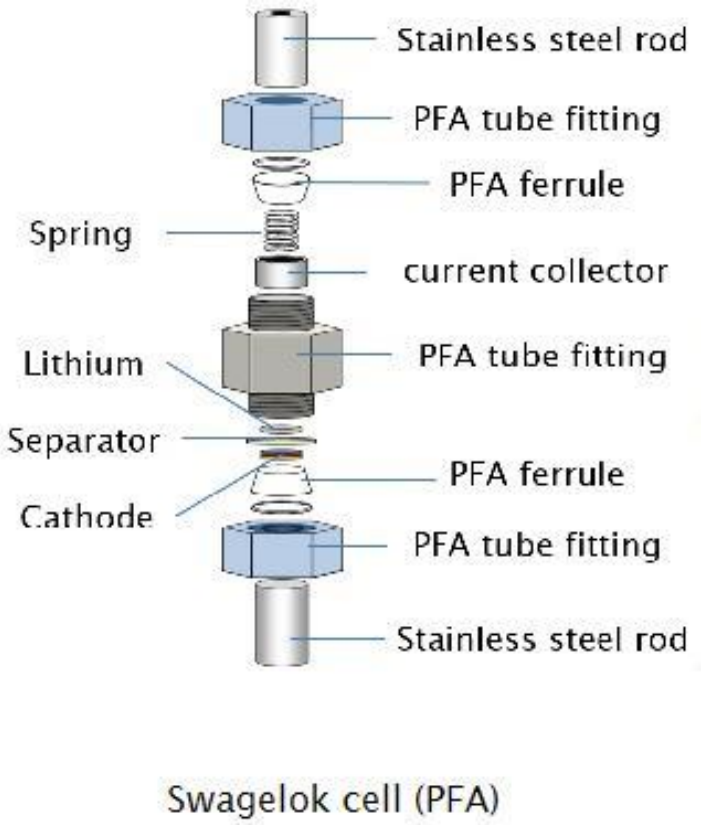

Figure 5.1 Schematic diagram of electrochemical testing cell for lithium sulfur battery tests. (Drawn by Jacob Locke)

5.3 Results and Discussion

5.3.1 Physical Characterization

5.3.1.1 Surface Area Analysis

Two types of carbon black – acetylene black (50 % compressed, Chevron Phillips Chemical Company) and Super C 65 (Timcal) were tested in this experiment. The surface areas of both carbons were measured using BET model as 75.9 $m^2 g^{-1}$ and 85.0 $m^2 g^{-1}$ respectively. Their surface areas are in the same magnitude, with Super C showing slightly higher surface area. The pore size distribution of the carbon was also measured and recorded in Figure 5.2. Both carbons had the similar pore volume from pore sizes under 10 nm, but the Super C had higher pore volume when the from pores between 10 and 50 nm, which can account for the higher surface area of Super C. In addition, from the shape of isotherms and the hysteresis loops of both carbon black samples (Appendix 5), it can be estimated that the shape of the pores was narrow slit-like.

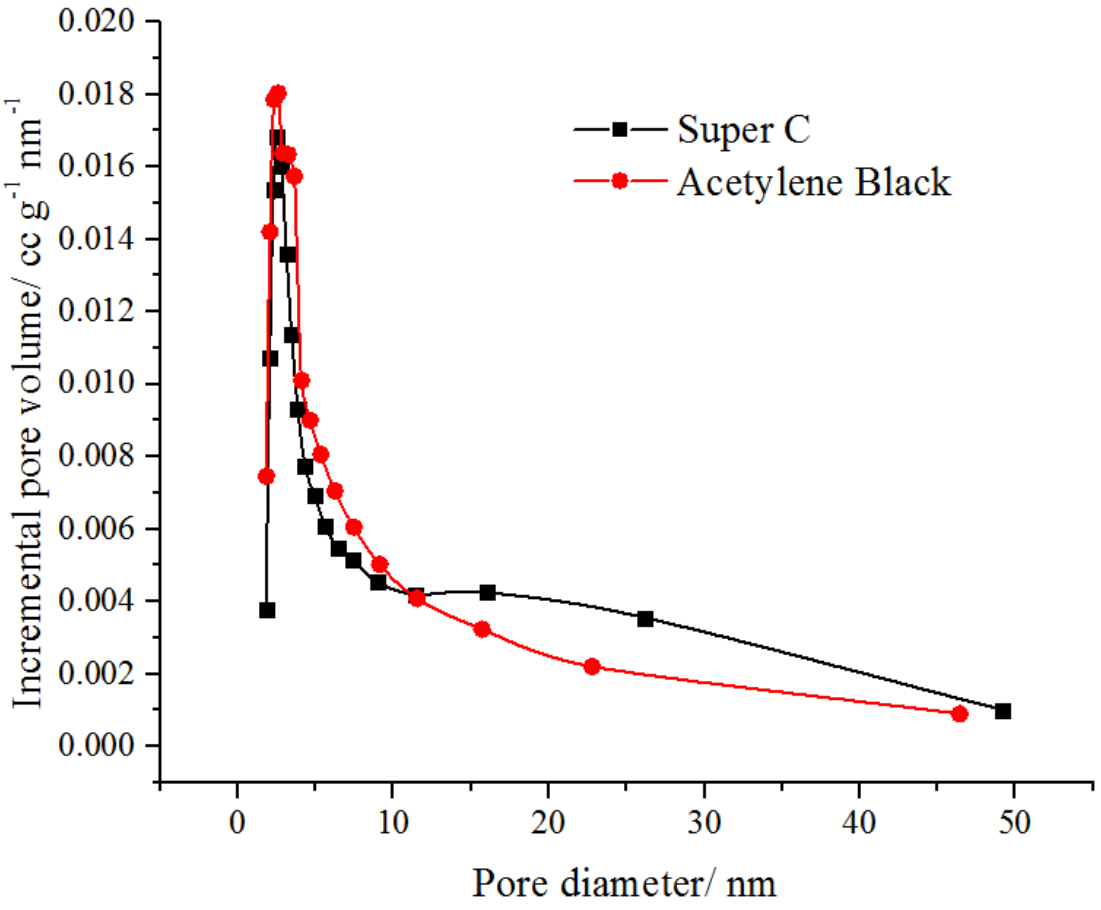

Figure 5.2 BJH pore size distributions of Super C and acetylene black.

The surface information of S/C composites prepared via different methods was also acquired. The surface areas of the carbon in the S/C composites were recorded in Table 5.1. The pore size distributions of acetylene black (AB) and S/AB composites prepared by different methods and with different sulfur contents were plotted in Fig 5.3. In this report, because the specific surface area of sulfur was approximately 2 $m^2 g^{-1}$, which was much smaller than the carbon, it was ignored in the calculation.

Table 5.1 shows that, the surface area of carbon decreased when the acetylene black was mixed with sulfur, which can be explained by the pore structure was blocked or filled by sulfur. For the composite prepared with heating method, the surface area further decreased when the sulfur loading increased to 50 wt%. However, for the sample prepared by ball milling, the surface area of carbon only decreased by a very small amount with more sulfur loaded. This result was supported by the pore volume information in Fig. 5.3.

Table 5.1 Specific surface areas of carbon in S/AB composites with different S contents and preparation methods.

Sulfur weight percent	Preparation method	Specific surface area ($m^2 g^{-1}$)
0	N/A	75.9
10	Ball milling	48.3
50	Ball milling	47.5
10	Heating	50.0
50	Heating	12.3

In Fig. 5.3, the pore size distributions of acetylene black show a very similar trend with the surface area. However, the pore size distribution only shows the relative ratio of pore volume to its size, it does not reflect the real contributions to the total pore volumes.

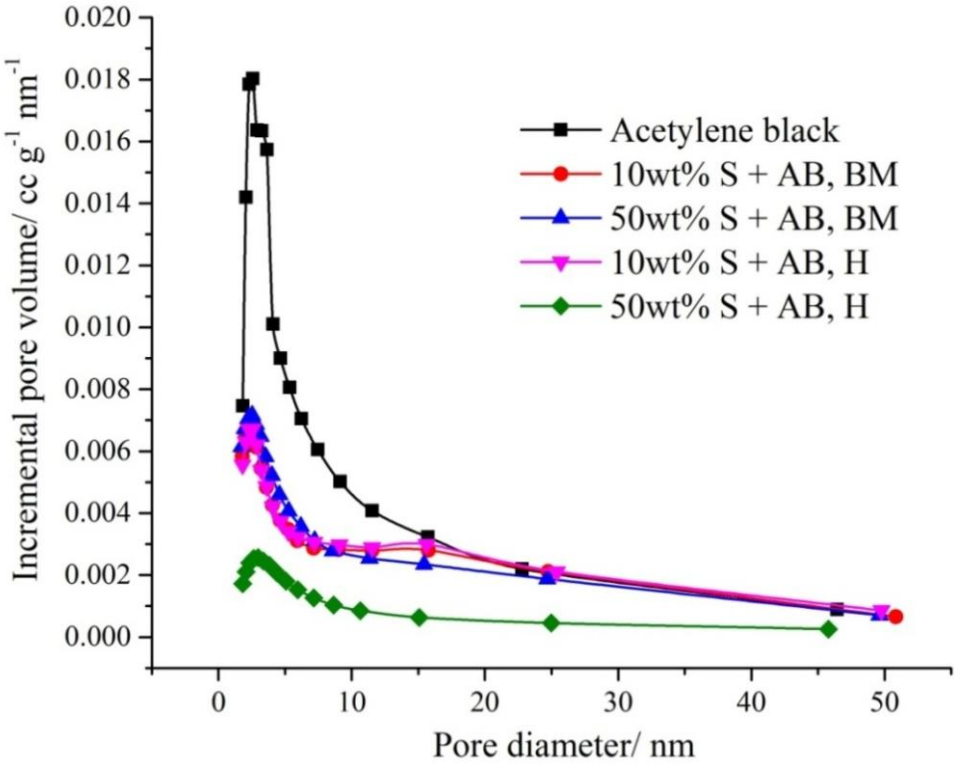

Figure 5.3 Pore size distributions of S/acetylene black composite (pore volume was calculated from the mass of carbon) with different sulfur content and prepared by ball milling (BM) and heating (H) methods.

When the sulfur content was relatively low (10 wt%), it can be observed from Fig 5.3 that the pore volume reduction is mainly contributed by pores with

diameter smaller than 15 nm; while for the pores larger than 15 nm, the pore volume was not affected. This suggests that the sulfur tends to fill up or cover the smaller pores first. In addition, different methods of preparation – heating (H) and ball milling (BM), have showed little effect on the surface area and pore volume. As the sulfur loading was raised to 50 wt%, the surface areas as well as the pore volumes have exhibited a sharp difference in the results obtained from two methods. This might be due to the fact that with low sulfur loading, the sulfur that ball milled with carbon covered the exterior pores while the melted sulfur also filled into those pores in preference. Therefore, although the mechanisms of pore blocking are different, they show similar results in the pore size distributions. When the sulfur loading was 50 %, the sulfur processed by ball milling still could not access to the inner pores, which explained why the specific surface area and pore volume of carbon remained approximately the same as composite with sulfur content of 10 wt%. On the other hand, the heated sulfur could diffuse into the finer porous structure of acetylene black, hence those pores which were unavailable to the sulfur using the ball milling method were filled up with melted sulfur and carbon surface was covered. It can also be deduced that those smaller pores are located at the interior parts of the carbon particles.

Table 5.2 Surface areas of carbon in S/Super C composites with different S contents and preparation methods.

Sulfur weight percent	Preparation method	Specific surface area ($m^2 g^{-1}$)
0	N/A	85.0
10	Ball milling	50.3
50	Ball milling	44.7
10	Heating	48.6
50	Heating	14.2

As shown in Table 5.2 and Fig. 5.4, similar results were also obtained from S/Super C composite. For Super C carbon that loaded with high percentage of sulfur, the preparation methods determined the surface area and pore volume. With lower sulfur loading, the surface area reduction was mainly due to the occupation of the exterior pores. However, the extra surface area and pore volume compared to acetylene black (shown in Fig. 5.2), which was attributed to

larger pores (D>15 nm), has been covered with low sulfur content. Therefore, from the conclusions drawn above, it can be referred that those extra pores were exterior pores.

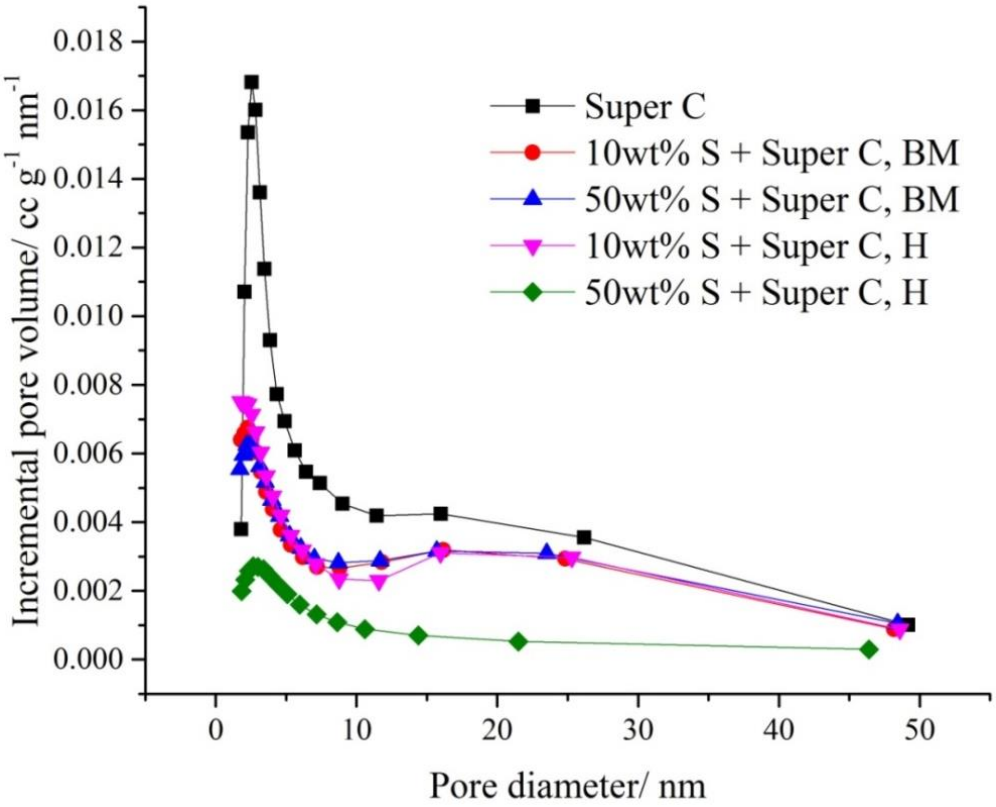

Figure 5.4 Pore size distributions of S/Super C composite (pore volume was calculated from the mass of carbon) with different sulfur content and prepared by different methods.

In order to have more in-depth information about the sulfur impregnation into the porous carbon, the total pore volume within the range of measurement was used for the analysis. As shown in Fig. 5.5, the total specific pore volume was plotted against the mass ratio of sulfur to carbon. From the graph, it can be seen that the specific surface area decreased with the ratio of sulfur to carbon, which suggested that sulfur continuously filled up the pores in carbon. Also, the data points show good linearity, indicating that the amount of sulfur inserted into porous structure was constant.

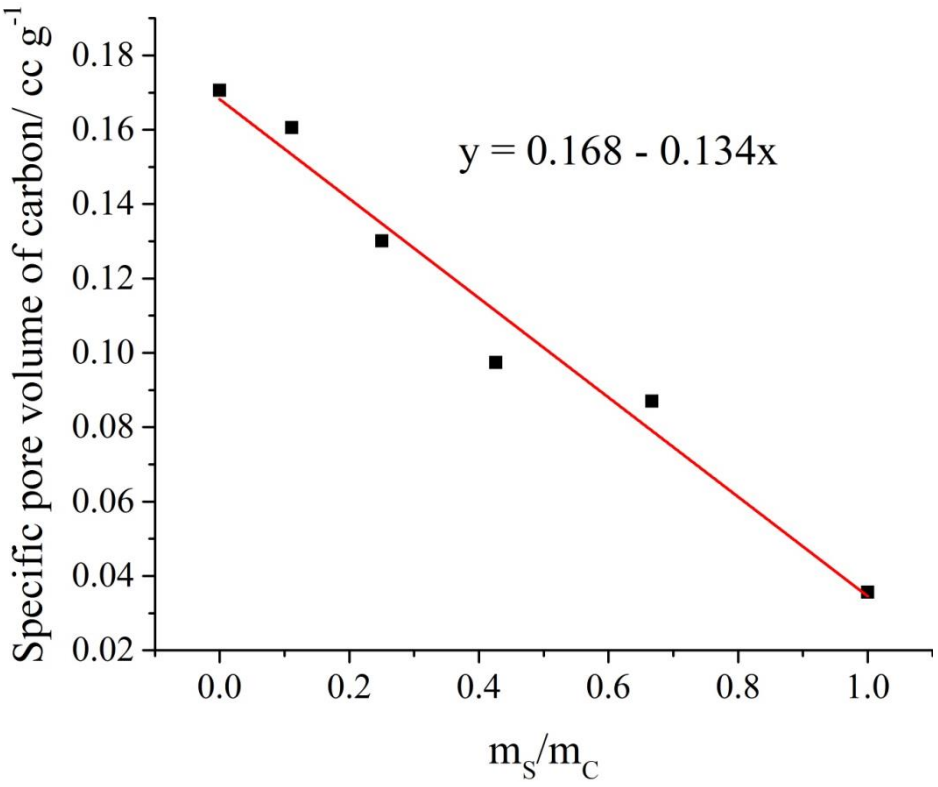

Figure 5.5 Specific total pore volume of acetylene black with different mass ratios of sulfur to acetylene black, prepared by heating method.

After the linear fit, the gradient of the curve is approximately -0.134 ml/g (of sulfur). This value indicates the pore volume that was occupied per unit mass of sulfur. Since the density of sulfur (rhombic) at room temperature was reported as approximately 2.07 g/ ml,[2] the theoretical volume of sulfur per gram would be 0.483 ml, which is much higher than the value obtained above. Therefore, it can be concluded that only part of sulfur (approximately) was contained in porous structure of acetylene black. Other characterization methods will be required to study the microstructures of sulfur/carbon composites.

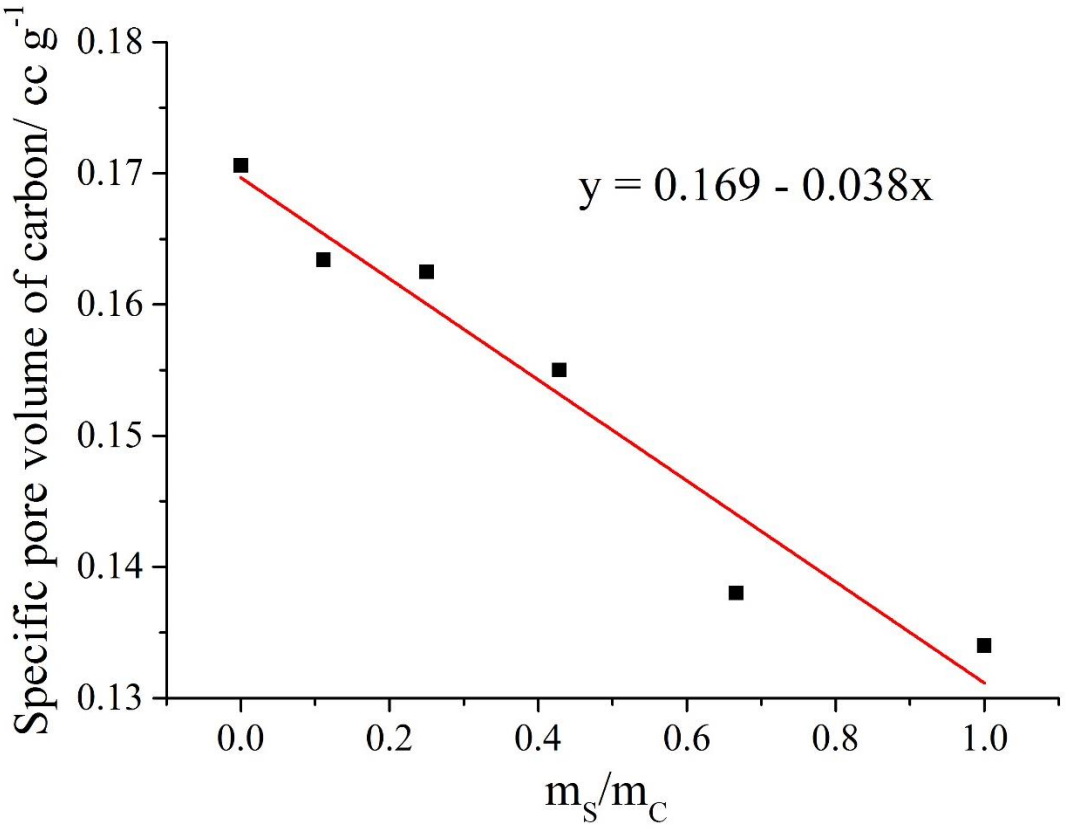

Figure 5.6 Specific total pore volume of acetylene black with different mass ratios of sulfur to acetylene black, prepared by ball milling method.

Fig. 5.6 shows the results from the same experiments as the above performed with S/AB composites prepared from ball milling method. The gradient of the linear fit curve is only -0.038 ml/g^{-1}, which is much smaller compared to the value in Fig. 5.5. This result shows that in the S/AB composites prepared via ball milling method, the pores were barely filled with sulfur. This result shows that only melted sulfur can infiltrate into the porous structure of carbon blacks.

5.3.1.2 XRD Analysis

The surface analysis has shown that with high sulfur content, different preparation methods can affect how sulfur was loaded in porous carbon. To have a more in-depth knowledge of the composites, XRD analysis was applied in the characterization. Fig. 5.7 shows the XRD patterns of sulfur, acetylene black and S/C composites. Sulfur has sharp peaks at 2θ between 20-40° which agree with the results in previous reports[3,4], while acetylene black has two wide bands at 2θ = 25° and 43°, which are assigned to disordered graphic (0 0 2) plane and overlapped (1 0 0) and (1 0 1)[5,6]. Therefore, they can be well distinguished from each other in the XRD pattern.

S/C composites prepared in different methods with 50 wt% sulfur loading were also analysed. When the composite was prepared with ball milling method, the XRD pattern was very similar to sulfur, with an insignificant background of carbon. This result suggested that when ball milled, instead of infiltrating the pores, sulfur will only cover on the surface of carbon, which agree with the surface analysis data. When the composite was prepared with heating method, the XRD pattern exhibit a very strong carbon back ground; on the top of it, the sulfur peak intensity was greatly reduced. In addition, the peak ratios changed and a new peak appeared (2 theta = 24°) after heating, which requires further investigation. Therefore, it can be concluded only part of sulfur was on the surface of carbon. This result also accorded with the surface analysis data that part of the sulfur was able to infiltrate the pores of carbon by heating. In addition, the peak height ratio and peak position of sulfur were also different after heating. It might be due to the fact that the crystalline structure of sulfur was changed after heating. To prove this, further experiments need to be performed.

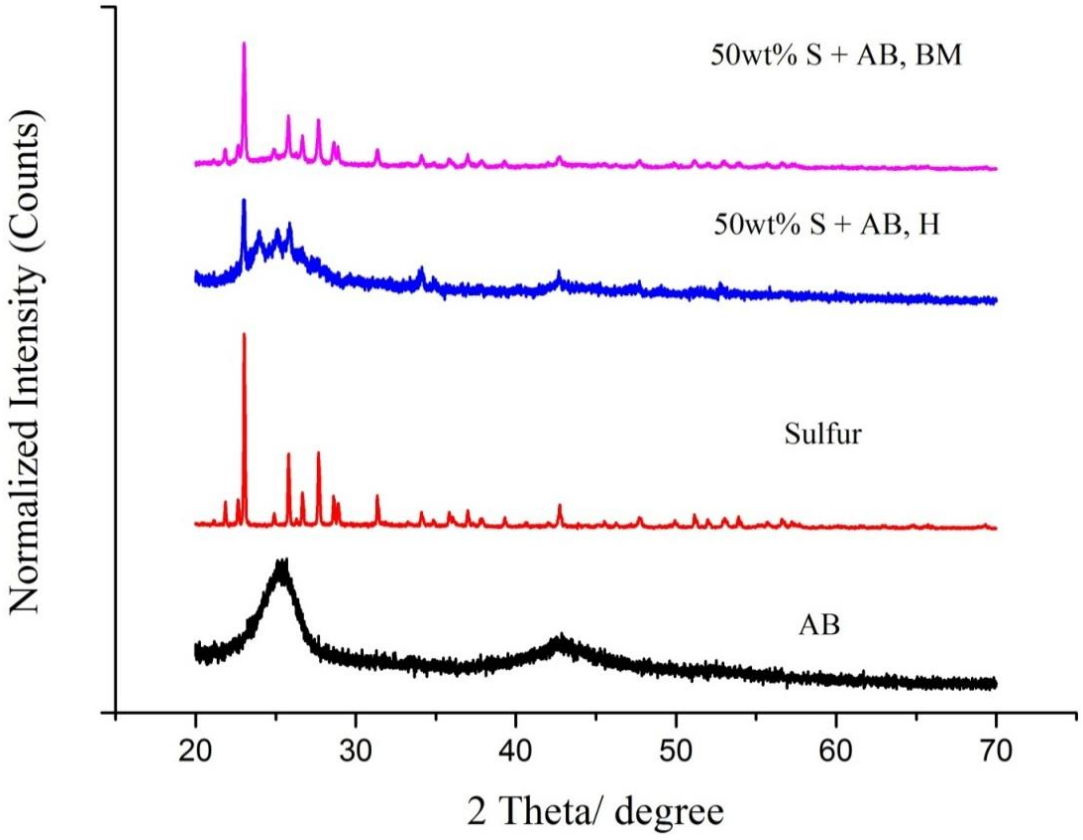

Figure 5.7 XRD patterns of acetylene black (AB), sulfur and sulfur/carbon composites prepared form ball milling (BM) and heating (H). The intensities were normalized to similar magnitude.

The XRD patterns of S/Super C (in Fig. 5.8) have also showed similar results – the S/C composite prepared in ball milling method had a weak carbon background and heating method resulted in strong carbon background with different sulfur peak height ratio and positions. To understand whether the crystalline structure of sulfur was changed during the heating process, sulfur was also heated under same condition without carbon. Although the product (see Appendix 6) shows colour change, no significant change can be observed in its crystalline structure. Therefore, the change in the XRD patterns might be resulted from other factors. One possible explanation might be that the porous structure of carbon might change the growth preferences of sulfur crystalline structure during its recrystallization.

In summary, the usage of both acetylene black and Super C as the conductive material for Li-S positive electrode exhibit similar properties in terms of how sulfur was loaded in the carbon. By ball milling the composite, the sulfur will only stay on the top of the carbon without filling its interior pores while the heating method will not only lead to the blockage of the pores, but also fill the pores.

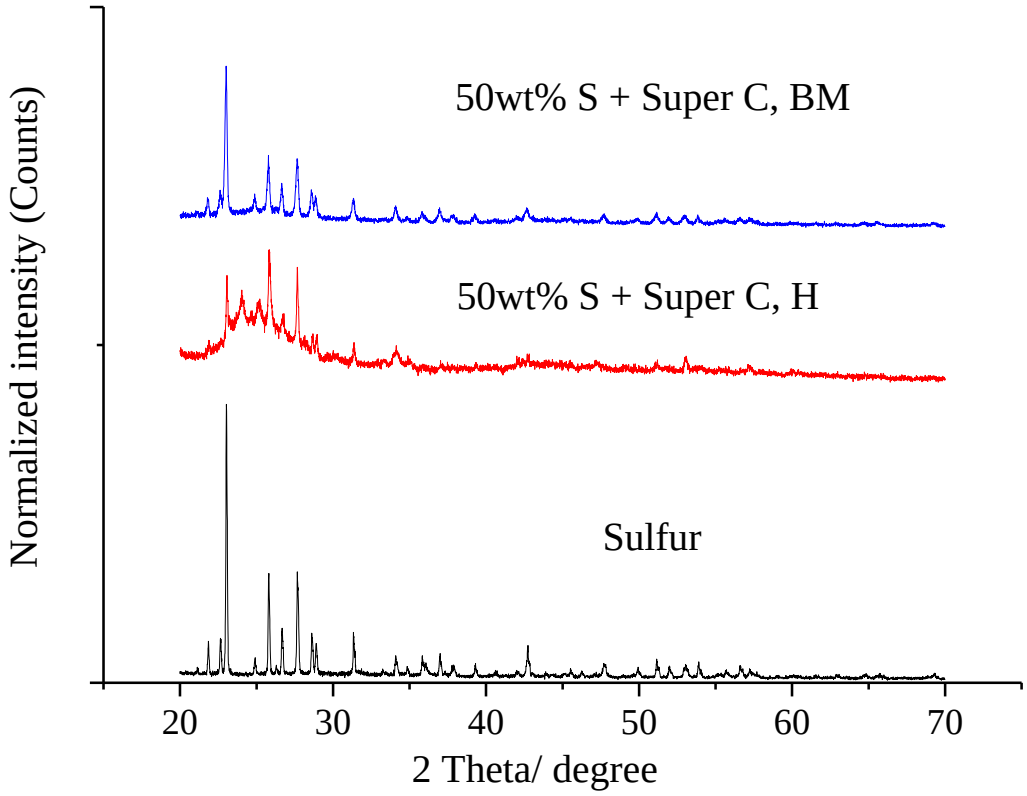

Figure 5.8 XRD patterns of sulfur and sulfur/Super C composites prepared form ball milling (BM) and heating (H) with 50 wt% sulfur content. The intensities were normalized to similar magnitude.

5.3.2 Electrochemical Tests

5.3.2.1 Cyclic Voltammetry Tests

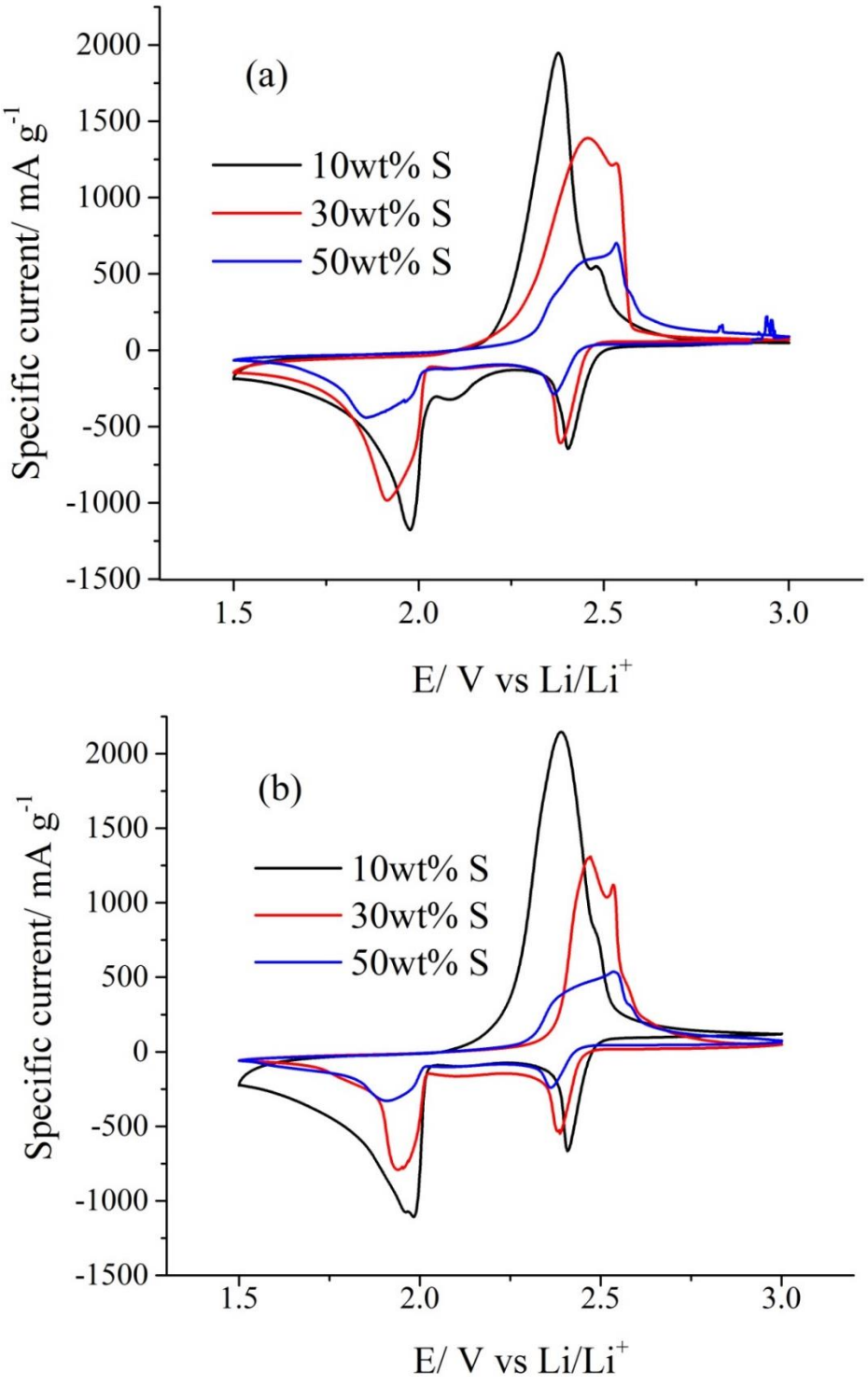

Figure 5.9Cyclic voltammogram of sulfur/acetylene black composites in different S/C ratio prepared by ball milling (a) and Heating (b). Mass of sulfur in the electrode was used to calculate the specific current. The scan rate was 100 □V s^{-1}.

Cyclic voltammograms of S/AB with different amounts of sulfur are shown in Fig. 5.9. The voltammograms show two main reduction peaks (2.4 V and 2.0 V) and one main oxidation peak (2.3–2.5 V, a small shoulder can be observed as a minor peak), which correspond to the two main discharge plateaus and one main charge plateau in typical discharge/charge profile of the Li–S battery demonstrated in Chapter 1.

It is noticeable that for both preparation methods, as the sulfur content increased, the specific current decreased. It is likely that with more sulfur, the available surface area of carbon in the composite became less. Therefore, the three-phase junction between the conductive material and the electrolyte decreased, leading to lower current. In addition, the peak separation was larger with higher sulfur/carbon ratio. This might be due to the high viscosity in solution resulted from the high polysulfide concentration.

Both S/C composite preparation methods exhibit similar peak positions and peak shapes. However, with higher content, ball milling method results in higher currents. This could be explained by that with higher sulfur content, the sample prepared with heating method resulted in a much lower specific surface area of carbon, and hence the difference became more significant in terms of the current.

5.3.2.2 Galvanostatic Cycling Tests

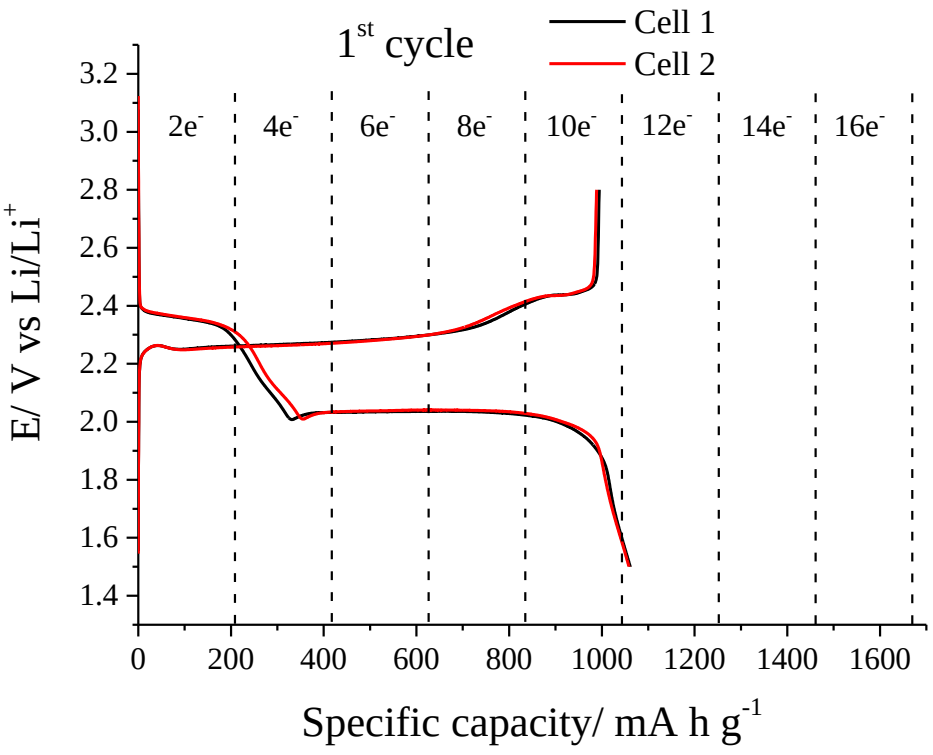

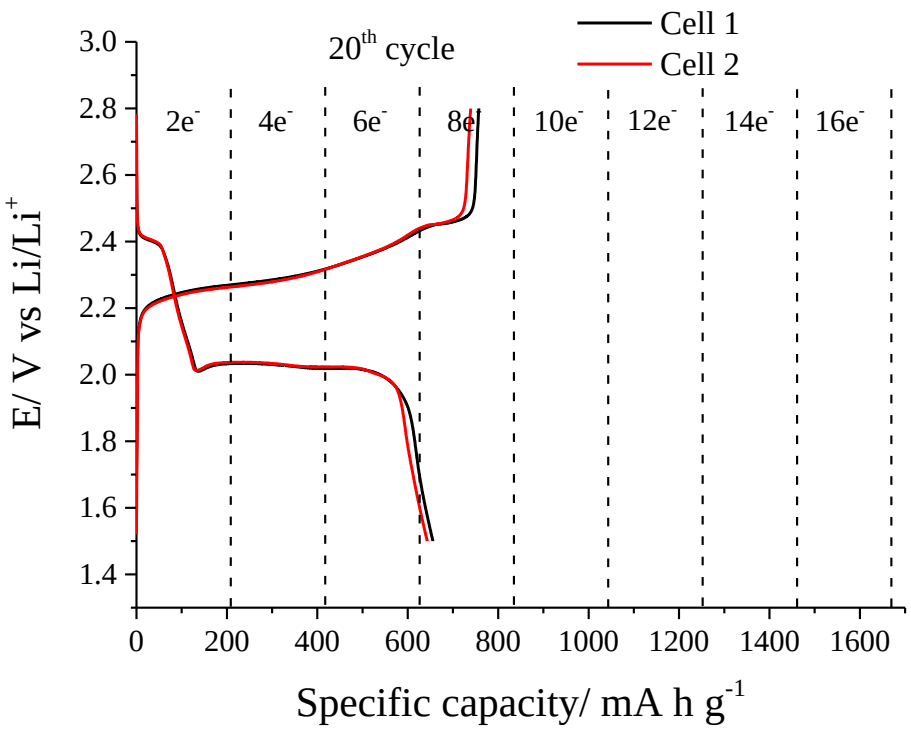

Figure 5.10 Discharge/charge voltage profiles at different cycles of two identical Li-S cells using S/AB positive electrode with 30 wt% sulfur prepared from heating method. The C-rate was 0.1 C.

To examine the cycling performance of the positive electrode materials with different sulfur loading and prepared from different methods, galvanostatic cycling with potential limit was performed. The reproducibility of the cycling results was also tested with multiple cells under same conditions (see Fig. 5.10). It can be seen that the reproducibility of the measurement is better than 90 % in terms of the values of the capacity, even after 20 cycles.

Fig. 5.11, 5.12 and 5.13 show the discharge/charge profiles of Li-S cells with different sulfur contents and via different preparation methods. Two distinguished discharge plateaus and two charge plateaus can be observed from the discharge profiles which agree with the peaks in the cyclic voltammograms. By comparing different sulfur contents, it can be seen that during discharge as the sulfur content increased, the potential of discharge plateaus decreased and the potential of charge plateaus increased. This observation agrees with the cyclic voltammogram results, which can also be attributed the limited available surface area on the positive electrodes. In addition, at the end of charge or discharge plateau, the profile of cells with low sulfur loading tended to have tails instead of sharp potential drops. This might be because the extra surface area and smaller amount of polysulfide led to a slow passivation of the positive electrode, resulting in discharge/charge tailing.

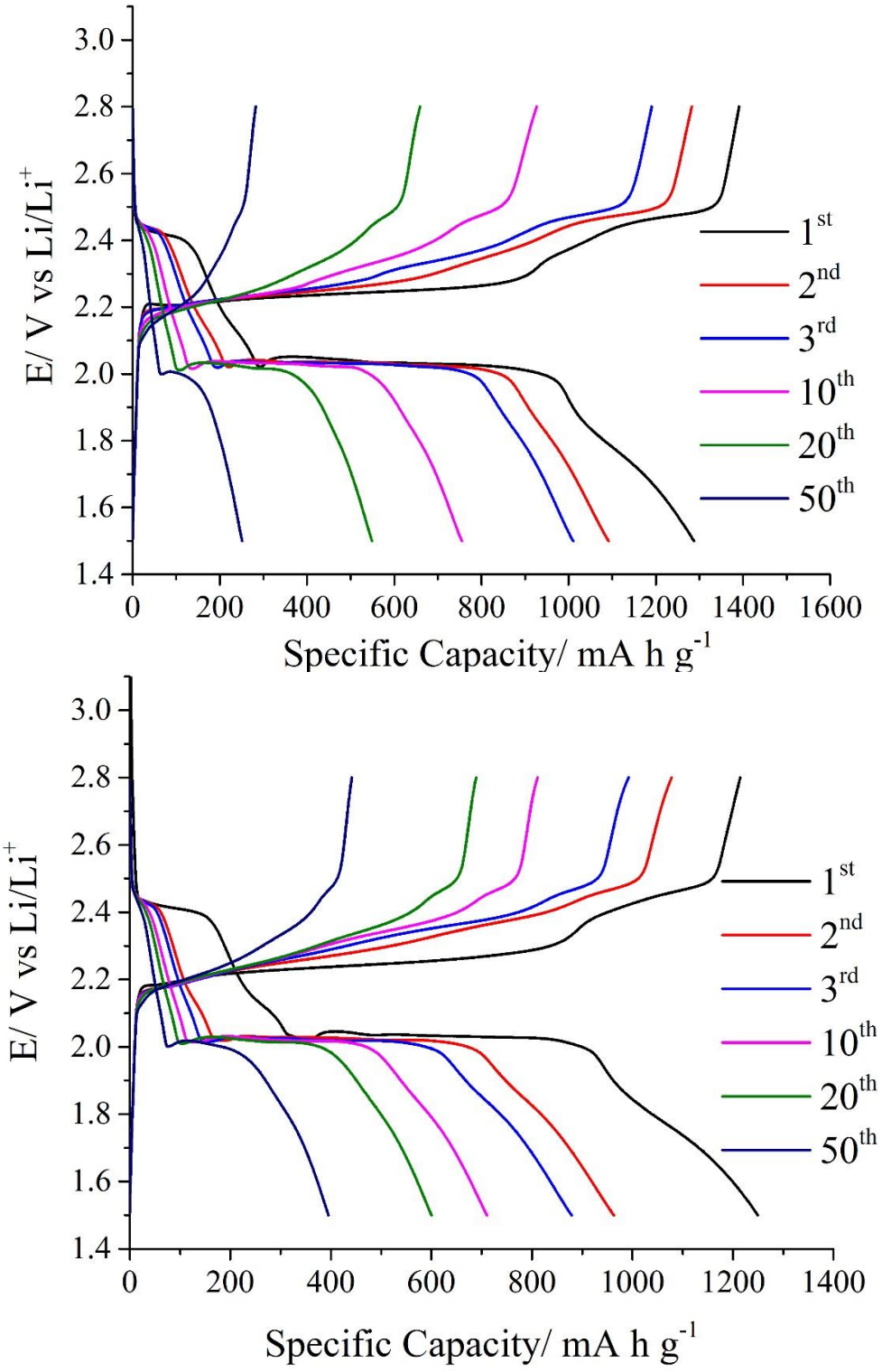

Figure 5.11 Discharge/charge voltage profiles of S/AB composites with 10 wt% sulfur prepared from ball milling (upper) and heating (lower) method. The C-rate was 0.1 C.

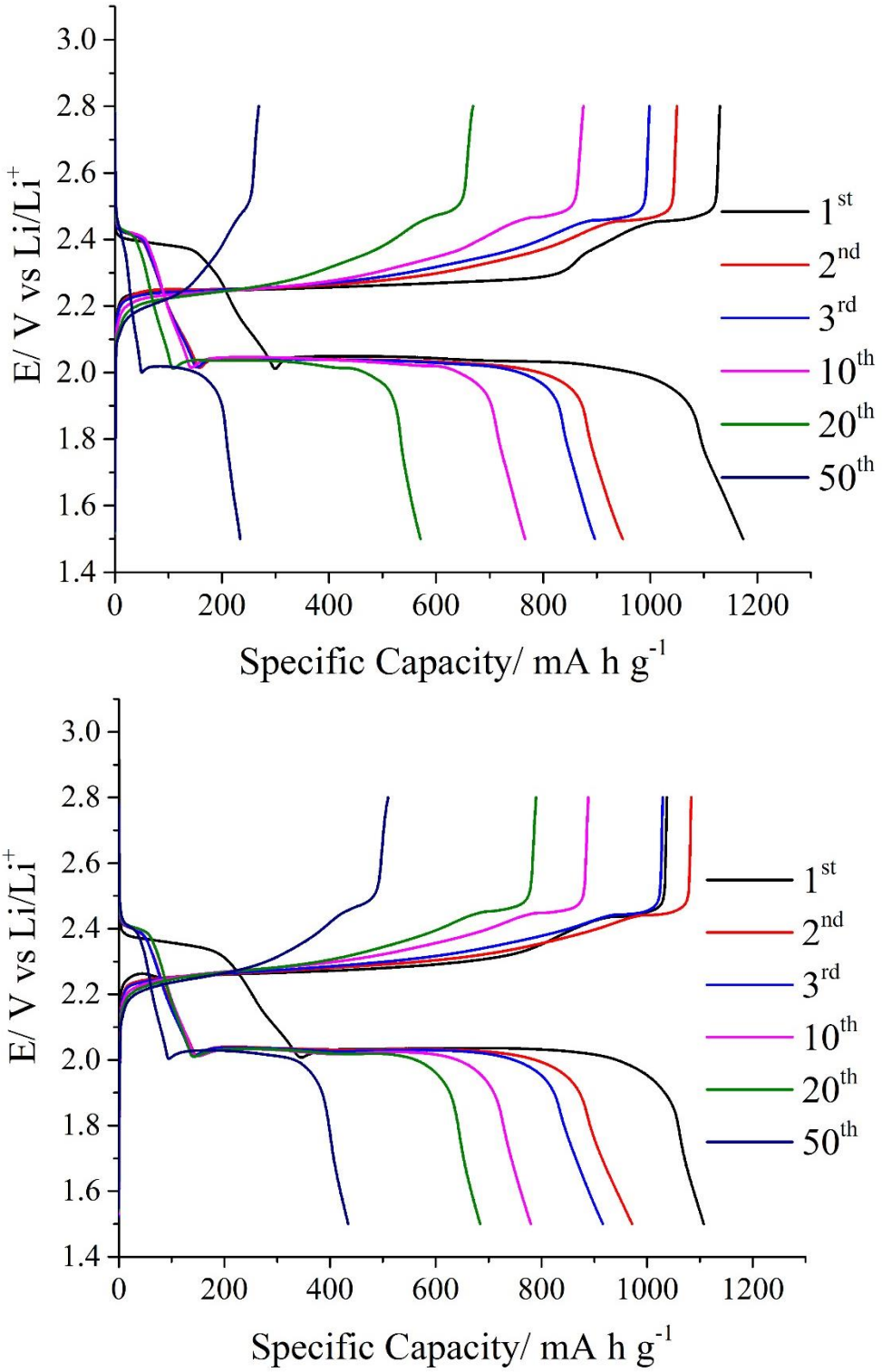

Figure 5.12 Discharge/charge voltage profiles of S/AB composites with 30 wt% sulfur prepared from ball milling (upper) and heating (lower) method. The C-rate was 0.1 C.

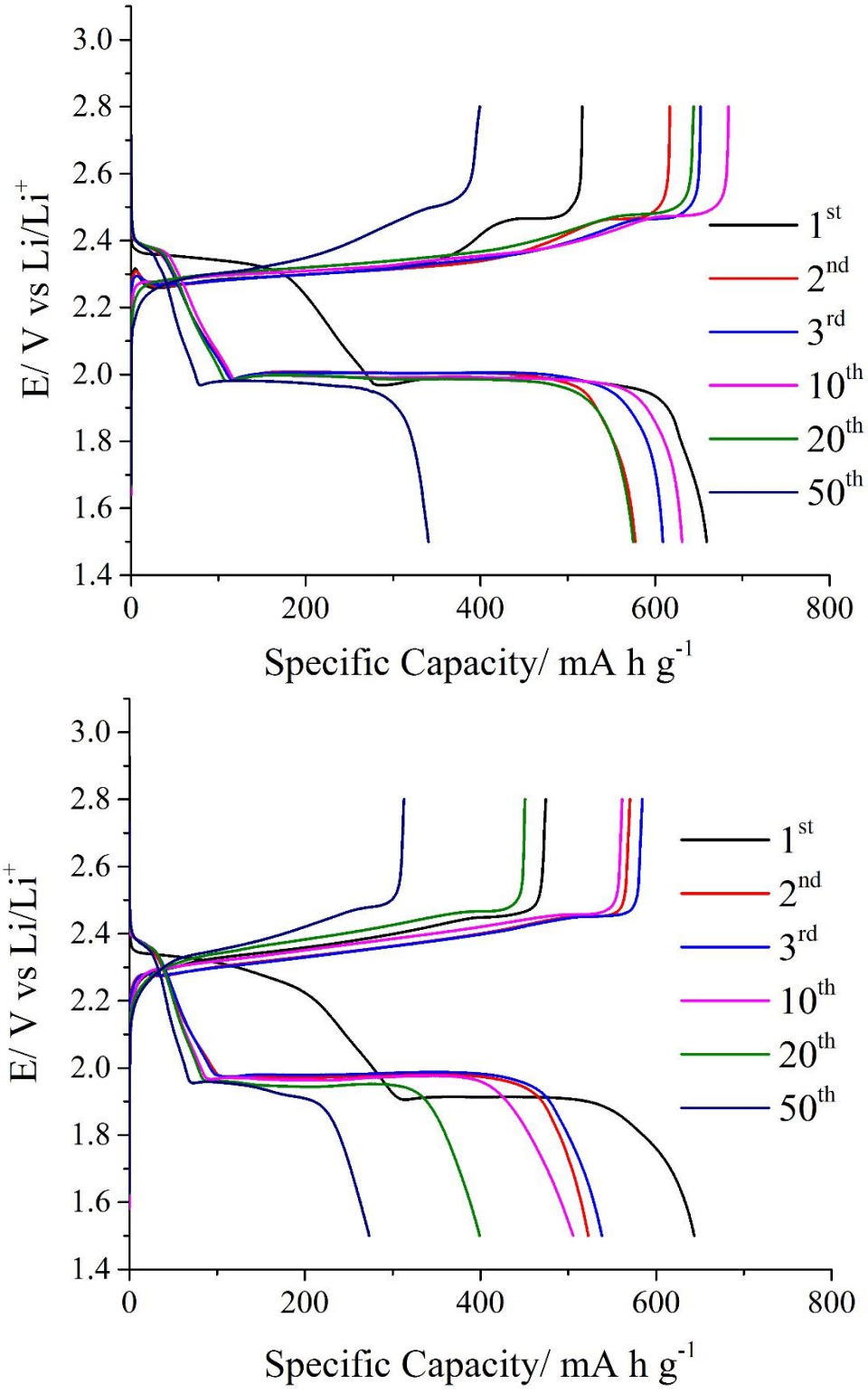

Figure 5.13 Discharge/charge voltage profiles of S/AB composites with 50 wt% sulfur prepared from ball milling (upper) and heating (lower) method. The C-rate was 0.1 C.

It can be noted that for the first discharge plateau in the first cycle, all cells exhibit very similar capacity of approximately 200 mA h g^{-1} while the theoretical value for the first plateau capacity was 209 mA h g^{-1}. This result indicated that

the conversion from S_8 to S_8^{2-} was almost complete; hence for cycling tests, the contact between sulfur and carbon was not an issue. However, after the first cycle, the capacities of the first plateau decreased significantly (less than 100 mA h g^{-1}), suggesting only a small portion of polysulfide was converted back to S_8.

No significant differences can be observed between different preparation methods when the sulfur contents are 10 wt% and 30 wt%. As the sulfur content increased to 50 wt%, the potentials of discharge plateau in the first cycle varied with different preparation methods. The sample prepared via heating treatment shows a much lower potential compared to the ball milled sample, which might be attributed to the limited availability of carbon surface caused by the sulfur impregnation.

As for different sulfur content, the cells with 10 wt% of sulfur show gradual potential decreases at the end of each discharge plateaus while the potential drop in the cells with 50 wt% sulfur is much steeper. The reason for the tailing might be that with higher sulfur content, the formation of insoluble polysulfide quickly blocked the surface area of carbon, resulting in a fast electrode passivation.

Table 5.3 Discharge capacities in the first cycle and the 50th cycle of sulfur/acetylene black composites with different sulfur contents and preparation methods.

Sulfur %	Preparation method	1st capacity/mA h g^{-1}	50th capacity/ mA h g^{-1}	Retention
10 wt%	Ball milling	1287	251	19.5 %
10 wt%	Heating	1249	395	31.6 %
30 wt%	Ball milling	1173	234	19.9 %
30 wt%	Heating	1107	434	39.2 %
50 wt%	Ball milling	659	340	51.6 %
50 wt%	Heating	643	273	42.5 %

The discharge capacities of the cells in the first cycle and the 50th cycle were also recorded in Table 5.3. In addition, specific capacities (per mass of sulfur) and Coulombic efficiencies of Li-S cells with different sulfur/carbon ratios and different preparation methods are plotted against the cycle numbers in Fig. 5.14,

Fig. 5.15 and Fig. 5.16. From Table 5.3, it can be seen that the first discharge capacities decreased with sulfur loading, which might be due to the decreasing available surface areas of carbon. However, as the cycling continued, cells with lower sulfur content suffered more severely from capacity fading. Assuming for all lithium metal electrodes the thickness of the passivation layers are the same, the amount of the polysulfides that would be consumed in this process would take a larger proportion in cells with lower sulfur content, therefore the capacity fading is more severe. Alternatively, it was suggested that higher polysulfide concentration might lead to better protection of lithium.[7]

The effects of different S/C composite preparation methods on the cycling performances were also investigated. In Table 5.3, the initial capacities exhibit little differences between different methods for all sulfur loadings. When the sulfur contents were 10 wt% and 30 wt%, heating treatment resulted in better capacity retention. In addition, the curve shapes in Fig 5.14 and Fig 5.15 show that compared to cells with S/C composites prepared from heating method, samples prepared by ball milling exhibit a steeper capacity decrease with cycle numbers compared to heated samples. But when the sulfur content was 50 wt% as shown in Fig. 5.16, samples prepared from the ball milling method show better performances. This finding implies that, when the sulfur loading was relatively lower, it was more important to keep sulfur in the pores structure in order to minimize the shuttle effect. As the sulfur content increased, the blocking effect of insoluble polysulfide appeared to be more significant. Therefore, the priority became creating more available surface area for the electrochemical reactions.

Considering the discussions above, there are multiple factors affecting the performance of Li-S cells. From the results obtained, it seems that the cell with 30 wt% sulfur content using heating method shows the best capacity per mass of sulfur after 50 cycles was due to the optimum combination of these conditions.

In terms of specific capacity during cycling, it can be concluded that when using acetylene black as the conductive material, heating methods should be adapted with lower sulfur content so the porous carbon can have better contact to sulfur; ball milling method should be used with respectively higher sulfur content in order to provide more surface area.

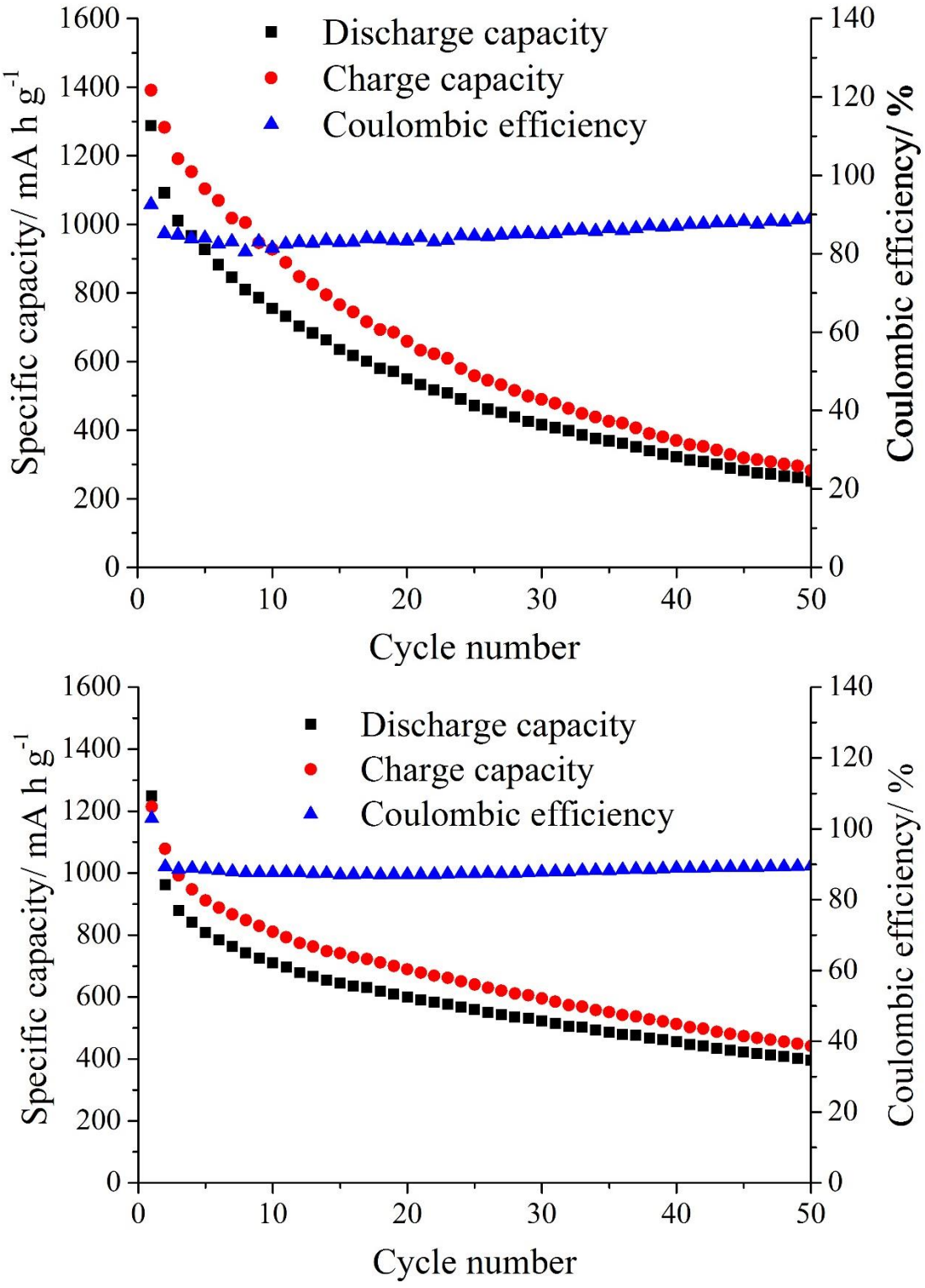

Figure 5.14 Capacities and Coulombic efficiencies of S/AB composites with 10 wt% sulfur prepared from ball milling (upper) and heating (lower) method. The C-rate was 0.1 C.

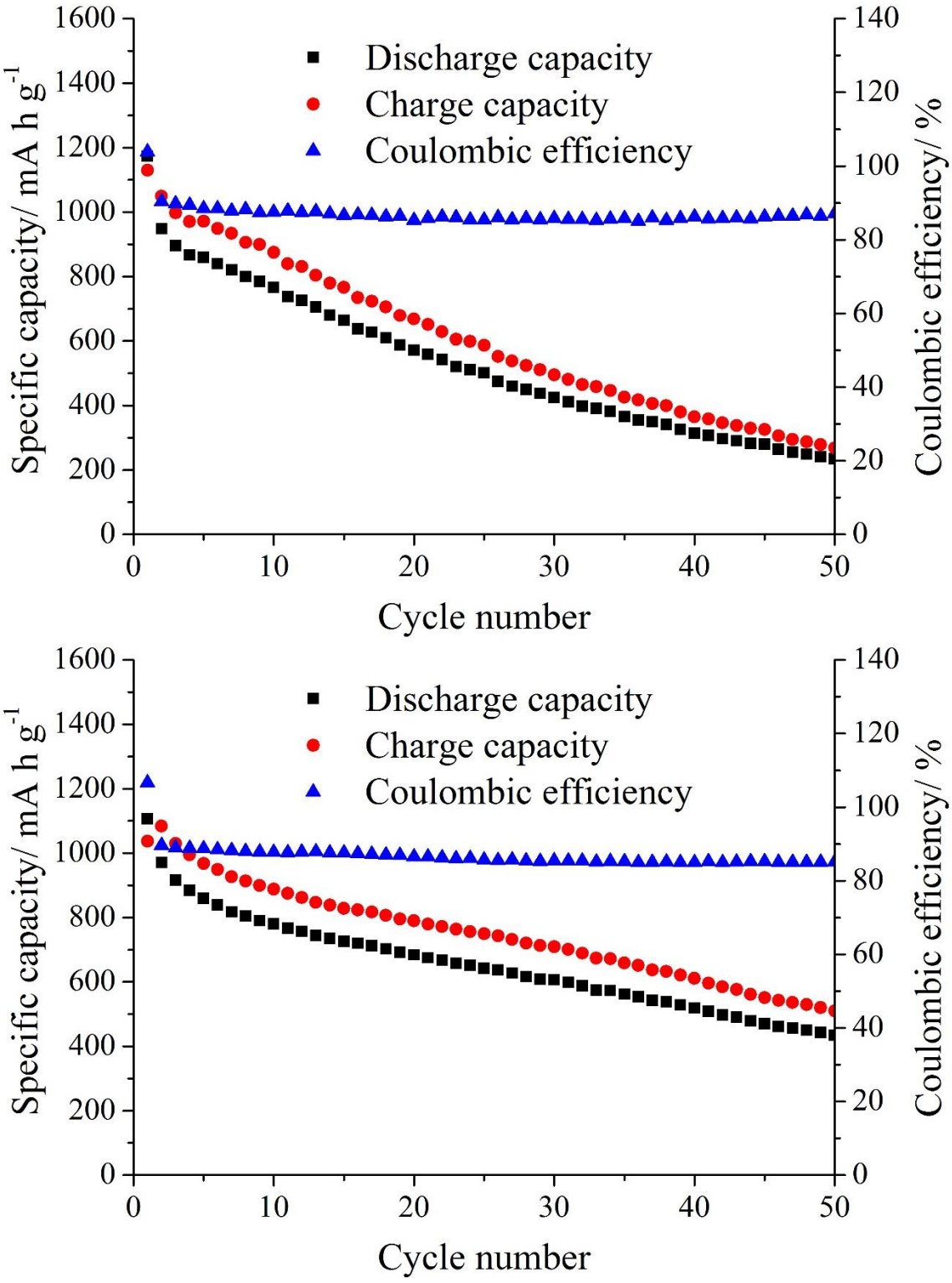

Figure 5.15 Capacities and Coulombic efficiencies of S/AB composites with 30 wt% sulfur prepared from ball milling (upper) and heating (lower) method. The C-rate was 0.1 C.

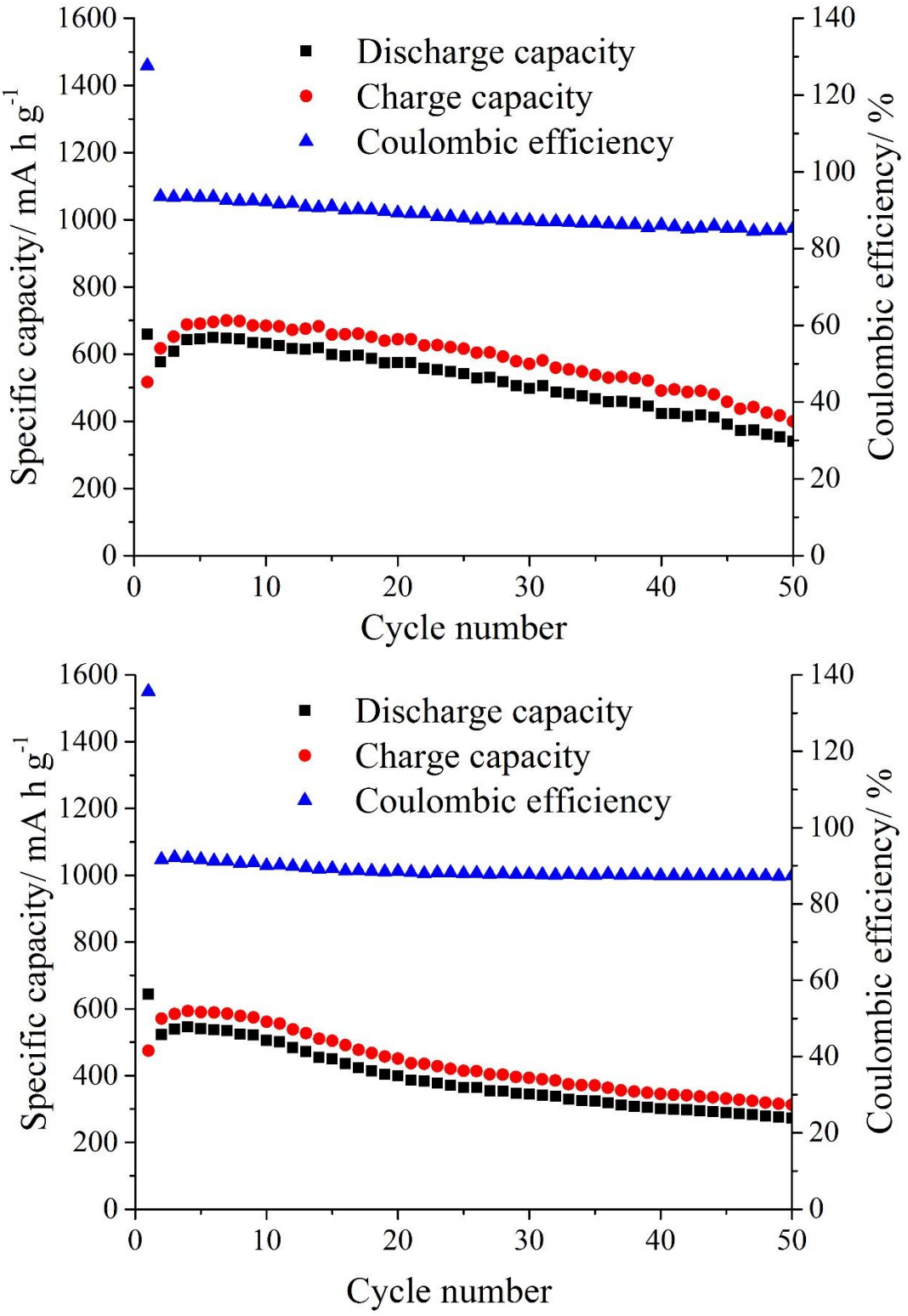

Figure 5.16 Capacities and Coulombic efficiencies of S/AB composites with 50 wt% sulfur prepared from ball milling (upper) and heating (lower) method. The C-rate was 0.1 C.

On analysing the Coulombic efficiencies (η), the following equation was used:

$\eta = 100\ \% \times (N^{th}\text{ discharge capacity}/N^{th}\text{ charge capacity})$ (Equation 5.1)

It can be seen that all cells, regardless of their preparation methods and sulfur loading, exhibit stabilised Coulombic efficiencies between 85 % and 90 % at the end of cycling. However, it can be noted that when the sulfur content is 50 wt%, the first cycle Coulombic efficiencies are above 120 %, suggesting that discharge capacities are significantly higher than the charge capacity. One of the reasons could be that after first discharge, the polysulfides were not converted back to S_8. An alternative explanation could be that polysulfides formed a passivation layer much faster at high concentration, therefore the sulfur loss is significant at the first cycle (presented in Fig. 5.17).

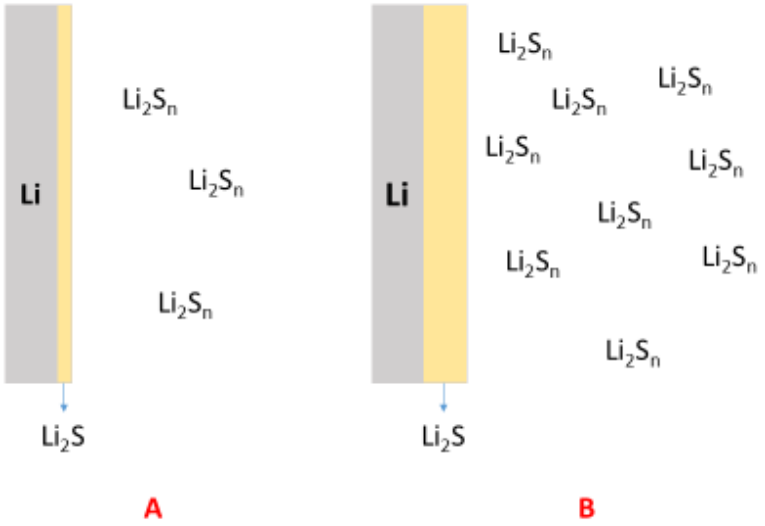

Figure 5.17 Schematic graphs of Li_2S passivation layer formed on lithium metal surface with low concentration (A) and high concentration (B) of polysulfide (Li_2S_n).

The overcharge in the lithium sulfur battery is commonly associated with shuttle mechanism, according to which high order polysulfides are reduced by the lithium. Therefore, it is likely that the shuttle mechanism can be suppressed at high sulfur content.

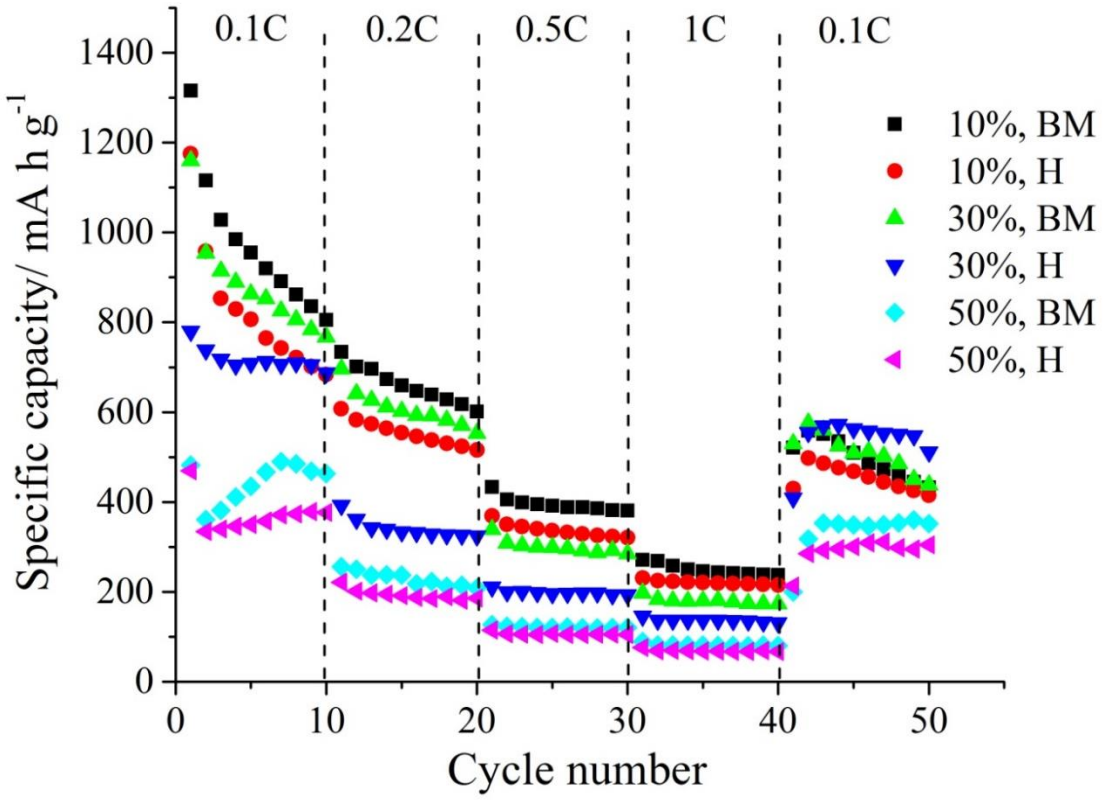

Figure 5.18 Rate performances of Li-S batteries of different sulfur contents and different S/AB composites preparation methods.

Rate performances were also tested for the cells above. Fig. 5.18 shows the discharge capacities of different cells under different discharge/charge rates of 0.1 C, 0.2 C, 0.5 C, 1 C and 0.1 C, each rate was applied for 10 cycles. From the figure, it can be seen that in general, the capacities of the cells decreased with increasing C-rates. But the capacities at the last 10 cycles were well retained after the high-rate cycling, suggesting the no degradation reaction occurred during the high C-rate cycling. The results show that higher capacities were retained under high C-rates for S/C composites prepared via ball milling method. It is likely that the extra pore volume and available surface area are responsible for the observed behaviour.

5.4 Summary

In this chapter, carbon blacks were used as the conductive material in Li-S batteries and the sulfur/carbon black composites with different sulfur contents and prepared via different methods were characterized.

From the surface area analysis, it can be concluded that the ball milling and heating methods resulted different pore size distributions in the sulfur/carbon black composites. Heating method could fill all the porous structures of the carbon blacks while ball milling method only filled part of the pores. XRD results prove that this might be due to the layered graphene structure of the carbon blacks, therefore only melted sulfur can fully fill up the pores.

The galvanostatic cycling performances show that the shuttling effected was mitigated by the increase of sulfur content. In addition, at lower sulfur content, heating achieved better capacity retentions with at higher sulfur content (50 wt%) ball milling exhibit better performance. The rate performances show that the high C-rate cycling would not affect the cells and ball milling show better performances under high-rate cycling.

5.5 Reference

1 H. P. Boehm, *Carbon N. Y.*, 1994, **32**, 759–769.

2 E. W. Washburn, *International Critical Tables of Numerical Data, Physics, Chemistry and Technology*, McGraw-Hill Book Company Inc., New York, 1st edn.

3 E. S. Shin, M.-S. Kim, W. Il Cho and S. H. Oh, *Nanoscale Res. Lett.*, 2013, **8**: 343.

4 L. Yin, J. Wang, X. Yu, C. W. Monroe, Y. NuLi and J. Yang, *Chem. Commun.*, 2012, **48**, 7868–7870.

5 Z. Q. Li, C. J. Lu, Z. P. Xia, Y. Zhou and Z. Luo, *Carbon N. Y.*, 2007, **45**, 1686–1695.

6 F. L. Wang and C. Hwang, *Appl. Catal. A-General*, 2004, **276**, 9–16.

7 R. Demir-Cakan, M. Morcrette, Gangulibabu, A. Gueguen, R. Dedryvere and J.-M. Tarascon, *Energy Environ. Sci.*, 2013, **6**, 176–182.

Chapter 6: Sulfur/Activated Carbon Composite Positive Electrode in Li-S Batteries

6.1 Introduction

Due to the high surface area and strong adsorbing ability, activated carbons have been widely applied in industrious area such as water filtering[1,2], sugar refinement[3,4], gas storage and purification[5-7], protein separation[8], catalysts[9,10] and energy storage.[11-16] A main difference between activated carbons and carbon blacks is their agglomerate structure. Agglomerates of carbon blacks are formed from the fusion of smaller particles while the activated carbon agglomerates are formed from the breakdown of larger particles to finer ones.[17]

As stated in Chapter 1, activated carbon has been widely studied as the conductive material in Li-S batteries. In this chapter, both physical and electrochemical properties of the activated carbon-sulfur composite will be characterized. In addition, an important difference between activated carbons and carbon blacks is their agglomerate structure.[17] The agglomerate size of activated carbons is usually greater than 2 μm, which is significantly larger than that of carbon blacks (30-40 nm). This can be reflected in the surface smoothness of their pellets (see Appendix 7). The pellet of carbon black is much smoother than activated carbon, indicating a smaller particle size.

6.2 Experimental Details

Same characterization techniques (surface information, XRD and electrochemical tests) and the preparation of S/C composites and electrode have been used as described in Chapter 5.2. In this chapter, two activated carbon will be tested: Elorit (Norit) and CA1 (Norit).

6.3 Results and Discussions

6.3.1 Physical Characterization

6.3.1.1 Surface Area Analysis

Using BET method, the surface area of Elorit and CA1 were measured as 586.0 $m^2 g^{-1}$ and 1060.8 $m^2 g^{-1}$ respectively, which are much higher than carbon blacks

as expected. In addition, using BJH model, their pore size distribution information was measured and compared in Fig. 6.1.

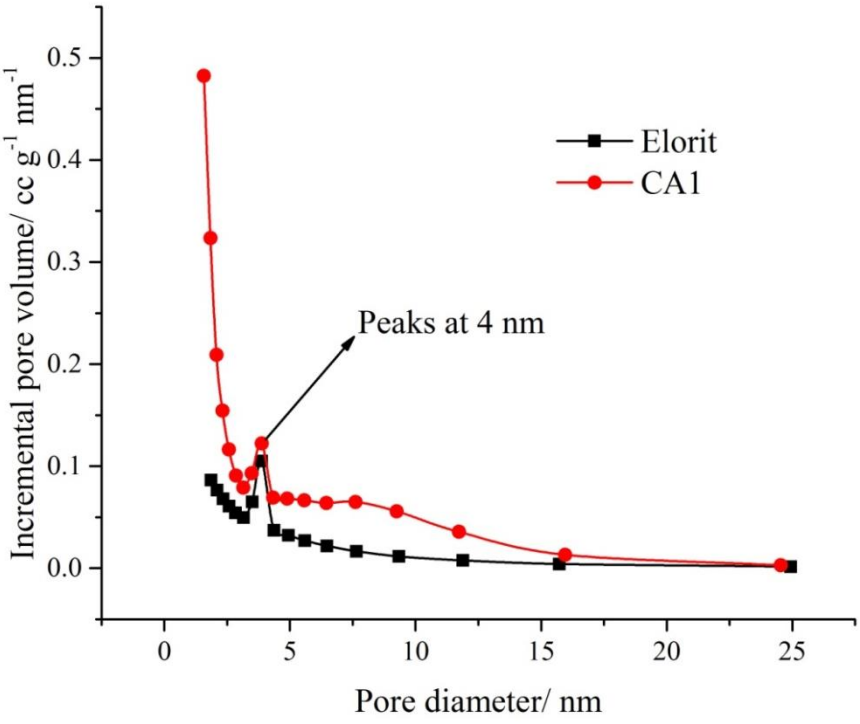

Figure 6.1 BJH pore size distributions of Elorit and CA1.

It is clear that CA1 had larger pore volumes than Elorit in all pore sizes, especially when the pore size is below 3 nm, which explain the fact that the specific surface area of CA1 is approximately twice as Elorit. However, due to the limitation of BJH method, the micropores structure cannot be accurately analysed. It can also be seen that in Fig. 6.1, both carbons had a peak at 4 nm, which is suggested as a common false peak in the desorption branch.[18] This false peak might be due to the large hysteresis loop in the isotherm (shown in Appendix 5). Hence, the pore volume corresponding to the peaks will not be considered in the discussion.

To study how the surface area changed with carbon loading, the surface properties of S/C composites were characterized. As recorded in Table 6.1, the surface area of unit mass of Elorit decreased as the carbon mixed with sulfur, which is similar in the case of carbon blacks. The surface area decreased further when the sulfur loading increased to 50 wt%. However, unlike carbon blacks, the surface area of Elorit did not change significantly as the preparing methods were different. In this case, both composites exhibited sharp decreases in surface areas, suggesting almost complete blockages of pores.

Table 6.1 Surface areas of carbon in S/Elorit composites with different S contents and preparation methods.

Sulfur weight percent	Preparation method	Specific surface area (m^2 g^{-1})
0	N/A	586.0
10	Ball milling	422.7
50	Ball milling	16.4
10	Heating	395.7
50	Heating	15.4

To better understand this result, pore size distributions were also measured and plotted in Fig. 6.2. It can be observed that compared to Elorit, the pore volume slightly decreased and did not vary evidently with different preparation methods when the sulfur content is 10 wt%, which agreed with the surface area in Table 6.1.

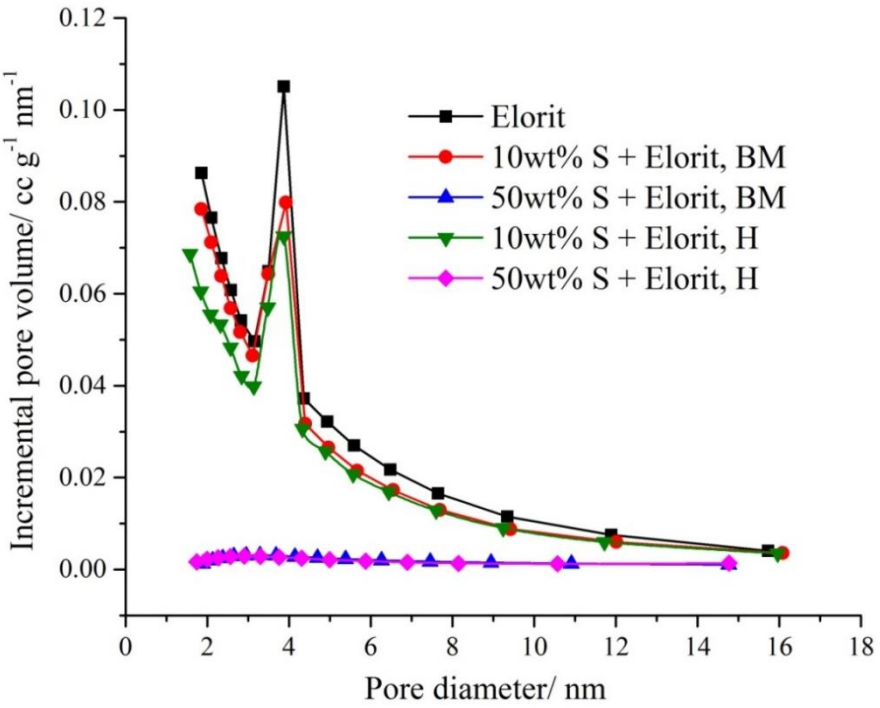

Figure 6.2 BJH pore size distributions of S/Elorit composite (pore volume was calculated from the mass of carbon) with different sulfur content and prepared by different methods.

In addition, it can be seen from Fig. 6.2 that the decrease in the pore volume is mainly contributed by the pores with diameter under 5 nm for the composite prepared with heating method. In contrast, the pore volume decrease for the

composite prepared with ball milling is contributed by pores larger than 5 nm. This might be attributed to that the melted sulfur has access and tendency to fill the relatively smaller pores, which agrees with the results with carbon blacks. As the sulfur loading increases to 50 wt%, neither composite shows available pore spaces. Since the results of carbon blacks showed that ball milling only led to the coverage of exterior surface area, it can be inferred that most of the pores that contributing to the surface area of Elorit were located at the exterior parts of the carbon particles. This can be explained by the preparation method for activated carbons are commonly through steam[19], acid[20], base[21] and other chemical[22,23] etching, which mainly create pores on the surface.

Table 6.2 Surface areas of carbon in S/CA1 composites with different S contents and preparation methods.

Sulfur weight percent	Preparation method	Specific surface area (m^2 g^{-1})
0	N/A	1060.8
10	Ball milling	917.9
50	Ball milling	134.9
10	Heating	784.7
50	Heating	87.6

Shown in Table 6.2, similar to the results from S/Elorit composites, the specific surface area of CA1 decreased as sulfur content increased. When the sulfur content is 10 wt%, heating method results in a smaller specific surface area of carbon, however this difference is not reflected in the pore size distribution in Fig. 6.3, in which two curves representing different methods show no distinctive difference. This might be due to two reasons: 1. as stated in Chapter 5, the pore size distribution figure does not accurately reflect the total pore volume or surface area of materials; 2. the inaccuracy of BJH model in the measurement of micropores, hence the difference is not shown in the pore size distribution diagram.

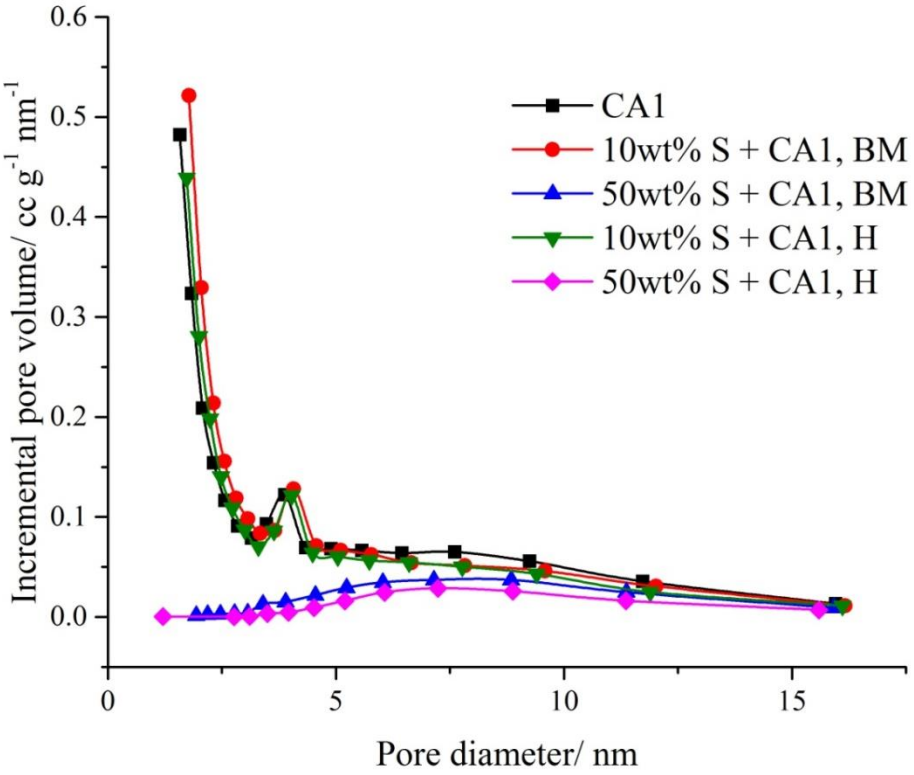

Figure 6.3 BJH pore size distributions of S/CA1 composite (pore volume was calculated from the mass of carbon) with different sulfur content and prepared by different methods.

From Fig. 6.3, it can be seen that at the sulfur loading of 50 wt%, most pores that smaller than 5 nm were blocked. Different from Elorit, CA1 retained some of its pore volume at larger pore size. This can further prove that the sulfur has the tendency to infiltrate the smaller pores first. It can be also noted that the ball milled composite had almost twice of the surface area and higher pore volume than the heated one. This difference might be due to that heating method can enhance the insertion of sulfur into larger pores.

In order to have a quantitative study about how the pore volume varies with the sulfur content, the total specific pore volume of Elorit was also obtained from the measurement. As shown in Fig. 6.4, the specific pore volume of carbon with different sulfur content was plotted. Similar to acetylene black, the data points exhibited good linearity, indicating the amount of sulfur inserting into pores was constant. After linear fit, the gradient of the curve was calculated as -0.513 ml/g, which could be understood as each gram of sulfur will occupy 0.513 ml pore volume. This value is higher than the specific volume of sulfur calculated in Chapter 5 (0.483 ml g^{-1}). This might be due to the fact that some very small pores could not be accessed by sulfur. Therefore, it can be deduced that when heated with Elorit, most of the sulfur (if not all) will impregnate in the porous structure.

This might be attributed to that the pores for activated carbon are mostly distributed on the particle surfaces, which are more accessible for melted sulfur.

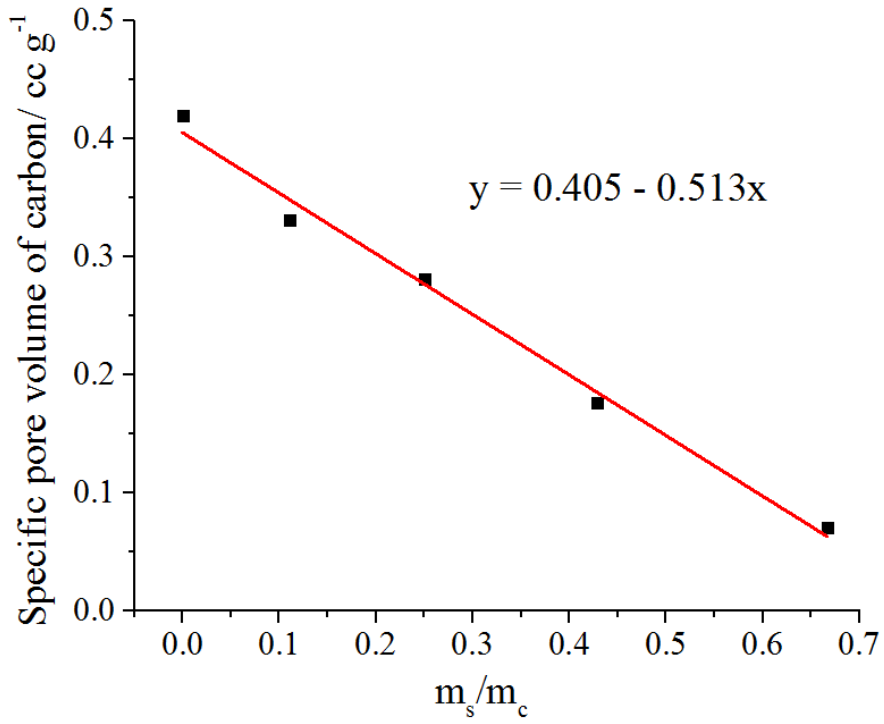

Figure 6.4 Specific total pore volume of carbon with different mass ratios of sulfur to Elorit in the S/C composites prepared via heating method.

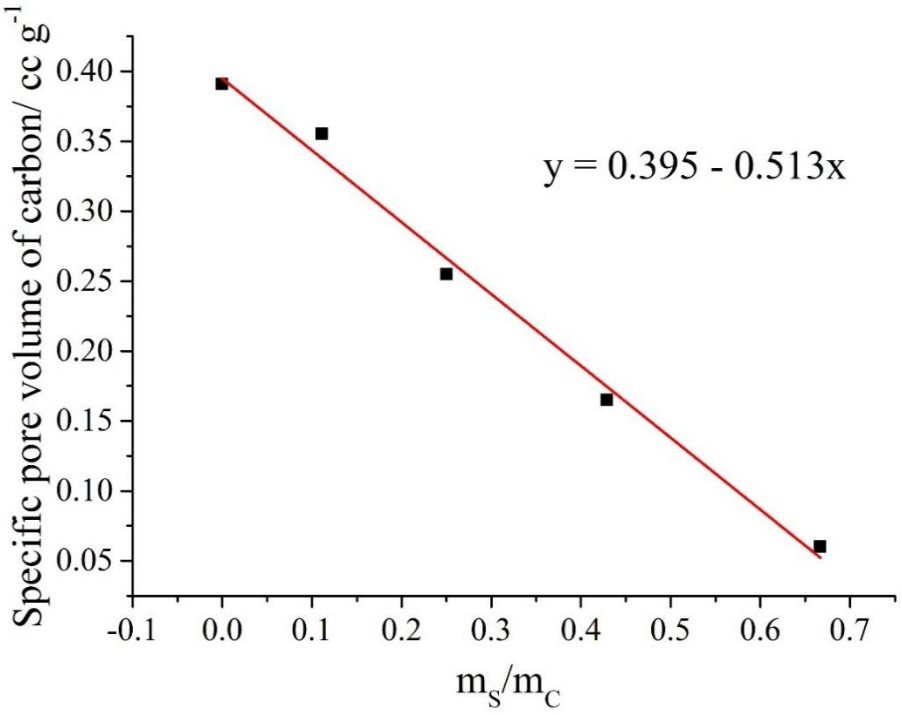

Figure 6.5 Specific total pore volume of carbon with different mass ratios of sulfur to Elorit in the S/C composites prepared via ball milling method.

As shown in Fig. 6.5, same experiments were performed with ball milled S/Elorit composites. Different from the results obtained in Chapter 5, the values of total pore volume show very little difference between two different preparation methods. This also suggests that the surface area properties of S/Elorit composites were not affected by the means of preparation. In addition, this result further proves that the pores in activated carbon are located on the surfaces of carbon particles. However, electrochemical tests are required in order to determine whether preparation methods will have effects on the properties of S/C composites.

6.3.1.2 XRD Analysis

XRD characterization was performed on the S/Elorit composites with sulfur content of 50 wt%. As it is shown in Fig. 6.6, compared to the XRD pattern of carbon blacks, Elorit exhibits a much broader diffraction band where 2θ is between 20 and 35°.

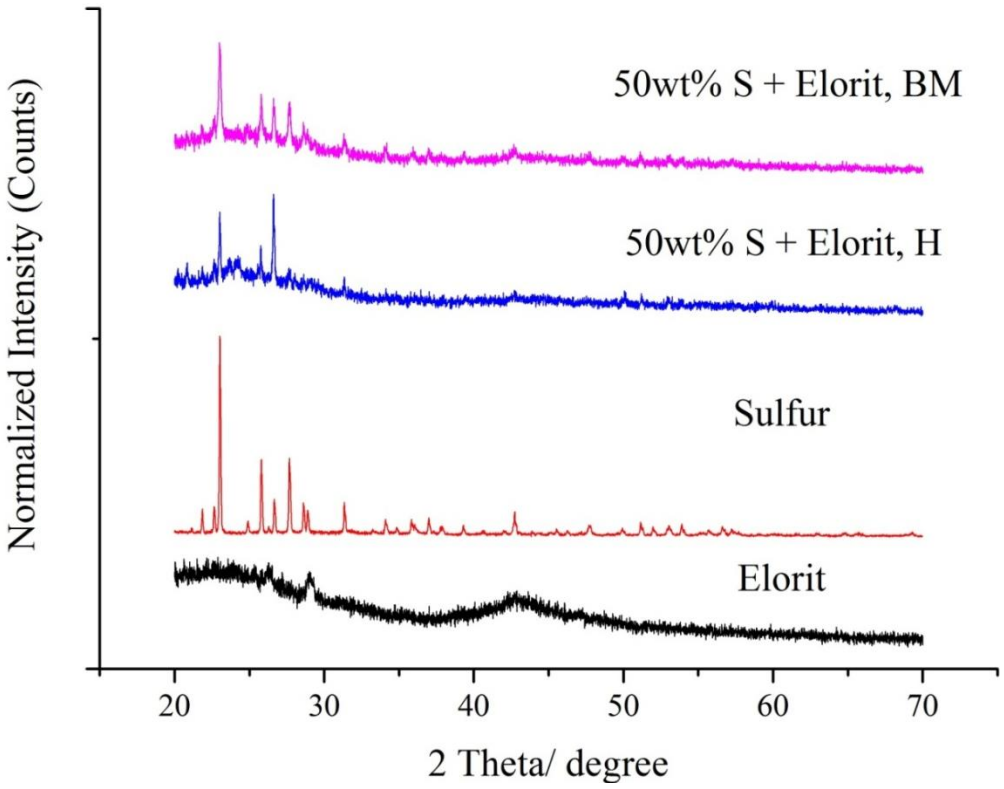

Figure 6.6 XRD patterns of Elorit, sulfur and sulfur/carbon composites prepared from ball milling (BM) and heating (H) method. The intensities were normalized to similar magnitude.

Similar to the results from carbon black, the diffraction data of ball milled sample showed a carbon back ground and retained most of the sulfur peaks with reduced intensity, indicating the surface of carbon particles was covered by

sulfur. However, the heated composites exhibited noticeably smaller carbon diffraction background than the S/carbon black composites. This result suggests that even after heating treatment a large portion of sulfur was still on the surface of carbon, which further supported the deduction made from BET and BJH results that most pores of activated carbon was distributed on the exterior part of the particles.

Moreover, from the peak height ratio, it can be observed that sulfur peak heights (especially for the peaks between 25 and 40°) are different between the ball milled sample and the heated one. Therefore, same conclusion as in Chapter 5 can be drawn that after the heating with porous carbon, the crystalline structure of sulfur was changed in the presence of porous structures.

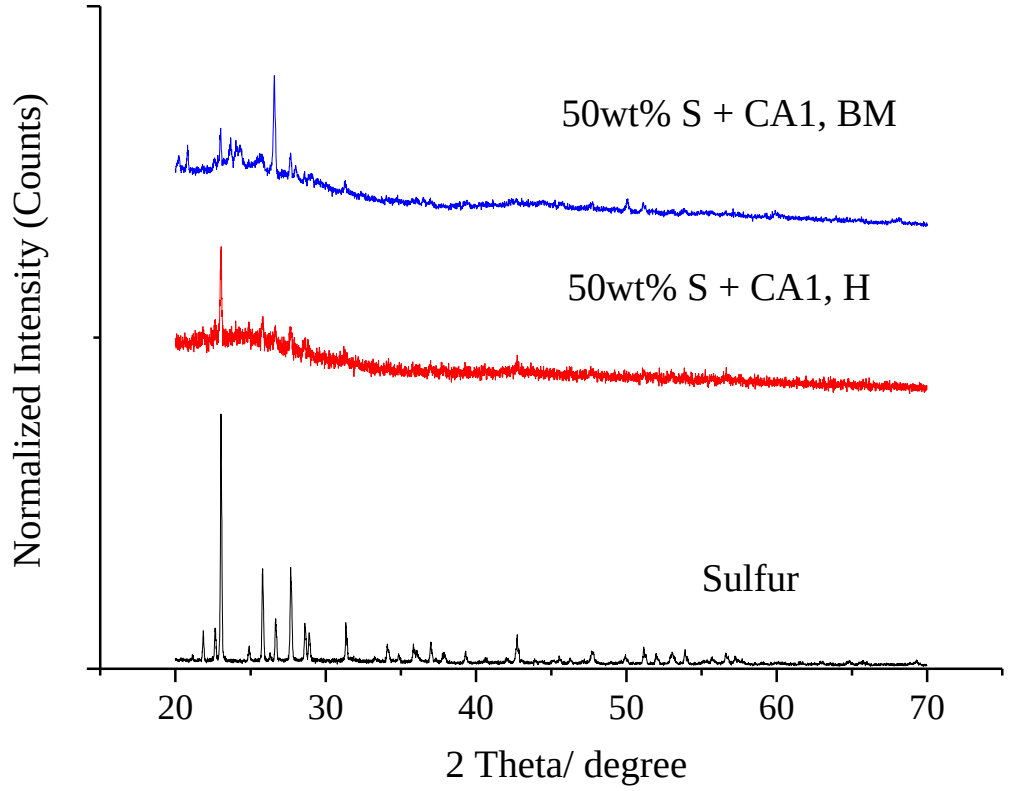

Figure 6.7 XRD patterns of sulfur and S/CA1 composites prepared in different methods with 50 wt% sulfur content prepared from ball milling (BM) and heating (H) method.

In Fig. 6.7, the XRD patterns of CA1 show that the sulfur peaks intensities were reduced for both S/C composites and the peak positions and ratios were also signifcantly changed. It might be due to that the sulfur might have reacted with the acidic functional groups on CA1, however, further study is required to prove this assumption.

6.3.2 Electrochemical Tests

6.3.2.1 Cyclic Voltammetry Tests

Cyclic voltammetry was used to characterise the S/Elorit composites. Two expected main reduction peaks and two oxidation peaks can be observed in the voltammograms from Fig. 6.8.

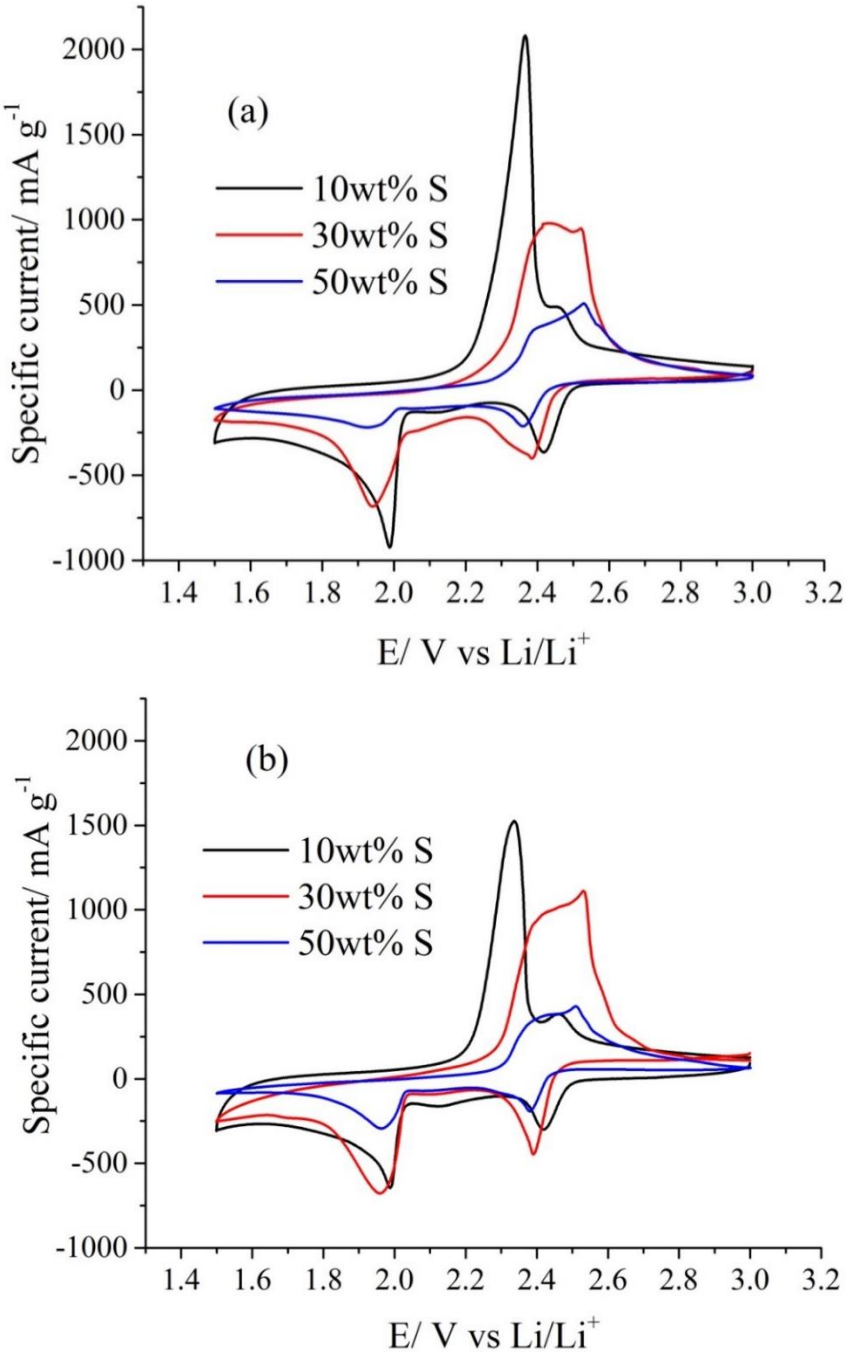

Figure 6.8 Cyclic voltammograms of S/Elorit composites in different S/C ratio prepared by ball milling (a) and Heating (b). Mass of sulfur in the electrode was used to calculate the specific current. The scan rate was 100 μV s^{-1}.

For different sulfur contents, the peak height and positions changed in similar trend as the sulfur/acetylene black composites – peak current decreased and larger overpotentials were obtained. The main difference is that when the sulfur loading is 10 wt%, the ball milled sample shows a much higher peak current compared to the heated one. This might be due to the higher surface area available within the sample.

6.3.2.2 Galvanostatic Cycling Tests

Table 6.3 Discharge capacities in the first cycle and the 50th cycle of sulfur/Elorit composites with different sulfur contents and preparation methods.

Sulfur %	Preparation method	1st capacity/mA h g^{-1}	50th capacity/ mA h g^{-1}	Retention
10 wt%	Ball milling	1413	423	29.9 %
10 wt%	Heating	1212	349	28.8 %
30 wt%	Ball milling	768	299	29.8 %
30 wt%	Heating	1152	373	32.4 %
50 wt%	Ball milling	400	174	43.5 %
50 wt%	Heating	573	229	40.0 %

Galvanostatic cycling tests were also performed on Li-S cells using Elorit as the conductive material. From Table 6.3, it can be seen that as the sulfur loading increases, the initial capacities decrease and the capacity retentions increase, which agree with the results where acetylene blacks are used as conductive materials. However, in this case, preparation methods had different effects on the cycling performance.

Ball milling method provides higher capacity compared to heating method when the sulfur content is 10 wt%, but when the sulfur loadings increase to 30 wt% and 50 wt%, S/Elorit composites prepared from heating achieved higher capacities.

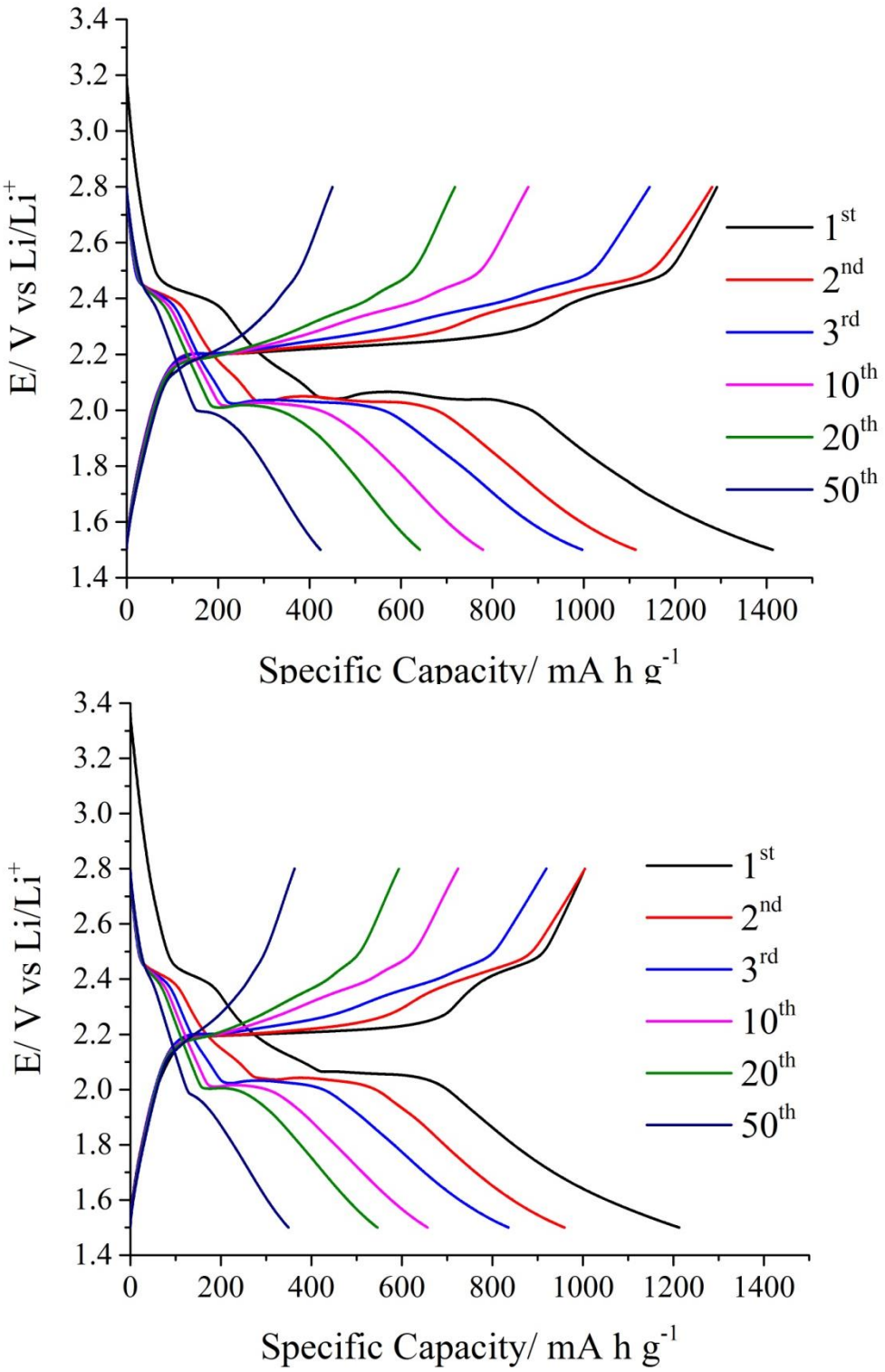

Figure 6.9 Discharge/charge voltage profiles of S/Elorit composites with 10 wt% sulfur prepared from ball milling (upper) and heating (lower) method. The C-rate was 0.1 C.

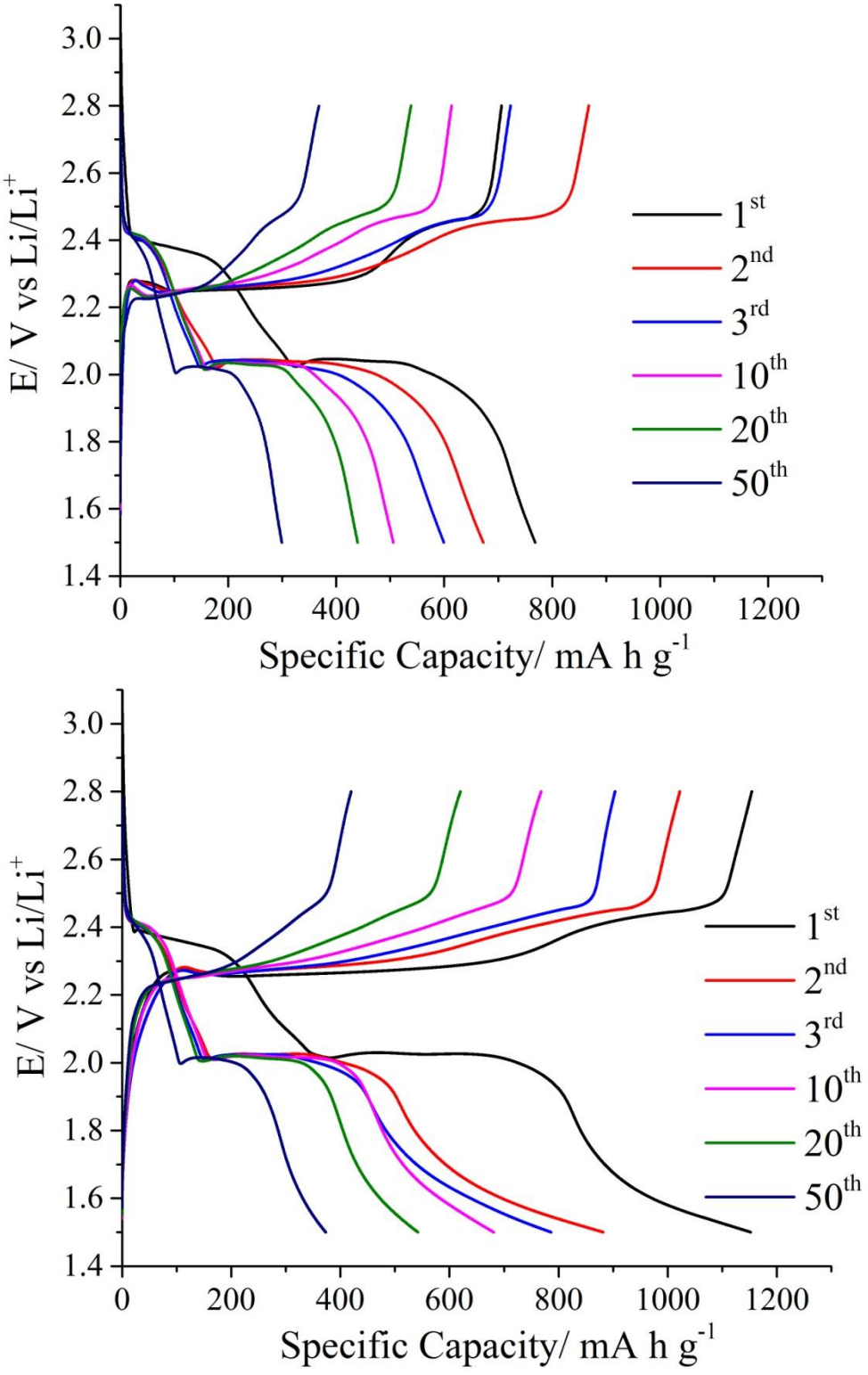

Figure 6.10 Discharge/charge voltage profiles of S/Elorit composites with 30 wt% sulfur prepared from ball milling (upper) and heating (lower) method. The C-rate was 0.1 C.

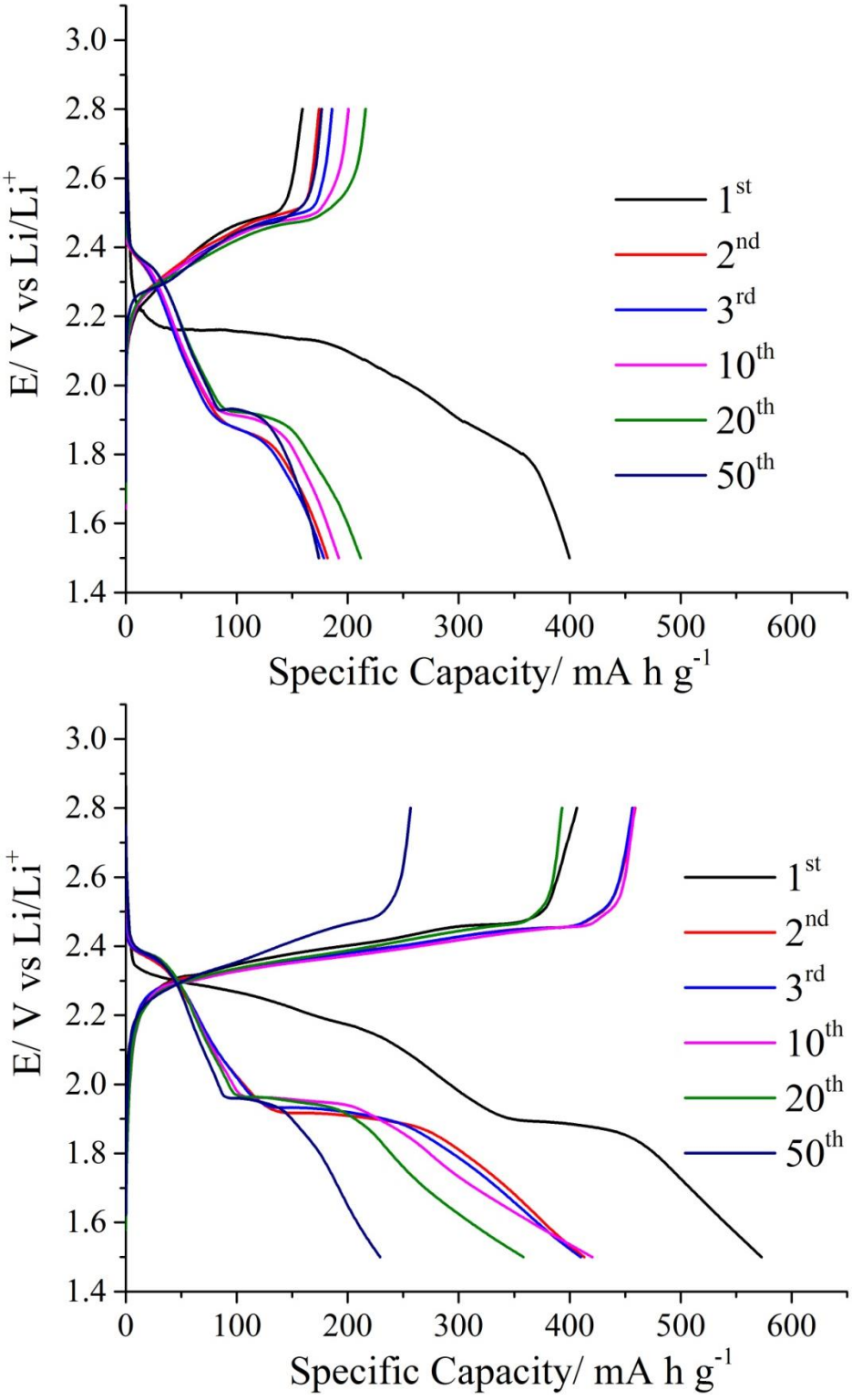

Figure 6.11 Discharge/charge voltage profiles of S/Elorit composites with 50 wt% sulfur prepared from ball milling (upper) and heating (lower) method. The C-rate was 0.1 C.

The discharge/charge profiles of Li-S cells using Elorit as conductive materials were plotted in Fig. 6.9-6.11. Similar to S/AB, when the sulfur content was 10 wt%, tailings can be observed at the end of the discharge/charge plateaus. In addition to that, at the beginning of the initial discharge, a slope also appeared before the first discharge plateau, contributing to a capacity of approximately 50 mA h g^{-1}. By comparing this slope to the discharge curve of carbon electrode without any sulfur (shown in Fig. 6.11), it can be seen that two curves almost overlapped before the first discharge plateau appeared. Therefore, it can be concluded that this slope was due to the discharge of double layer on the carbon electrode surface.

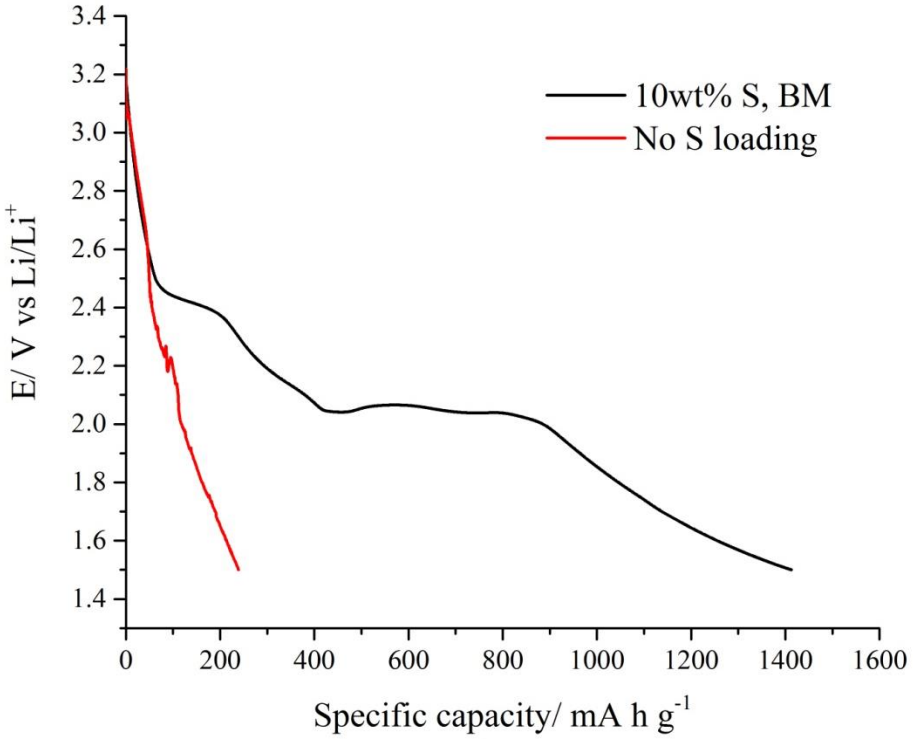

Figure 6.12 Discharge voltage curves of S/Elorit electrode and Elorit electrode without sulfur. 10 wt% of PTFE was added in the electrode to substitute the mass of sulfur and the specific capacity was calculated based on the mass of the extra PTFE added. The C-rate was 0.1 C.

The effect of sulfur loading on the electrochemical performance is similar to that observed in the experiments of S/AB composites in Chapter 5. The capacities from the second discharge plateaus decreased significantly with the increase of sulfur content while the first discharge plateaus almost remained the same. In addition, it can be seen heating methods provided longer second discharge plateaus.

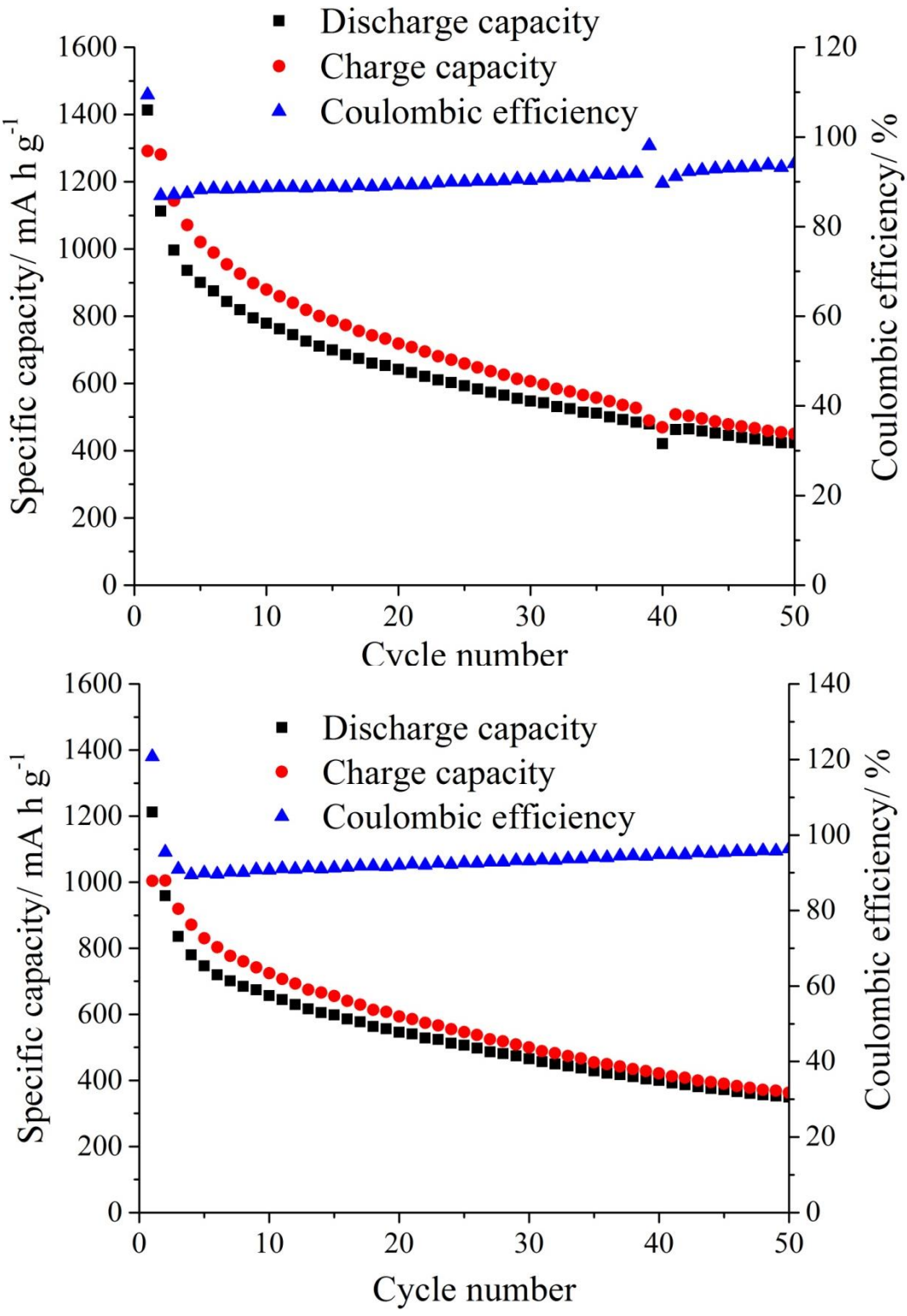

Figure 6.13 Capacities and Coulombic efficiencies of S/Elorit composites with 10 wt% sulfur prepared from ball milling (upper) and heating (lower) method. The C-rate was 0.1 C.

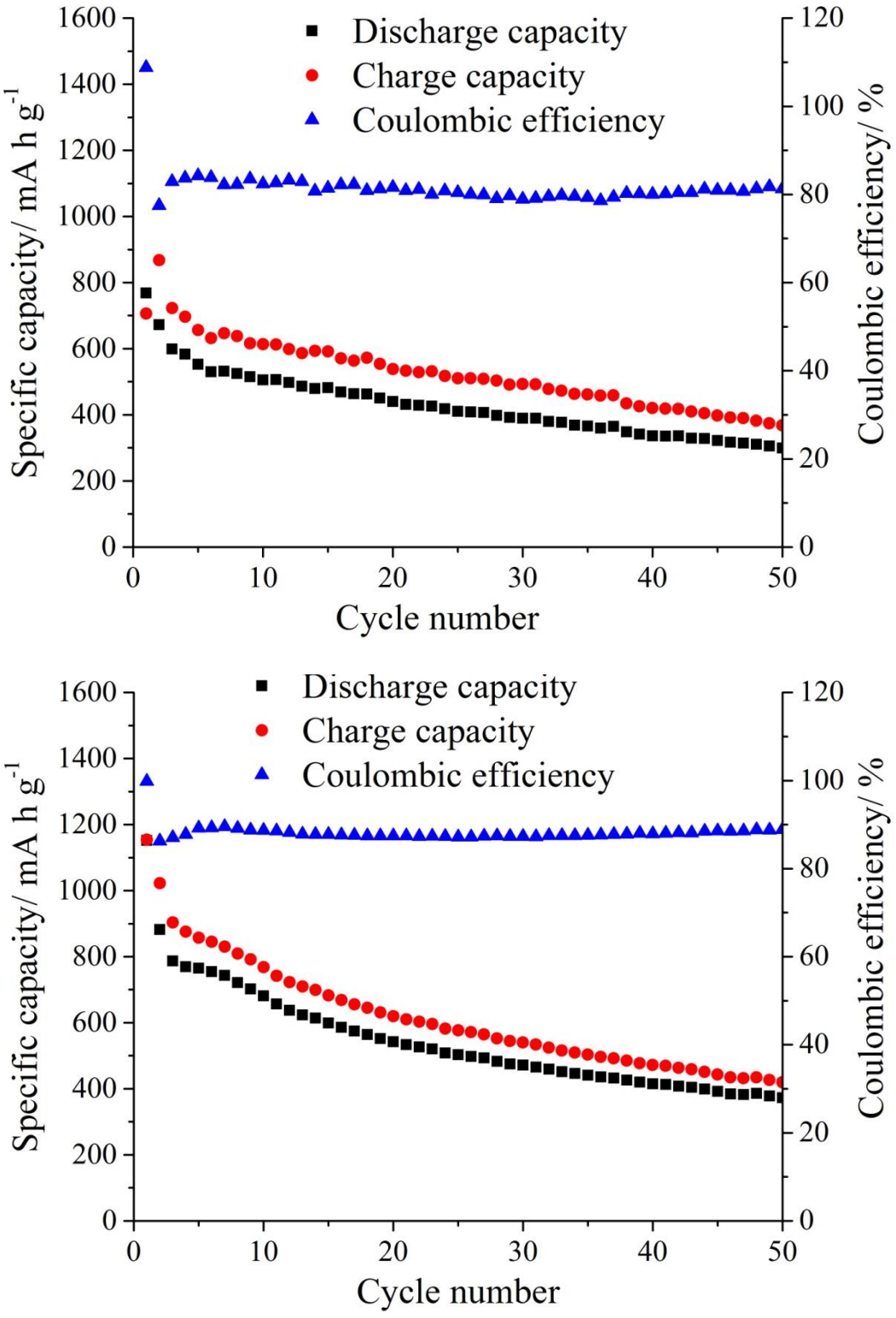

Figure 6.14 Capacities and Coulombic efficiencies of S/Elorit composites with 30 wt% sulfur prepared from ball milling (upper) and heating (lower) method. The C-rate was 0.1 C.

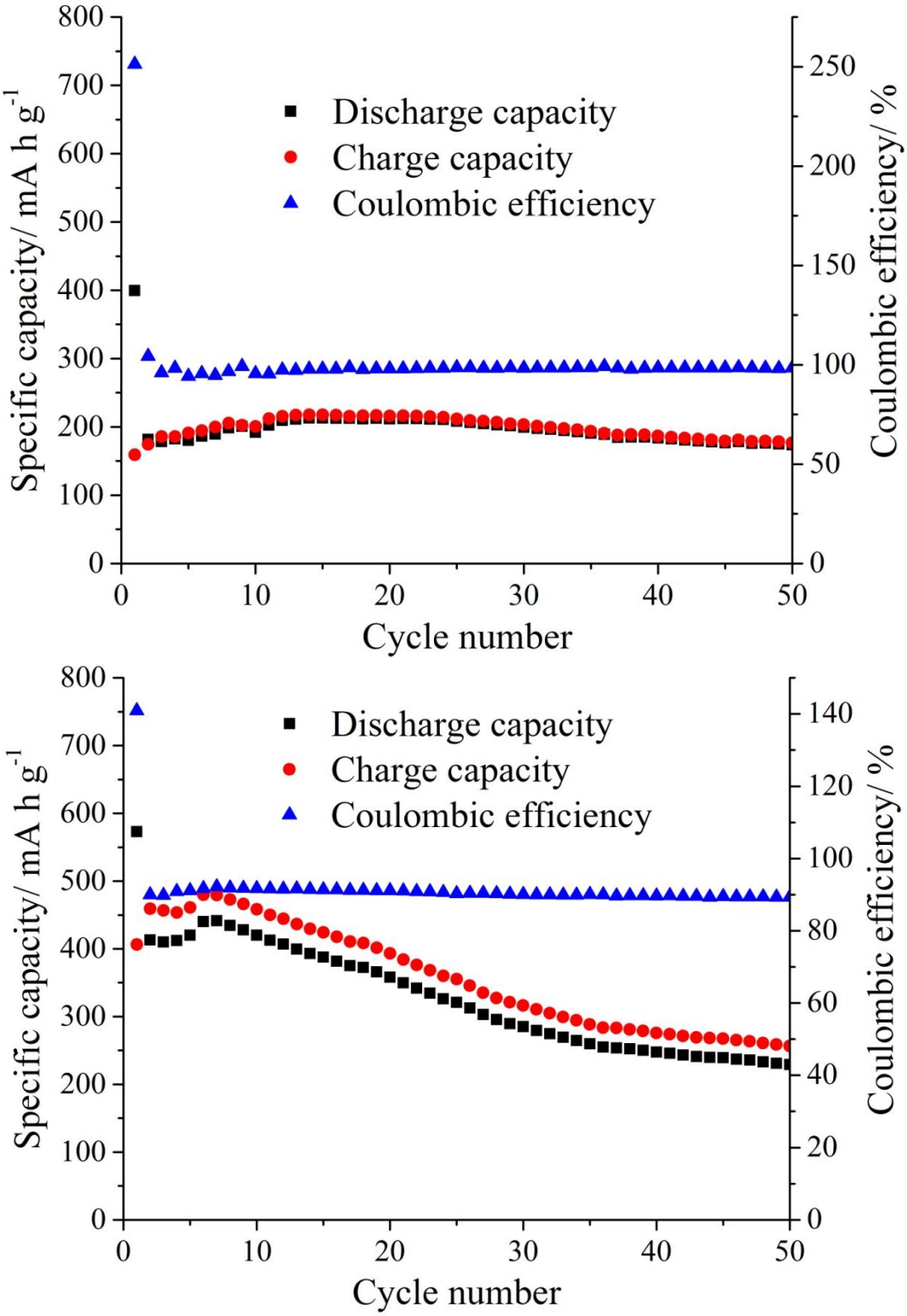

Figure 6.15 Capacities and Coulombic efficiencies of S/Elorit composites with 50 wt% sulfur prepared from ball milling (upper) and heating (lower) method. The C-rate was 0.1 C.

The Coulombic efficiencies and specific capacities against cycle numbers were also plotted in Fig. 6.13-6.15. Generally speaking, the values of Coulombic efficiency are stabilized after the 5th cycle. Different from S/AB composites, when the sulfur loading was 10 wt%, the Coulombic efficiencies of the cells were much higher, suggesting less severe shuttle effects. As a result, after the 50th cycle, they achieved the highest specific capacity per mass of sulfur. It was likely that the highly (micro) porous structure was better at retaining polysulfide at low concentrations.

In addition, the heating method exhibited higher Coulombic efficiencies when sulfur content was below 50 wt%. This might be due to the better loading of sulfur in carbon's porous structure. Similar to the results in Chapter 5, when the sulfur loading was 50 wt%, very small amount of capacity was obtained from the first charge sequence which might be due to the formation of passivation layer. Therefore the Coulombic efficiency of the first cycle was much higher than 100 %.

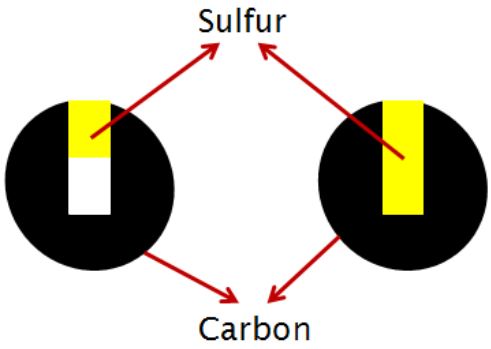

Figure 6.16 Suggested schematic diagram of how sulfur is impregnated into carbon's porous structure: by ball milling (left) and by heating (right).

When the sulfur content was 50 wt%, an opposite result was obtained: compared to ball milling, heating method provided much higher capacity over 50 cycles. Although there was no distinct difference between two composites in their surface analysis, the contacts between sulfur and carbon in two composites might be significantly different. In a microporous structure, the blockage of the pores can be either of the two scenarios in Fig. 6.16. In one case, the melted sulfur inserted and fully occupied the pores; in the other case, the sulfur only blocked the entrance of the pores. However, this difference in the sulfur insertion could not be observed using nitrogen absorption method because in both samples the pores were blocked by the sulfur and become unavailable for nitrogen adsorbates. This might be the reason why different preparation methods result in similar results in the total pore volume as it is shown in Fig. 6.5.

If the sulfur is only blocking the entrance of the pores, the contact between sulfur (polysulfide) and carbon might be poorer compared to the sample in which sulfur had a full contact with carbon.

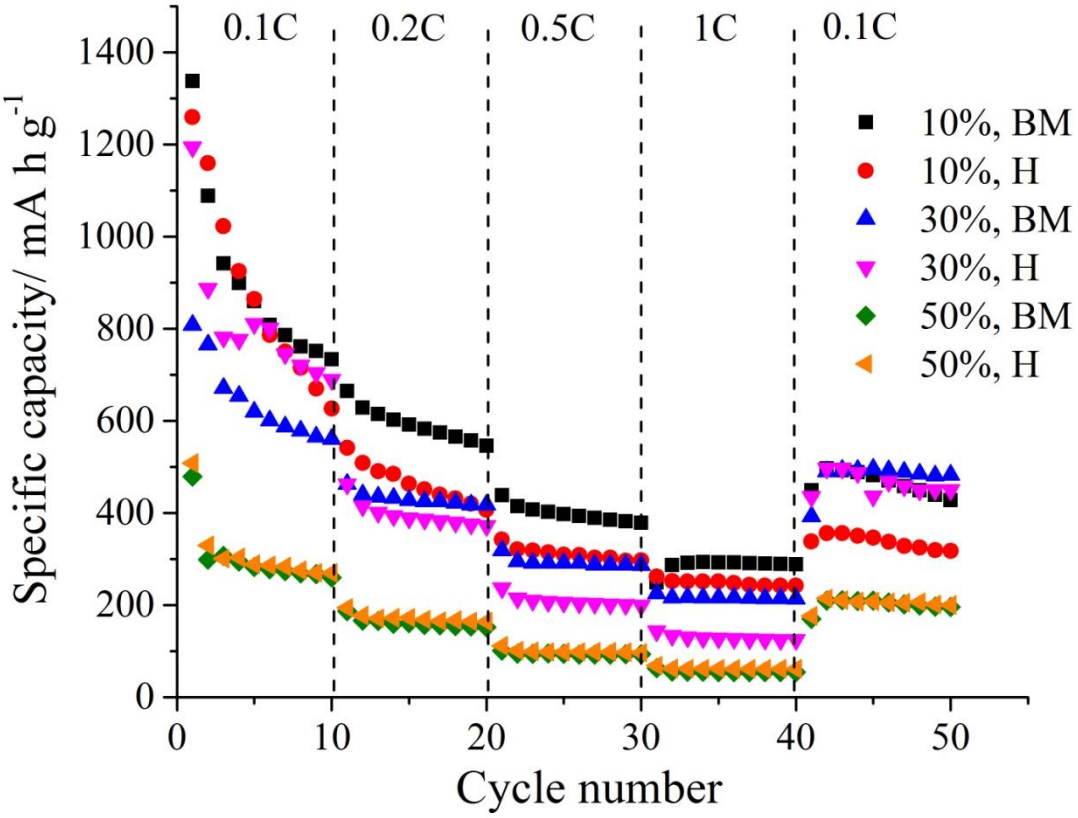

Figure 6.17 Rate performances of Li-S batteries of different sulfur contents and different S/Elorit composites preparation methods.

As shown in Fig. 6.17, the capacities of Li-S cells were measured under different C-rates (0.1 C, 0.2 C, 0.5 C, 1 C and 0.1 C), each rate lasted 10 cycles. After higher C-rate cycling, the capacities were retained to the similar values according to the trend from the first 10 cycles, showing that cycling under high C-rate did not cause irreversible damage to the cells. It can be seen that when the sulfur loading was 10 wt% and 30 wt%, positive material prepared from ball milling method achieved higher capacity retention with the increase of C-rate. The higher surface areas of ball milled S/C composites allowed more polysulfide species to be reduced in a shorter amount of time and larger pore volumes allowed better diffusion of polysulfides.

6.4 Summary

In this chapter, sulfur/activated carbon composites were prepared and characterized as the positive electrode materials of Li-S batteries.

From the surface area and pore size analysis, it can be learned that the pore sizes of activated carbons are mainly distributed at microporous range. In addition, the heating and ball milling methods show no distinctive difference in the specific surface areas and the XRD patterns, which could be due to the fact that the pore structures were mainly created on the surface of carbon particles during the activation process. The values of pore volumes also show that by heating sulfur and Elorit together, most of sulfur was incorporated into the pores of carbon. This result is different from the result obtained from Chapter 5, in which sulfur only insert into carbon pores by heating.

As for the electrochemical behaviour, the capacities of the S/Elorit composites decrease significantly with the increase of the sulfur content. This might be also due to the fact that the mass transfer is difficult in microporous carbon. At high (50 wt%) sulfur content, the heating method achieved higher capacity, which could be explained by the better impregnation of sulfur in the pores. By comparing the cycling performance with S/activated carbon and the results of S/carbon black composites in Chapter 5, the S/carbon black composites provide better capacity at higher sulfur content and S/activated carbon composites show better capacity at lower sulfur content.

6.5 Reference

1 D. Mohan and C. U. Pittman Jr., *J. Hazard. Mater.*, 2006, **137**, 762–811.

2 C. Namasivayam and D. Kavitha, *Dye. Pigment.*, 2002, **54**, 47–58.

3 E. S. Hertzog and S. J. Broderick, *Ind. Eng. Chem.*, 1941, **33**, 1192–1198.

4 E. W. Harris, *Ind. Eng. Chem.*, 1942, **34**, 1057–1060.

5 N. P. Wickramaratne and M. Jaroniec, *ACS Appl. Mater. Interfaces*, 2013, **5**, 1849–1855.

6 R. J. Abumaizar, W. Kocher and E. H. Smith, *J. Hazard. Mater.*, 1998, **60**, 111–126.

7 S. Sircar, T. C. Golden and M. B. Rao, *Carbon N. Y.*, 1996, **34**, 1–12.

8 M. T. Stone and M. Kozlov, *Langmuir*, 2014, **30**, 11846–11846.

9 K. Kohler, R. G. Heidenreich, J. G. E. Krauter and M. Pietsch, *Chem. Eur. J.*, 2002, **8**, 622–631.

10 J. Matos, J. Laine and J. M. Herrmann, *Appl. Catal. B-Environmental*, 1998, **18**, 281–291.

11 Z. Fan, J. Yan, T. Wei, L. Zhi, G. Ning, T. Li and F. Wei, *Adv. Funct. Mater.*, 2011, **21**, 2366–2375.

12 D. Y. Qu and H. Shi, *J. Power Sources*, 1998, **74**, 99–107.

13 M. A. de la Casa-Lillo, F. Lamari-Darkrim, D. Cazorla-Amoros and A. Linares-Solano, *J. Phys. Chem. B*, 2002, **106**, 10930–10934.

14 T. Brousse, M. Toupin and D. Belanger, *J. Electrochem. Soc.*, 2004, **151**, A614–A622.

15 D. Hulicova-Jurcakova, M. Seredych, G. Q. Lu and T. J. Bandosz, *Adv. Funct. Mater.*, 2009, **19**, 438–447.

16 J. Gamby, P. L. Taberna, P. Simon, J. F. Fauvarque and M. Chesneau, *J. Power Sources*, 2001, **101**, 109–116.

17 K. Kinoshita, *Carbon, Electrochemical and Physicochemical Properties*, John Wiley & Sons, Inc., 1988.

18 D. Zhao, Y. Wan and W. Zhou, *Ordered Mesoporous Materials*, Wiley-VCH, Singapore, 2013.

19 F. Rodríguez-Reinoso, M. Molina-Sabio and M. T. González, *Carbon N. Y.*, 1995, **33**, 15–23.

20 J. LAINE, A. CALAFAT and M. LABADY, *Carbon N. Y.*, 1989, **27**, 191–195.

21 M. A. Lillo-Ródenas, D. Lozano-Castelló, D. Cazorla-Amorós and A. Linares-Solano, *Carbon N. Y.*, 2001, **39**, 751–759.

22 J. Hayashi, A. Kazehaya, K. Muroyama and A. P. Watkinson, *Carbon N. Y.*, 2000, **38**, 1873–1878.

23 F. Caturla, M. Molina-Sabio and F. Rodríguez-Reinoso, *Carbon N. Y.*, 1991, **29**, 999–1007.

Chapter 7: Other Modifications to Li-S Batteries

7.1 The Effect of $LiNO_3$

7.1.1 Introduction

It has been reported that $LiNO_3$ salt was used as an electrolyte additive in the Li-S battery system to suppress the shuttle mechanism.[1-5] The results showed that with addition of $LiNO_3$, a stable SEI layer could be formed on the surface of lithium metal negative electrode (shown in Fig 7.1) so the continuous reduction reaction on the lithium electrode would be stopped. The characterisation on the electrode surface showed that the composition of the passivation layer were mainly Li_2S, Li_2S_2, Li_xNO_y and Li_xSO_y[2,5]. As a result, significant cycling efficiency improvements were exhibited after adding $LiNO_3$ to the electrolyte.

Figure 7.1 Illustration of the formation of SEI layer on Li metal in the Li-S battery.

$LiNO_3$ was then further studied in the Li-air battery system as an electrolyte additive[6-8]. It was suggested that a layer of Li_2O would be formed in the presence of $LiNO_3$, which provided protection for the lithium metal electrode. By adding $LiNO_3$ to the electrolyte, improved cycling performance was achieved.

In this section, lithium nitrate salt was dissolved in the electrolyte (1 M LiTFSI in DOL: TEGDME = 1: 1) that used in Chapter 5 and 6 with the concentration of 0.2 M. Other experimental conditions were the same as described in Chapter 5 and 6. The positive electrodes were prepared via ball milling method with 30 wt% sulfur content and acetylene black as conductive material.

7.1.2 Results and Discussion

7.1.2.1 Galvanostatic Cycling Tests

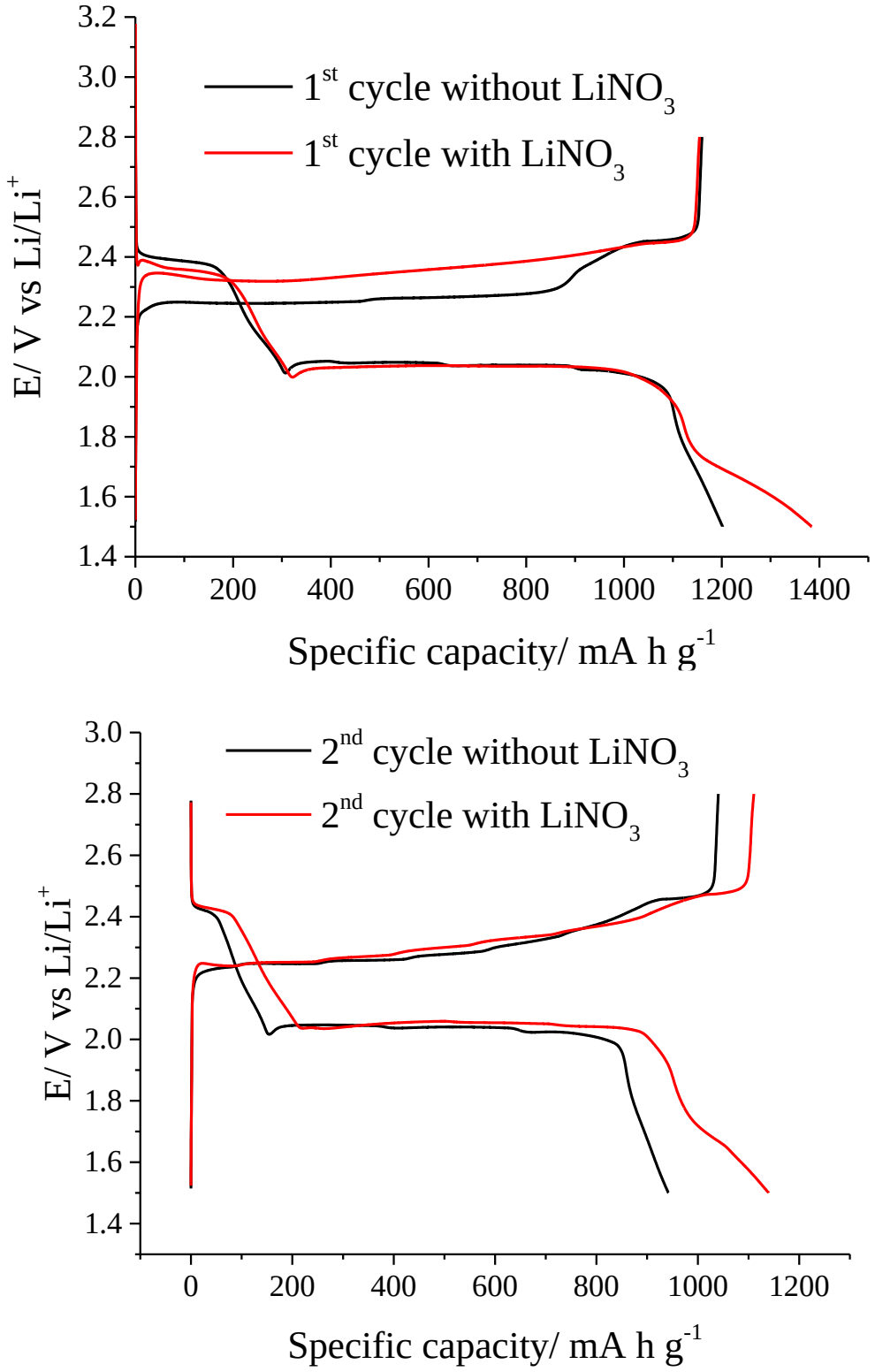

Figure 7.2 Galvanostatic discharge/charge profiles of Li–S cells (positive electrode: 30 wt% S/AB, ball milled) using electrolytes with and without $LiNO_3$ as additive. The C-rate is 0.1 C.

The discharge/charge profiles of Li-S cells with and without $LiNO_3$ are shown in Fig. 7.2. From the profiles of the first cycle, it can be observed that at the end of the discharge, where an additional reduction process occurred around 1.7 V, contributing a capacity of approximately 200 mA h g^{-1}. This reaction might be related to the irreversible reduction of $LiNO_3$ as previously reported.[9] Therefore, a deep discharge might not be suitable for the Li-S battery when $LiNO_3$ is used as the additive.

As for the charging process, it is clear that after adding $LiNO_3$ the potential of charge plateau increased by approximately 0.1 V. This difference might be attributed to the increased internal resistance from the formation of SEI layer or the reduction product of $LiNO_3$.

During the second cycle, it can be seen that the cell with $LiNO_3$ provided a higher discharge capacity. Furthermore, the charge capacity is almost equal to the discharge capacity, suggesting a Coulombic efficiency approximately 100 %. Different from the first cycle, the potential of charge plateau is the same as the cell without $LiNO_3$.

Fig. 7.3 shows the cycling performances of Li-S cells with and without $LiNO_3$ as electrolyte additive. In this experiment, sulfur/acetylene black composite with 30 wt% sulfur content prepared via ball milling method was used as the positive material. It can be seen that the specific capacities were slightly increased by the addition of lithium nitrate. More importantly, it can be seen that the Coulombic efficiency was improved from approximately 85 % to 100 %. This result agreed with the previous results, which attributed the improved Coulombic efficiency to that the formation of SEI layer on Li metal could stop the polysulfide from being reduced by lithium.

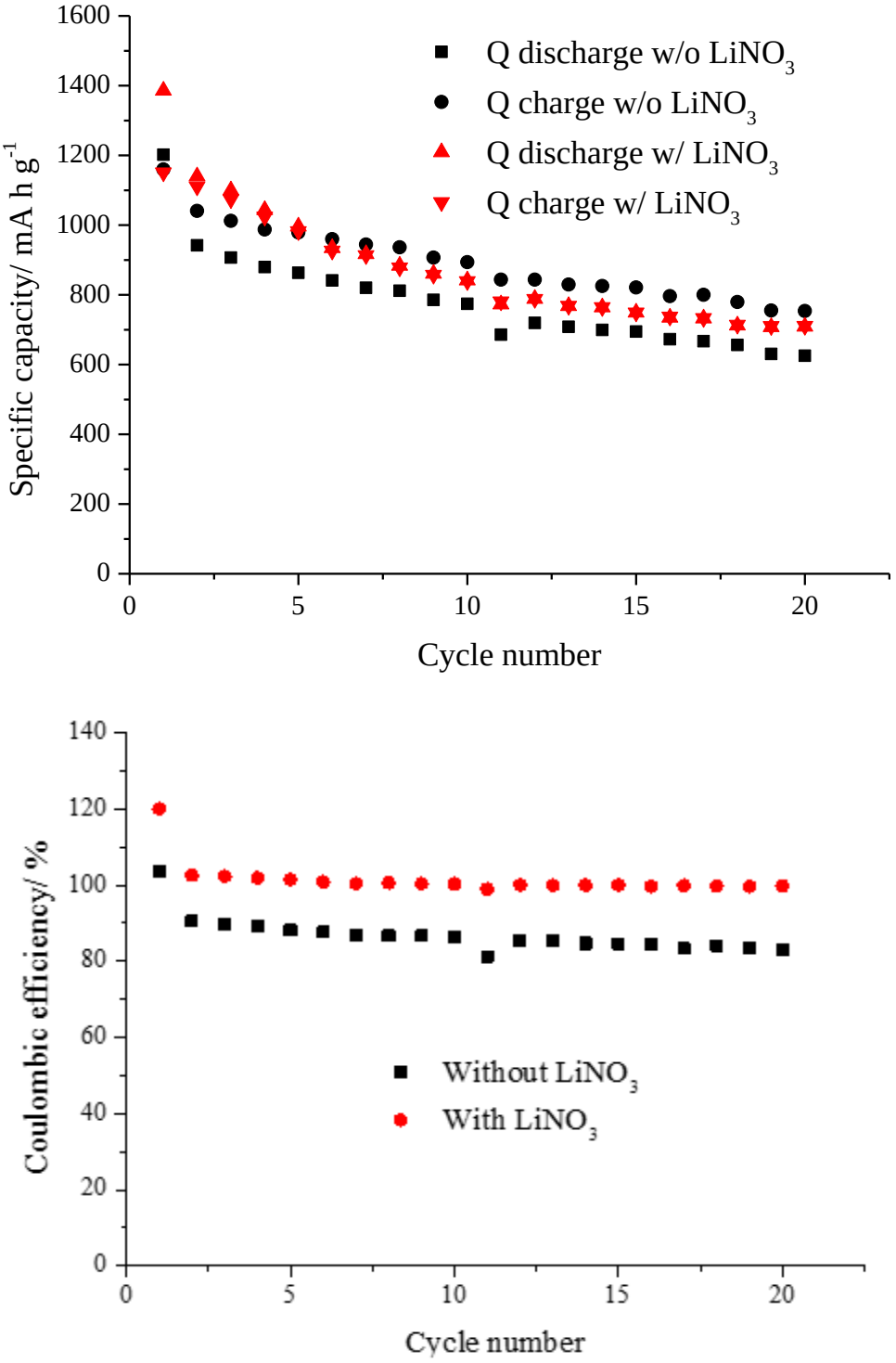

Figure 7.3 Specific discharge/charge capacities and Coulombic efficiencies of Li-S cells with and without adding $LiNO_3$ as electrolyte additive. The C-rate was 0.1 C.

7.1.2.2 Electrochemical Impedance Spectroscopy

To have a better understanding of the effect of the addition of $LiNO_3$, impedance spectrometry was used to characterize the cells before and after

cycling. The frequency range was chosen between 100 mHz and 100 KHz. The impedance spectroscopy was performed on the charged cells. Therefore, before the impedance spectra were recorded, the cells were rested for at least 5 hours until the open circuit potentials were stabilised around 2.4 V. As shown in Fig. 7.4, the Nyquist impedance spectra of cells with and without lithium nitrate were recorded and compared.

The shape of the spectra before cycling suggested that the system can be described using an equivalent circuit shown in Fig. 2.9. Therefore, the interfacial resistance can be represented by the diameter of the semicircle in the spectra.

From both impedance spectra in Fig. 7.4, it can be seen that the interfacial resistance R_{ct} between the electrolyte and the electrode was much higher before cycling than the resistance after cycling. This could be due to the insulating nature of sulfur. In the absence of lithium nitrate, it can be seen that another semicircle was formed in the impedance spectra after 10 cycles. After 20 cycles, the interfacial resistance became larger. This result suggests that a new electrolyte-electrode interface was formed, which is assumed to be the precipitation of insoluble lithium polysulfides on the lithium electrode.

In the presence of $LiNO_3$ in the electrolyte, it can be seen that the shape of the curve still showed one semicircle after cycling. The interfacial resistance decreased to about 4 ohms after 10 cycles and increased by only 0.5 ohms after 20 cycles. It is likely that the stabilized interfacial resistance was resulted from the formation of the SEI layer. Therefore polysulfides reduction on lithium electrode and the shuttling effect was suppressed.

In addition, from difference in the values of internal resistance between two cells (less than 2 ohms), it can be concluded that the difference in the first charge potential, which requires a resistance of approximately 200 ohms under the applied current, does not result from the formation of an SEI layer.

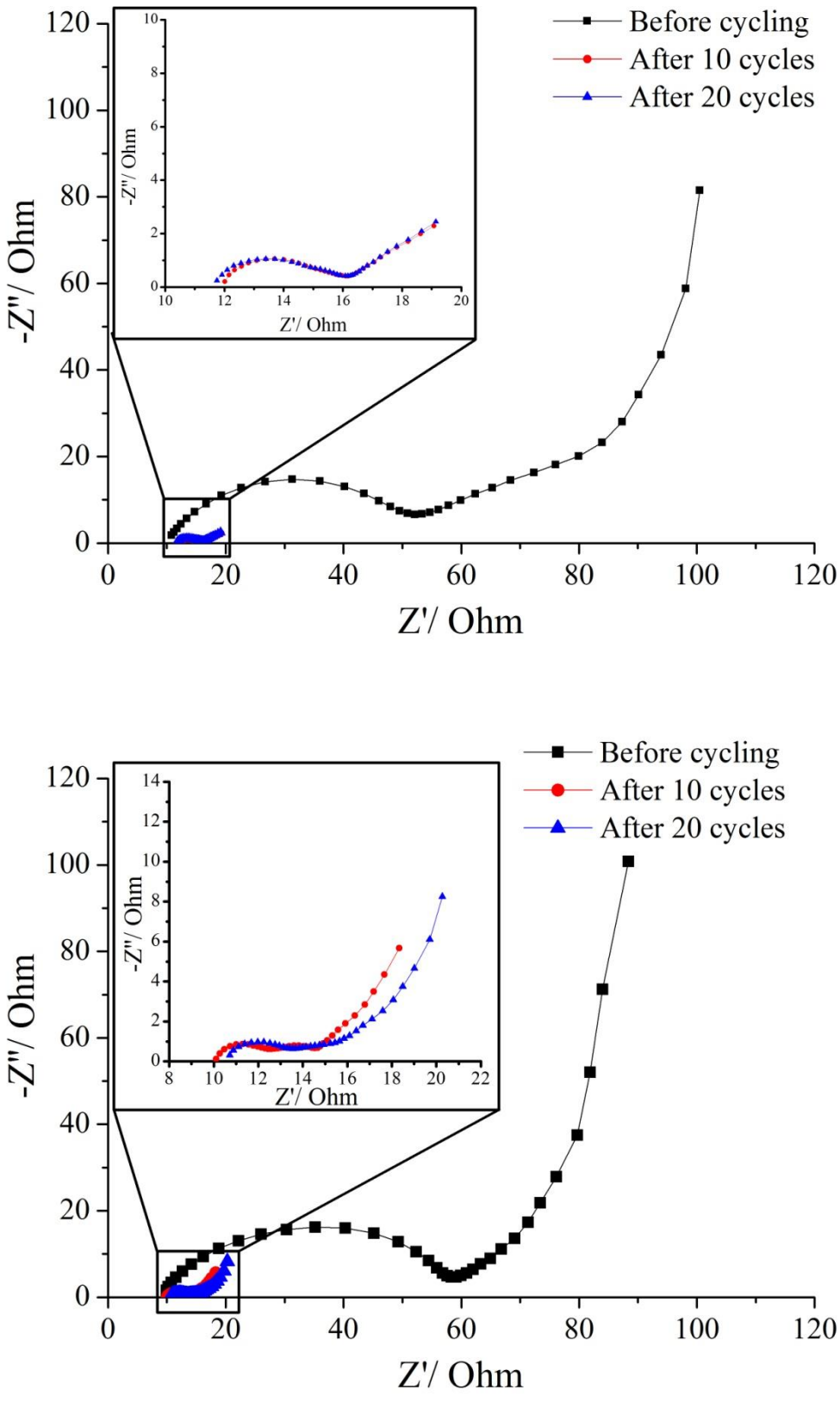

Figure 7.4 Potentiostatic electrochemical impedance spectra of the Li-S with (upper) and without (lower) $LiNO_3$ as electrolyte additive. The frequency range is 0.1 ~ 100 K Hz.

7.2 Using Li-ion Conducting Ceramic Separators

7.2.1 Introduction

In order to fundamentally eliminate the shuttle effect in the Li-S battery systems, solid state electrolyte was introduced as an alternative. One of the main challenges lies in improving the Li-ion conductivity in the solid electrolyte. The emergence of solid electrolyte possessing high Li-ion conductivity[10] (12 mS cm^{-1} at room temperature) had made the realisation of all-solid-state lithium sulfur batteries possible.

Various types of solid electrolyte have been proposed. One of the choices is polyethylene oxide (PEO) loaded with nanoparticles such as ZrO_2[11] and $LiAlO_2$[12]. Other types of solid-state electrode like Li_2S-SiS_2[13], thio-LISICON[14] and Li_2S-P_2S_5 ceramics[15,16] were also investigated as potential candidates.

Instead of using solid-state electrolyte, Li-ion conducting materials can be also used as an additional separator in the lithium sulfur battery to stop the diffusion of lithium polysulfide to the negative electrode (shown in Fig. 7.5). Previously, Li-ion conducting ceramics (Ohara) have been used as solid electrolytes in both Li-ion batteries[17,18] and fuel cells[19].

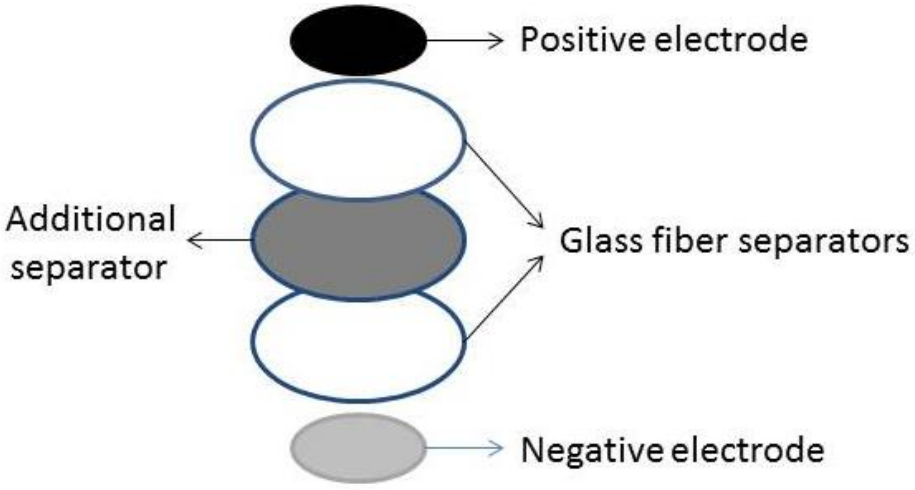

Figure 7.5 Schematic diagram of Li-S cell with an additional separator

In this section, lithium-ion conducting glass-ceramic (Ohara, 1 inch, round) was chosen as the additional separator. As a result, glass fibre separators with 25 mm diameter and larger Swagelok cells were used.

7.2.2 Results and Discussion

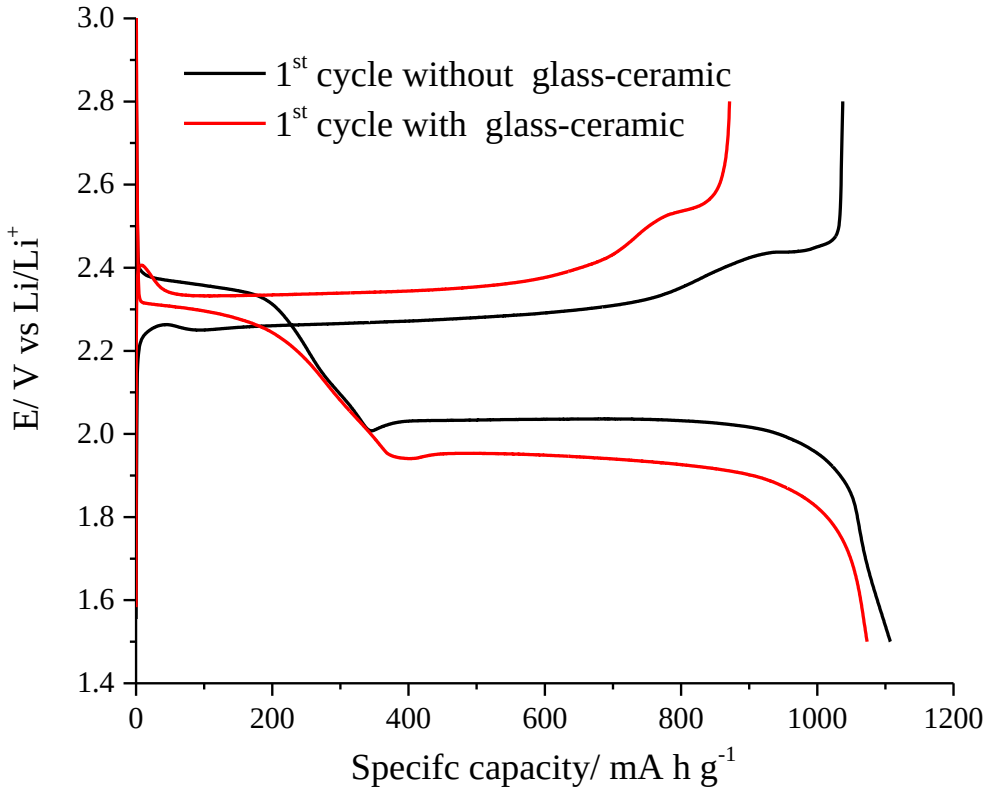

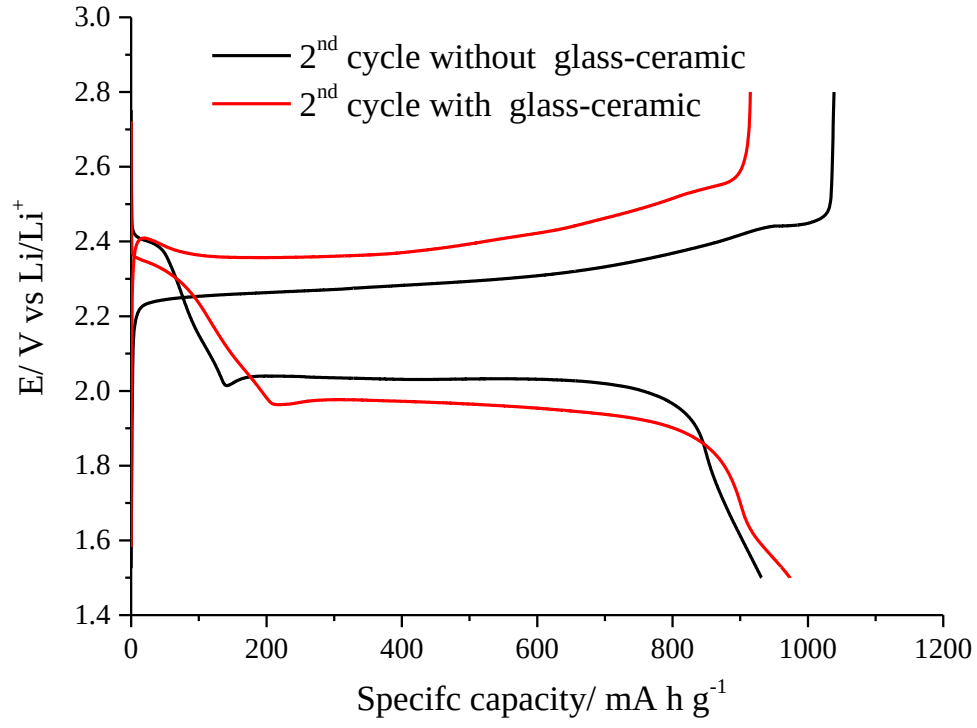

Figure 7.6 Galvanostatic discharge/charge profiles of Li–S cells (positive electrode: 30 wt% S/AB, ball milled) with and without glass-ceramic. Discharge rate is 0.1 C.

The first discharge/charge profiles of the Li-S cells with and without conducting glass-ceramic are plotted in Fig. 7.6. From the discharge/charge profiles, it can be seen that the cell with glass-ceramic exhibits lower discharge potential and higher charge potential with the value of approximately 0.1 V. The cause for the potential differences is assumed to be attributed to the resistance of the glass-ceramic separator. By using the Equation 7.1, the conductivity of the glass-ceramic can be calculated where R is the resistance (c.a. 200 ohms), L is the thickness (c.a. 60 micrometres) and A is the area (c.a. 0.785 cm^2). The calculated conductivity was 1.53×10^{-4} S cm^{-1}, which agreed with the value provided by the seller which is quoted to be between 1×10^{-4} and 4×10^{-4} S cm^{-1}.

$$\sigma = RL/A \quad \text{(Equation 7.1)}$$

It can be also seen that the first charge capacity was reduced with the addition of the glass ceramic, which is reflected by the improved Coulombic efficiency shown in Fig. 7.7. This is an evidence of the suppressed shuttling effect. However, lower capacities and faster capacity fading were observed by adding the glass-ceramic separator. The reason for that is not clear. It could be related to degradation of the glass-ceramic, but further work is needed to clarify this point. In addition, the cell designs also need to be improved in the future.

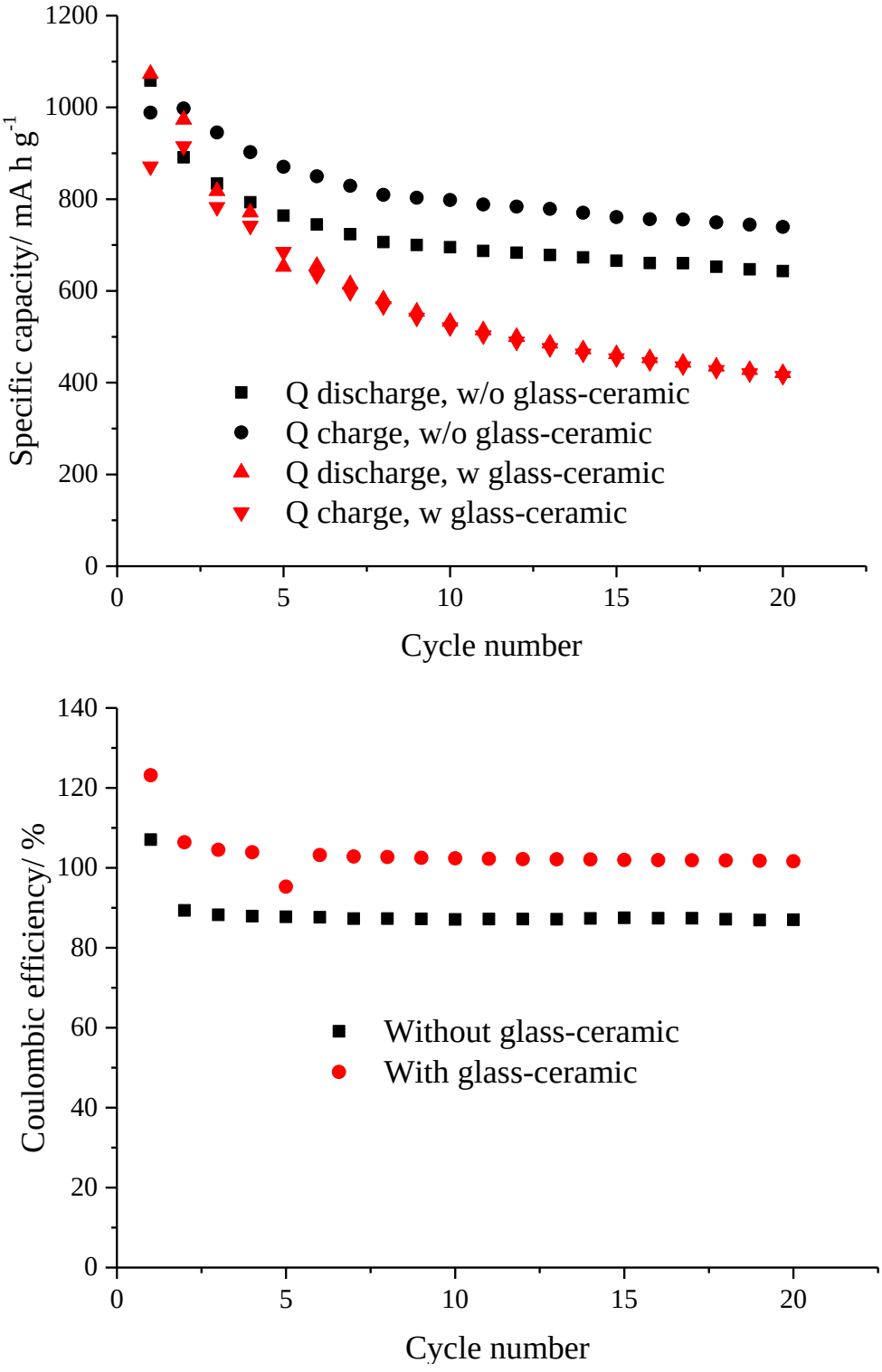

Figure 7.7 Discharge capacities and Coulombic efficiencies of Li–S cells with and without glass–ceramic (G–C) separator. The discharge rate was 0.1 C.

After cycling the cells were took apart and examined. As shown in Figure 7.8, from the colours of the two separators, it can be seen that the glass–fibre separator contacting with sulfur electrode became brown (the original colour was white), which was due to the polysulfides residues in the separator. Since the colour change also occurred to the middle part of the glass–ceramic separator, it

is possible that the colour change was the result of the attack from the polysulfides. More experiments need to be done in order to find out whether this discolouration will affect the performance of the separator. Colour change was not observed in the glass-fibre separator contacting with lithium. This is another evidence to prove that the glass-ceramic separator have successfully stopped the diffusion of polysulfides to the lithium metal.

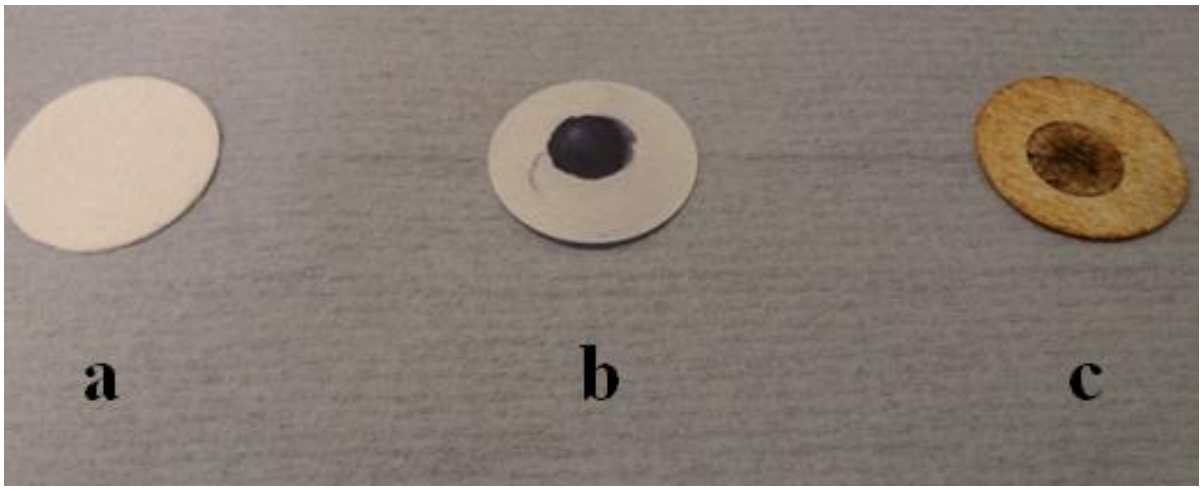

Figure 7.8 Picture of glassy-fibre separator contacting with Li (a), the glass-ceramic separator (b) and the glassy-fibre separator contacting with S/C electrode (c) after 20 cycles. The picture was taken right after the cell was dissembled.

In this chapter, two methods have been tested to improve the Coulombic efficiency of Li-S cells. Although using a physical barrier (e.g. glass-ceramic separator) can completely supress the shuttling effect, its low ion conductivity and fragility are limiting its applications in Li-S cells. In addition, its high cost might not be favourable for practical use. The usage of electrolyte additives (e.g. $LiNO_3$) achieved good Coulombic efficiencies with relatively low cost, but the side reaction with $LiNO_3$ is a potential obstacle for deep discharge.

7.3 Washing Sulfur/Carbon Composite with Carbon Disulfide (CS_2)

7.3.1 Introduction

Previously, Wang et al.[20] suggested that by immersing S/C composites in CS_2, sulfur could be washed out from the pores due to the high solubility of sulfur in CS_2[21]. The pore size distribution measurements showed that the sulfur in the

relatively larger pores were more easily to be washed out. After the washing process, the cell was able to operate reversibly over 800 cycles with a 1.8 C discharge/recharge rate. The good cycling performance was attributed to the integration of a micropore reactor, a mesopore ion reservoir, and carbon as electron conductor.

In this experiment, similar washing steps were added to the S-Elorit composite preparation process. 1.25 g of S/C composite with 50 wt% sulfur content prepared via heating method was mixed with 10 ml of CS_2 (Sigma-Aldrich, ACS reagent, 99.9 %) and stirred for 5 min and 15 min respectively. Then the mixture was quick filtered with filter paper (Whatman). By drying the solid under vacuum overnight, the washed S-Elorit composite was resulted. The electrode preparation and cell assembling were the same as described in Chapter 5.

7.3.2 Results and Discussion

7.3.2.1 Pore Size Distribution Analysis

Surface area tests were performed in order to learn the effect of washing process on the sulfur impregnation in the porous structure. As shown in Fig. 7.9, part of the pore size was recovered by the washing process, suggesting a significant amount of sulfur in Elorit was dissolved in CS_2. From the pore size distribution, it can be seen that the recovered pores mainly had diameters above 4 nm, suggesting the sulfur in small pores was less likely to be washed off. In addition, by extending the washing time to 15 minutes, it can be seen that only a small amount of sulfur was further washed. Since under room temperature, the solubility of sulfur was approximately 24 wt%[21], which was much higher than the sulfur concentration when all sulfur was dissolved. Therefore, it is possible that after 5 minutes, the remaining sulfur in the composites, which mainly in micropores, was much less accessible for CS_2.

Two methods were used to determine the amount of sulfur remaining in the composites. One approach was to calculate the weight of sulfur lost during the washing process by weighing the mass of S/C composite before and after washing step. In this case, the sulfur remaining in the composites can be calculated.

Alternatively, cumulative pore volume obtained from BJH experiments can be used to calculate the sulfur content. In Chapter 6 (Fig. 6.4), the relationship

between the specific total pore volume of carbon and the sulfur content in heated sulfur/Elorit composite was obtained and expressed by:

$$y = 0.405 - 0.513x \quad \text{(Equation 7.2)}$$

In which y is the total pore volume (cc g^{-1}) and x is the weight ratio of sulfur to carbon. Therefore, using this equation, the sulfur content can be determined by solving the cumulative pore volumes. The sulfur contents calculated via both methods were recorded in Table 7.1. Both methods showed very similar values of sulfur contents. Because errors might occur during the filtering process, the value obtained from the second method is used in this section.

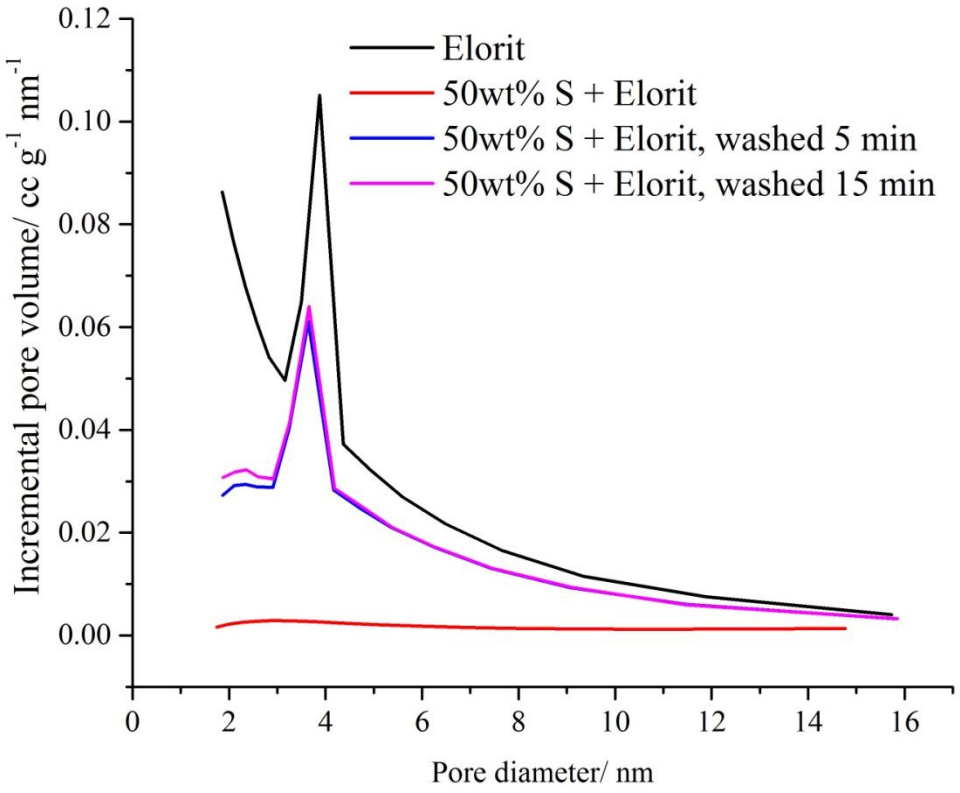

Figure 7.9 BJH pore size distributions of Elorit, S/Elorit composites before and after washing with CS_2.

Table 7.1 Sulfur content of CS_2 washed S/C composites calculated from different methods.

Preparation time	Sulfur content by weighing method/ wt%	Sulfur content by calculating pore volume/ wt%
5 min	19.8	21.3
15 min	18.9	20.6

7.3.2.2 Galvanostatic Cycling Tests

In order to examine the effect of the washing step on the electrochemical performance, galvanostatic cycling performance of the washed S/C composite was tested and compared to the unwashed S/C composite with similar sulfur content (20 wt%) in Fig. 7.10 and Fig. 7.11. In this section, the S/C composite washed for 15 min was tested.

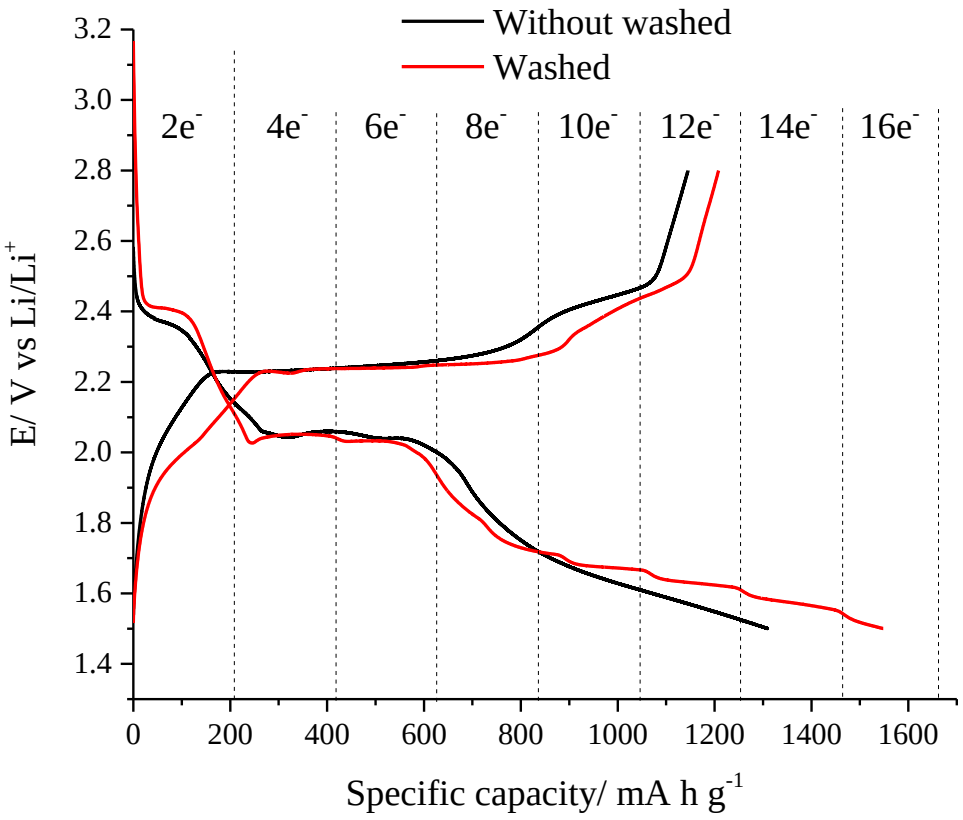

Figure 7.10 First discharge and charge profiles of Li–S cells using S/Elorit positive electrodes with 20 wt% sulfur content prepared with and without washing steps. The C-rate was 0.1 C.

In the first discharge/charge profile of Li–S cells in Fig. 7.10, dash lines were drawn to distinguish different electron numbers was added to or drawn from sulfur (S_8 molecule was used to present sulfur). From the graph, it can be seen that two cells had similar discharge plateaus before the 8th electrons was added to sulfur, which represented the complete formation of Li_2S_2:

$$8Li^+ + S_8 + 8e^- \rightarrow 4Li_2S_2 \text{ (Equation 7.3)}$$

After that the discharge profile of the S/C composite without washing showed a smooth slope at the end of discharge. On the other hand, the washed S/C

composite showed multiple plateaus, each of these plateaus had a capacity approximately equal to one electron transfer of sulfur. These plateaus suggest that there might be distinguishable redox species with stable discharge potentials, which needs more experimental data to confirm. The formation of these plateaus might be explained by the special structure of S/C composite resulted from the distribution of sulfur in the porous structure after the washing process – the smaller pores acted as the container for sulfur and the new cavities in carbon acted as a reaction chambers for dissolved lithium polysulfides However, at the second discharge, these small plateaus could not be seen again, which might be due to that after charged again, the unique structure of washed S/C composite could not be recovered. During the first charging, a much lower charge potential was obtained when the first two electrons were drawing from the sulfur.

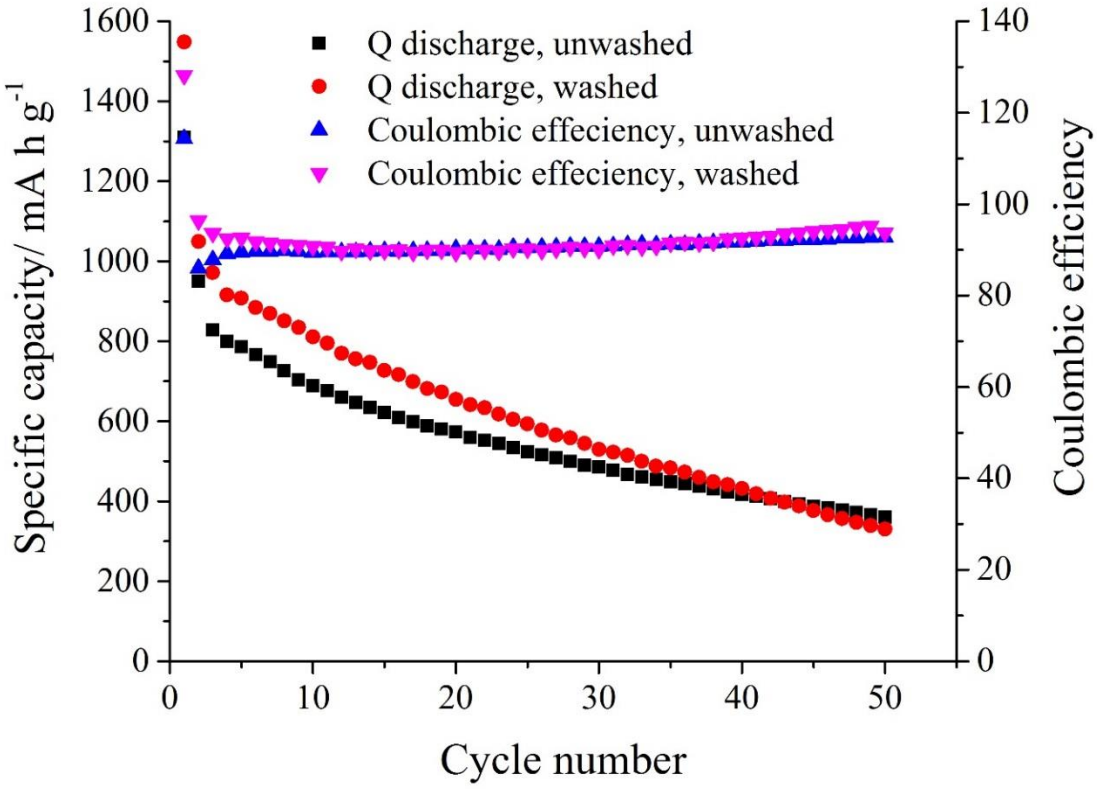

Figure 7.11 Discharge capacities and Coulombic efficiencies of Li-S cells using S/Elorit positive electrodes with 20 wt% sulfur content prepared with and without washing steps. The C-rate was 0.1 C.

From Fig. 7.11, it can be seen that after the washing step, the capacities for the first 20 cycles were improved, which might be attributed to the structure of S/C composite resulted from washing step. After 20 cycles, the capacity fading

became more severe and two cells showed similar capacities after 30 cycles, which could be due to the fact that after a few cycles, the composites in the positive electrodes became the same with or without the washing step. In addition, both cells showed similar Coulombic efficiencies.

7.4 Summary

In this chapter, different modifications have been made to Li-S cells in order to improve their performances.

By adding 0.2 M of $LiNO_3$ to the electrolyte as additive, the Coulombic efficiency was significantly enhanced and the cycling capacities were slightly improved. From the results of electrochemical impedance spectroscopy, the improvement might be due to the formation of stable SEI on the surface of electrodes.

In addition, Li-ion conductive glass-ceramic was used as an additional separator in the Li-S cells. The result has shown that despite the large internal resistance resulted from the glass-ceramic, the Coulombic efficiency was indeed improved and the shuttling of polysulfides was also greatly suppressed.

Lastly, the S/C composite with 50 wt % sulfur content was washed with CS_2 solvent. From the pore size distributions, it can be seen that sulfur in the larger pores was more likely to be washed off. The galvanostatic cycling results did not show significant improvement after adding the washing step. From the discharge curve, multiple discharge plateaus were observed. It is assumed that these plateaus represent different polysulfide species.

7.5 Reference

1 X. Liang, Z. Y. Wen, Y. Liu, M. F. Wu, J. Jin, H. Zhang and X. W. Wu, *J. Power Sources*, 2011, **196**, 9839–9843.

2 D. Aurbach, E. Pollak, R. Elazari, G. Salitra, C. S. Kelley and J. Affinito, *J. Electrochem. Soc.*, 2009, **156**, A694–A702.

3 S. S. Zhang and J. A. Read, *J. Power Sources*, 2012, **200**, 8277–8282.

4 R. Xu, J. C. M. Li, J. Lu, K. Amine and I. Belharouak, *J. Mater. Chem. A*, 2015, **3**, 4170–4179.

5 S. Xiong, K. Xie, Y. Diao and X. Hong, *J. Power Sources*, 2014, **246**, 840–845.

6 B. Sun, X. Huang, S. Chen, J. Zhang and G. Wang, *RSC Adv.*, 2014, **4**, 11115–11120.

7 J. Uddin, V. S. Bryantsev, V. Giordani, W. Walker, G. V. Chase and D. Addison, *J. Phys. Chem. Lett.*, 2013, **4**, 3760–3765.

8 W. Walker, V. Giordani, J. Uddin, V. S. Bryantsev, G. V Chase and D. Addison, *J. Am. Chem. Soc.*, 2013, **135**, 2076–2079.

9 S. S. Zhang, *J. Electrochem. Soc.*, 2012, **159**, A920–A923.

10 N. Kamaya, K. Homma, Y. Yamakawa, M. Hirayama, R. Kanno, M. Yonemura, T. Kamiyama, Y. Kato, S. Hama, K. Kawamoto and A. Mitsui, *Nat. Mater.*, 2011, **10**, 682–686.

11 J. Hassoun and B. Scrosati, *Adv. Mater.*, 2010, **22**, 5198–5201.

12 X. Zhu, Z. Wen, Z. Gu and Z. Lin, *J. Power Sources*, 2005, **139**, 269–273.

13 N. Machida, K. Kobayashi, Y. Nishikawa and T. Shigematsu, *Solid State Ionics*, 2004, **175**, 247–250.

14 T. Kobayashi, Y. Imade, D. Shishihara, K. Homma, M. Nagao, R. Watanabe, T. Yokoi, A. Yamada, R. Kanno and T. Tatsumi, *J. Power Sources*, 2008, **182**, 621–625.

15 M. Nagao, A. Hayashi and M. Tatsumisago, *Electrochem. Commun.*, 2012, **22**, 177–180.

16 A. Hayashi, T. Ohtomo, F. Mizuno, K. Tadanaga and M. Tatsumisago, *Electrochem. Commun.*, 2003, **5**, 701–705.

17 C. Yada, Y. Iriyama, T. Abe, K. Kikuchi and Z. Ogumi, *Electrochem. Commun.*, 2009, **11**, 413–416.

18 J. Xie, N. Imanishi, T. Zhang, a. Hirano, Y. Takeda and O. Yamamoto, *J. Power Sources*, 2009, **189**, 365–370.

19 K. Liu and C.-A. Wang, *Electrochem. Commun.*, 2014, **48**, 147–150.

20 D. W. Wang, G. M. Zhou, F. Li, K. H. Wu, G. Q. Lu, H. M. Cheng and I. R. Gentle, *Phys. Chem. Chem. Phys.*, 2012, **14**, 8703–8710.

21 B. Meyer, J. Austin and D. Jensen, *J. Chem. Eng. Data*, 1971, **13**, 364–366.

Chapter 8: Conclusions

8.1 Conclusions on Li-Air Batteries

As a potential alternative of electric vehicle battery, Li-air battery has been widely investigated due to its high theoretical specific capacity and energy. However, one of the main problem remain to be solved in a non-aqueous Li-air battery system is that the final product of the oxygen reduction reaction (Li_2O_2) will form a passivation layer on the electrode and lead to capacity fading.

Previously, many attempts have been made to avoid the passivation such as using porous carbons with high surface areas as positive electrodes or using catalysts/mediators in the system. In this work, the main aim is to find homogeneous mediators for both ORR and OER.

First, ethyl viologen (EtV) was examined as the mediator for ORR. Using UV/Vis spectroscopy, the reaction stoichiometry between oxygen and EtV was measured. The results showed that EtV could facilitate a 2-electron reduction of oxygen in aprotic solvents. Further results showed that EtV and superoxide underwent a reversible reaction in the presence of high Li^+ concentrations, which could be helpful in order to decrease the lifetime of superoxide radicals. The reaction mechanism was also determined by kinetic analysis, showing that Li^+ was involved in the reaction between EtV and superoxide radicals. Preliminary electrochemical tests were performed to examine the electrochemical behaviour of EtV. The galvanostatic cycling results showed that EtV could greatly enhance the discharge capacity of oxygen reduction in the test cell. The study of ORR mediators in non-aqueous electrolytes is relatively a new area. Compared to heterogeneous catalysts such as Pt in aqueous systems[1-3], homogeneous mediators like EtV shows better reaction rate and lower expenses. Its cycling performances require further study before it can be applied in a Li-air battery.

Next, bis-terpyridine cobalt ($Co^{II/III}(terpy)_2^{2+/3+}$) was tested as an OER mediator in Li-air batteries. The results from UV/Vis spectroscopy showed that $Co^{III}(terpy)_2^{3+}$ could reversibly oxidise lithium peroxide to oxygen, forming $Co^{II}(terpy)_2^{2+}$. The effect of electrolytes were also studied: by comparing diglyme, TEGDME and $Pyr_{14}TFSI$, diglyme was determined as the most suitable electrolyte solvent. On the one hand, galvanostatic cycling results showed that $Co(terpy)_2^{2+}$ improved the charge capacity of Li-air batteries due to the mediation effect. On the other hand, $Co^{III}(terpy)_2^{3+}$ improved the discharge capacity as a catalyst for OER, which

significantly alleviate the electrode passivation. Compared with other homogeneous OER mediators such as TTF[4], TEMPO[5] and LiI[6], this cobalt compound shows a good reaction reversibility and cycling stability. Therefore, it can be concluded that bis-terpyridine cobalt could be potentially chosen as a mediator in Li-air cells. However, further cycling tests with a better cell design are required to have a better understanding of its properties.

8.2 Conclusions on Li-S Batteries

Apart from Li-air battery system, Li-S battery is another promising energy storage system for electric vehicles. The high abundancy and low costs of sulfur have made Li-S battery a favourable choice. However, the insulating property of sulfur and the sulfur/polysulfide shuttling effect still require more investigation. As a result, porous carbons have been widely chosen as the conductive materials for Li-S batteries. In this work, two types of carbons were tested: carbon blacks and activated carbons.

First, the sulfur/carbon composites were prepared by different methods (ball milling and heating) and different mass ratio. By characterising the composites by the surface area (BET model) and pore size distribution (BJH model) measurement, it could be inferred that for carbon blacks, different preparation methods resulted in different sulfur impregnation. The heated sulfur/carbon black composites showed marked pore volume decrease in carbon while the ball milled composites showed little pore volume change. In addition, the quantitative analysis showed that even heated sample showed incomplete sulfur insertion. Which might be due to the layered structure of carbon black particles. For sulfur/activated carbon, both methods showed complete sulfur insertion into the pores, which may be due to the pores of activated carbon are located on the surfaces of the carbon particles. The XRD measurements were also performed, the results agreed with the assumptions above.

The electrochemical performances of those composites were tested using Swagelok cells. In general, the cells suffered low initial capacities with higher sulfur loading, which might be due to the limited numbers of three-phase junctions for electrolyte, carbon and sulfur species. However, the capacity retention was better with higher sulfur loading. As for different methods, the difference was not very clear at low sulfur loading. At higher sulfur loading, the heating method showed higher capacity for activated carbon and inferior cycling performance for carbon black. A few assumptions have been proposed, however,

no clear conclusion can be made at this point, which might require further investigation. With 50wt% sulfur loading, the initial capacity (650 mA h/g) and the capacity after 50 cycles (400 mA h/g) are still much lower than the highest reported capacities[7] (1070 mA h/g for the first cycle and 973 mA h/g after 100 cycles). Therefore, improvements still need to be done in terms of cell design and electrode preparation.

Furthermore, some modifications have been made to Li-S cells. By adding $LiNO_3$ to the electrolyte, the Coulombic efficiencies were significantly improved. By adding a glass-ceramic separator, the shuttle effect was suppressed, however the inner resistance significantly increased. By washing S/C composite with CS_2 well defined discharge plateaus were observed, which requires further study.

8.3 Reference

1 N. M. Marković and P. N. Ross, Jr., *Surf. Sci. Rep.*, 2002, **45**, 117–229.

2 P. Strasser, S. Koh, T. Anniyev, J. Greeley, K. More, C. Yu, Z. Liu, S. Kaya, D. Nordlund, H. Ogasawara, M. F. Toney and A. Nilsson, *Nat Chem*, 2010, **2**, 454–460.

3 J. R. Kitchin, J. K. Nørskov, M. A. Barteau and J. G. Chen, *J. Chem. Phys.*, 2004, **120,** 10240–10246.

4 Y. Chen, S. A. Freunberger, Z. Peng, O. Fontaine and P. G. Bruce, *Nat Chem*, 2013, **5**, 489–494.

5 B. J. Bergner, A. Schürmann, K. Peppler, A. Garsuch and J. Janek, *J. Am. Chem. Soc.*, 2014, **136**, 15054–15064.

6 H.-D. Lim, H. Song, J. Kim, H. Gwon, Y. Bae, K.-Y. Park, J. Hong, H. Kim, T. Kim, Y. H. Kim, X. Lepró, R. Ovalle-Robles, R. H. Baughman and K. Kang, *Angew. Chem. Int. Ed.*, 2014, **53**, 3926–3931.

7 N. Jayaprakash, J. Shen, S. S. Moganty, A. Corona and L. A. Archer, *Angew. Chemie-International Ed.*, 2011, **50**, 5904–5908.

Appendices

Appendix 1

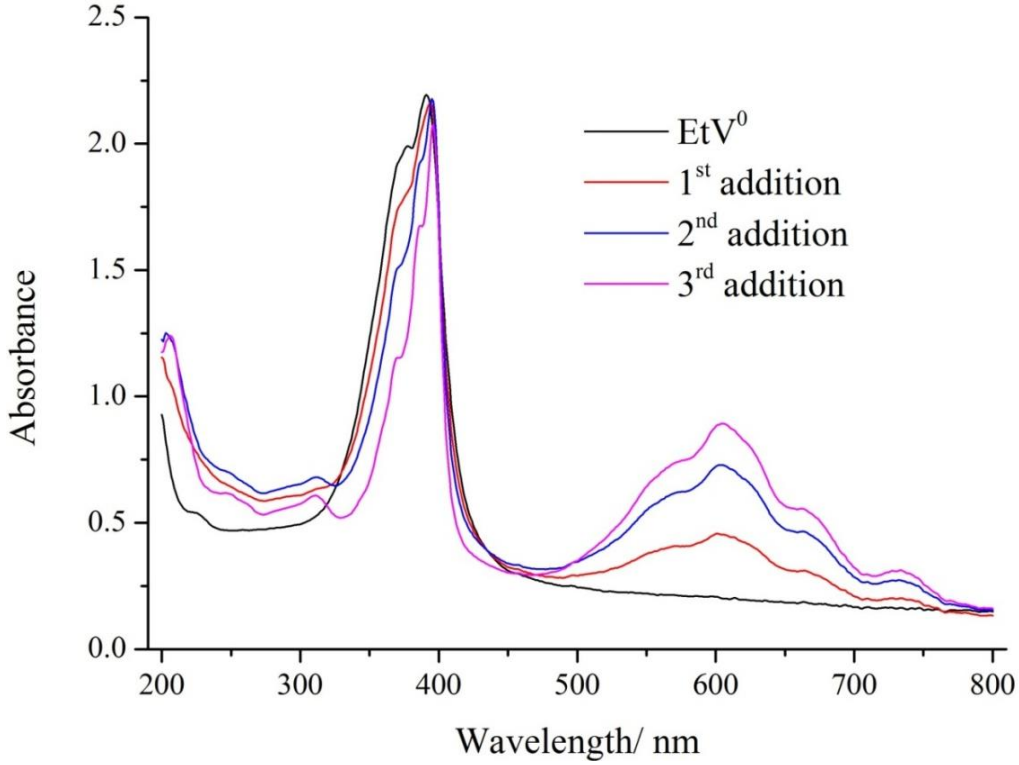

Figure A 1 UV-Vis spectra measuring the stepwise additions of EtV^{2+} solution into an EtV^{0} solution in the same concentration of 0.05 mM.

Appendix 2

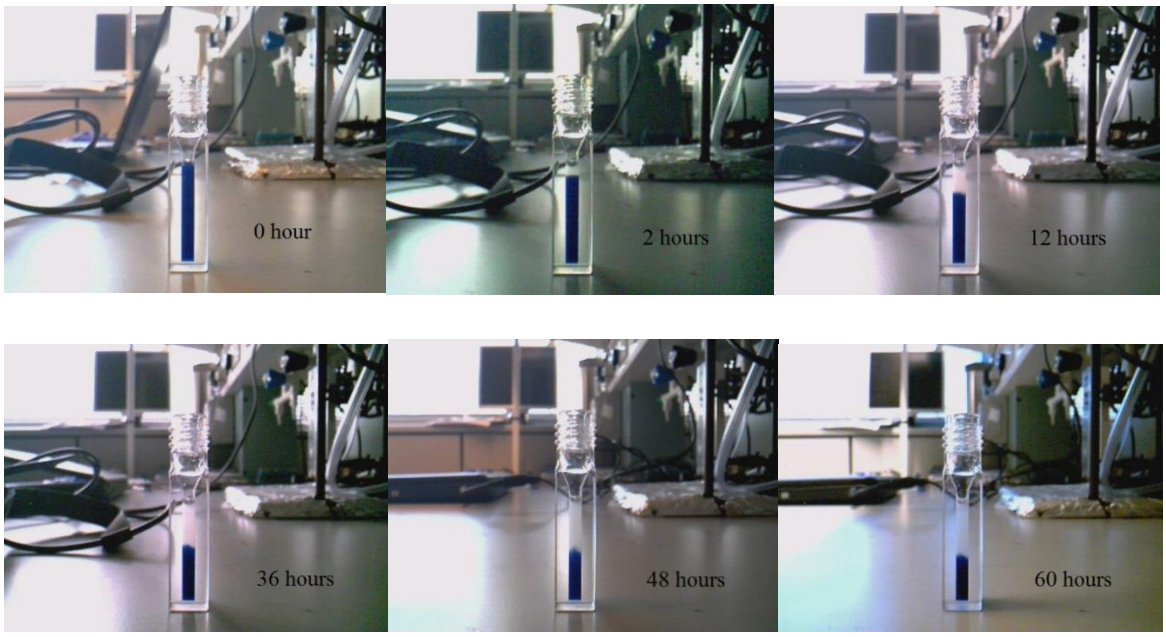

Figure A 2 Photos of 1 mM EtV^{+} solution in $Pyr_{14}TFSI$ exposed in the open air for different periods of time.

Appendix 3

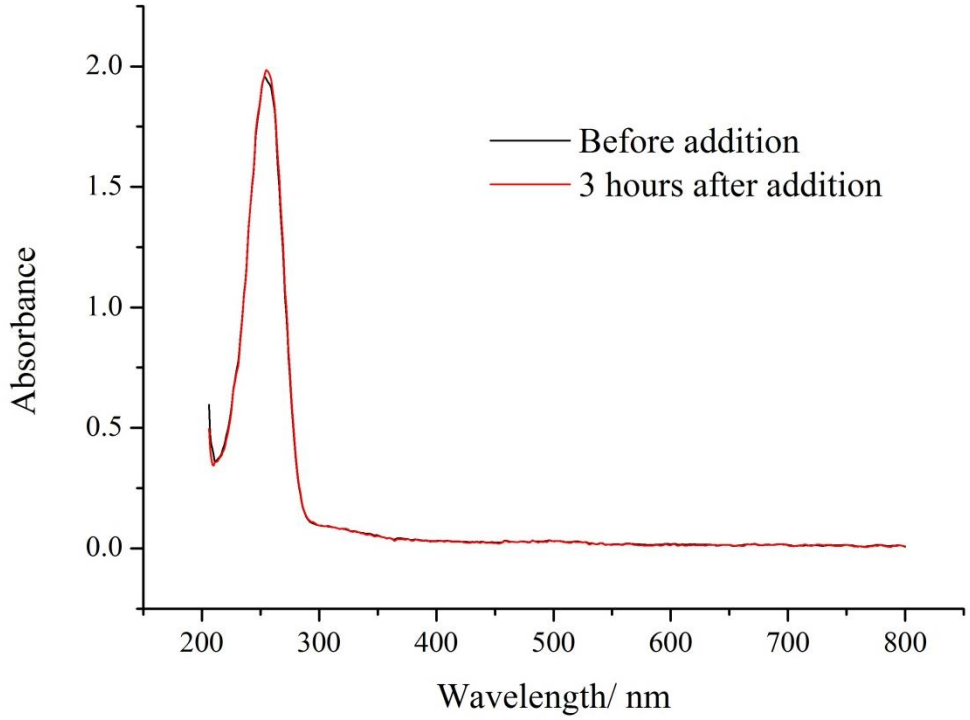

Figure A 3 UV-Vis spectra of 1 mM of KO_2 in acetonitrile before and 3 hours after addition of 300 mM LiTFSI.

Appendix 4

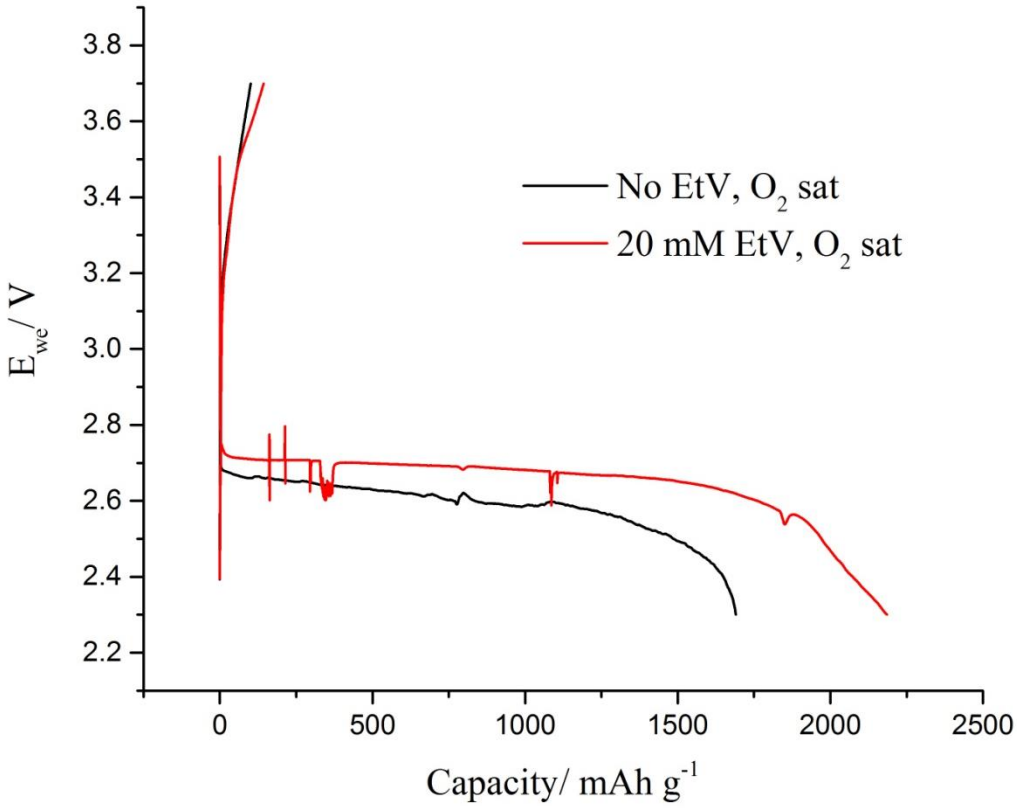

Figure A 4 Galvanostatic discharge curve of cells using carbon coated glassy carbon electrode in diglyme containing 0.1 M LiTFSI, with and without 20 mM EtV.

Appendix 5

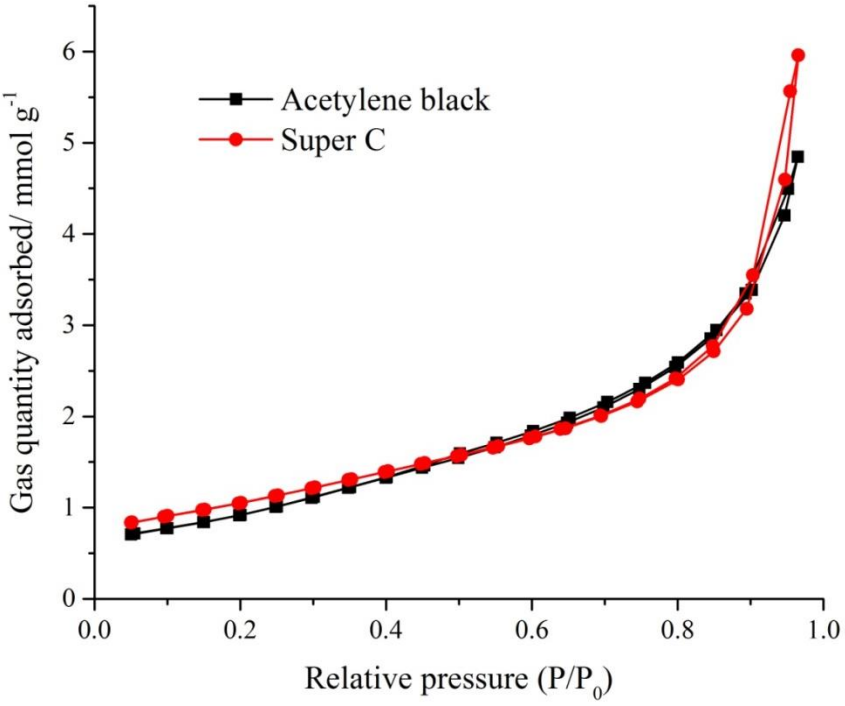

Figure A 5 Nitrogen adsorption/desorption isotherms of acetylene black and Super C.

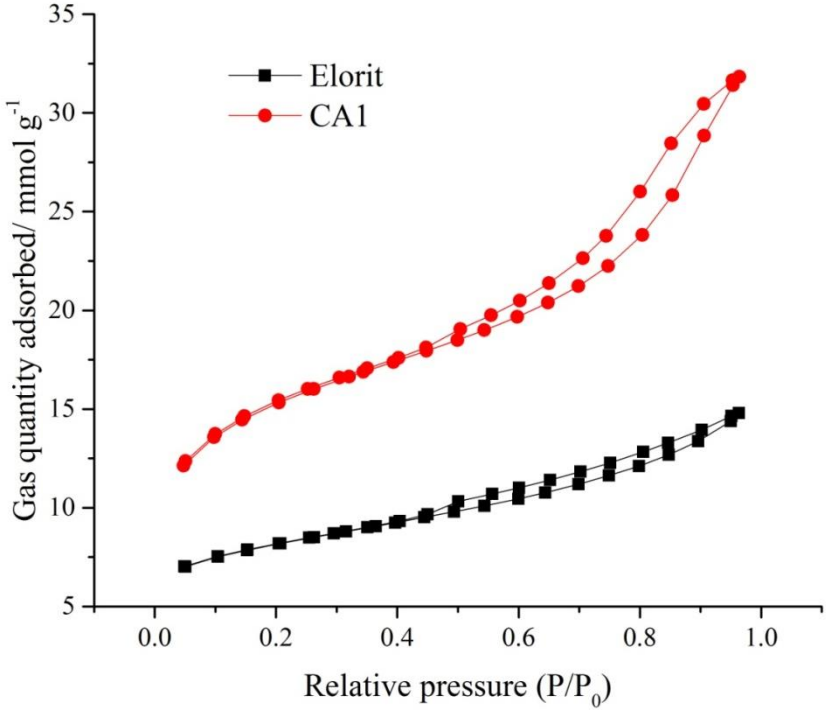

Figure A 6 Nitrogen adsorption/desorption isotherms of Elorit and CA1.

Appendix 6

Figure A 7 Sulfur powders before (left) and after (right) heating treatment.

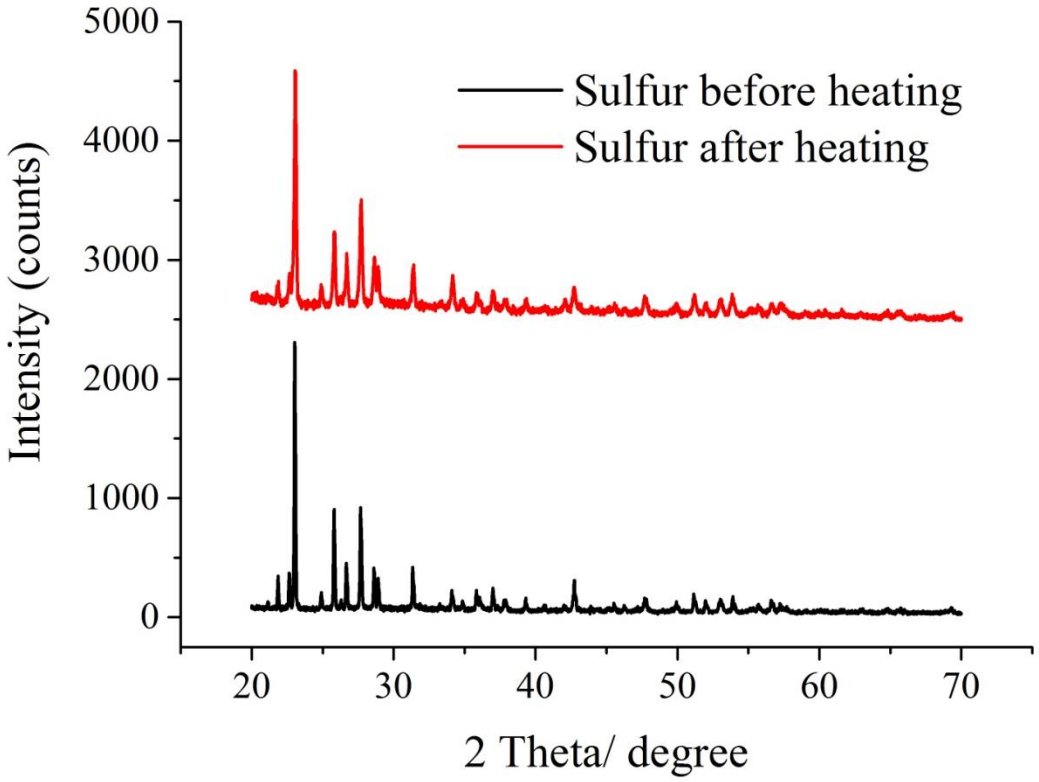

Figure A 8 XRD patterns of sulfur before and after heating treatment.

Appendix 7

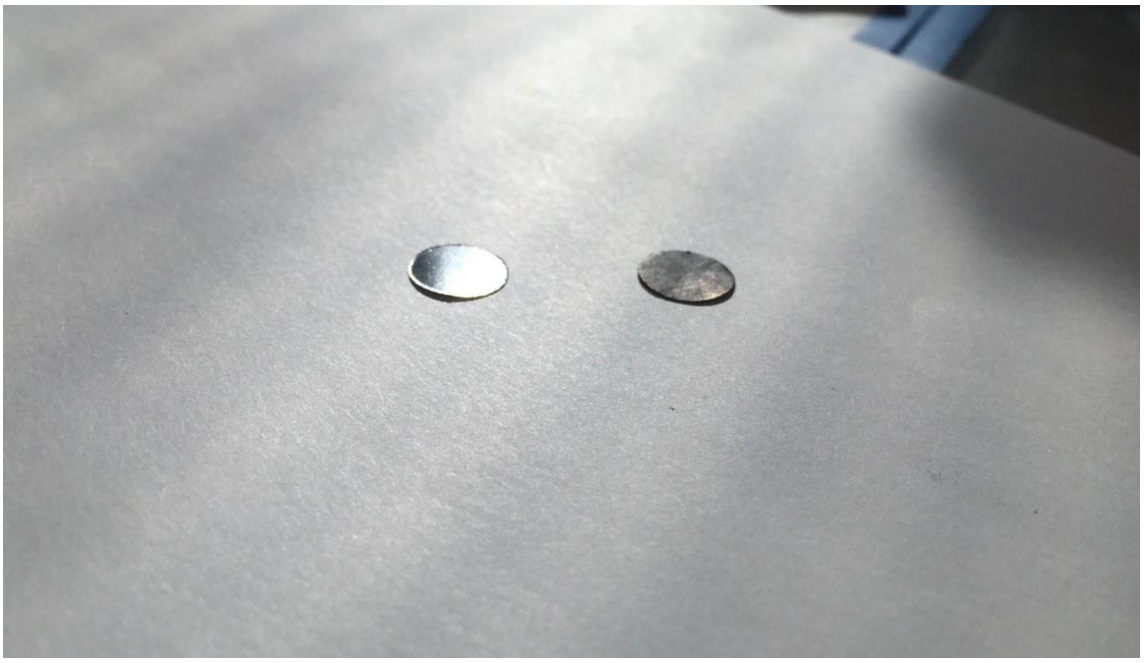

Figure A 9 Carbon (left – acetylene black; right – Elorit) pellets with 20 wt% PTFE under light.

Title:	Lithium–Air Battery: Promise and Challenges
Author:	G. Girishkumar, B. McCloskey, A. C. Luntz, et al
Publication:	Journal of Physical Chemistry Letters
Publisher:	American Chemical Society
Date:	Jul 1, 2010

PERMISSION/LICENSE IS GRANTED FOR YOUR ORDER AT NO CHARGE

This type of permission/license, instead of the standard Terms & Conditions, is sent to you because no fee is being charged for your order. Please note the following:

- Permission is granted for your request in both print and electronic formats, and translations.
- If figures and/or tables were requested, they may be adapted or used in part.
- Please print this page for your records and send a copy of it to your publisher/graduate school.
- Appropriate credit for the requested material should be given as follows: "Reprinted (adapted) with permission from (COMPLETE REFERENCE CITATION). Copyright (YEAR) American Chemical Society." Insert appropriate information in place of the capitalized words.
- One-time permission is granted only for the use specified in your request. No additional uses are granted (such as derivative works or other editions). For any other uses, please submit a new request.

If credit is given to another source for the material you requested, permission must be obtained from that source.

BACK CLOSE WINDOW

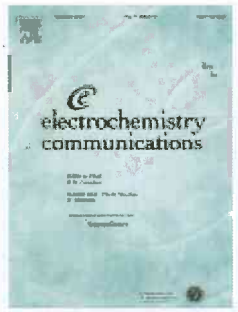

Title:	A redox shuttle to facilitate oxygen reduction in the lithium air battery
Author:	Matthew J. Lacey,James T. Frith,John R. Owen
Publication:	Electrochemistry Communications
Publisher:	Elsevier
Date:	January 2013

Order Completed

Thank you very much for your order.

This is a License Agreement between Luyi Yang ("You") and Elsevier ("Elsevier"). The license consists of your order details, the terms and conditions provided by Elsevier, and the payment terms and conditions.

Get the printable license.

License Number	3693041239742
License date	Aug 20, 2015
Licensed content publisher	Elsevier
Licensed content publication	Electrochemistry Communications
Licensed content title	A redox shuttle to facilitate oxygen reduction in the lithium air battery
Licensed content author	Matthew J. Lacey,James T. Frith,John R. Owen
Licensed content date	January 2013
Licensed content volume number	26
Licensed content issue number	n/a
Number of pages	3
Type of Use	reuse in a thesis/dissertation
Portion	figures/tables/illustrations
Number of figures/tables/illustrations	1
Format	both print and electronic
Are you the author of this Elsevier article?	No
Will you be translating?	No
Original figure numbers	Scheme 1
Title of your thesis/dissertation	Batteries beyond lithium-ion: investigation of Li/air battery and Li/S battery
Expected completion date	Sep 2015
Estimated size (number of pages)	200
Elsevier VAT number	GB 494 6272 12
Permissions price	0.00 USD
VAT/Local Sales Tax	0.00 USD / 0.00 GBP
Total	0.00 USD

ORDER MORE... CLOSE WINDOW

Title: TEMPO: A Mobile Catalyst for Rechargeable Li-O2 Batteries

Author: Benjamin J. Bergner, Adrian Schürmann, Klaus Peppler, et al

Publication: Journal of the American Chemical Society

Publisher: American Chemical Society

Date: Oct 1, 2014

PERMISSION/LICENSE IS GRANTED FOR YOUR ORDER AT NO CHARGE

This type of permission/license, instead of the standard Terms & Conditions, is sent to you because no fee is being charged for your order. Please note the following:

- Permission is granted for your request in both print and electronic formats, and translations.
- If figures and/or tables were requested, they may be adapted or used in part.
- Please print this page for your records and send a copy of it to your publisher/graduate school.
- Appropriate credit for the requested material should be given as follows: "Reprinted (adapted) with permission from (COMPLETE REFERENCE CITATION). Copyright (YEAR) American Chemical Society." Insert appropriate information in place of the capitalized words.
- One-time permission is granted only for the use specified in your request. No additional uses are granted (such as derivative works or other editions). For any other uses, please submit a new request.

If credit is given to another source for the material you requested, permission must be obtained from that source.

BACK CLOSE WINDOW

nature publishing group

Title:	A highly ordered nanostructured carbon-sulphur cathode for lithium-sulphur batteries
Author:	Xiulei Ji, Kyu Tae Lee and Linda F. Nazar
Publication:	Nature Materials
Publisher:	Nature Publishing Group
Date:	May 17, 2009

Order Completed

Thank you very much for your order.

This is a License Agreement between Luyi Yang ("You") and Nature Publishing Group ("Nature Publishing Group"). The license consists of your order details, the terms and conditions provided by Nature Publishing Group, and the payment terms and conditions.

Get the printable license.

License Number	3693050605007
License date	Aug 20, 2015
Licensed content publisher	Nature Publishing Group
Licensed content publication	Nature Materials
Licensed content title	A highly ordered nanostructured carbon-sulphur cathode for lithium-sulphur batteries
Licensed content author	Xiulei Ji, Kyu Tae Lee and Linda F. Nazar
Licensed content date	May 17, 2009
Type of Use	reuse in a dissertation / thesis
Volume number	8
Issue number	6
Requestor type	academic/educational
Format	print and electronic
Portion	figures/tables/illustrations
Number of figures/tables/illustrations	1
High-res required	no
Figures	Schematic diagram of the sulphur (yellow) confined in the interconnected pore structure of mesoporous carbon, CMK-3
Author of this NPG article	no
Your reference number	None
Title of your thesis / dissertation	Batteries beyond lithium-ion: investigation of Li/air battery and Li/S battery
Expected completion date	Sep 2015
Estimated size (number of pages)	200
Total	0.00 USD

ORDER MORE... CLOSE WINDOW

Title: Graphene-Wrapped Sulfur Particles as a Rechargeable Lithium–Sulfur Battery Cathode Material with High Capacity and Cycling Stability

Author: Hailiang Wang, Yuan Yang, Yongye Liang, et al

Publication: Nano Letters

Publisher: American Chemical Society

Date: Jul 1, 2011

PERMISSION/LICENSE IS GRANTED FOR YOUR ORDER AT NO CHARGE

This type of permission/license, instead of the standard Terms & Conditions, is sent to you because no fee is being charged for your order. Please note the following:

- Permission is granted for your request in both print and electronic formats, and translations.
- If figures and/or tables were requested, they may be adapted or used in part.
- Please print this page for your records and send a copy of it to your publisher/graduate school.
- Appropriate credit for the requested material should be given as follows: "Reprinted (adapted) with permission from (COMPLETE REFERENCE CITATION). Copyright (YEAR) American Chemical Society." Insert appropriate information in place of the capitalized words.
- One-time permission is granted only for the use specified in your request. No additional uses are granted (such as derivative works or other editions). For any other uses, please submit a new request.

If credit is given to another source for the material you requested, permission must be obtained from that source.